Ultrasonic Evaluation of Microstructure in Pipe Steels

by

Jacob Kennedy

A thesis submitted in partial fulfillment of the requirements for the degree of

Master of Science

in
Materials Engineering

Department of Chemical and Materials Engineering
University of Alberta

Abstract

Traditionally in pipeline steels and welds, ultrasonic testing (UT) has been used for crack and/or flaw detection. The work presented in this Thesis explores the use of this technique to characterize the microstructure of pipe steels. Ultrasonic velocity calculations, for shear and longitudinal waves, done with the stiffness tensor of a 1050 steel showed that shear velocity exhibits a greater difference between structures such as ferrite, mixed ferrite-pearlite, and martensite, than longitudinal velocity. Experiments were carried out, through thickness skelp investigation of L80 and X70 steels, annealing of interstitial free steel and structure variation in L80, 4130 and 5160. The ultrasonic velocity and attenuation of shear and longitudinal waves were measured through the thickness of L80 and X70 pipe skelps and did not vary significantly. XRD was performed through the thickness as well. Interstitial free steel was ultrasonically tested at room temperature after different annealing times. Both shear and longitudinal ultrasonic velocity changed as recrystallization progressed, while attenuation changed during grain growth. Structure variations after heat treatment in L80, 4130 and 5160 all showed a decrease in ultrasonic shear wave velocity in martensite when compared with mixed structure of ferrite and pearlite, confirming the velocity calculation results. The longitudinal velocity did not vary with structure. The attenuation of both shear and longitudinal waves also decreased in martensite compared with mixed ferrite-pearlite. Both shear and longitudinal ultrasonic waves had properties which varied with different structural properties and had the potential to be useful tools in microstructural characterization. The ultrasonic shear velocity showed a decrease from ferrite-pearlite (3268 m/s) to martensite (3207 m/s) as did the longitudinal attenuation (0.25 dB/mm for ferrite-pearlite and 0.17 dB/mm for martensite)

Acknowledgements

I would like to thank my supervisors Professor Hani Henein and Professor Douglas Ivey for their support and guidance. I would also like to thank Dr. Barry Wiskel for his input and counsel through the entirety of this work. Thanks to the post-doctoral fellows and students in the Advanced Materials and Processing Laboratory (AMPL), as well as Advaita Bhatnagar for her assistance with the metallography done for the L80. I could not have done this without all of you.

Special thanks also to Evraz Inc. NA, Trans-Canada Pipelines, Enbridge, Alliance Pipelines and UT Quality for their sponsorship of this work along with the Natural Sciences and Engineering Research Council (NSERC) of Canada.

Thanks to my family and friends for their help. I would also like to thank Jaime, a better partner could not have been found to support and encourage me through this work.

Table of Contents

List of Tables

List of Figures

List of Symbols and Acronyms

Symbol/Acronym	Description	Units
200	200°C Oil Cooled	
ΔA	Amplitude Difference	dB
a	Lattice Parameter	nm
A	Annealed	
AC	Air Cooled	
AL	Longitudinal Attenuation	dB/mm
AsP	Shear Attenuation Parallel To Rolling Direction	dB/mm
AsT	Shear Attenuation Transverse To Rolling Direction	dB/mm
B	Bainite	
b	Direction Of Burgers Vector	
C200	Coated 200°C Oil Cooled	
CAC	Coated Air Cooled	
C_{ij}	Component Of Stiffness Tensor	
C_{mn}	Spherical Harmonics Coefficient	
COC	Coated Oil Cooled	
CWC	Coated Water Cooled	
D	Grain Size	mm
Ds	Domain Size	nm
EBSD	Electron Backscattered Diffraction	
F	Ferrite	
f	Ultrasonic Frequency	Hz
FC	Furnace Cooled	
FE	Finite Element	
F-P	Ferrite-Pearlite	
H1	6hr At 770°C After Austenization	
H2	69hr At 770°C After Austenization	
H3	16.5hr At 770°C No Austenization	
HAGB	High Angle Grain Boundaries	
HAZ	Heat Affected Zone	
IF	Interstitial Free	
J	Texture Index	
LAGB	Low Angle Grain Boundaries	
LP	Lorentz Polarization Factor	
LUT	Laser Ultrasonic Testing	
M	Martensite	
Mo	Elastic Modulus	MPa
N	Normalized	

NDT	Non Destructive Testing	
OC	Oil Cooled	
OQ	Oil Quenched	
P	Particle Displacement Direction	
Q	Quenched	
QT1	1hr 650ºC Temper	
QT2	1hr 205ºC Temper	
R	Reflection Coefficient	Unitless
SAE	Society Of Automotive Engineers	
SS	Stainless Steel	
T	Tension	N
t	Time	s
TEM	Transmission Electron Microscope	
UT	Ultrasonic Testing	
UTS	Ultimate Tensile Strength	MPa
V	Ultrasonic Velocity	m/s
V1, V2, V3	Calculated Ultrasonic Velocities	m/s
VL	Longitudinal Velocity	m/s
Vs	Shear Velocity	m/s
VsP	Shear Velocity Parallel To Rolling Direction	m/s
VsT	Shear Velocity Transverse To Rolling Direction	m/s
WC	Water Cooled	
WQ	Water Quenched	
X	Material Thickness	mm
XRD	X-Ray Diffraction	
Y	Young's Modulus	MPa
YS	Yield Strength	MPa
Z	Acoustic Impedance	sPa/m3
A	Attenuation	dB/mm
α_1	First Critical Angle	degrees
α_2	Second Critical Angle	degrees
αA	Angle Of Incidence	degrees
B	Refracted Angle	degrees
E	Strain	mm/mm
λ	Wavelength	mm
P	Density	kg/cm3
ρ_{dis}	Dislocation Density	cm/cm3
φ_i	Texture Weighting Factor	

Introduction

Ultrasonic testing is a non-destructive test (NDT) commonly used in the oil and gas industry. Ultrasonics can be used both for testing of new construction and in-service equipment. They are most commonly used for testing new welds for defects and in-service equipment for corrosion. A thorough knowledge of how the ultrasonic wave behaves in the material is needed for accurate testing. Other researchers have investigated many steels and metals ultrasonically, but none have looked specifically at the pipeline and casing steels commonly used in the oil and gas industry. This work aims to investigate steels used in this industry in Alberta using conventional ultrasonic testing to see how microstructural characteristics affect the ultrasonic velocity and attenuation in a material.

This thesis is divided into five chapters. The literature review in Chapter 1 presents an introduction to steel microstructures and ultrasonic waves as well as a review of work done by others. Idealized calculations are done in Chapter 2 to find the ultrasonic velocity in different steel microstructures. Chapter 3 presents the experimental procedure used for each section of this work. Five sets of experiments were conducted, through thickness analysis of X70 and L80 pipe skelp using ultrasonic testing and X-ray diffraction (XRD), ultrasonic evaluation of an interstitial free (IF) steel air cooled after different annealing times, the effect of cooling rate on L80 microstructure, mechanical properties and ultrasonic velocity/attenuation, and analysis of heat treated 4130 and 5160 steels with industrial equipment. Chapter 3 tabulates the results found in each experiment. Discussion of these results can be found in Chapter 4, while Conclusions and Recommendations are in Chapter 5.

Chapter 1 Literature Review

Work done by other researchers is presented on steel microstructure, ultrasonic testing, ultrasonic wave properties and the effects of microstructure on both the ultrasonic velocity and attenuation. In addition, a review of the Rietveld refinement method for quantitative x-ray diffraction (XRD) analysis is presented.

1.1 General Concepts in Steel Microstructure

This section contains a brief overview of the steel microstructures found in this work. The steels used in this work include X70 pipeline steel, L80 casing steel, interstitial free (IF) steel, 4130 alloy steel and 5160 spring steel. Each is presented with a representative micrograph as well an overview of its structure and formation. The concept of preferential orientation or texture is also presented.

1.1.1 Phase and Structure

The properties of steel are highly dependent on the microstructure. Microstructure is affected by many factors, including processing and composition. The steels used in this work encompass both conventional steels, which are processed to take advantage of their carbon content to gain strength, and microalloyed steels, which are strengthened without high carbon contents but rather with grain refinement and precipitation. Further information on microalloyed steels and their processing is given in [1] [2] [3] [4] [5]. In this work non-microalloyed steels are heat treated to obtain specific microstructures, while the microalloyed steel is investigated in the as received state. The following sections present a basic introduction to some common microstructures found in steel.

1.1.1.1 Ferrite

Ferrite (F) is one of the most common phases found in steel. Upon equilibrium cooling all the steels used in this work (<0.7 wt% C) would contain some ferrite, as shown in the iron-iron carbide phase diagram (Figure 1.1) [6].

Ferrite can have many morphologies including polygonal and acicular [7]. Polygonal ferrite appears as large equiaxed grains like those shown in Figure 1.2. Polygonal ferrite normally appears white in bright field optical microscopy, as the grain boundaries etch preferentially to the ferrite grains. This is the case in Figure 1.2.

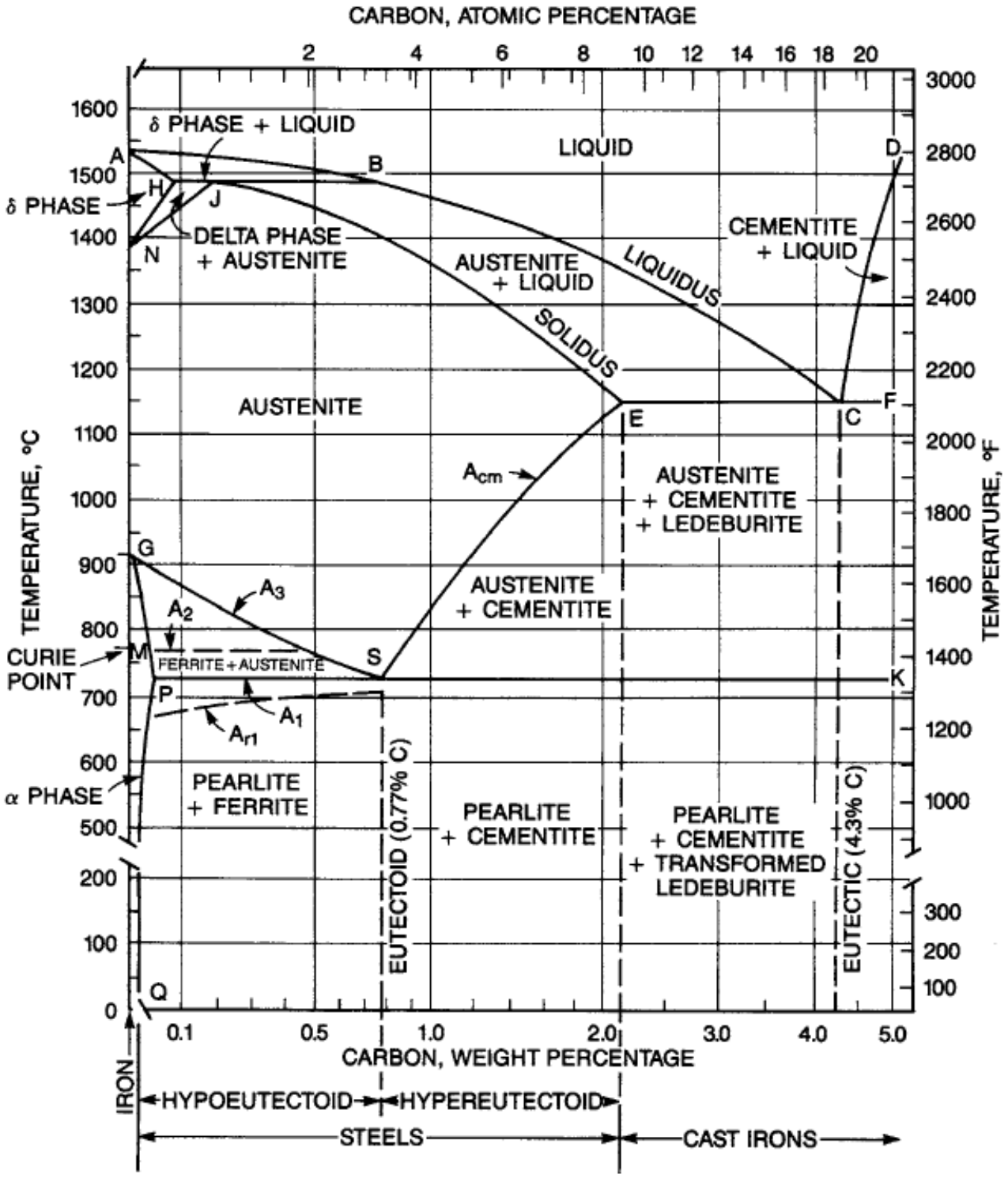

Figure 1.1: Fe-Fe_3C Phase Diagram [6]

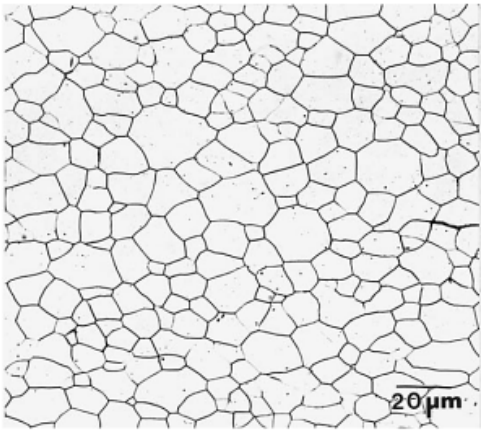

Figure 1.2: Polygonal Ferrite in 0.02 wt% C Steel [7]

An acicular microstructure (Figure 1.3) can be found in some microalloyed steels and is composed of fine ferrite plates or laths that are interwoven [3]. Acicular ferrite is formed by intergranular nucleation. This can be encouraged in microalloyed steel with titanium additions to form titanium oxides which act as ferrite nucleation sites. Vanadium additions have also been found to enhance intergranular nucleation [3].

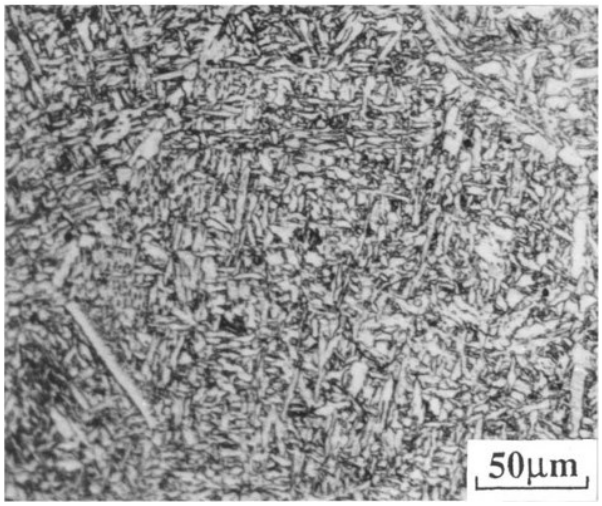

Figure 1.3: Acicular Ferrite in Microalloyed Steel [3]

1.1.1.2 Pearlite

Pearlite is a eutectoid structure of cementite (Fe_3C) and ferrite [8]. Most commonly pearlite appears as dark lamellae (Fe_3C) in a white background (ferrite). This is because cementite etches more quickly than the ferrite and appears darker than the ferrite in optical micrographs, such as Figure 1.4 from a near eutectoid steel.

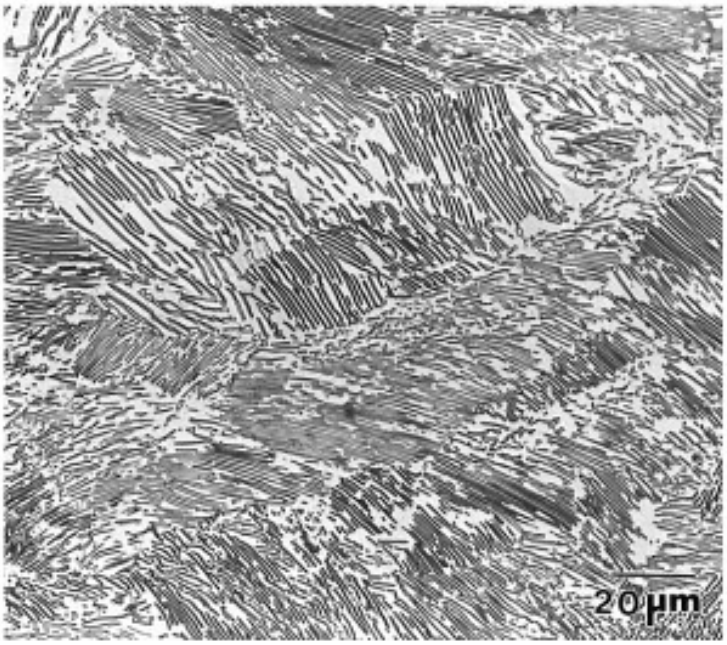

Figure 1.4: Pearlite in 0.8 wt% C Steel [7]

Ferrite-pearlite (F-P) mixed microstructures occur more often than the single structure micrographs shown in Figure 1.2 and Figure 1.4. Ferrite has a lower carbon solubility compared with the higher temperature austenite phase, as shown in the phase diagram (Figure 1.1). The ferrite formed as austenite cools has much less carbon in the matrix than the austenite, resulting in increased carbon content in the austenite. When the carbon content is too high in the austenite to form ferrite the pearlitic structure is formed instead with regions of ferrite (iron rich) and cementite (carbon rich) interspersed with each other [9]. An example of such a mixed F-P structure is shown in Figure 1.5.

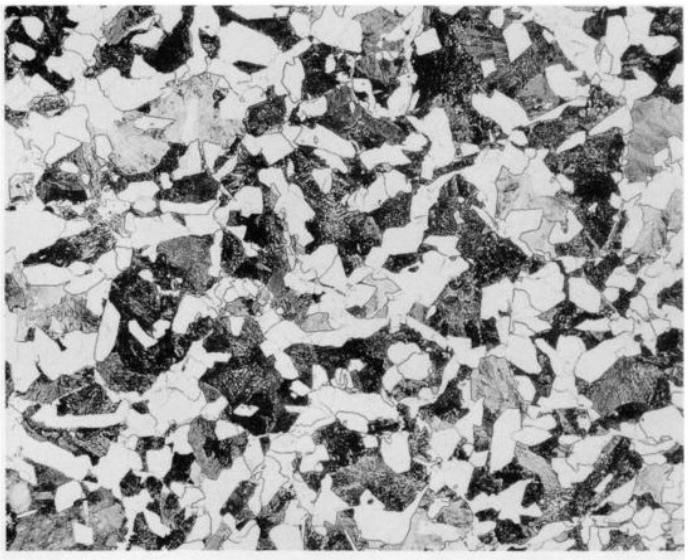

Figure 1.5: Mixed Ferrite-Pearlite Microstructure in 0.25 wt% C Steel [8]

1.1.1.3 Bainite

Bainite (B) can be formed when austenite is cooled at intermediate rates between that of air cooling and quenching [7]. Bainite is made up of ferrite and cementite, like pearlite, but in a different structure. Bainite has an acicular ferrite morphology with carbides as discrete particles [8]. Coarser bainite formed at higher temperatures with carbides at lath boundaries is called upper bainite, while finer bainite formed at lower temperatures with carbides preferring planes within the laths is called lower bainite. A sample micrograph of a bainitic structure is shown in Figure 1.6.

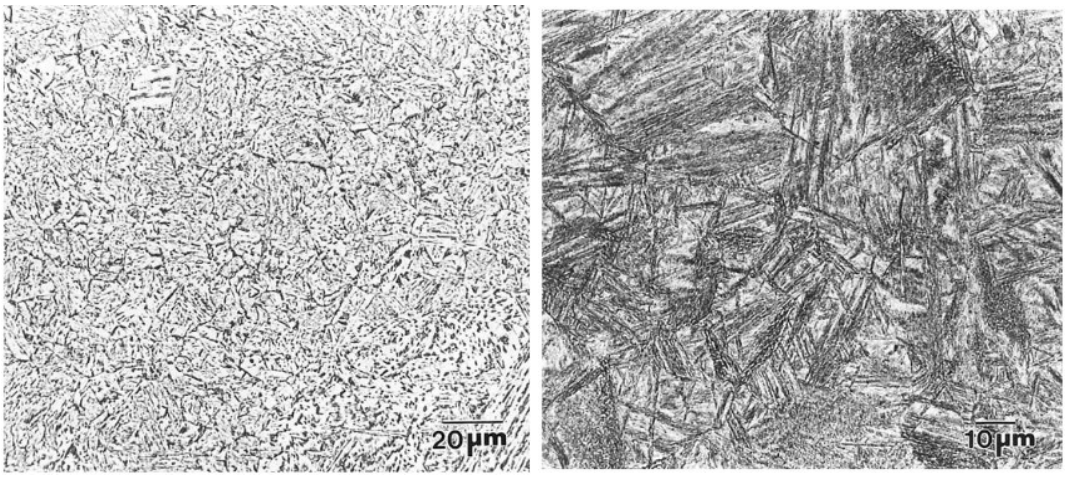

(A) (B)

Figure 1.6: (A) Upper and (B) lower Bainitic Microstructure in 8720 (0.2 %C) Steel [7]

1.1.1.4 Martensite

Martensite (M) is a structure formed by a diffusionless transformation from austenite to a supersaturated solution of carbon in iron [8]. A high cooling rate is normally required to form martensite. Martensite is characterized by a plate or lath type structure [10]. Plate martensite is more commonly formed in high carbon, nitrogen or high nitrogen alloys. Lath martensite forms when sheaves or packets of martensite grow together in parallel groups whereas plate martensite forms when the grains do not form parallel to each other and the first to form is larger than those formed after. Accommodation effects are formed when the plates impinge on one another. An example of each lath and plate type martensitic structure are shown in Figure 1.7.

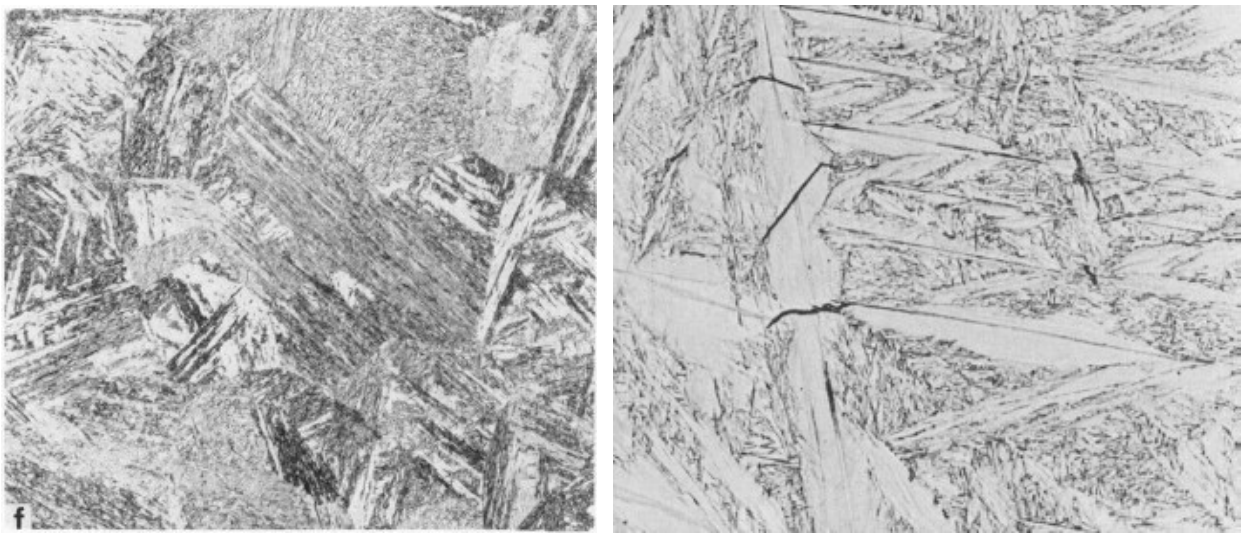

Figure 1.7: (A) Lath Martensite (Fe-0.2 %C) and (B) Plate Martensite (Fe-3.38 %Si-0.5 %C) [10]

1.1.2 Crystallographic Texture

In a polycrystalline material each crystal can have its own orientation. If these orientations are not random and some orientations occur more often than others, the material has a preferential orientation or crystallographic texture. Further information on this subject can be found in [11] [12] [13] [14] [15]. Texture can be caused by the preferential growth of grains along a direction during solidification or lattice rotations by slip or twinning during working [11]. An example of this is shown in the inverse pole figure for an extruded aluminum rod shown in Figure 1.8. The greater density of lines near the <111> and <100> indicates crystals (grains) with these orientations are more frequently encountered in the sample as opposed to those with <110> orientations which have few markings.

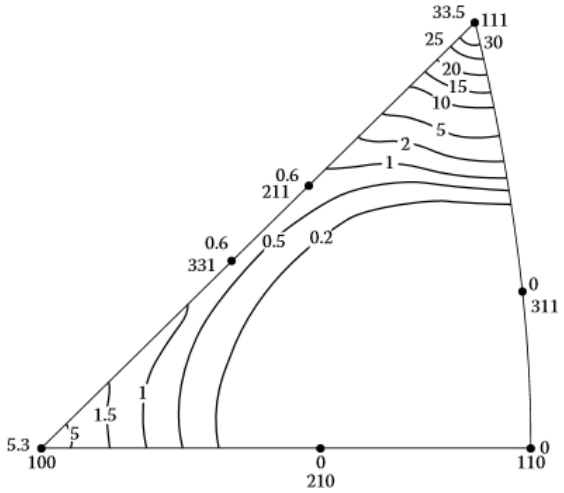

Figure 1.8: Inverse Pole Figure For Extruded Aluminum Rod [11]

1.2 General Concepts in Ultrasonic Testing

Ultrasonic testing describes the use of ultrasonic waves to find sub-surface information about an object of interest. This can vary from medical uses, such as finding tumours [16] or gall stones [17], to industrial uses in flaw detection within construction materials [18], with the latter being of greater interest in materials science. The first patent for using ultrasonic waves for flaw detection in metals was in 1942 by Firestone [19]. However, the concept of using sound waves for quality control was present long before then with the testing of railway wheels by striking them with a hammer like a bell. If the wheel was not to specifications, the sound waves created would audibly vary from the norm and the wheel would be rejected [20]. This example illustrates the basic principles of ultrasonic testing. A wave is introduced into a material, travels through the material, and then the properties of the wave are analyzed to identify and locate the presence of any defects (Section 1.2.3) or how the structure of the material (Sections 1.4 and 1.5) has affected the wave.

1.2.1 Wave Types

When an ultrasonic transducer strikes a material it causes waves to be formed much like a stone into water [21]. An ultrasonic transducer is most commonly a piezoelectric crystal which converts an electrical signal into mechanical motion. Electrical current causes the piezoelectric to deform in one direction or the other [20]. By using rapidly oscillating alternating current, the piezoelectric can strike the material rapidly enough to induce an ultrasonic wave. Human hearing ranges from 5 Hz to 15 kHz, whereas ultrasonic testing normally occurs between 500 kHz and 15 MHz, with weld inspection normally around 2.25 MHz. When the transducer strikes the material, it applies a force and since the molecules in the material are not absolutely rigid they will move in response and in turn apply a force to other molecules. The stress imposed by the ultrasonic transducer is far below the elastic limit of the material [21], so the molecule will eventually return to its original position much like a pendulum would [22]. When the molecule moves it also pulls neighboring molecules along with it. As each molecule moves its neighbors, the motion propagates through the material resulting in an ultrasonic wave

The molecular oscillation can form different types of waves, though longitudinal, shear, surface and plate are the most common [21]. There are also Love waves, which form in a specific section or layer of a material [22]. Plate waves, also known as Lamb waves, form in materials only a few wavelengths thick, since these waves occur throughout the entire thickness of the material [21]. They are complex waves that have a multitude of possible velocities depending on the material properties and dimensions, as well as the frequency of the wave. Surface waves, or Rayleigh waves, are so called because they move along the surface of a material rather than penetrating into the bulk. Their velocity is approximately 90% of shear waves under identical conditions. Figure 1.9 shows these wave types schematically.

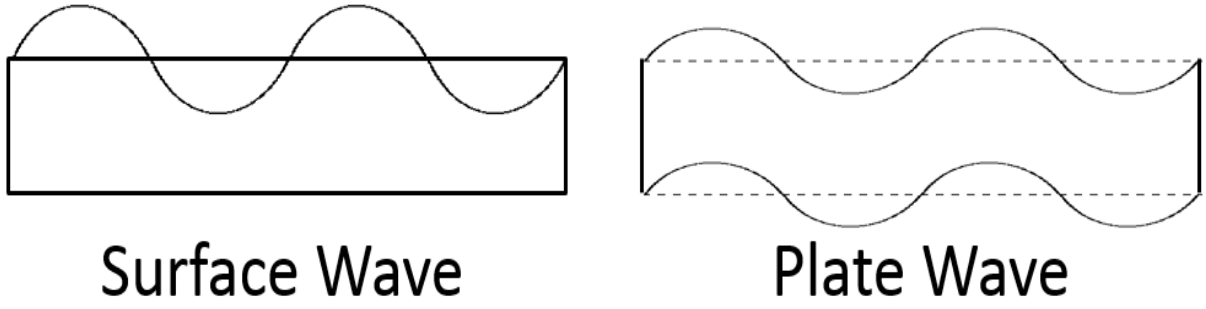

Figure 1.9: Surface (Rayleigh) Wave and Plate (Lamb) Wave

Shear and longitudinal waves can travel through the bulk of a material [21]. In a shear wave, also called a transverse wave, the particle motion is perpendicular to the direction of the wave. This can be visualized as a wave in a rope; as each section of the rope travels up or down, the wave itself moves along the length of the rope. Shear waves require strong attraction between particles so as when they move they pull other particles with them; as such, they cannot occur in gases or liquids with low viscosity. Shear waves travel with approximately 50% of the velocity of longitudinal waves. Longitudinal waves, or compression waves, also travel through the bulk of a material. In a longitudinal wave, particle motion is parallel to wave direction. This forms zones of alternating compression and rarefaction. This is similar to squeezing and releasing a section of a spring, where each section of the spring moves closer or further from its neighboring sections in the same direction as the wave propagates. The two wave types are of particular importance, since they can travel through the bulk of a material such as a pipe wall to evaluate it. These wave types can be seen schematically in Figure 1.10.

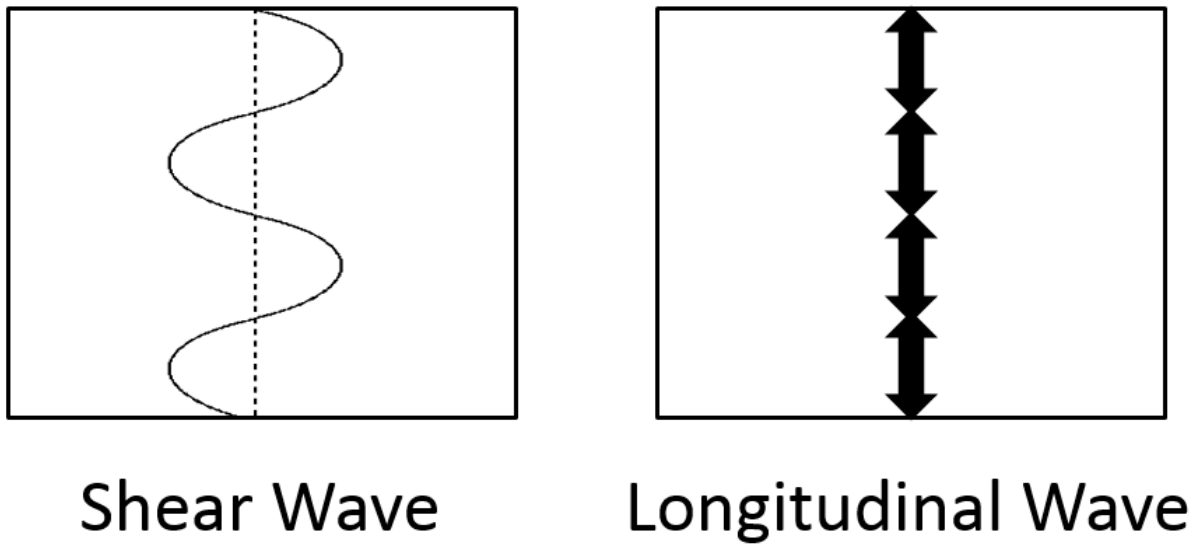

Figure 1.10: Shear (Transverse) and Longitudinal (Compression) Waves

1.2.2 Interfaces

When an ultrasonic wave crosses an interface between two materials, its path is affected. If the properties of both materials are known, the resultant behavior of the wave can be found. At each interface the wave can be both refracted and reflected. This can be seen in Figure 1.11, where a wave moves from the top left of the material and is refracted towards the bottom right and reflected to the top right [23].

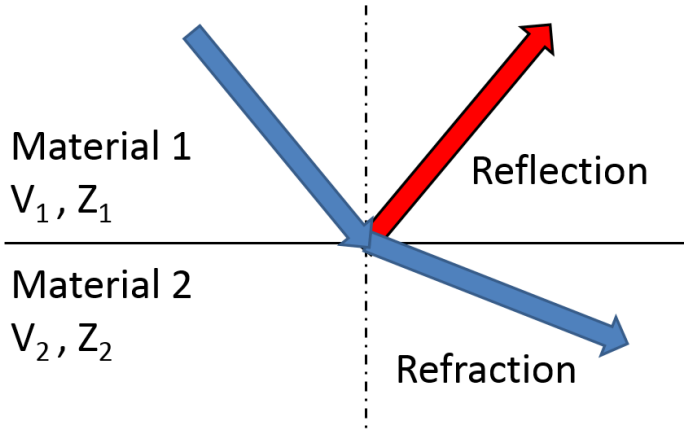

Figure 1.11: Wave Reflection and Refraction at an Interface

The portion of the wave reflected can be calculated using Equation 1.1, where R is the reflection coefficient (unitless), Z_1 (sPa/m^3) is the acoustic impedance of the initial material and Z_2 (sPa/m^3) is the acoustic impedance of the material the wave is travelling into [24].

$$R = \left(\frac{Z_2 - Z_1}{Z_2 + Z_1}\right)^2 \tag{1.1}$$

The amount of energy in the wave is constant, so the transmission coefficient or amount of wave not reflected would simply be one minus R. Acoustic impedance can be calculated using the material density and velocity of sound in a material.

$$Z_1 = \rho_1 V_1 \tag{1.2}$$

where ρ_1 (g/cm^3) is the material density and V_1 (cm/s) is the velocity of sound in the material [21]. Since the velocity of shear and longitudinal waves differ, so too would their acoustic impedance in a material and the reflection coefficient for a given interface of two materials. Similarly, the refraction angle of the wave can be calculated from the velocities of the wave in each material and the incidence angle (Snell's Law).

$$\frac{\sin \alpha A}{\sin \beta} = \frac{V_1}{V_2} \tag{1.3}$$

V_1 is the velocity of a wave in the material before the interface, V_2 is the velocity of a wave after the interface, αA is the angle of incidence and β is the refracted angle. Both the angle of incidence and the refracted angle are measured from the normal to the interface. Figure 1.12 shows this schematically.

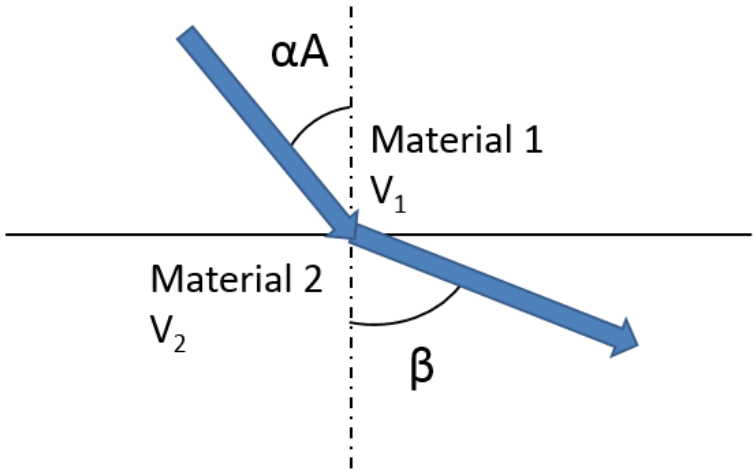

Figure 1.12: Snell's Law

Since a shear and longitudinal wave have differing velocities in a material, they would also have differing refracted angles from one another in the same material. When a wave encounters an interface it refracts a wave of the same type but can also generate a wave of a different type. This is known as mode conversion [23]. A critical angle is achieved when a wave type has a refracted angle of 90° [25] and is not propagated in the material. The first critical angle is where a longitudinal wave no longer penetrates into the bulk; the second critical angle is where a shear wave does not propagate through the bulk. The first critical angle is shown in Figure 1.13A as α_1 and the second critical angle is shown in Figure 1.13B as α_2.

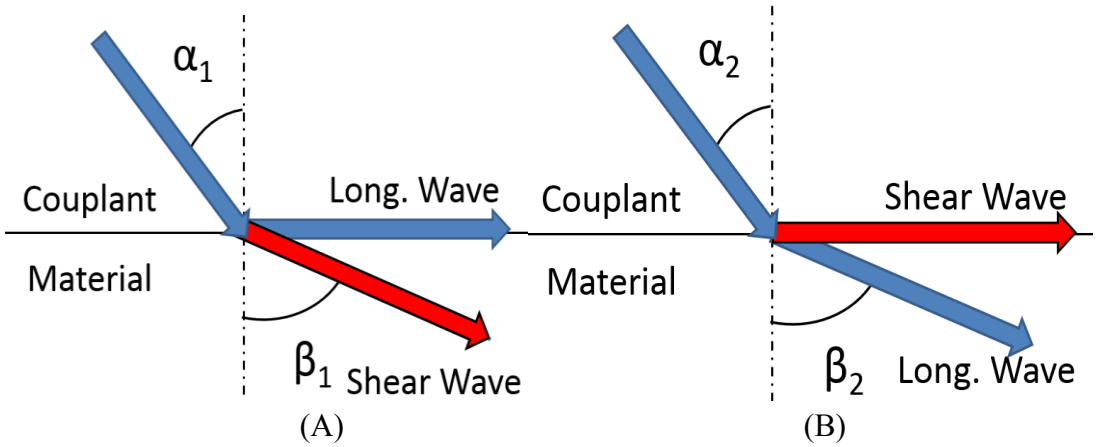

Figure 1.13: First (A) and Second (B) Critical Angles

When performing ultrasonic tests, it is necessary to have only one wave type present. If multiple wave types are present, the backwall reflections (peaks formed by the wave reflecting off the back face of the sample) would be confused among the wave types and useful information could not be obtained. These critical angles are used to ensure only one wave type is propagated into the bulk of the material. Another way to prevent a shear wave from forming is to set the incident angle of the ultrasonic wave perpendicular to the material surface [25].

1.2.3 Flaw Detection

A primary use of ultrasonic testing is in flaw detection. Ultrasonic testing is dependent on properties of both the ultrasonic wave and material being tested. The frequency of the wave is critical as it determines sensitivity, resolution and penetration [21]. Both resolution and sensitivity increase as frequency increases. Sensitivity is how easily a flaw is detected and resolution is how small a flaw can be detected. In contrast, penetration, how far the wave can travel into a material, decreases as frequency increases so a balance of these characteristics is needed to determine the desired frequency.

Two main methods of ultrasonic testing are pulse-echo and pitch-catch [20]. In the pulse-echo method a single transducer is used both for generating the wave and detecting the reflected response. In pitch-catch one transducer generates the wave, while another is used to detect the response. Both shear waves and longitudinal waves can be used with either method. An example of longitudinal wave pitch-catch testing is through thickness testing where transducers are placed on either side of a material. The transducer on one side emits a pulse and the other detects the wave after it has travelled through the material. Conversely, this could be done with pulse-echo, in which case the transducer would emit a pulse as well as detect the wave after it has reflected from the other side of the material. In the scenario for pitch-catch the wave travels through the bulk material once, whereas in pulse-echo the wave travels through the material twice, once to the other side then the reflection back to the transducer. If a flaw was present, it could be detected by either method. In pulse-echo the reflection of the wave from the flaw would cause a detected wave before the bulk beam was detected. This is because the bulk beam must pass through the entire material before being detected, whereas the reflected beam travels through less material. In pitch-catch the detected beam from the flaw would have less energy than the beam in flaw-free material because of the reflection. This occurs because the flaw has different acoustic properties than the bulk material. Pulse-echo is used whenever possible, since only one transducer needs to be used.

Analysis based on compression waves is mostly limited to thickness measurement and detection of flaws parallel to the material surface. The wave is propagated into the material perpendicular to the surface to avoid mode conversions. Shear waves are used for the detection of flaws in other orientations, as well as in regions such as weldments where the surface is not sufficiently smooth or flat to facilitate placing a transducer directly above the area of interest. The ultrasonic beam has

the greatest sensitivity to flaws which exist orientated perpendicular to the beam's direction of travel [20]. Longitudinal waves are often used to detect flaws parallel to the surface near regions which will be tested with shear waves, as these flaws can confuse detection done with shear waves and are more easily detected with longitudinal waves. Care must also be taken with respect to weld geometry when using ultrasonic non-destructive testing (NDT) for example, the initial angle of incidence must be calculated such that the wave will intersect perpendicular to the original angle of the base metal in a weld to best detect lack of sidewall fusion. Shear waves also have an advantage in that their smaller velocity in a material means they also have a shorter wavelength for a given frequency. Beams with shorter wavelengths can detect smaller flaws [25].

1.3 Ultrasonic Velocity and Attenuation

The two ultrasonic wave properties critical to this work are the ultrasonic wave velocity and attenuation. The velocity is how fast the wave can travel in a material, while the attenuation is the rate of energy loss by the wave as it travels through a material.

1.3.1 Ultrasonic Velocity

Ultrasonic velocity refers to the speed at which an ultrasonic wave propagates through a material. This velocity is dependent both on the frequency and wave type of interest [26], both characteristic of the wave. The velocity of the wave is also affected by the material it is travelling through. Of critical importance is the material's stiffness and density. Using only this information, a generalized ultrasonic velocity can be calculated irrespective of the frequency and wave type [27].

$$V = \sqrt{\frac{T}{\rho}} \tag{1.4}$$

where T (N) is the tension in the system, representative of the material stiffness, and ρ is the material density (g/cm^3). This equation can be further modified for specific wave types by taking into account Poison's ratio [22] or the stiffness tensor of the material [28]. While initially appearing simple, exact calculations of ultrasonic velocity are incredibly complex and require immense knowledge of the material in question to be accurate. Section 1.4 explores many of the features in a material that affect the velocity of an ultrasonic wave.

1.3.2 Ultrasonic Attenuation

Ultrasonic attenuation is the loss of energy as the wave travels through a material [20]. These energy losses come from a variety of sources, which can be categorized into transmission losses,

interference effects and beam spreading [21]. One form of transmission loss is absorption, which occurs by the conversion of mechanical energy into heat. Heating occurs during compression and cooling during rarefaction, since the heat flow moves much more slowly than the ultrasonic wave; these cycles reduce the energy of the wave. Absorption is more pronounced for higher wave frequencies. Scattering is another form of transmission loss. As the wave moves through a material, energy is lost as portions of the beam are refracted or reflected out of the main beam path. Scattering is caused by grain boundaries and small inclusions, as well as microstructural changes and other interfaces where acoustic velocity and impedance change. Interference effects are largely caused at interfaces. A piezoelectric crystal is not completely homogeneous and causes many ultrasonic waves to be formed instead of a single homogeneous wave. These waves act together to form the general ultrasonic beam; their reactions near the interface are known as near field effects. When the beam encounters an interface, each individual wave can react slightly differently. This causes some interference between waves and thus a loss of beam energy. Interfaces are never perfectly smooth and irregularities cause interference from refraction differences. The far field of an ultrasonic beam is the region after the interferences, caused by the interface, and do not largely affect the beam. Beam spreading occurs in the far field of a wave. Beam spread is the increase in wave front size as the beam travels.

These effects all work together to attenuate the ultrasonic wave. The amount the beam is attenuated (α) in dB/mm can be calculated experimentally [29].

$$\alpha = \frac{20}{2x} \log(\Delta A) \tag{1.5}$$

where x (mm) is the thickness of the sample and ΔA (dB) is the change in amplitude between sequential reflections. Many of the same factors which affect the ultrasonic velocity in a material also affect the attenuation. Section 1.5 looks at some material features and their effects on ultrasonic attenuation; however, less work has been done using attenuation to look at material features compared with ultrasonic velocity.

1.4 Ultrasonic Velocity and Microstructure

Many microstructural characteristics have been found to affect the ultrasonic velocity in a material. These include the phases or structures present, precipitates, the orientation of the material's crystal structure, the grain size and stresses acting on the material.

1.4.1 Ultrasonic Velocity and Morphology

Microstructure plays a critical role in a material's properties. Efforts have been made to show that microstructure not only affects the mechanical properties of materials, but also affects the ultrasonic properties. Investigations into plain carbon steels (AISI 10XX) have shown that

quenched martensitic samples have significantly lower ultrasonic velocity than annealed thick ferrite-pearlite samples [30]. The 1045 steel samples were austenitized at 840°C and then either water quenched, oil quenched, normalized or annealed. The water quenched sample produced a martensitic structure while the oil quenched sample produced fine F-P, the normalized sample produced coarser F-P and the annealed sample produced the coarsest F-P. After heat treatment the samples were tested with 5 MHz ultrasonic shear waves; the resultant velocities are shown in Figure 1.14.

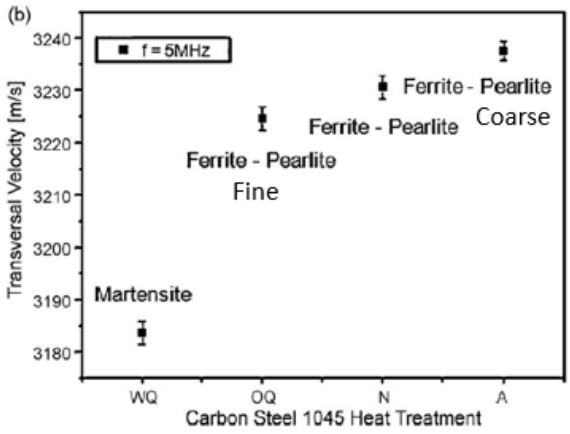

Figure 1.14: Transverse Ultrasonic Velocities for Heat Treated 1045 Samples [30]

The velocity is much slower in martensite than in the ferrite-pearlite samples. This is because each structure has unique elastic properties. Work done on alloyed steels (AISI 4140 and 5140) had similar findings, showing that coarse pearlite-ferrite had a higher velocity (3250 m/s) than martensite (3200 m/s) [31]. The study also showed that bainite had a velocity (3235 m/s) between that of martensite and ferrite-pearlite. Using laser ultrasonics at high temperature, velocity has been shown to increase as austenite transforms into ferrite or pearlite [32]. Similar work has also been done on other steels [33] [34] [35]. The velocity of sound is then highly dependent on the microstructure of the material investigated.

1.4.2 Ultrasonic Velocity and Precipitates

The ultrasonic velocity was also found to vary with microstructure in cast iron, depending on the graphite content in the matrix and graphite morphology (flakes vs nodular) [36]. Similarly, precipitation progression with aging in a 2024 aluminum-copper alloy was shown to affect the ultrasonic velocity [37]. Both hardness and ultrasonic velocity reached a maximum value after 10 hours of aging at 463 K, which corresponded to a maximum volume fraction of precipitates. Ultrasonic velocity was found to be more sensitive to precipitation in Ni-based superalloys than hardness, as the velocity began increasing during nucleation while the hardness remained constant until the precipitates grew beyond a minimum size [38]. The shear velocity was found to be a better indicator of precipitation, as it showed a greater change (1.17%) than the longitudinal velocity

(0.59%) as precipitation progressed [39]. The first order differential of the ultrasonic velocity was seen to remain relatively constant with increasing temperature, but showed significant increases at temperatures corresponding to the precipitation reactions [40]. Looking at the first order differential eliminated the effect of temperature on the visualization of the velocity trend. The presence of precipitates then also affects the ultrasonic velocity, however work has not been done to determine the limits on precipitate size or volume fraction and their effects on ultrasonic velocity.

1.4.3 Ultrasonic Velocity and Orientation

Anisotropic materials produce unique problems for ultrasonic inspection. Since these materials have differing elastic properties along different directions, the velocity of an ultrasonic wave varies with the direction the wave is propagating [41]. In an isotropic material the wave front and energy propagation directions are aligned; this is not the case in an anisotropic material. Figure 1.15 was produced by Lane et al. using finite element analysis of the two models.

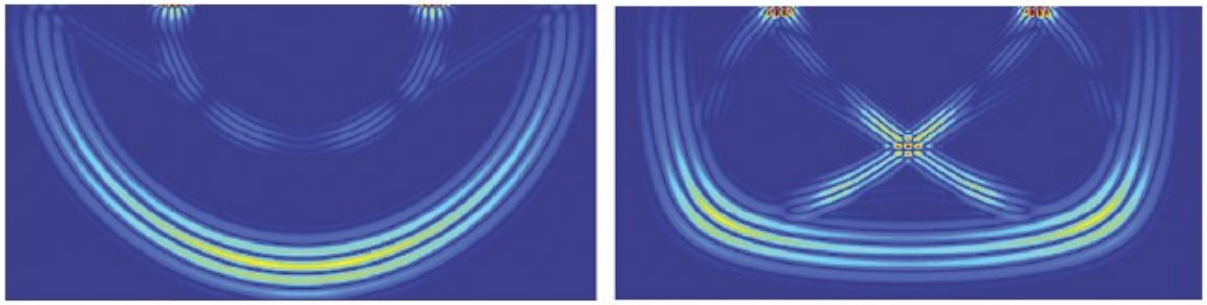

Isotropic Anisotropic

Figure 1.15: FE Analysis showing propagation shape of UT Waves in Two Models [41]

Figure 1.15 shows the difference in wave propagation between an isotropic and anisotropic single crystal material. The anisotropic crystal modelled was a CMSX-4 superalloy aligned so "the (010) plane was in the plane of the FE mesh and the [001] direction was aligned vertically with the mesh" [41]. This radical departure of wave behaviour from an isotropic to anisotropic material will affect the velocity of the waves and thus will influence any UT analysis. In anisotropic materials the two shear and longitudinal waveforms found in isotropic materials are not present, but exist in as many as three modes, one longitudinal and two shear [42]. Lane et al. also developed a model to predict the velocity in a single crystal of CMSX-4 superalloy. Using the solution for the longitudinal waveform, a minimum velocity of 5194 m/s and a maximum velocity of 6316 m/s were found for the <001> and <111> directions, respectively [28]. Figure 1.16 shows a map of longitudinal velocity according to crystallographic direction.

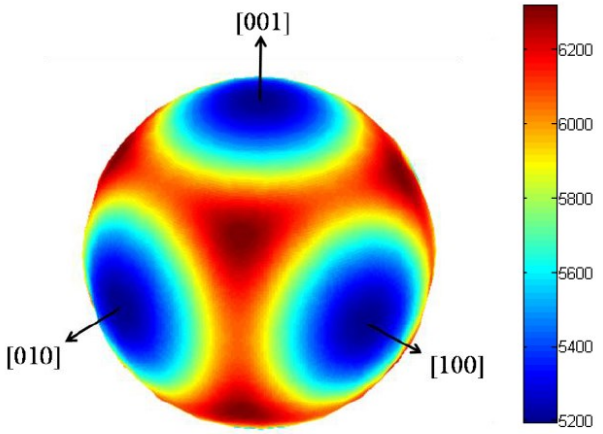

Figure 1.16: Ultrasonic Longitudinal Velocity in a Single Crystal of CMSX-4 (m/s) [28]

This map was developed for single crystal turbine blades, since it can greatly increase the accuracy of ultrasonic readings. If the crystallographic direction in the single crystal is known, then a fairly accurate velocity for the wave traveling through the blade can be calculated and flaw detection and sizing will be greatly improved.

Crystallographic directions can also have an effect on ultrasonic velocity in polycrystals, such as rolled steel skelp. Anisotropy and texture can be of critical importance. In addition to the effects of microstructure, the specific texture found in a material has an effect on its ultrasonic properties. Cold rolled stainless steel (SS) sheet showed a distinct change in ultrasonic velocity as the sheet was rotated, with the rolling direction having the lowest velocity and the highest velocity being perpendicular to the rolling direction [43]. The results of the work by Dixon are shown in Figure 1.17.

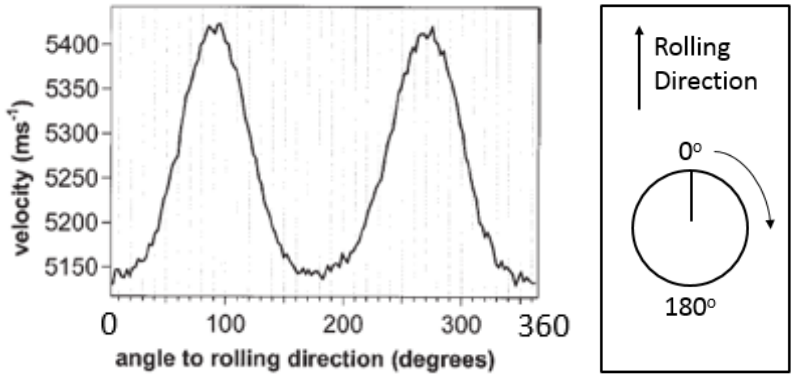

Figure 1.17: Velocity Change with Rotation of Steel Sheet (Rolling Direction= 0°) [43]

It was also found that upon annealing, the behaviour between the directions changed. Similarly, longitudinal waves in an austenitic stainless steel weld had the lowest velocity when aligned with the solidification direction and the maximum velocity when perpendicular to the solidification

direction, with a lower minimum opposite the solidification direction [42]. There has been little work done on modelling these effects in polycrystals unlike the single crystal turbine presented above. Orientation of crystals and texture in polycrystals is then critical to ultrasonic velocity.

1.4.4 Ultrasonic Velocity and Grain Size

The ultrasonic velocity is also sensitive to the grain size in a material. Ultrasonic velocity was found to decrease in austenitic stainless steel as grain size increased [44]. The shear velocity was found to be more sensitive than the longitudinal velocity; both velocities decreased as the grain size increased. This behaviour is not unique to metals and can also be found in other materials like rocks such as marble [45] or composite materials [46] where the velocity increased with grain size. The shear velocity was also found to accurately reflect the recovery and recrystallization stages of annealing in stainless steel, with a slight increase in velocity during recovery and a sharp increase from the beginning to the end of recrystallization [47]. This was also seen using laser ultrasonics to observe the phenomena in-situ in both stainless and IF steel [48].

1.4.5 Ultrasonic Velocity and Stress

The ultrasonic velocity of a material also changes with applied stress [49]. A simple equation for finding the ultrasonic velocity of a stressed material is [50]:

$$V = \sqrt{\frac{Mo}{\rho}}\left[1 + \frac{C}{2Mo}\varepsilon\right] \tag{1.6}$$

where Mo (MPa) is the elastic modulus of the material, ε (mm/mm) is the resultant strain from the applied stress, ρ (kg/m^3) is the material density and C (unitless) is the third order anharmonic constant from the power series:

$$\sigma = M\varepsilon + C\varepsilon^2 + D\varepsilon^3 \ldots \tag{1.7}$$

Since this value is rarely recorded for a material, Equation 1.6 is not practically useful and calibrations must be run on the specific material of interest instead of calculating the effects [51]. A common method is to use the birefringence of ultrasonic shear waves in an unstressed material and compare it to the stressed material [52]. Ultrasonics have been used to successfully measure residual stress in railroad wheels, where induction heating was used to simulate stresses found in service wheels and changes in ultrasonic velocity correlated with destructive analysis performed after ultrasonic testing [53]. Other work was also successful in looking at railway wheel residual stress with ultrasonic velocity [54] [55]. Similar work done on steel rail showed good correlation between residual stress and ultrasonic velocity [56] [57].

1.4.6 Ultrasonic Velocity Summary

The morphology, precipitates, crystallographic orientation, grain size and stress were all found to affect the ultrasonic velocity in different materials. Table 1.1 shows a summary of the materials examined for each microstructural characteristic, as well as those examined with laser ultrasonics (LUT) or conventional ultrasonics (UT).

Table 1.1: Summary Of Ultrasonic Velocity Work

	Materials Tested	Methods
Morphology	medium carbon steel, SS	LUT, UT
Precipitation	Fe, Al, Ni	LUT, UT
Orientation	CMSX4, SS sheet, SS weld	UT
Grain Size	SS, IF Steel	LUT, UT
Stress	Ni-Fe, Cu, Al, Steel Parts	UT

The pipe steels investigated in this work have not been previously analyzed using conventional ultrasonic testing for velocity. IF steel has been looked at with laser ultrasonics at high temperature, but not at room temperature using conventional ultrasonic testing. The knowledge gained from these works will be applied to the steels used in this work.

1.5 Ultrasonic Attenuation and Microstructure

The ultrasonic attenuation in a material is also affected by the characteristics of its microstructure. The phases and structures present, precipitates, crystallographic orientation, grain size and dislocations all affect the attenuation.

1.5.1 Ultrasonic Attenuation and Morphology

Similar to the ultrasonic velocity, morphology and structure of a material can have a great effect on the attenuation of an ultrasonic wave. In the same study on 1045 as presented above by Freitas et al. [30], the attenuation of the ultrasonic wave decreased as the microstructure changed from martensite to fine ferrite-pearlite to coarse ferrite-pearlite, as shown in Figure 1.18.

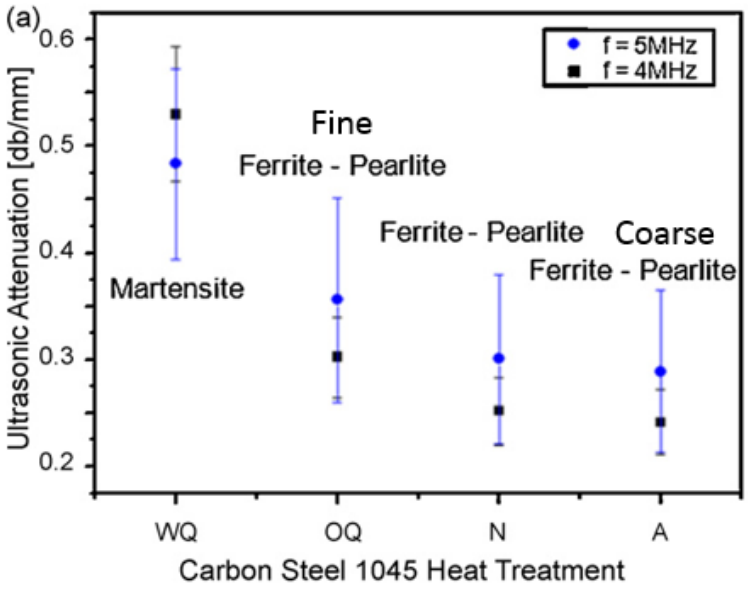

Figure 1.18: Ultrasonic Transverse Attenuation for Heat Treated 1045 Samples [30]

The ultrasonic attenuation was higher in martensite than in the ferrite-pearlite samples. Microstructural differences have been investigated much less with attenuation than velocity; however, the limited work done has shown that structure does have an effect on attenuation.

1.5.2 Ultrasonic Attenuation and Precipitation

When the velocity increases due to precipitation, the attenuation also increases. This occurred in the study by Belan on cast iron [36], as well as the study by Kumaran on 2024 Al-Cu alloys [37]. The precipitation reactions in a 8090 Al-Li alloy were also seen to cause spikes in the ultrasonic attenuation, in agreement with the previous works [40]. Precipitation then has an effect on ultrasonic attenuation.

1.5.3 Ultrasonic Attenuation and Orientation

Attenuation in an anisotropic Zn bar was found to vary between the radial and axial directions of the bar [58]. The attenuation was found to be greatest along <110> directions and least along <100> directions for longitudinal waves in MgO [59] and Cu [60]. The dependence of attenuation was not found only in cubic structures, but also hexagonal single crystal Zn [61]. Attenuation was also found to vary with incidence angle in rolled product, similar to the behavior for velocity [62]. Elongated grains in stainless steel and Al had attenuations highly dependent on preferential grain orientation as well [63]. Orientation and texture then have an important effect on ultrasonic attenuation.

1.5.4 Ultrasonic Attenuation and Grain Size

Gran size is also known to affect the attenuation of an ultrasonic wave. An example of this is the increase in attenuation values as the austenization temperature is increased in a SAE 52100 steel quenching operation [64]. This was attributed to both the dissolution of carbides as the temperature increased and the coarsening of martensite. The relationship between the grain size of the material and the wavelength of the ultrasonic wave is critical to scattering. Three distinct regions of scattering exist: "When grain size is less than 0.01 times the wavelength, scatter is negligible. Scattering effects vary approximately with the third power of grain size, and when the grain size is 0.1 times the wavelength or larger, excessive scattering may make it impossible to conduct valid ultrasonic inspections" [21]. Attenuation can be used to calculate grain size [65].

(λ>>D) Rayleigh regime $$\alpha = K_r D^3 f^4 \quad (1.8)$$

(λ~D) Stochastic regime $$\alpha = K_s D f^2 \quad (1.9)$$

(λ<<D) Diffusion regime $$\alpha = K_d / D \quad (1.10)$$

where f is the ultrasonic frequency (Hz), λ is the ultrasonic wavelength (mm), D is the average grain size (mm), α is the attenuation coefficient (dB/mm) and the K (units depend on equation) values are material constants. In the Rayleigh regime the equation is based on the assumption that multiple scattering effects can be ignored due to a small scattering energy [66]. These equations show that if the Rayleigh or Stochastic regime are satisfied, i.e., wavelength greater than or close to the grain size, the attenuation will increase with grain size. In the Diffusion regime, i.e., wavelength less than the grain size, attenuation will decrease as the grain size increases [65]. These equations take into account total attenuation caused by transmission losses, interference effects and beam spreading. In steel, the Rayleigh regime is most often encountered [44] [67]. This is clearly shown in Figure 1.19 where a longitudinal ultrasonic velocity (V_L) of 5900 m/s and a shear velocity (V_s) of 3250 m/s at 10 MHz have wavelengths 4.5 and 8.2 times greater than the average grain size, 72 μm, in the steel. If the velocity were constant in this case, the frequency would need to exceed 40 MHz to leave the Rayleigh regime. Within the Rayleigh regime, the increase in ultrasonic attenuation (α (dB/mm)) with grain size (D (mm)) has been used to quantify the grain size in railway wheels [67]. The results are shown across multiple frequencies in Figure 1.20.

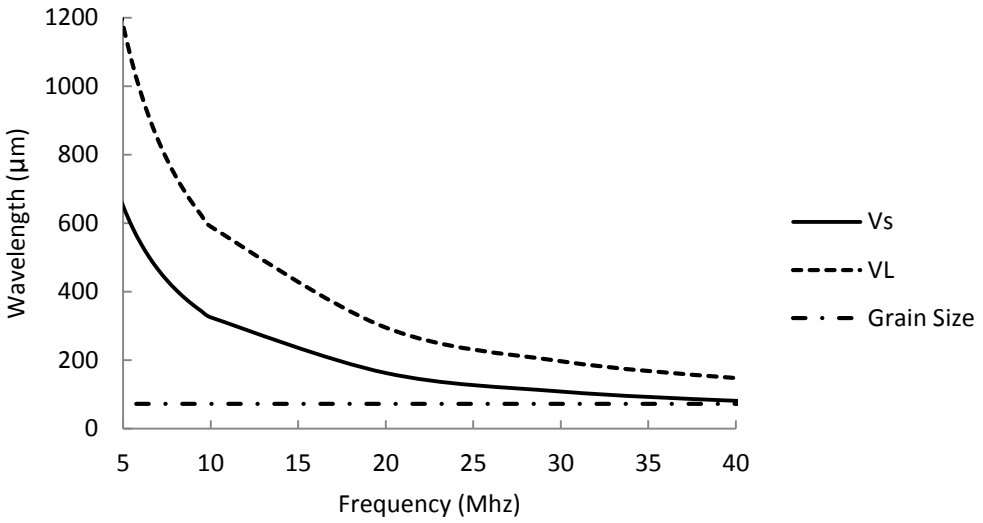

Figure 1.19: Frequency and Wavelength of Ultrasonic Waves and Grain Size

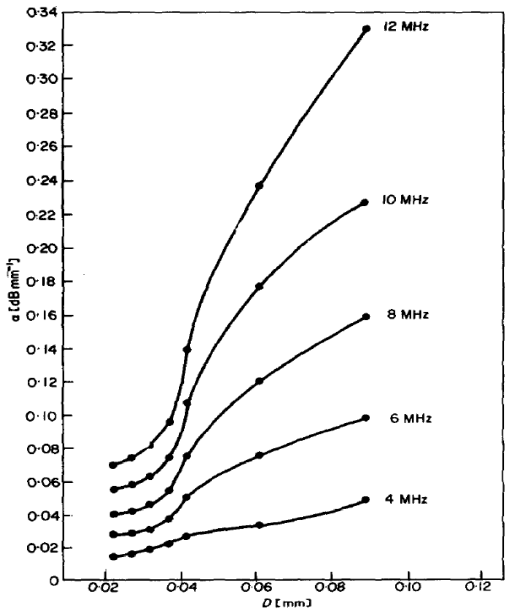

Figure 1.20: Attenuation (α)-Grain Size (D) Relation in Steel Railway Wheels [67]

Other techniques have also been developed using ultrasonic attenuation to determine grain size. The ratio between peak heights across multiple frequencies was found to correlate well with grain size in stainless steel using laser induced ultrasonics [48], where the peak height at each frequency is analogous to the ultrasonic attenuation. The peak height method was also successfully used in marble [68]. The velocity and attenuation can be used together as well. The parameter log (v (dα/df)), where v is the ultrasonic velocity, α the attenuation and f the frequency, was found to correlate with grain size in both the Rayleigh and Stochastic regions in multiple metals and alloys [69]. The relationship between grain size and attenuation has also been used for the location of the

HAZ in steel weldments, where the attenuation was lower than in the base and weld metals [70] [71]. The type of wave also has an effect on the attenuation [71]. A longitudinal wave is more resilient to attenuation than a shear wave [72]. Attenuation also increases as frequency increases, as seen in Figure 1.20. This increased frequency can increase attenuation to such a degree that useful data can no longer be obtained [71]. Grain size is then of critical importance to ultrasonic attenuation.

1.5.5 Ultrasonic Attenuation and Dislocation Density

Dislocation density is another material property which has an effect on ultrasonic behaviour [73]. The relationship between dislocation density and ultrasonic properties is often used during studies of material fatigue [74]. These measurements are often done using ultrasonic resonance and looking at the damping, analogous to attenuation, rather than using an ultrasonic beam propagating through a bulk material [75]. The attenuation was found to decrease in Sn while the dislocation density increased [76]. Similar behaviour was found in NiTi shape memory alloys [77]. During fatigue the attenuation reaches a peak and then decreases to a level somewhat higher than the initial attenuation [78] [79]. The changes in attenuation as fatigue progresses are caused by changes in dislocation mobility and density [80]. The difference in initial and final attenuation is attributed to a buildup in dislocation density at "point clouds" at either end of the region swept by dislocations during fatigue [74]. This shows that dislocation density is also an important material property for ultrasonic attenuation.

1.5.6 Ultrasonic Attenuation Summary

The morphology, precipitates, crystallographic orientation, grain size and dislocations all were found to affect the ultrasonic attenuation. Table 1.2 shows a summary of the materials examined for each microstructural characteristic as well as whether laser ultrasonics (LUT) or conventional ultrasonics (UT) were employed.

Table 1.2: Summary of Ultrasonic Attenuation Work

	Materials	Methods
Morphology	medium carbon steel, SS	UT
Precipitation	Fe, Al	UT
Orientation	Zn, MgO, Cu, SS sheet, Al	UT
Grain Size	medium carbon steel, SS	LUT, UT
Dislocations	Cu, SS, Sn, IF, CS	UT

Many materials have been looked at with ultrasonic attenuation, but the pipe steels investigated in this work have not. The information found in previous works on other materials will then be applied to the pipe steels used in this work.

1.6 Summary

Steel can contain many different microstructures. Of interest to this work are ferrite, pearlite, martensite and bainite. Each one has unique characteristics and appearance from the others which allow them to be distinguished from one another. Ultrasonic waves can exist with different wave types. Shear and Longitudinal waves which penetrate into materials are most useful when looking at pipe steel and other bulk materials. The velocity of an ultrasonic wave depends on the elastic properties of the material it is propagating through. The velocity of shear and longitudinal waves was found to depend on the structure or morphology of the material investigated, precipitates within the material, crystallographic orientation of the material relative to the propagation direction of the wave, grain size in the material and stress within the material. The ultrasonic attenuation also changes with material properties such as morphology, precipitates, orientation, grain size and dislocation density in metals and alloys.

Understanding of how the ultrasonic wave behaves in a material is critical to flaw detection. While much work has been done with ultrasonics and metals little has been done on the pipe steels used in the oil and gas industry. Chapter 2 looks at different methods of calculating the ultrasonic velocity in ferrite, ferrite-pearlite and martensite using data obtained from a 1050 steel to see what microstructural characteristics could be replicated in simulations and how they affected the calculated ultrasonic velocity. Calculations were also done to see if longitudinal or shear waves were more suitable for phase differentiation. Since ultrasonic velocity and attenuation have been shown to be affected by many materials properties experiments were conducted on both L80 and X70 pipe skelps to see if the ultrasonic properties changed through the thickness of the skelp. Changes in ultrasonic properties through the thickness of the skelp would make flaw detection inaccurate if not accounted for. XRD was also performed through the thickness of these skelps to measure the texture, dislocation density and microstrain through the skelp to see if they changed and if so how that affected the ultrasonic wave. Discussion of these experiments is found in Section 4.1. Additionally since grain size was seen to affect the ultrasonic properties in different materials experiments were conducted on IF steel cooled to room temperature after different times at elevated temperatures to see how the ultrasonic properties changed as annealing progressed, discussion of which can be found in Section 4.2. To see if phase or structure differentiation was possible in pipe steels samples of an L80 casing steel were austenitized and cooled at different rates to obtain different structures. The structures and materials properties were then compared to the ultrasonic velocity and attenuation, this discussion is found in Section 4.3. Further studies were done on 4130 and 5160 steels using industrial equipment rather than laboratory to see if correlations found in the L80 could be detected in other steels using industrial practices.

Chapter 2 Velocity Calculations

Since the ultrasonic velocity was shown in Section 1.4 to be a useful characteristic in the determination of microstructure, calculations were done to predict velocities in various idealized steel microstructures. These calculated velocities were used to predict if shear or longitudinal waves were better for morphology differentiation. Critical materials properties were found for a 1050 plain carbon steel and these were used as the basis for the calculation methods. One calculation used the true anisotropic characteristics of the grains, one used the Young's modulus and one was based on the assumption that steel grains could be approximated as isotropic. The isotropic assumption calculations were then used to predict the effects of grain size and preferential orientation on ultrasonic velocity.

2.1 Anisotropic Velocity Formulation

Since orientation was seen to be an important factor in finding ultrasonic velocity in Section 1.4, calculations were done to find the ultrasonic velocity in anisotropic grains. Since the grains are anisotropic, the Young's modulus is not a true representation of their elastic properties and the stiffness tensor in its entirety must be used instead. The velocity equation is then the Christoffel equation [41].

$$\left(C_{ijkl}d_j d_l - V^2\rho\delta_{ik}\right)p_k = 0 \tag{2.1}$$

C_{ijkl} is the stiffness tensor, d_j and d_l are the wave propagation directions, V is the phase velocity of the wave, ρ is the density of the material, δ_{ik} is the Kroenecker delta function and p_k is the particle displacement direction. To solve the Christoffel equation, it is converted into matrix form by substituting in the λ constants [81].

$$\begin{bmatrix} \lambda_{11} - \rho V^2 & \lambda_{12} & \lambda_{13} \\ \lambda_{12} & \lambda_{22} - \rho V^2 & \lambda_{23} \\ \lambda_{13} & \lambda_{23} & \lambda_{33} - \rho V^2 \end{bmatrix} \begin{bmatrix} p_1 \\ p_2 \\ p_3 \end{bmatrix} = \begin{bmatrix} 0 \\ 0 \\ 0 \end{bmatrix} \tag{2.2}$$

The λ values are functions of C_{IJ}, the elements of the stiffness tensor in the Voigt notation ($C_{ijkl} \rightarrow C_{IJ}$) of the material. In addition, n_j and n_l are taken into account as the direction cosines (m, n and l) of the wave. If the crystal structure of the grains is assumed to be cubic, then the stiffness tensor is simplified into three components, C_{11}, C_{12} and C_{44}. The λ values from Equation 2.2 are then expressed as:

$$\begin{aligned}
\lambda_{11} &= l^2 C_{11} + (m^2 + n^2) C_{44} \\
\lambda_{22} &= m^2 C_{11} + (l^2 + n^2) C_{44} \\
\lambda_{33} &= n^2 C_{11} + (l^2 + m^2) C_{44} \\
\lambda_{12} &= ml(C_{12} + C_{44}) \\
\lambda_{13} &= nl(C_{12} + C_{44}) \\
\lambda_{23} &= mn(C_{12} + C_{44})
\end{aligned} \tag{2.3}$$

Table 2.1 shows the values of 3 elastic constants and material properties for 3 morphologies of an SAE 1050 steel critical to the velocity calculations [82].

Table 2.1: Elastic Properties of 1050 Steel [82]

Material	Elastic Constants (GPa)	Young's Modulus (GPa)	Poisson's ratio	Density (g/cm^3)
Martensite	C_{11} 268.5 C_{44} 79.04 C_{12} 111.2	203.5	0.2921	7.709
Ferrite-Pearlite	C_{11} 273.7 C_{44} 82.13 C_{12} 110.05	210.3	0.2877	7.835
α - Ferrite	C_{11} 232 C_{44} 115.92 C_{12} 135	211	0.2888	7.851

The determinant of the matrix in Equation 2.2 can be described as a cubic function of V^2 with three real roots. Figure 2.1 shows this function of V^2 along the [110] direction of a ferrite grain.

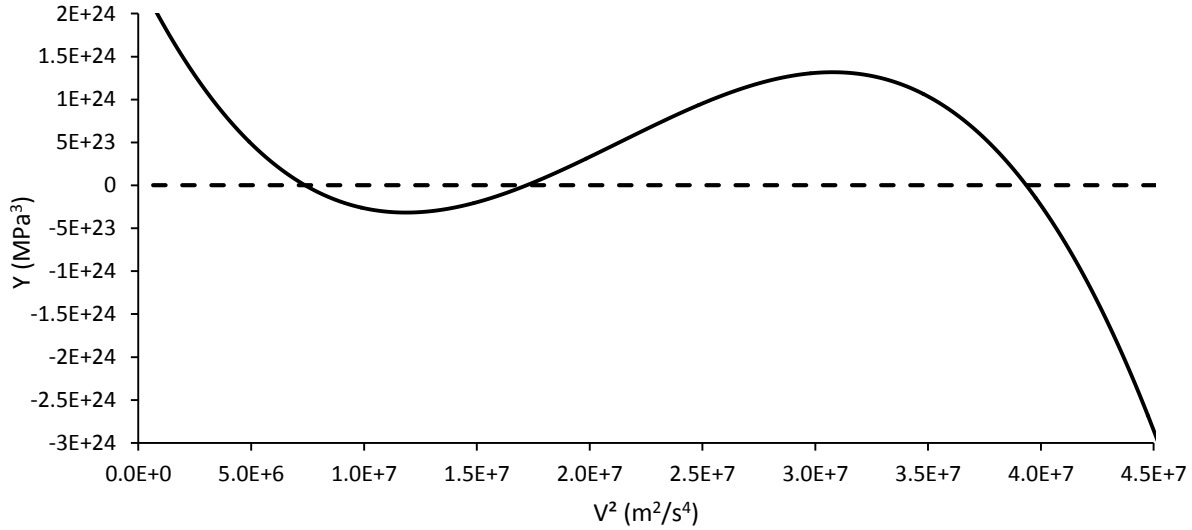

Figure 2.1: Determinant of Christoffel Equation Matrix for Ferrite Along [110]

These roots correspond to three ultrasonic velocities, two shear wave modes and one longitudinal mode. The difference between the velocities is the particle displacement axis. For example, for a wave propagating down the Z-axis of a material, the wave is a longitudinal wave if the particles are displaced along the Z-axis. If the displacement is along the X axis or Y axis, the wave is a shear wave. In an isotropic material there is no difference in properties along the X or Y axis, so the velocities are the same. In an anisotropic material the properties are not necessarily the same along the X or Y axis, so the shear velocity can differ depending on the particle displacement direction relative to the propagation direction. The difference in axis propagation is shown in Figure 2.2.

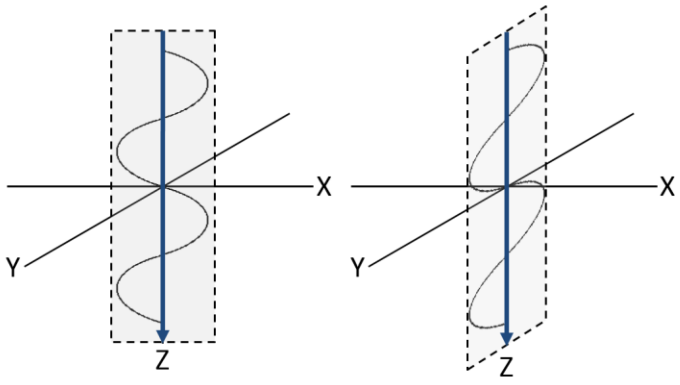

(A) (B)

Figure 2.2: Shear Wave Particle Displacement Along the (A) X-Axis and (B) Y-Axis

The roots of the function shown in Figure 2.1 are 7.4×10^6, 1.72×10^7 and 3.935×10^7 m^2/s^2, the values for V^2. The velocities along the <110> direction are then 2720, 4147 and 6273 m/s for the two shear then longitudinal mode respectively. These values can be compared with the specific formulas [83] for finding ultrasonic velocities along the <110> direction.

$$V_1 = \sqrt{\frac{C_{11}+C_{12}+2C_{44}}{2\rho}}$$
$$V_2 = \sqrt{\frac{C_{11}-C_{12}}{2\rho}} \quad (2.4)$$
$$V_3 = \sqrt{\frac{C_{44}}{\rho}}$$

From these equations the ultrasonic velocities for ferrite along the <110> direction are 6273, 4147 and 2719 m/s, which agree with those found by using the roots of the determinant. Since the velocities agree between the determinant and established equations, this method of solving the Christoffel equation can then be used to find the ultrasonic velocities along any direction in the grain.

2.2 Anisotropic Velocity Results

The determinant of the Christoffel equation matrix was used to find ultrasonic velocities for every direction in the three morphologies of 1050 steel with the elastic properties shown in Table 2.1. Maxima and minima directions were identical between the morphologies; for simplicity the results for ferrite will be presented. The calculated longitudinal velocities, V_1, are shown in Figure 2.3, where a sphere containing a single crystal of the material is presented. Velocities are shown on the surface of the sphere as a colour spectrum with blue being the slowest waves and red being the fastest.

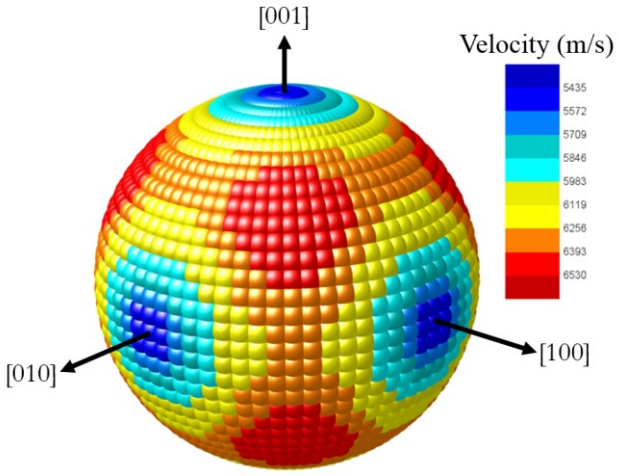

Figure 2.3: Ferrite Longitudinal Velocities Along Different Crystallographic Directions (V_1)

The maximum velocity was found to be 6529 m/s along the <111> directions and the minimum velocity was 5436 m/s along the <001> directions. The <011> directions were also found to be local maxima. Similarly, both shear wave velocities were calculated, V_2 and V_3, and are shown in Figure 2.4 with the same colouring as in Figure 2.3.

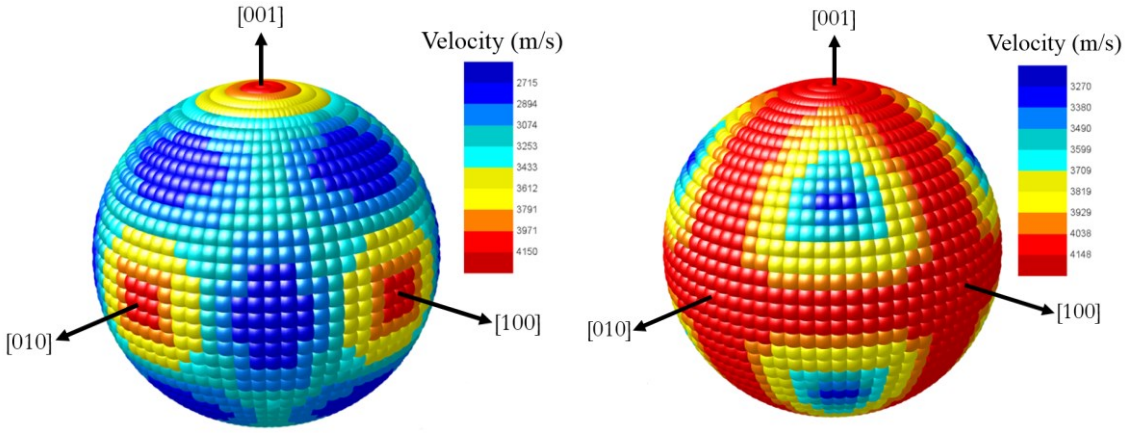

(A) (B)

Figure 2.4: Ferrite Shear Velocities (A) V_2 and (B) V_3 Along Different Crystallographic Directions

The maximum velocities were along the <001> directions for V_2 and along the entire planes between the <001> directions for V_3. In both cases the maximum velocity was 4147 m/s. The minimum velocity for V_2 was along the <011> directions and was 2719 m/s, while for V_3 the minimum velocity was 3272 m/s along the <111> direction. There were local maxima in V_2 along the <111> directions.

2.2.1 Anisotropic Polycrystal

A series of anisotropic grains cannot be easily simulated. An ultrasonic transducer does not create a single wave but rather a beam consisting of many waves with similar direction. In the isotropic case these waves all refract identically since their velocities are the same in both grains. For the anisotropic case, it is possible for a wave besides the wave being simulated to travel faster through the grain and eventually reach the detecting transducer before the wave of interest to produce a signal. At each interface there are multiple of possible wave velocities and thus a multiple of possible refraction angles. This is illustrated in Figure 2.5.

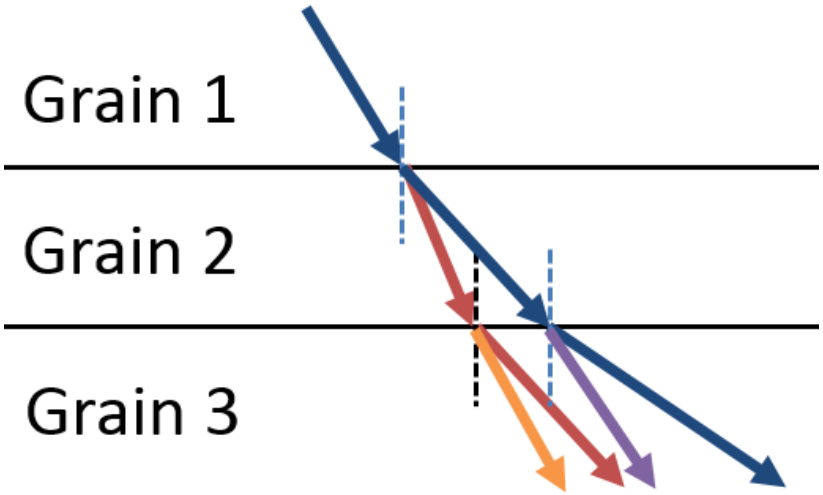

Figure 2.5: Complication of Snell's Law in Anisotropic Grains Due to Differing Wave Velocities

Instead of simulating a single wave, a multitude of waves must be considered and the mode of their times taken as the wave time to calculate the effective velocity. This is why in experimental ultrasonic tests the backwall reflection peaks are not perfect and have width. Instead of simulating grains using Snell's law for refraction, a wave perfectly perpendicular to the sample surface can be considered as it will not refract and will travel directly through the sample. Using this method, the effective velocity is equal to the average of the velocities in each of the grains encountered. Since the velocities of each grain are unaffected by refraction in this case, it is useful to compare the velocities found in each morphology.

If the effects of refraction are discounted and the wave is perpendicular to the face of the sample, the total velocity through a number of grains can be calculated.

$$V_{total} = \frac{\sum_{i=1}^{N} \varphi_i V_i}{N} \tag{2.5}$$

V_{total} is the velocity of the wave in the sample, N is the number of directions the wave travels along, V_i is the velocity of the wave along each direction and φ_i is a texture weighting factor. V_i can be found using the Christoffel equation and the crystallographic direction of travel. When φ_i is equal to one for every direction there is no texture or preferred orientation present. This is the equivalent of the texture index (J) being equal to one. If a preferred orientation exists φ_i is greater than one for the preferred directions or less than one for those that are not preferred. Calculations were done to find the total velocity in each morphology with no preferential orientation (J=1, φ_i=1 for all directions) as well as the maximum and minimum velocities possible (J=∞, φ_i=0 for most directions). The maximum, minimum and texture free (J=1) velocities for each morphology are shown in Table 2.2.A graphical comparison of the three velocities in each morphology is shown in Figure 2.6.

Table 2.2: Anisotropic Single Crystal Ultrasonic Velocities in 1050 Steel

		Max (m/s)	Min (m/s)	J=1 (m/s)
Ferrite	V_1	6529	5436	6047
	V_2	4147	2719	3340
	V_3	4147	3272	3985
Ferrite-Pearlite	V_1	5915	5910	5913
	V_2	3238	3232	3234
	V_3	3238	3234	3237
Martensite	V_1	5907	5905	5905
	V_2	3202	3194	3198
	V_3	3202	3197	3201

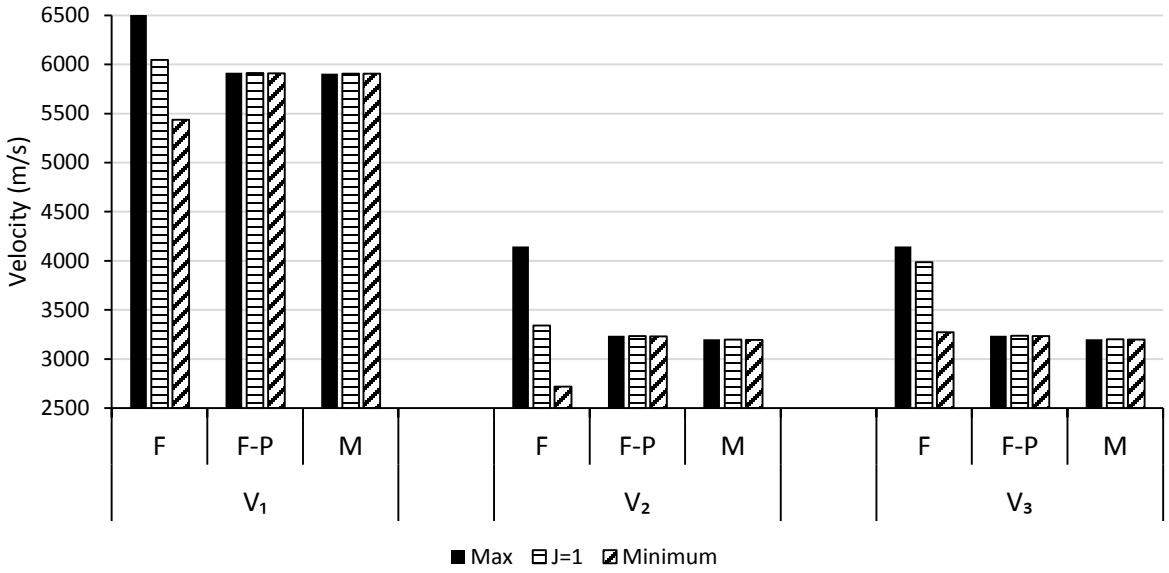

Figure 2.6: Comparison of Anisotropic Ultrasonic Velocities

Figure 2.6 shows that the ultrasonic velocities in ferrite overlap with those in both martensite and ferrite-pearlite for V_1 and V_2 but not V_3; however, practically it is not known whether a measured shear wave is V_2 or V_3 so they should be considered together. The ferrite-pearlite velocities are always greater than the martensite velocities; however, the difference is only in the range of 7-38 m/s, whereas ferrite can be hundreds of m/s faster or slower than either. It is then important to consider the fraction of the time that the velocity of a particular morphology is faster than the others. Ferrite-pearlite will not be presented since its velocities are faster than martensite 100% of the time and only differ from the comparison of ferrite and martensite, shown in Figure 2.7, by 1%. Martensite showed lower velocities than ferrite-pearlite along all directions and ferrite-pearlite was slower than ferrite along 74% of directions for shear waves and 65% of directions for longitudinal waves.

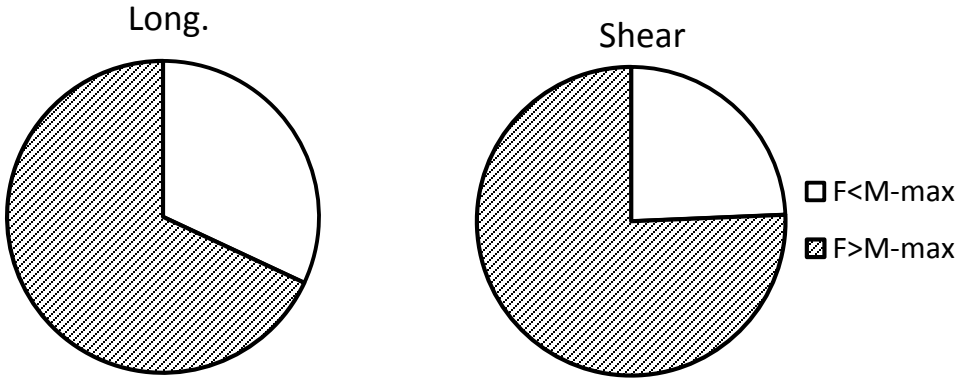

Figure 2.7: Amount of Velocity Overlap between Ferrite and Martensite

While ferrite has a much greater range of velocities than martensite, its velocities are only lower than the maximum martensite velocity 33% of the time for longitudinal waves and 25% of the time for shear waves. This means the majority of ferrite velocities are greater than any martensite velocities. This also means that shear waves should prove more useful for determining the difference between ferrite and martensite than longitudinal waves, since there is less velocity overlap.

Another useful value which arises in the anisotropic simulations is the difference between V_2 and V_3, called birefringence. This can easily be found experimentally by rotating a shear wave transducer by 90°. The difference in shear velocities ranged from 0-1428 m/s in ferrite but only 0-8 m/s in martensite. The ferrite birefringence only overlapped with martensite 6% of the time, which indicates it could be a good measurement for differentiating between martensite and ferrite.

The anisotropic simulations show that martensite and ferrite-pearlite have similar but distinct ultrasonic velocities, while ferrite can have velocities both faster and slower than the other morphologies. Ferrite velocities, however, are faster than the others for the majority of directions for both shear and longitudinal waves. In addition, the difference between the shear wave mode velocities can be much greater in ferrite and only overlaps with the values for other morphologies a fraction of the time.

2.3 Young's Modulus Velocity Calculations

Since steel is an anisotropic material, the Young's modulus (Y) is dependent on orientation. In order to simplify the analysis, calculations were done where, rather than treating steel as anisotropic, each grain was taken to be isotropic. In an anisotropic material such as steel a stiffness tensor is required to accurately predict elastic behaviour in all directions [84]. In an isotropic material, the stiffness tensor is simplified to one component which is the Young's modulus of the material, i.e., $Y=C_{11}$. A cubic anisotropic material has three elastic constants, C_{11}, C_{12} and C_{44}, which make up its stiffness tensor [84]. Y is also equal to C_{11} in an anisotropic material along the <100> direction [85]. In its simplest form, the velocity of sound in a material can be approximated using the density and Young's modulus of a material [22].

$$V_o = \sqrt{\frac{Y}{\rho}} \tag{2.6}$$

V_o is the generic velocity of sound, Y is the Young's modulus and ρ is the density of the material [22]. This equation is for a generic wave in a solid. Since shear and compression waves move with differing velocities in a given material, further equations are needed. The velocity of a shear wave in a material can be calculated if the Poisson's ratio is also considered [22].

$$V_S = \sqrt{\frac{Y}{2\rho(1-\sigma^2)}} = V_o\sqrt{\frac{1}{2(1+\sigma)}} \tag{2.7}$$

σ is the Poisson's ratio for the material. Similarly, the velocity of a compression wave can be calculated [22].

$$V_L = \sqrt{\frac{Y(1-\sigma)}{\rho(1+\sigma)(1-2\sigma)}} = V_o\sqrt{\frac{(1-\sigma)}{(1+\sigma)(1-2\sigma)}} \tag{2.8}$$

These equations were used with the material properties in Table 2.1 to find the shear and longitudinal velocities in each morphology. The longitudinal velocities were slower than those calculated in Section 2.2 but differed by less than 5%, while the shear velocities were 15% faster. The velocities found with the Young's modulus are shown in Table 2.3.

Table 2.3: Shear (Vs) and Longitudinal (V_L) Velocities Using Young's Modulus

	V_S (m/s)	V_L (m/s)
Ferrite	3829	5925
Ferrite-Pearlite	3825	5913
Martensite	3799	5898

These velocities are much closer to one another than those found with the Christoffel equation, meaning that differentiation between phases would be more difficult if the Young's modulus method is true than the Christoffel method.

2.4 Isotropic Velocity Calculation Formulations

In order to simulate the effects of grain size and texture changes through grains where refraction of the wave occurred, the Christoffel equation could not be implemented easily as discussed in Section 2.2.1. Rather than treat each grain as anisotropic, each morphology of interest was treated as three separate materials. The three elastic constants found for each morphology were used as separate Young's moduli for a unique material to simplify the calculations. For example, martensite is represented as three unique materials, M_1, M_2 and M_3. In M_1, the Young's modulus is equal to the C_{11} value found for martensite, while in M_2 it is C_{44} and in M_3 it is C_{12}. This allowed each calculation to be done with the assumption of isotropy intact, while still allowing for differences between grains of each morphology.

In order to find the first critical angle, as described in Section 1.2.2, where a shear wave is propagated in the bulk but a longitudinal wave is not, the velocity of both waves must be known in both the couplant and the bulk. The refracted angle of the longitudinal wave is set to 90° to prevent it from entering the bulk and α can be calculated by modifying Snell's law.

$$\sin\alpha = \frac{V_{L-couplant}}{V_{L-bulk}} \sin 90 \tag{2.9}$$

where $V_{L\text{-couplant}}$ is the longitudinal velocity in the couplant and $V_{L\text{-bulk}}$ is the longitudinal velocity in the bulk. The resultant shear wave refracted angle can then be calculated using the shear wave velocities and the calculated α.

$$\sin\beta = \frac{V_{S-bulk}}{V_{S-couplant}} \sin\alpha \tag{2.10}$$

where $V_{S\text{-couplant}}$ is the shear velocity in the couplant and $V_{S\text{-bulk}}$ is the shear velocity in the bulk. If the Poison's ratio, Young's modulus and density of a material are known, then the velocity, initial angle of incidence for single wave type penetration and resultant directions can all be calculated. The elastic constants from Table 2.1 can then be used to calculate the velocity of shear and longitudinal waves in grains with the specific Young's moduli using Equations 2.2 and 2.3. It is assumed that each of the grains is a pure single crystal with no other features that could potentially affect its ultrasonic velocities, i.e., no low angle grain boundaries, strain fields or precipitates. Values are also found for a suitable couplant, Ultragel II [86]. The calculated velocities for each of the three materials representing each morphology, as well as the couplant, are given in Table 2.4.

Table 2.4: Velocities and Acoustic Impedance of 1050 Steel

Morphology	Material	Elastic constant	V_S (m/s)	V_L (m/s)
-	Ultragel II [86]	-	-	1650
Martensite	M_1	C_{11}	4252	6601
	M_2	C_{44}	2307	3581
	M_3	C_{12}	2736	4248
Ferrite-Pearlite	F-P_1	C_{11}	4287	6627
	F-P_2	C_{44}	2348	3630
	F-P_3	C_{12}	2718	4202
α - Ferrite	F_1	C_{11}	3948	6110
	F_2	C_{44}	2791	4319
	F_3	C_{12}	3012	4660

These velocities were used to carry out several simulations to see how grain size, morphology and texture may affect the ultrasonic velocities. These calculations simulated a material with a number of grain boundaries parallel to the sample faces being tested by ultrasonic transmission from a transducer on the top sample face to one on the opposite sample face. The assumption was also made that the time taken for the wave to travel through the couplant on either side of the sample

was identical for each simulation, i.e., the thickness of the couplant remained constant, and thus was not considered when comparing velocities. Figure 2.8 shows the simulation setup.

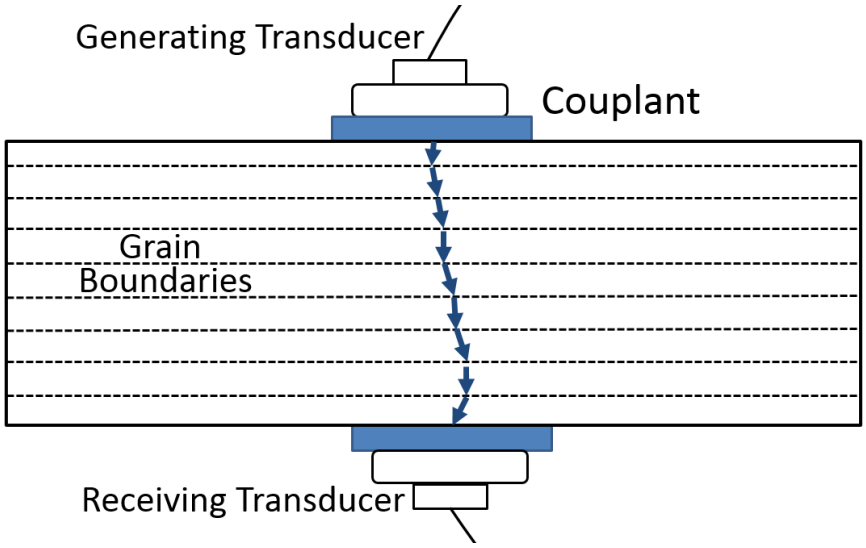

Figure 2.8: Experimental Setup for Simulations

The critical angles were calculated between the couplant and the first grain of each simulation. Shear wave simulations used the first critical angle as the angle of incidence for the wave and longitudinal wave simulations used the second critical angle. Snell's law was further used to calculate the refraction of the wave at each grain boundary. The refracted angle from each interface is the incident angle at the next interface. Figure 2.9 shows this continuation through a bulk material.

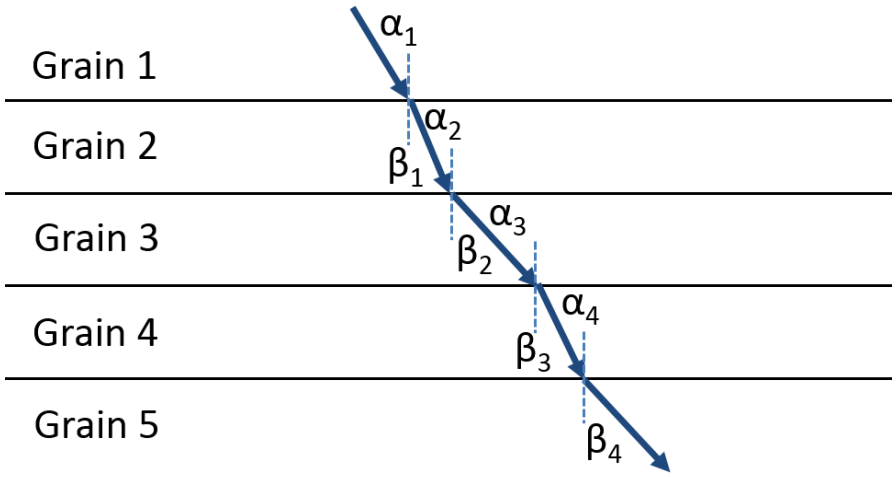

Figure 2.9: Incident and Refracted Wave Angles Through a Bulk Material

The distance the wave travels through each grain can be easily calculated once the refracted wave angle is known. Since each grain has a known velocity, the time it takes the wave to travel this

distance can also be found. The sum of these times can then be used with the known sample thickness to find the effective, or measured, velocity of the wave.

$$D = \frac{GS}{\cos(\beta)} \tag{2.11}$$

$$t_{grain} = \frac{D}{V_{wave}} \tag{2.12}$$

$$V_{eff} = \frac{\sum t_{grain}}{T_s} \tag{2.13}$$

GS is the distance between grains perpendicular to the sample thickness, D is the distance the wave travels in the grain, β is the refracted angle, t_{grain} is the time the wave takes to pass through the grain, V_{wave} is the velocity of the wave in the grain, T_s is the thickness of the sample and V_{eff} is the final output velocity which is analogous to the measured velocity from experimentation.

2.5 Isotropic Assumption Velocity Simulations

The methods described in Section 2.4 were used to calculate the ultrasonic velocity for a variety of grain arrangements. Initial simulations considered a sample consisting of nine equally sized grains of a single structure, ferrite, ferrite-pearlite or martensite. Three sample grain orders, or textures, were developed which represented each grain type equally and contained every interface possible between each type. These textures are shown in Table 2.5, where the grain name is taken from the component of the stiffness tensor used as the Young's modulus.

Table 2.5: Isotropic Nine Grain Test Textures

	Grain 1	Grain 2	Grain 3	Grain 4	Grain 5	Grain 6	Grain 7	Grain 8	Grain 9
Texture 1	C_{11}	C_{44}	C_{12}	C_{44}	C_{11}	C_{12}	C_{11}	C_{12}	C_{44}
Texture 2	C_{12}	C_{44}	C_{11}	C_{44}	C_{11}	C_{12}	C_{11}	C_{44}	C_{12}
Texture 3	C_{44}	C_{12}	C_{11}	C_{44}	C_{12}	C_{44}	C_{11}	C_{12}	C_{11}

These textures were tested for each morphology with grain sizes equal to 15, 50 and 100 μm to see if changing the grain size had an effect on velocity. Figure 2.10 shows the results of this simulation for martensite shear waves.

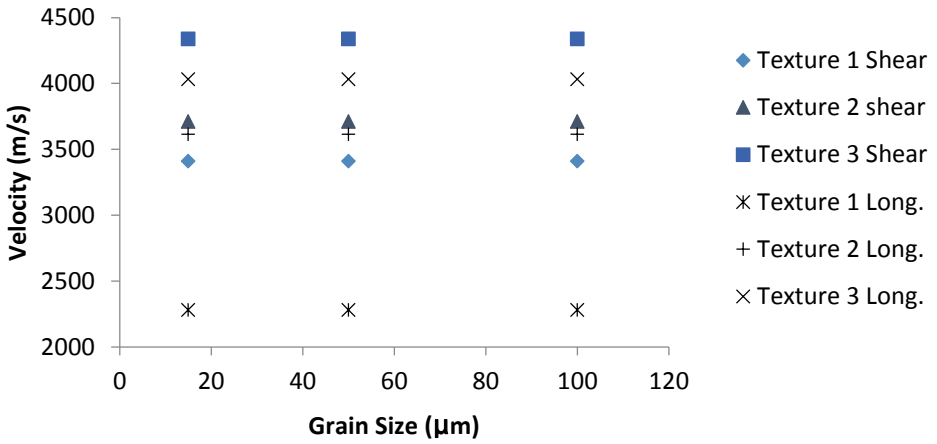

Figure 2.10: Martensite Nine Grain Simulation for Grain Size Effect

Each texture had a unique velocity which remained constant regardless of grain size. Since the overall thickness of the simulated samples increased as the grain size increased and the refracted angles between grains remained constant, the velocity did not change with grain size. Each texture had a unique velocity, which remained constant regardless of grain size. It is also of note that the velocity ranges of both shear and longitudinal waves overlap depending on the texture. The velocities of each morphology and texture were compared with a grain size of 15 µm. Figure 2.11 shows the resultant shear and longitudinal velocities.

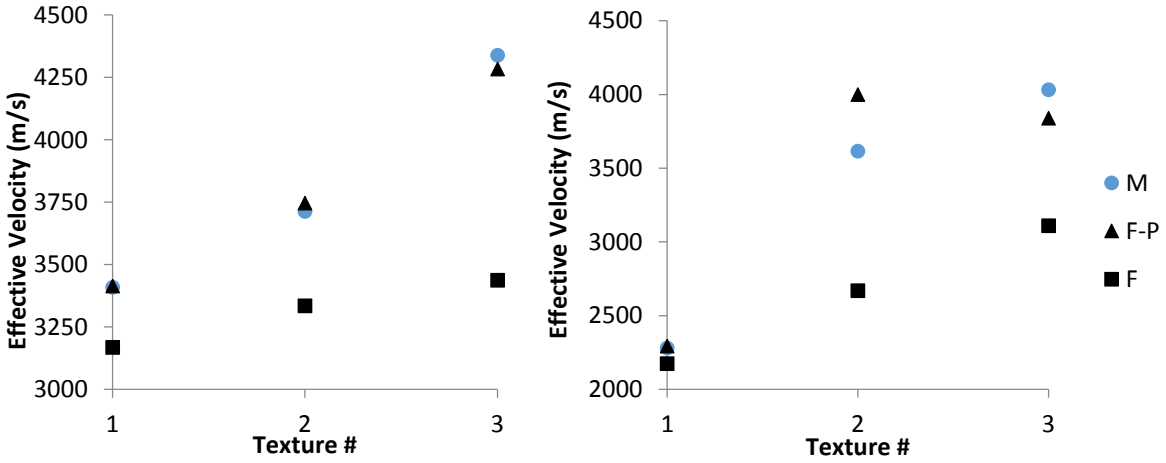

(A) (B)

Figure 2.11: Effective (A) Shear and (B) Longitudinal Velocities for Nine Grain Simulation

The martensite and ferrite-pearlite velocities remain close to one another, while the ferrite velocity is much lower for each texture. However, texture has a much greater effect on velocity than morphology, especially for longitudinal waves. Depending on the texture, martensite or ferrite-pearlite could have higher velocities and ferrite with texture 3 has a higher velocity than all three

morphologies with texture 1. This indicates that texture is a very important factor when comparing ultrasonic velocities.

In order to further investigate these effects, simulations were conducted for a sample which was 10 mm thick. To look at the effect of grain size, grain sizes of 1, 15, 50 and 100 µm were evaluated. Since the thickness of the sample was held constant, unlike the nine grain simulations, the number of grains in the simulation ranged from 100 for the largest grains to 10,000 for the smallest. Figure 2.12 shows the resultant shear and longitudinal velocities from these simulations.

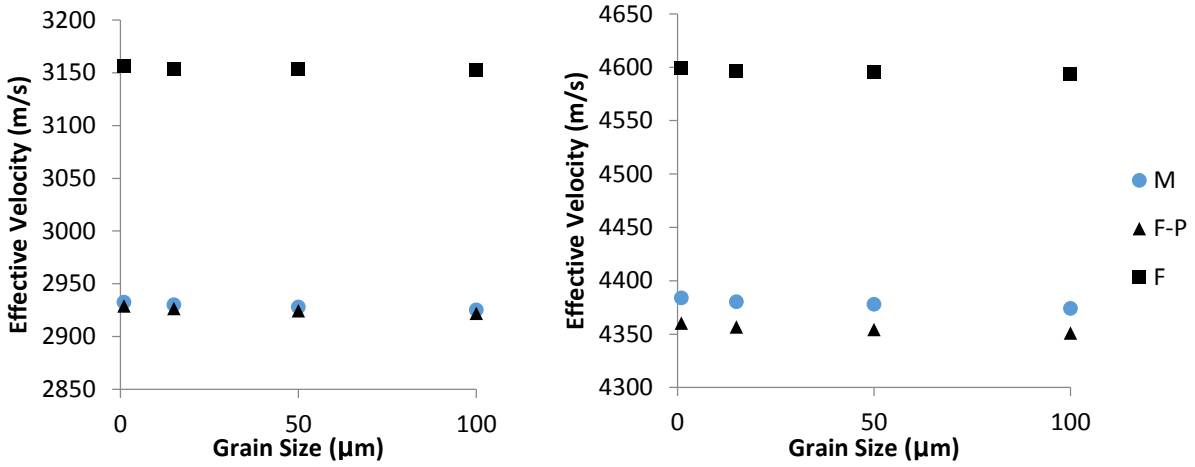

(A) (B)

Figure 2.12: Effective (A) Shear and (B) Longitudinal Velocities with Grain Size

In contrast to the nine grain simulations, when many more grains are considered the velocity of ferrite becomes much higher than that for martensite or ferrite-pearlite. Additionally, a change in grain size results in a small change in velocity. As the grain size increases the velocity decreases; however, this change is only a half a percent in the most drastic case. Both the nine grain and the 10 mm simulations show agreement that velocity is not a suitable indicator of grain size, since in both cases there is no significant change in velocity with grain size.

Further simulations were conducted to see the effect of texture on a 10 mm thick sample. Four sample textures were developed that equally represented each of the sample grains and their respective interfaces, while being different from one another. This is similar to the approach for the nine grain textures, but the system contained 666 grains, each with a thickness of 15 µm. Each texture had the same number of each grain type, but the order in which they were encountered by the wave was different for each texture. The results of these simulations are shown in Figure 2.13.

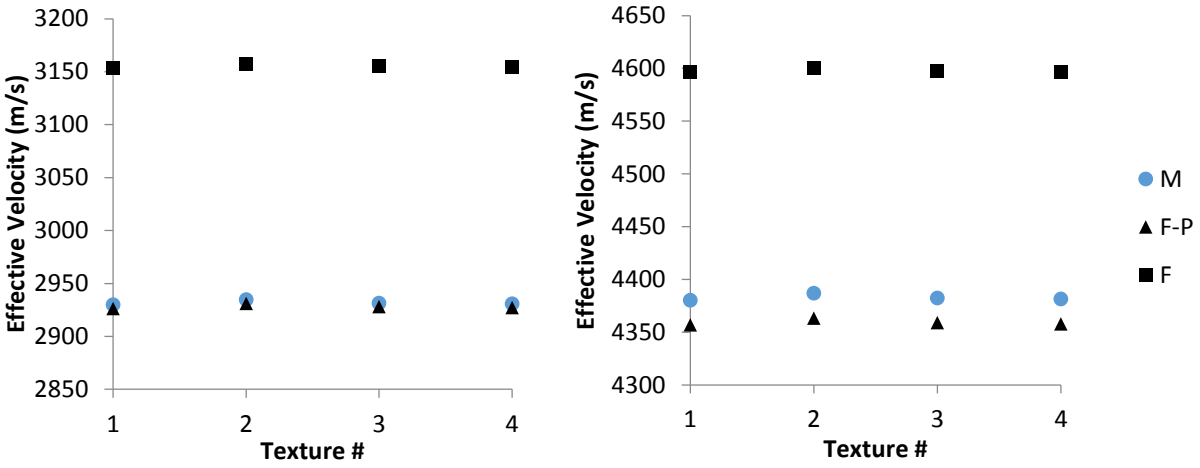

(A) (B)

Figure 2.13: Effective (A) Shear and (B) Longitudinal Velocities with Grain Order

The textures do have an effect on the velocities; however, the effect is less than what was seen in the nine grain model. The effect of orientation order is drastically decreased once large numbers of grains are considered. There is no overlap in longitudinal velocity as texture changes; however, the shear velocities of ferrite and ferrite-pearlite do overlap slightly depending on grain order. These velocities are significantly lower than those found with the Young's modulus or Christoffel equation. In order to further see the effects of texture, simulations were run in the same manner as the grain order tests but with a preferred grain orientation. In each test half of the grains were set to one orientation, with the remainder split evenly between the other two orientations. Figure 2.14 shows both the shear and longitudinal velocities calculated with these preferential orientations.

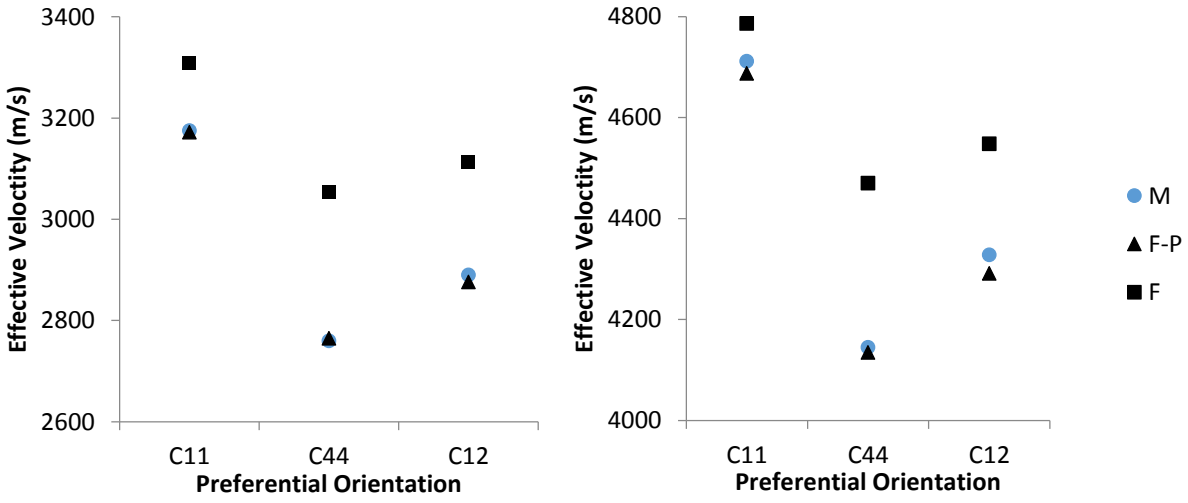

(A) (B)

Figure 2.14: Effect of Preferential Orientation on (A) Shear and (B) Longitudinal Velocity

When a preferred orientation occurs, the resultant velocities depend highly on which orientation is emphasized. When equal portions of each grain are present, there is not significant overlap in velocities; however, when a preferred orientation is present both the shear and longitudinal velocities show significant overlap between morphologies. Texture or preferential orientation is then a significant variable in determining ultrasonic velocities.

2.6 Summary

Velocity calculations for both the anisotropic and isotropic assumptions showed that orientation and texture are critical to the ultrasonic velocity. Grain size was found, in the isotropic case, to have little effect on the velocity. The isotropic assumption was found to produce velocities much slower than those for the Young's modulus or anisotropic calculations. Textureless velocities for each morphology from each method are shown in Table 2.6.

Table 2.6: Textureless Velocities for Each Calculation Method

	Isotropic Grains		Young's Modulus		Anisotropic (J=1)		
	Vs (m/s)	VL (m/s)	Vs (m/s)	VL (m/s)	Vs1 (m/s)	Vs2 (m/s)	VL (m/s)
Ferrite	3155	4598	3829	5925	3340	3985	6047
Ferrite-Pearlite	2928	4359	3825	5913	3234	3237	5913
Martensite	2932	4598	3799	5898	3198	3201	5905

The calculations show that Shear velocity should be better than longitudinal velocity at differentiating between morphologies since there is less overlap between the velocities found in each structure in shear waves than longitudinal. The Young's modulus approximation gave similar longitudinal velocities to the Christoffel method but its inability to differentiate between the two shear modes make it less useful since the shear modes are better at morphology differentiation. The isotropic method allowed grain size analysis but did not produce velocities which agreed with the other methods. Additionally it showed that orientation had a large effect on velocity which makes the isotropic assumption critical to this method invalid. Both the Young's modulus and isotropic methods while simpler than the anisotropic Christoffel method do not sufficiently describe the ultrasonic velocities to be useful in this work.

Chapter 3 Experimental Methods and Results

This chapter details the experimental methods used in this work for each set of experiments, as well as the tabulated results obtained from each. A brief overview of the steels used is given, followed by the ultrasonic testing methodology. The procedures used for through thickness investigation of L80 and X70 skelp to see how ultrasonic properties varied in each skelp, interstitial free (IF) steel annealing to see the effect of recrystallization and grain growth on ultrasonic properties, L80 microstructure variation and finally industrial tests to see the effect of microstructure, are presented. Tabulated results are presented in this section for reference, the discussion of these results is found in Chapter 4.

3.1 Steels Studied

Five different steels were analyzed using ultrasonic testing as well as other methods. Two of the steels, L80 and X70, are commonly used pipe steels while the other three, interstitial free (IF), 5160 and 4130, are used in other applications. Both the pipe steels were received in the as rolled condition, i.e., skelp before being processed into pipe. The 4130 and IF steels were also received as rolled product, as bar in the case of 4130 and sheet for IF. The 5160 was taken from a fully processed leaf spring intended for installation into a Chrysler automobile.

The pipe steels were provided by Evraz Inc. NA from production runs; Evraz also provided the IF steel from their sources. L80 is a pipe casing used in sour gas environments. Fully processed L80 pipe must have a specified minimum yield strength of 80 ksi or ~550 MPa. Normally these pipes are quench and tempered after forming to achieve the desired properties. X70 is a microalloyed steel used primarily for linepipe in the oil and gas industries. X70 has a specified minimum yield strength of 70 ksi or about 480 MPa. IF steels are more commonly used for part fabrication rather than piping, since they have good ductility and formability. Abbreviated chemistries provided for these steels are shown in Table 3.1.

Table 3.1: Abbreviated Steel Chemistries (wt%) for X70, L80 and IF Steels

	X70	L80	IF
C	0.044	0.244	0.003
Mn	1.71	0.99	0.018
Si	0.25	0.2	-
Cr	0.24	0.16	-
Mo	0.072	0.014	-
Nb, Ti, V	0.086	0.032	0.049

4130 is a common machining steel used for fabrication of parts, such as bearings or gears, which are then heat treated to obtain desirable properties. 4130 has good machinability and is often used in resistance welding applications. 5160, in contrast, is a poorly weldable steel with a much higher

carbon content than the other steels investigated. It is primarily used in heavy springs such as the automobile leaf spring that was supplied. Since these steels were not obtained directly from their manufacturers, exact chemistries were not provided; however, the alloying guidelines for both grades are given in Table 3.2.

Table 3.2: Alloying Requirements (wt%) for 5160 and 4130 Steels

	5160 [87]	4130 [88]
C	0.55-0.65	0.28-0.33
Mn	0.75-1.0	0.40-0.60
Si	0.20-0.35	0.2-0.35
Cr	0.70-0.90	0.8-1.10
Mo	-	0.15-0.25

3.2 Ultrasonic Testing Methodology

The methods and procedure used to ultrasonically test the samples prepared in this work are described below. Each sample was tested in the same manner to get results as comparable as possible between each other.

3.2.1 Ultrasonic Equipment

Ultrasonic testing was conducted using a Socomate USPC7100LA ultrasonic pulser/receiver. The pulser/receiver was used either with an Olympus V202-RM longitudinal wave transducer or an Olympus V221-BA-RM shear wave transducer. Both transducers had an operating frequency of 10 MHz and an incidence angle of 0^o. The piezo-electric element in each transducer had a diameter of 6.5 mm. Sonotec shear gel was used for shear wave tests and synthetic SAE 5W30 motor oil for the longitudinal tests. Shear waves require a viscous couplant to propagate, while longitudinal waves can propagate in most fluids. Sonotec shear gel was suggested for the shear wave couplant and motor oil for the longitudinal wave couplant by the manufacturer of the transducers [89]. The USPC7100LA pulser/receiver was connected directly to a desktop PC and controlled with proprietary Socomate software. This software can report ultrasonic wave times as short as 10 ns while the receiver itself is accurate to 5 ns. A custom Labview application was made in order to obtain more accurate wave times directly from the receiver.

3.2.2 Pressure and Thickness Effects

Before the experimental samples could be ultrasonically tested, the effect of pressure on the transducer had to be determined as well as whether samples as thin as 1 mm could be tested. Two experiments were devised to determine the effect of sample thickness and transducer pressure on ultrasonic velocity. Both experiments were carried out on water quenched samples of 4130 steel. After quenching, seven samples were machined and surface ground to different thicknesses in 1

mm increments from 7 mm to 1 mm thick. The 7 mm thick sample was used to see the effect of transducer pressure on ultrasonic velocity. Couplant was placed on the sample followed by the transducer and three 500 g weights; then the weights were removed. This setup is shown in Figure 3.1.

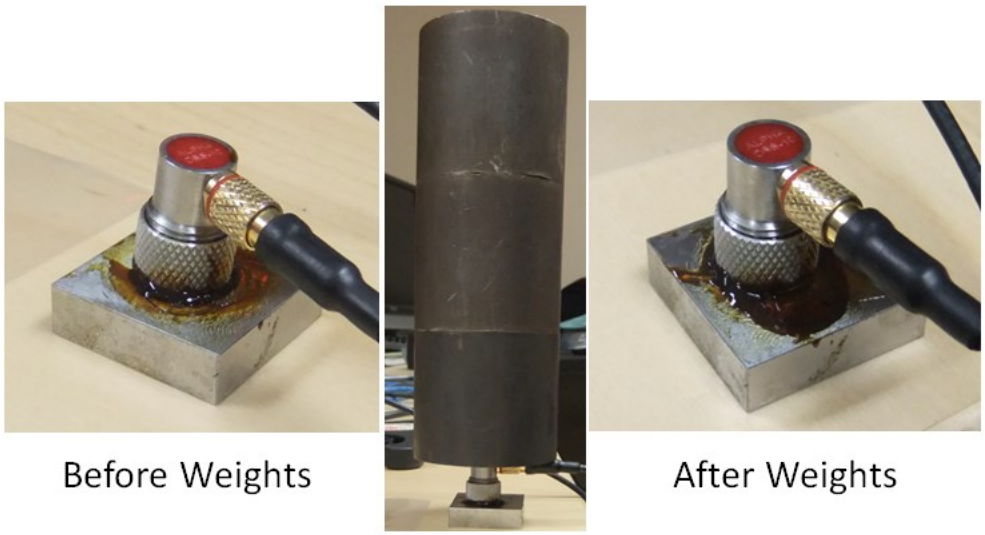

Figure 3.1: Transducer Pressure Experimental Setup

As the weights were placed and removed any variation in the signal received was noted. When the weights were added, the height of backwall reflections increased. When the weights were removed, the peak heights were not affected. This shows that the weight or pressure on the transducer is not directly an important factor. The increase in signal height as weights were applied is the result of the couplant spreading over the surface of the sample. Once the weights were removed, the couplant remained spread and, as such, the peak heights did not decrease. When performing ultrasonic tests, it is then important to apply enough pressure to spread the couplant until the peak heights reach a maximum. It is not necessary to continually apply pressure during the test, only when placing the transducer on the sample. The peak heights are shown in Figure 3.2.

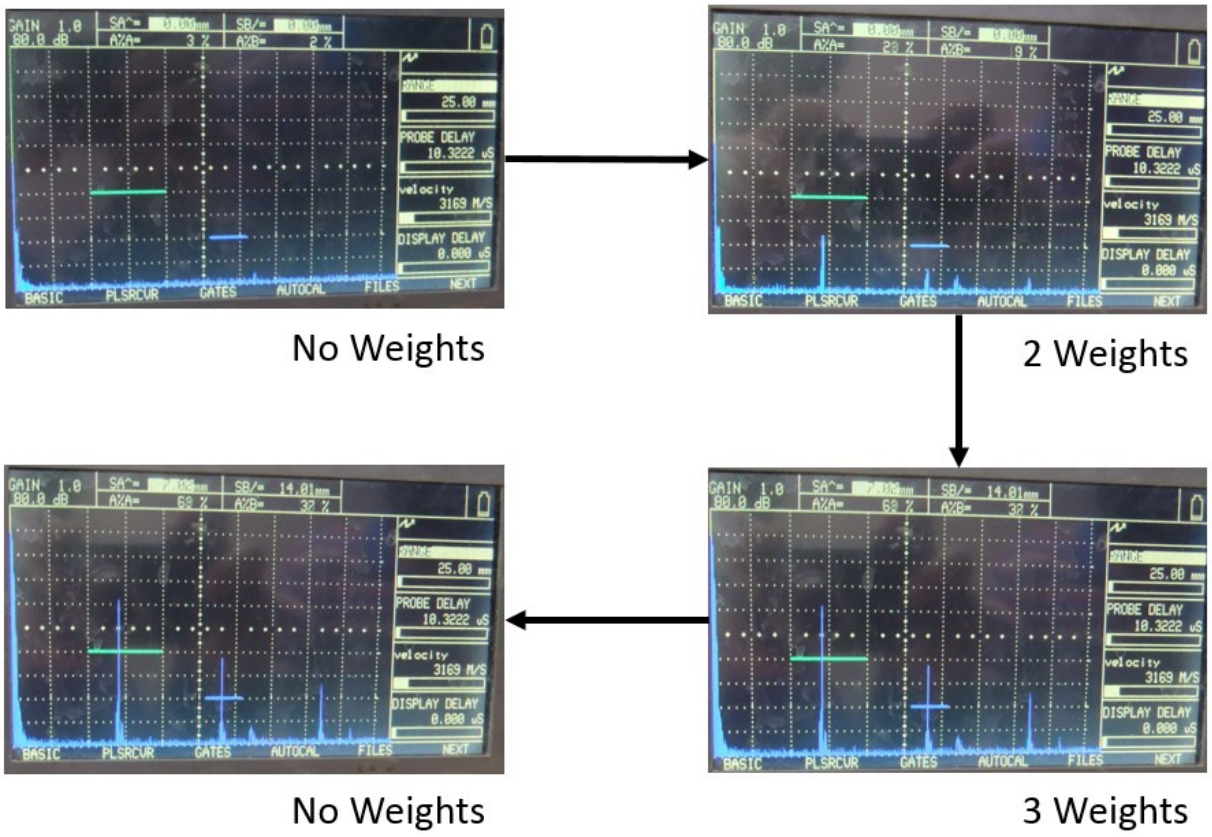

Figure 3.2: Peak Heights from Weight Application and Removal

All 7 thicknesses were then tested by clamping the sample, couplant and transducer together to ensure the couplant was spread sufficiently. The resultant signals were recorded and are shown for the 6 mm to 1 mm samples in Figure 3.3.

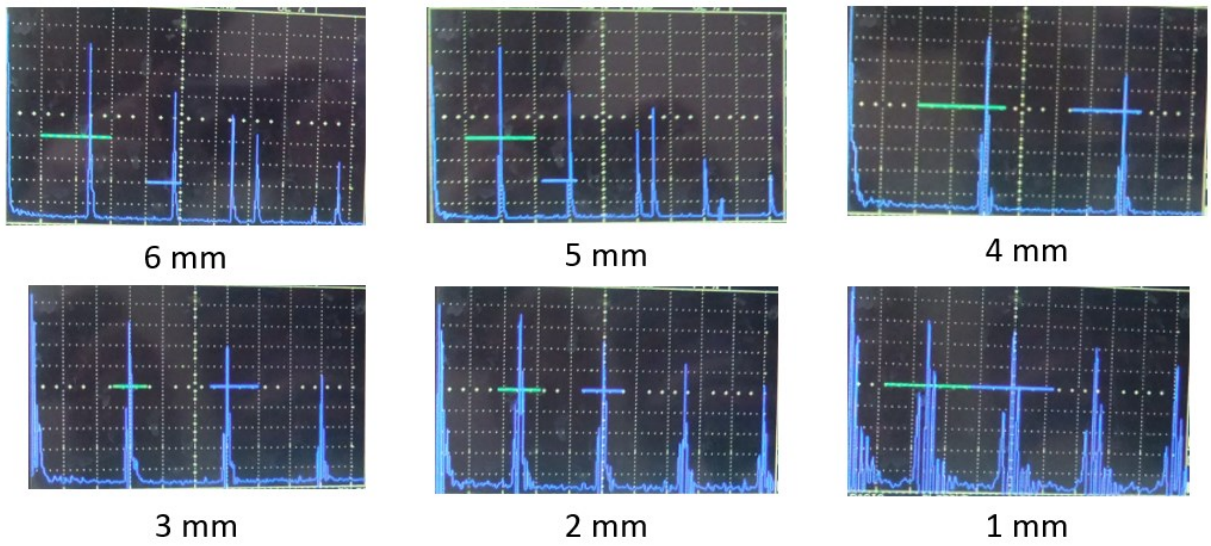

Figure 3.3: The Effect of Reducing Thickness of 4130 Steel on Ultrasonic Signals

The signal did not change significantly from the 7 mm thick sample to the 3 mm sample. The peaks began showing more noise around the central peak in the 2 mm thick sample and showed significant noise in the 1 mm thick sample. The gates, horizontal lines in Figure 3.3 where data is collected, could still be positioned for both noisy samples such that only the highest peak was captured, allowing velocity and attenuation readings to be obtained, but much more care and time had to be taken. The ideal minimum thickness for ultrasonic testing is then 3 mm, although samples as thin as 1 mm can still be successfully tested.

3.2.3 Experimental Setup

Ultrasonic tests began with measuring the thickness of each sample with a Mitutoyo MDC-Lite digital micrometer with a resolution of 0.001 mm. Each sample was measured six times and the average of these measurements was taken as the thickness of the sample. Table 3.3 shows an example of these thickness measurements for a small L80 sample, which was austenitized and then air cooled. The sample had an initial machined thickness of 3 mm but was then surface ground to remove any scale or oxidized layer.

Table 3.3: Sample Thickness Measurements

Average Thickness (mm)	Standard Deviation (mm)
2.863	0.002

Next the couplant was placed on the sample. For shear wave tests the transducer had to be "worked" into the couplant by using firm pressure and rotating the sample. This was done to minimize the distance the wave travels through the couplant and to ensure the wave data is accurate and repeatable. Since the longitudinal wave couplant is much less viscous, this was not required for longitudinal tests; however, two metal pieces with a combined weight of 135 g were placed on top of the longitudinal transducer to keep it steady and to prevent the connecting wire from knocking it over. Figure 3.4 shows the setup for both shear and longitudinal tests for the L80 sample described in Table 3.3.

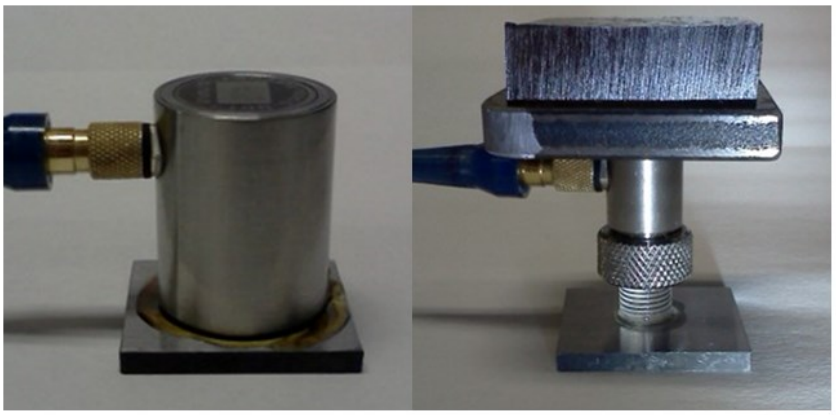

A B

Figure 3.4: Experimental Setup for (A) Shear and (B) Longitudinal Tests

Both shear and longitudinal transducers had an acrylic delay block, 6 mm for shear waves and 10 mm for longitudinal waves, which is used to minimize background noise particularly in thin samples. The initial sample backwall reflection time includes the time for the wave to travel through the delay block as well as the sample. The block is removable on the longitudinal transducer, but not on the shear transducer. The delay block was used for all longitudinal tests, since it made peak identification and gate placement significantly faster and simpler. Without the delay block backwall reflections appeared as a cluster of peaks, whereas with the delay block the cluster was reduced to a single peak. Figure 3.5 shows the difference in signal output for the same sample using the transducer without and with the delay block.

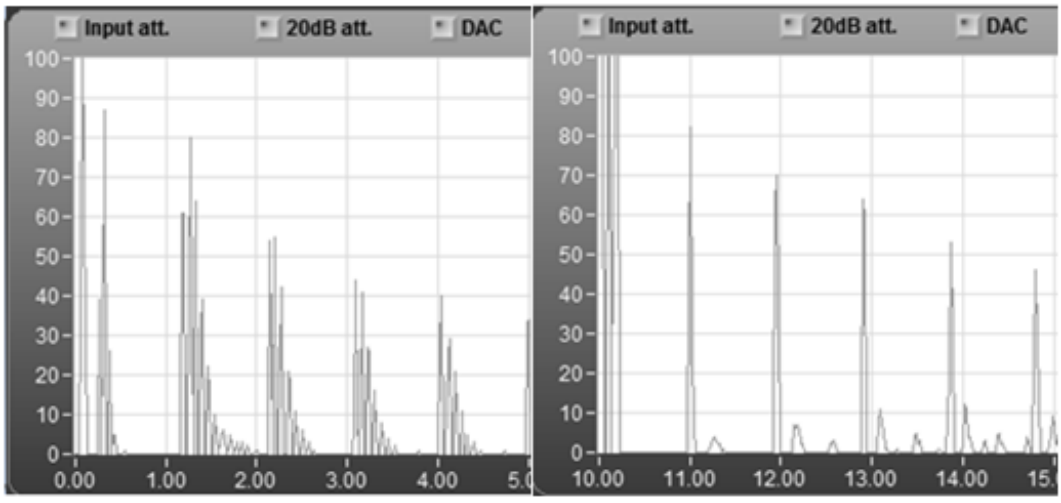

Figure 3.5: Longitudinal Wave Signal Without (A) and With (B) 10 mm Delay Block

3.2.4 Velocity Measurements

Samples were tested with longitudinal waves as well as twice using the shear wave probe, once with the wire from the probe oriented parallel to the rolling direction and once with the wire oriented transverse to the rolling direction. The two shear wave directions corresponded to a maximum and minimum in shear wave velocity, which is analogous to the V_2 and V_3 velocities calculated in Section 2.1. Figure 3.6 shows the transverse oriented shear wave signal received for the air cooled sample with each backwall reflection numbered.

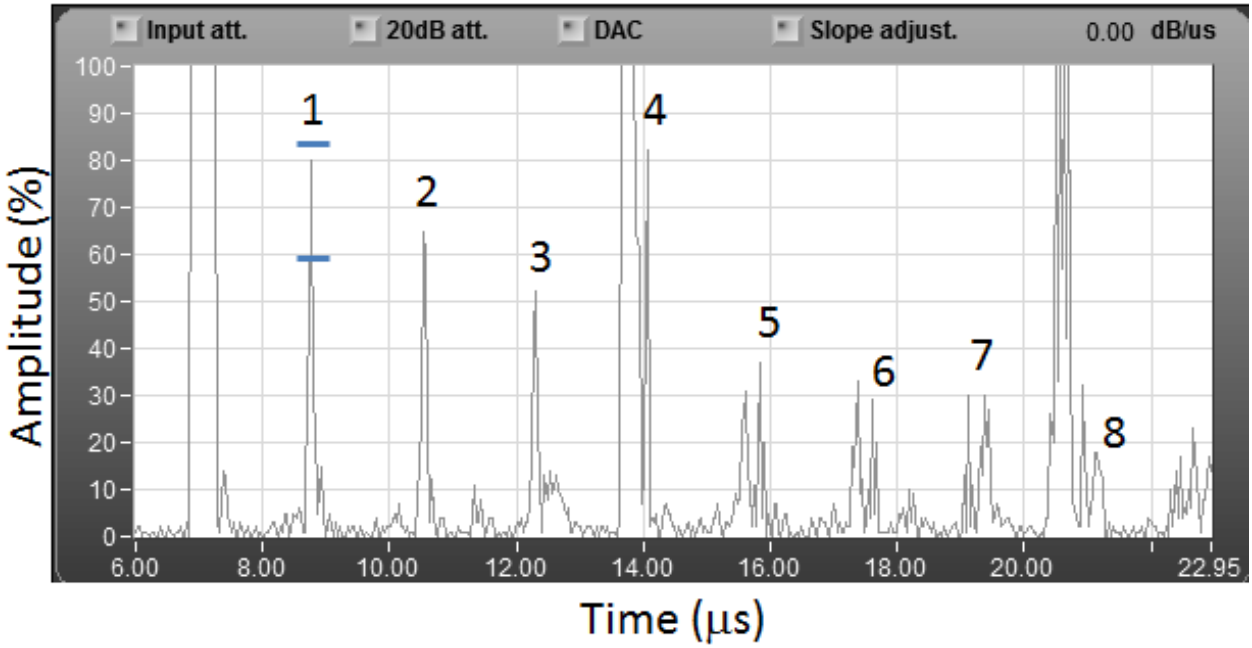

Figure 3.6: Transverse Oriented Shear Wave Signal (Air Cooled L80)

Figure 3.6 shows the intensity of the received signal vs. time. A backwall is the peak in intensity when the wave has reflected from the back surface of the sample and returned to the transducer. The first backwall corresponds to the first reflection. The second backwall is obtained from the wave that reflects off the surface near the transducer, after passing through the sample once, and then travels through the bulk again and returns to the transducer. This is shown in Figure 3.7, where each time a red arrow returns to the transducer a backwall peak is formed. The first red arrow is the first backwall, the second red arrow is the second backwall, etc. The backwalls are thus named since each peak formed is the result of a reflection off the back face, or wall, of the sample.

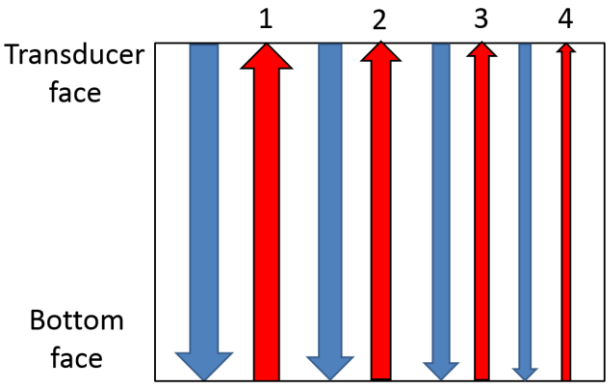

Figure 3.7: Ultrasonic Backwall Reflections

The horizontal lines, called a gate, are visible at the first backwall in Figure 3.6 and show where the Labview application will capture a time value. The location of the gate can be adjusted in the software to be placed on any peak. The application takes the point with the highest amplitude located inside the gate and reports its time value. The transducer is continuously pulsing in real time to generate the signal shown in Figure 3.6. The Labview application collects 120 of these pulses and averages them to provide a final time value. This results in some time values being reported more accurately than 5 ns. The horizontal width of the gate can be adjusted to be wider to quickly capture the first backwalls or to be narrower to ensure the correct peak is captured in the later backwalls. The software also reports the amplitude of this point. Table 3.4 shows these values for the above test.

Table 3.4: Amplitude and Time for Backwall Reflections (Air Cooled L80)

Backwall	Time (ms)	Amplitude (%)
1	8.800	80
2	10.560	65
3	12.325	52
4	14.090	76
5	15.850	35
6	17.610	28
7	19.370	24
8	21.137	18

The velocities between the backwalls were obtained by dividing twice the sample thickness, since the wave travels through the sample twice per reflection, by the difference in time between consecutive reflections. The velocity for the test was obtained by taking the average of these values. Figure 3.8 shows the individual backwall velocities as well as the net test velocity.

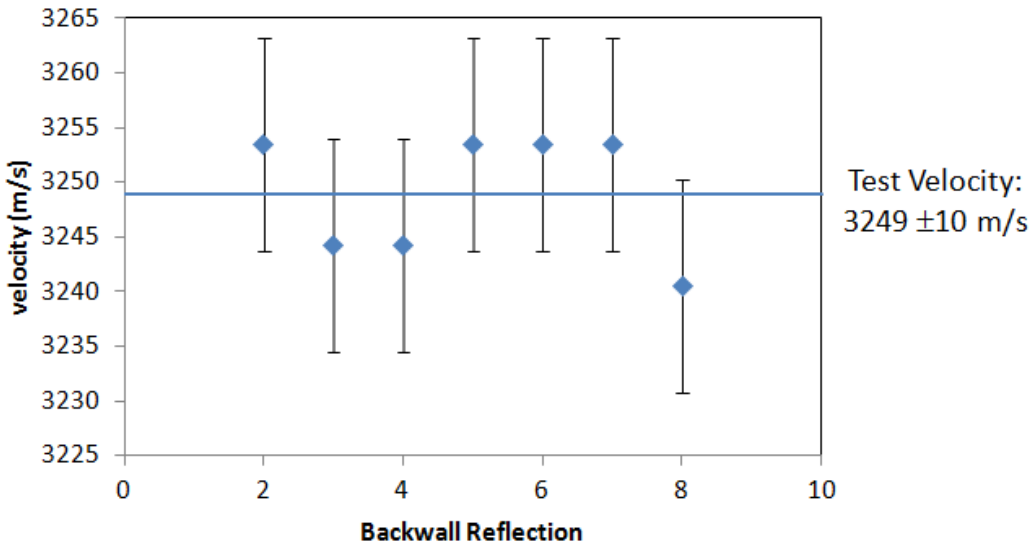

Figure 3.8: Backwall and Final Test Velocities (Air Cooled L80)

3.2.5 Attenuation Measurements

Attenuation can be found between each backwall using Equation 1.5. However, in some cases other factors may affect the amplitude of a backwall reflection, skewing the results. Error was calculated in the same manner as velocity, by finding maximum and minimum values possible. Figure 3.9 shows the attenuation values between each backwall reflection for the example sample.

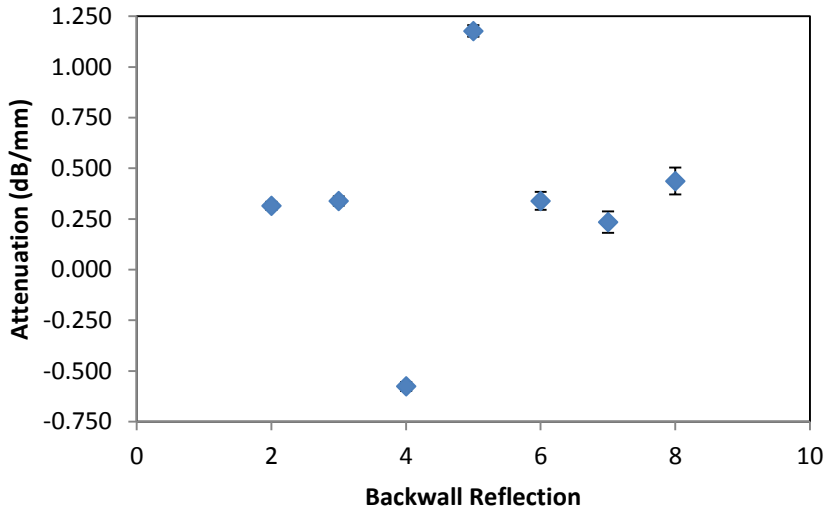

Figure 3.9: Attenuation Values between Backwall Reflections (Air Cooled L80)

The attenuation values between the third and fourth and fourth and fifth backwall reflections are significantly different than those between the remaining reflections. In some cases it can be difficult to determine which reflections accurately represent the sample attenuation and which are

affected by other factors. In order to identify which reflections are erroneous, the time and amplitude data were plotted for each sample and an exponential trend line was fit was made. Reflections, which did not match the trend line, were removed until a good fit was observed and a minimum R^2 value of 0.99 was obtained. Figure 3.10 shows this plot for the sample.

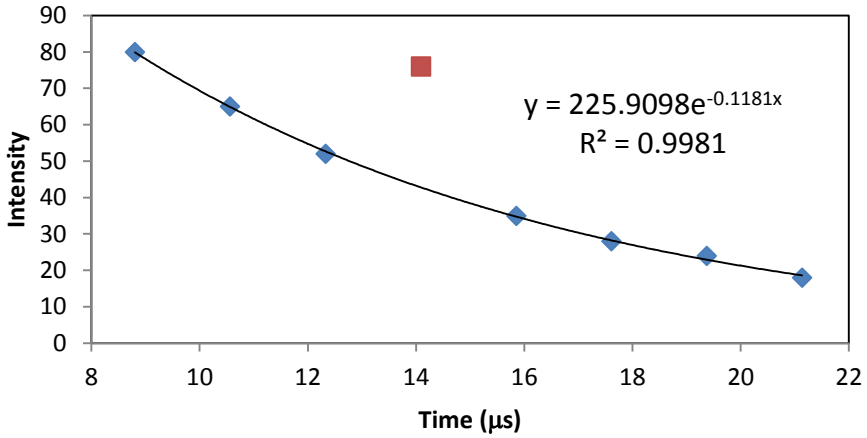

Figure 3.10: Intensity-Time Plot for Location of Erroneous Reflections (Air Cooled L80)

The fourth backwall reflection does not fit the trend shown by the remaining reflections. This accounts for why both attenuation values related to the fourth backwall were significantly different from the others. Once the erroneous points had been identified, the trend line equation was used to calculate amplitudes for the time of each backwall reflection; these amplitudes were then used to find the attenuation between each. These were then averaged in the same manner as the velocities to find an overall sample attenuation. The attenuation between each backwall reflection and the overall sample attenuation are shown in Figure 3.11.

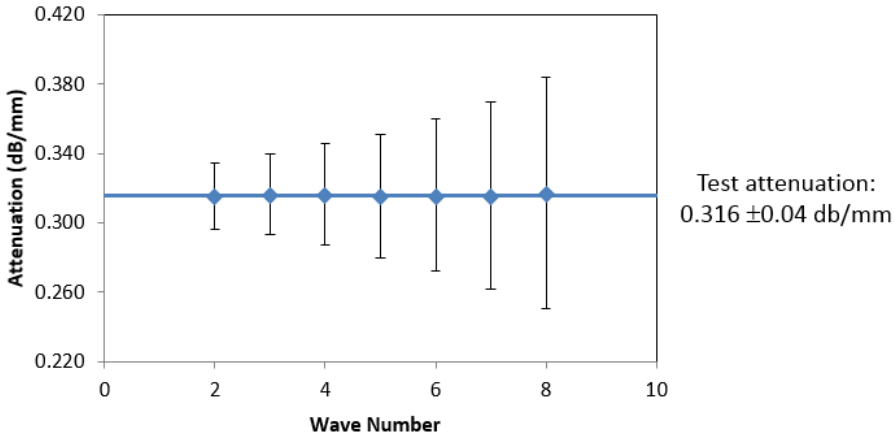

Figure 3.11: Calculated Backwall and Final Test Attenuation (Air Cooled L80)

The initial spike in the signal at approximately 7 µs in Figure 3.6 is the reflection caused by the integral delay block in the shear transducer; similar spikes are also present at 14 and 21 µs from

further reflections. Since the fourth backwall reflection in this sample is at 14.09 μs, its amplitude is affected by the delay block reflection and is much higher than it would be otherwise. This skews the attenuation values related to it and necessitates the amplitude mapping used. In this case the errant amplitude could be easily identified without amplitude mapping; however, in some noisier samples determining which reflections were not representative was much more difficult and mapping was required to get accurate and repeatable attenuation data.

3.2.6 Ultrasonic Measurement Uncertainty

The equipment used for each ultrasonic test provided data for the independent variables: time, peak height and sample thickness. The accuracy of the instruments for reporting these variables is, 5 ns for time, 0.001 mm for thickness and 1% for peak height. The independent variables have a non-linear relationship (Equations 1.4 and 1.5) with the dependent variables of interest (velocity and attenuation). The effect of the accuracy of the instruments on the range of the dependent variables is of interest in order to assess any trends in results obtained. The maximum velocity was found using the maximum thickness and minimum time possible; this was then compared with the reported value to find the positive error, while the minimum thickness and maximum time were used to find the negative error. These values were found for each reflection of a test and were averaged to find the error velocity. The maximum and minimum times, thickness, velocity and error values for the L80 sample presented above are shown in Table 3.5. The reported velocity for this test was 3249 m/s with an error of ±10 m/s.

Table 3.5: Ultrasonic Shear Velocity Error (Air Cooled L80)

	Measured Time (μs)		Thickness (mm)		Velocity (m/s)		Error (m/s)	
Reflection	max	min	max	min	max	min	positive	negative
1	8.8025	8.7975	2.8635	2.8625				
2	10.5625	10.5575	2.8635	2.8625	3244	3263	10	10
3	12.3275	12.3225	2.8635	2.8625	3234	3254	10	10
4	14.0925	14.0875	2.8635	2.8625	3234	3254	10	10
5	15.8525	15.8475	2.8635	2.8625	3244	3263	10	10
6	17.6125	17.6075	2.8635	2.8625	3244	3263	10	10
7	19.3725	19.3675	2.8635	2.8625	3244	3263	10	10
8	21.1395	21.1345	2.8635	2.8625	3231	3250	10	10

Similarly, the error in the attenuation was calculated by finding the possible minimum and maximum values and averaging their difference from the reported value. These values are shown in Table 3.6. The calculated attenuation for this test was 0.316 dB/mm with an error of ±0.04 dB/mm.

Table 3.6: Ultrasonic Attenuation Error (Air Cooled L80)

Amplitude (%)	attenuation (dB/mm)	Error (dB/mm)

wave	max	min	max	min	positive	negative
1	80.5	79.5	0.3	0.3	0.02	0.02
2	65.5	64.5	0.4	0.3	0.03	0.03
3	52.5	51.5	-0.6	-0.6	0.02	0.02
4	76.5	75.5	1.2	1.1	0.03	0.03
5	35.5	34.5	0.4	0.3	0.05	0.05
6	28.5	27.5	0.3	0.2	0.06	0.06
7	24.5	23.5	0.5	0.4	0.07	0.07
8	18.5	17.5				
				Average:	0.04	0.04

The uncertainty in time measurement is the main contributor to the uncertainty in ultrasonic velocity. If the equipment used in the laboratory were to be used in industry, the default 10 ns resolution would be sufficient for accurate measurements. The issue with time resolution in the samples tested in this work is related to the thin nature of the materials being tested with industrial equipment. The samples in this work ranged in thickness from ~0.9 mm to 3.5 mm, which is significantly thinner than the full skelp thickness of the L80 and X70 steels, which are 9 mm and 15 mm, respectively. Figure 3.12 shows how the velocity uncertainty decreases as the sample thickness increases, using the resolution of our equipment and an assumed velocity for the air cooled L80 sample discussed above. The shaded region shows the range of sample thicknesses tested, which have much higher uncertainties than samples which are 9-15 mm thick.

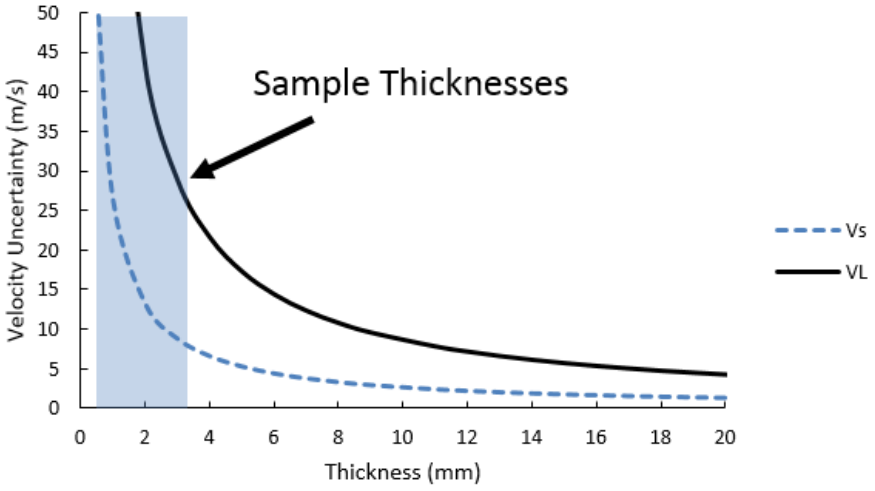

Figure 3.12: Ultrasonic Velocity Uncertainty vs. Sample Thickness

3.3 Pipe Skelp Through Thickness Investigation

Ultrasonic testing was done through the thickness of two pipe skelps to see how their ultrasonic properties varied. X-ray diffraction (XRD) was also done through the thickness of these skelps and compared with the ultrasonic properties.

3.3.1 Experimental Design

Investigations were carried out on samples taken through the thickness of two different pipe skelp grades, L80 and X70. Both sections were obtained as flat skelp from production runs, which would be further processed into pipe of their respective grade. In order to investigate these skelp samples, 24 mm x 38 mm x 1 mm thick samples were obtained through the thickness of each. To obtain these samples, bars were first cut from each skelp along the rolling direction as illustrated in Figure 3.13.

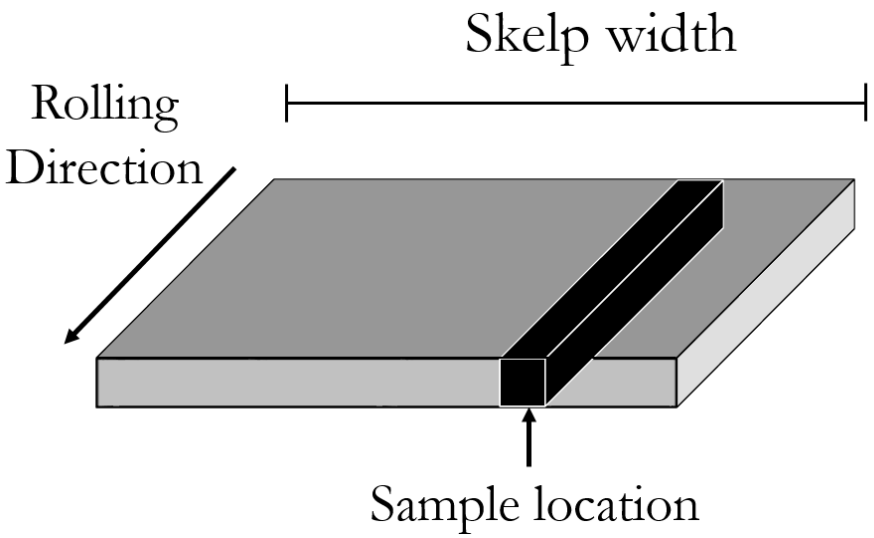

Figure 3.13: Location of Sample Bars in Skelp

Samples were then obtained from each bar through the thickness of the skelp. Cutting was done to minimize the length of the bar used and to keep samples as close to the same location as possible. Figure 3.14A shows sample locations through the X70 bar and Figure 3.14B shows locations through the L80 bar. Once cut, the samples were then surface ground to produce parallel faces and a consistent surface finish.

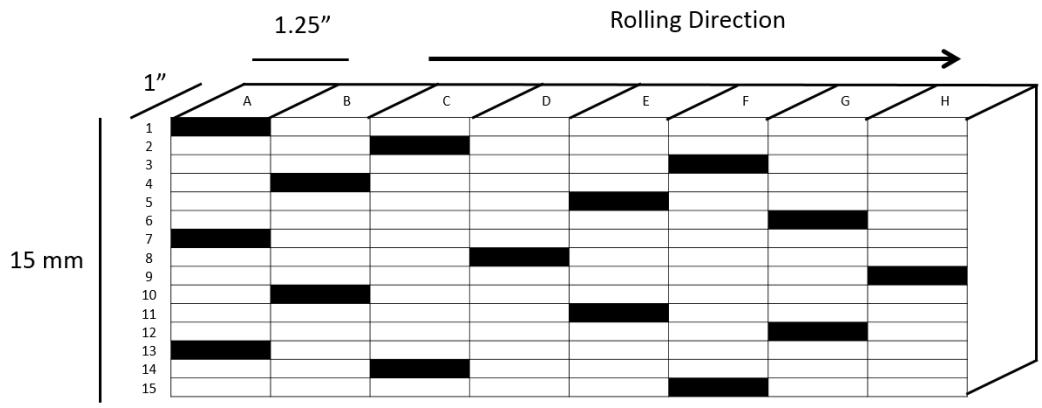

(A)

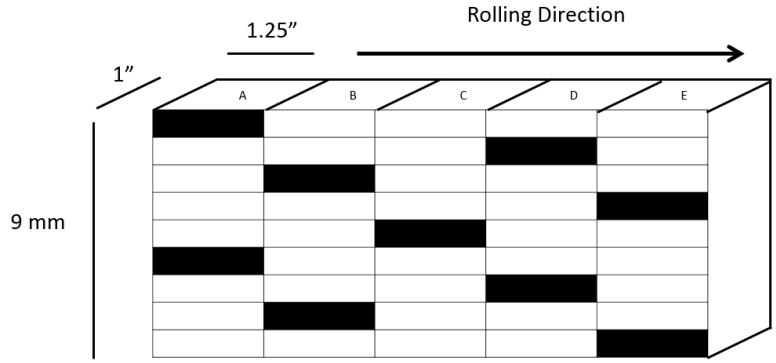

(B)

Figure 3.14: Sample Locations Through the Thickness of (A) X70 and (B) L80 Bars.

3.3.2 XRD Analysis

The sectioned samples were characterized using X-ray Diffraction (XRD). Testing was performed using a Rigaku rotating anode RU-200B XRD system equipped with a copper x-ray source and graphite monochromator. The divergence slit was 1° and the monochromator slit was 0.8 mm. The scanning range was from 10° to 110° with a 0.05° step size and 2° per minute scanning speed. Before each set of samples was tested, a LaB_6 calibration sample was run.

In order to analyze the data obtained from XRD, Rietveld refinement was done using TOPAS Academic Software, Version 5. This software was used to obtain the spherical harmonics coefficients for preferential orientation (C_{mn}), domain size (D_s) and microstrain (ε), as described in Section 1.6, for each sample. The same software was used to obtain the instrument parameters and calibration from the LaB_6 samples. These include the error in setting the 2θ zero point (Zero_Error), corrections for peak asymmetry due to axial divergence (Simple_Axial_Model), the background function (bkg) and Cagliotti parameters for the instrument profile (UVW). The background function was approximated as a sixth order or lower polynomial. In addition to the sample data, instrument information was entered. The Lorentz-polarization (LP) factor is a measure of the degree of polarization of the radiation, with zero being unpolarised and 90 being

completely polarized. For the instrument used, with a copper source and graphite monochromator, the LP factor was 26.4. To account for the wavelength used, a factor for the source was entered, CuKα1(0.001). Figure 3.15 shows an example of a LaB_6 XRD pattern.

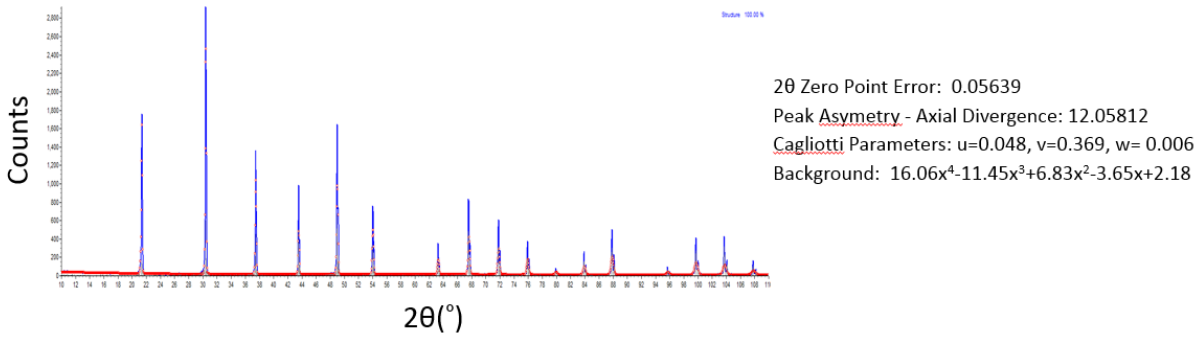

Figure 3.15: LaB_6 XRD Pattern and Instrument Parameters

From the LaB_6 pattern, the 2θ zero point error was found to be 0.05639°, the peak asymmetry axial divergence was 12.05812, the Cagliotti U, V, W parameters were 0.048, 0.369 and 0.006, respectively, and the background function was $16.06x^4-11.45x^3+6.83x^2-3.65x+2.18$. Using these instrument parameters, the steel sample parameters could be inputted and analyzed. All steel samples were primarily ferrite; peaks were not seen or detected for any other phases. The parameters acquired from the LaB_6 calibrations were set as constants in order to find the parameters of interest for each steel sample. A sample XRD pattern for an L80 steel sample, from the top face of the skelp, is shown in Figure 3.16. From Rietveld fitting of the pattern, the domain size was found to be 143 nm, the microstrain was $1.1x10^{-3}$ and the lattice parameter was 0.2869 nm. The spherical harmonics coefficients C_{41} and C_{61} were found to be 0.157 and -0.060, respectively.

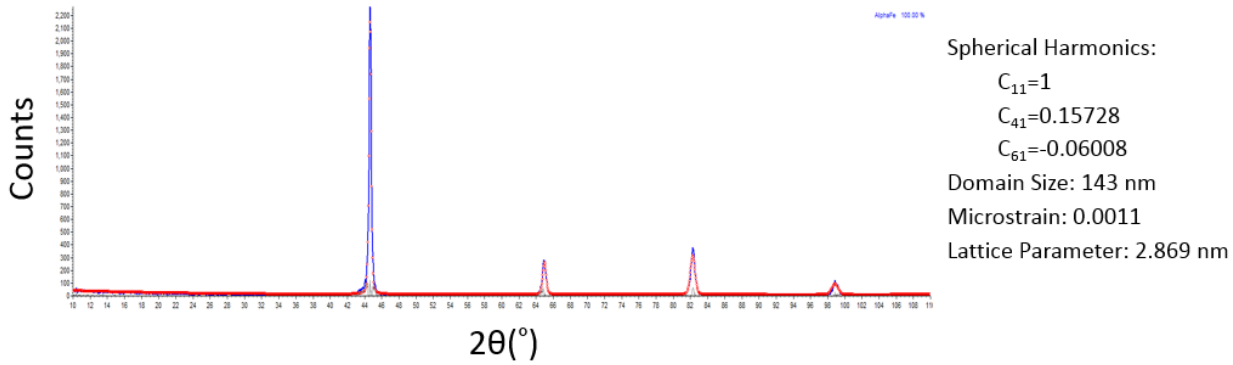

Figure 3.16: Sample L80 (Sample Depth of 1 mm) XRD Pattern and Obtained Parameters

Issues with sample preparation and Rietveld refinement cast doubt on the results obtained from XRD analysis. X-rays do not penetrate deeply into the bulk of material tested but provide data only

for near surface material. The samples used in this work were machined and surface ground which can create a work hardened surface layer. The XRD patterns for these samples could then be greatly affected by this work hardened layer. In order to obtain accurate, representative diffraction patterns from the samples, the work hardened layer would have to be removed by a process such as electropolishing. It would also be necessary to independently verify the information obtained from Rietveld refinement with a more direct measurement technique, such as transmission electron microscopy, to ensure that the Rietveld quantities obtained, such as domain size and dislocation density, are meaningful. Neither removal of the work hardened layer nor independent verification of parameters were performed for the through thickness samples. Analysis of the results from XRD of these samples is presented in Appendix B rather than in the main body of the thesis, because of the uncertainty introduced by these factors.

3.3.3 Ultrasonic Tests

The samples were ultrasonically tested as described in Section 3.2 to find ultrasonic velocity and attenuation. The ultrasonic values were then compared with the parameters found using XRD, as well as their location through the skelp, to determine any correlations. The ultrasonic properties, velocity and attenuation, are shown in Table 3.8 for L80 and Table 3.7 for X70 samples.

Table 3.7: X70 Through Thickness Ultrasonic Properties

	Long		Shear (P)		Shear (T)	
Sample	Velocity (m/s)	Attenuation (dB/mm)	Velocity (m/s)	Attenuation (dB/mm)	Velocity (m/s)	Attenuation (dB/mm)
1	5968	0.30	3234	0.39	3157	0.45
2	5941	0.31	3279	0.27	3174	0.35
3	5922	0.22	3275	0.42	3174	0.55
4	5915	0.32	3273	0.41	3144	0.52
5	5936	0.30	3284	0.40	3172	0.44
6	5941	0.35	3271	0.37	3158	0.38
7	5949	0.32	3267	0.36	3117	0.53
8	5936	0.31	3279	0.48	3171	0.33
9	6018	0.50	3342	0.51	3166	0.52
10	5932	0.31	3281	0.38	3165	0.43
11	5945	0.32	3290	0.37	3169	0.40
12	5937	0.41	3294	0.36	3164	0.51
13	5920	0.36	3247	0.40	3172	0.30
14	5931	0.32	3305	0.27	3113	0.44
15	5927	0.29	3280	0.30	3155	0.33

Table 3.8: L80 Through Thickness Ultrasonic Properties

Sample	Long		Shear (P)		Shear (T)	
	Velocity (m/s)	Attenuation (dB/mm)	Velocity (m/s)	Attenuation (dB/mm)	Velocity (m/s)	Attenuation (dB/mm)
1	5912	0.30	3279	0.60	3245	0.44
2	5904	0.33	3281	0.50	3256	0.54
3	5899	0.30	3274	0.56	3243	0.66
4	5904	0.33	3291	0.64	3255	0.65
5	5904	0.35	3291	0.58	3265	0.62
6	5904	0.38	3284	0.47	3246	0.69
7	5899	0.33	3282	0.55	3249	0.73
8	5894	0.29	3291	0.60	3252	0.71
9	5899	0.29	3276	0.55	3243	0.61

3.4 Interstitial Free Steel Annealing

Interstitial free steel was annealed to see how processing affected ultrasonic properties. Interstitial free steel was chosen to simplify the analysis, since it has a low carbon content so only ferrite with very few precipitates should form.

3.4.1 Experimental Design

To investigate the effect of annealing on ultrasonic waves, interstitial free steel was obtained in the form of rolled sheet. Samples, 24 mm x 38 mm in size, were shear cut from the sheet so directionality could be easily seen and to provide enough material for metallography and ultrasonic testing. Two sets of samples were prepared. The first set was placed in a box furnace and heated to 700ºC. The samples were held at this temperature with a sample removed every five minutes and air cooled until one hour had passed. This is shown schematically in Figure 3.17 with approximate cooling rates.

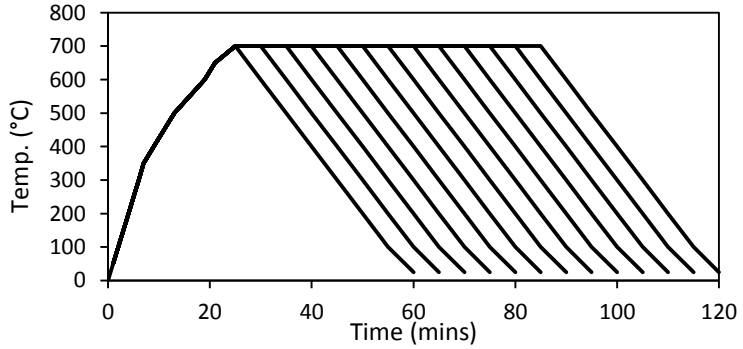

Figure 3.17: Heat Treat Schematic of IF Samples Held at 700ºC

The second set of samples was heated to 775ºC and then samples were removed every 30 minutes and air cooled until two hours had passed. A schematic of this heat treating process is shown in Figure 3.18.

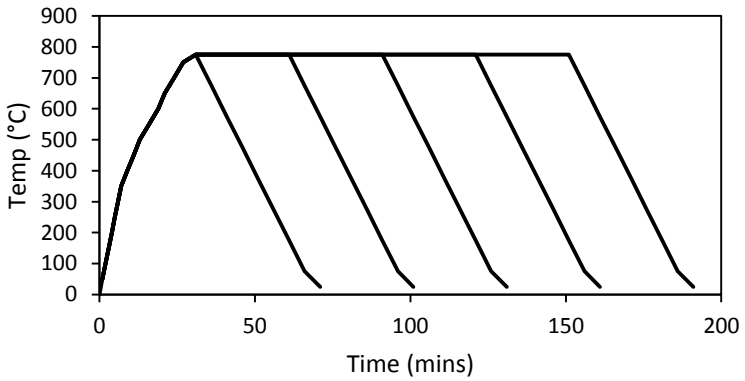

Figure 3.18: Heat Treat Schematic of IF Samples Held at 775ºC

Once heat treatment was complete and the samples were cooled to ambient temperature, a section of each sample (~6 mm x 24 mm) was removed for metallography, using a water cooled precision diamond saw.

3.4.2 Metallography

The sectioned samples were mounted using two part epoxy and then ground and polished using an autopolisher; the final polishing compound was one micron diamond slurry. Etching was done using 2% Nital followed by Marshall's reagent. Marshall's reagent consists of equal parts of 30% hydrogen peroxide (Part A) and 5 mL concentrated sulfuric acid and 8 g oxalic acid mixed with 100 mL of water (Part B) [90]. Samples were immersed in the reagent for approximately thirty seconds with the surface vertical to prevent pitting. The sizes of the grains were then observed qualitatively to see the effect of holding time and temperature. Five microhardness indents were performed on each of the 700ºC and 775ºC hold samples, with a 1 kg load and dwell time of 14 s, using a Wilson automatic microhardness indenter. Table 3.9 shows the results of the microhardness tests for the 700ºC samples, while Table 3.10 shows the results for the 775ºC samples.

Table 3.9: Microhardness of IF Steel Held at 700ºC

Hold Time (min)	0	5	10	15	20	25	30	35	40	45	50	55	60
Hardness (HV1)	115	88	91	86	88	86	88	85	86	86	86	85	85

Table 3.10: Microhardness of IF Steel Held at 775ºC

Hold Time (min)	0	30	90	120	160
Hardness (HV1)	83	75	76	72	72

3.4.3 Ultrasonic Tests

The samples were ultrasonically tested as described in Section 3.2 to determine the ultrasonic velocity and attenuation. The ultrasonic properties are shown in Table 3.11 for the 700ºC holds and Table 3.12 for the 775ºC holds.

Table 3.11: Ultrasonic Properties for IF Held at 700ºC

	Long		Shear (P)		Shear (T)	
Hold Time (min)	Velocity (m/s)	Attenuation (dB/mm)	Velocity (m/s)	Attenuation (dB/mm)	Velocity (m/s)	Attenuation (dB/mm)
0	6197	0.72	3160	0.70	3065	0.76
5	6284	0.97	3152	0.90	3065	1.31
10	6227	0.72	3140	0.60	3049	0.65
15	6305	0.68	3206	1.38	3081	1.13
20	6273	0.68	3156	1.07	3053	0.77
25	6292	0.65	3157	0.69	3070	0.83
30	6269	0.74	3152	0.56	3059	0.87
35	6255	1.15	3140	1.08	3061	0.89
40	6288	0.63	3156	0.95	3056	0.69
45	6312	0.87	3189	1.25	3073	1.15
50	6241	1.05	3168	0.79	3071	1.26
55	6328	0.74	3182	0.76	3083	0.70
60	6377	0.86	3204	0.93	3102	0.85

Table 3.12: Ultrasonic Properties for IF Held at 775ºC

	Long		Shear (P)		Shear (T)	
Hold Time (min)	Velocity (m/s)	Attenuation (dB/mm)	Velocity (m/s)	Attenuation (dB/mm)	Velocity (m/s)	Attenuation (dB/mm)
0	6294	0.78	3147	0.78	3063	0.85
30	6504	0.68	3219	0.83	3113	0.90
60	6431	0.81	3172	0.80	3057	0.81
90	6409	0.94	3144	1.13	3045	0.76
120	6445	0.90	3166	1.12	3055	1.01

3.5 L80 Steel Microstructure Variation

L80 pipe skelp was heat treated to see how changes in microstructure affected the ultrasonic properties. Small bars were initially tested followed by longer bars, which could also be tensile tested in addition to ultrasonic and hardness testing.

3.5.1 Experimental Design

To investigate the effect of microstructure on ultrasonic waves, an L80 steel, containing 0.244 wt% C and 0.99 wt% Mn among other alloying elements, was processed to obtain different structures. Sixteen samples, 24 mm x 38 mm x 3mm thick, were machined from the skelp about a quarter of the way through the thickness. Half of these samples were then coated in Quickrete fireplace mortar to slow their cooling after heat treatment. All 16 samples were heated in a box furnace to 1000°C and immediately removed. This was done to austenitize them in a manner approximating that done to industrial L80. The samples were cooled in a variety of ways ranging from air cooled (AC) to water quenched (WC). Table 3.13 shows the various cooling media and sample designations.

Table 3.13: L80 Cooling Media and Sample Designations

	CAC	AC	200-COC	200-OC	COC	OC	CWC	WC
Quenching medium	Air	Air	200°C Oil	200°C Oil	Oil	Oil	Water	Water
Coating	yes	-	yes	-	yes	-	yes	-

Samples cooled in 200°C canola oil were held for three minutes and then water quenched. The oil quenched samples used Quenchfast brand quenching oil. Figure 3.19 shows all L80 sample heat treatments schematically, with approximate cooling rates.

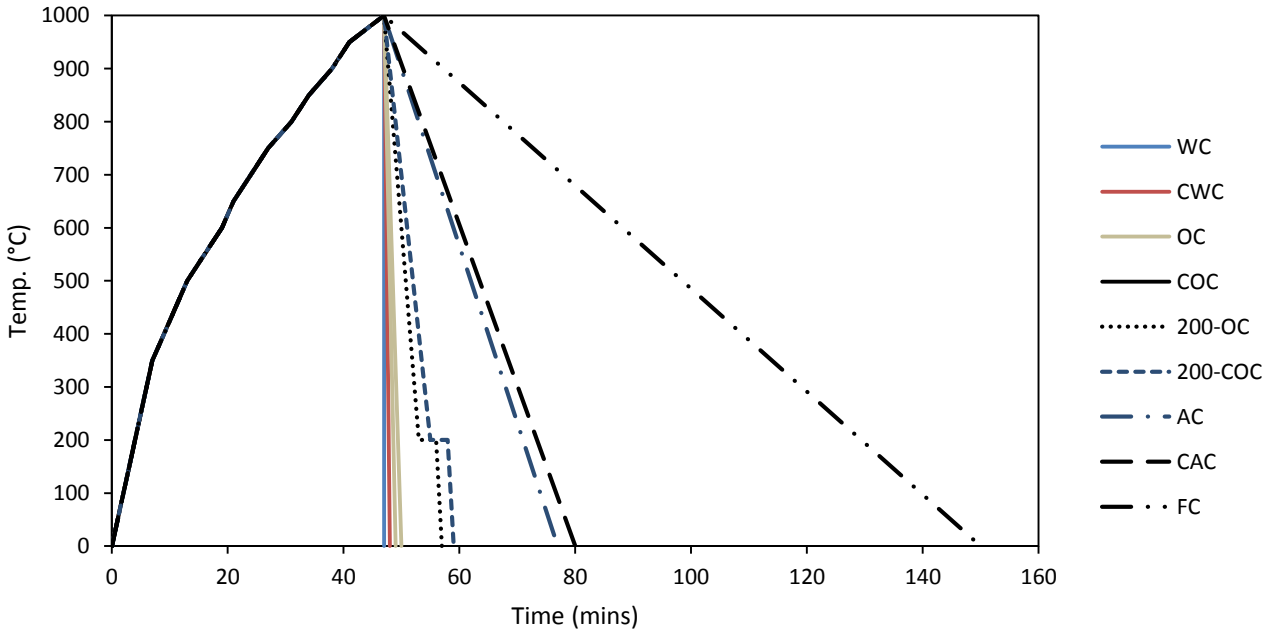

Figure 3.19: L80 Small Sample Heat Treatment Schematic. Times Are Approximate.

After heat treatment the samples were surface ground to remove scale and to generate parallel faces with consistent surface roughness. They were then ultrasonically tested as detailed in Section 3.3. After ultrasonic testing, a quarter inch section of each sample was removed with a water cooled diamond saw and mounted in epoxy. The mounted samples were ground and polished with an autopolisher to a final polish with one micron diamond slurry and then etched with 2% Nital. The microstructure of each sample was qualitatively evaluated using an optical microscope.

In order to obtain more statistically significant data, additional samples were tested. The samples were rough machined from the same L80 skelp to a size corresponding to 240 mm x 20 mm x 4 mm, so that multiple ultrasonic readings could be taken from each sample, metallographic samples could be prepared and tensile samples could be machined. In addition to the heat treatments described in Table 3.13, furnace cooled (FC) samples were also produced with the long bars. Samples were processed in four batches, three batches without cooling in hot oil and a fourth batch where coated and uncoated samples were cooled in the hot oil. The time taken to heat the samples to 1000^{o}C ranged from 43 to 48 minutes. Figure 3.20 shows these heating profiles, the time was measured as the furnace heated with readings taken every 50^{o}C.

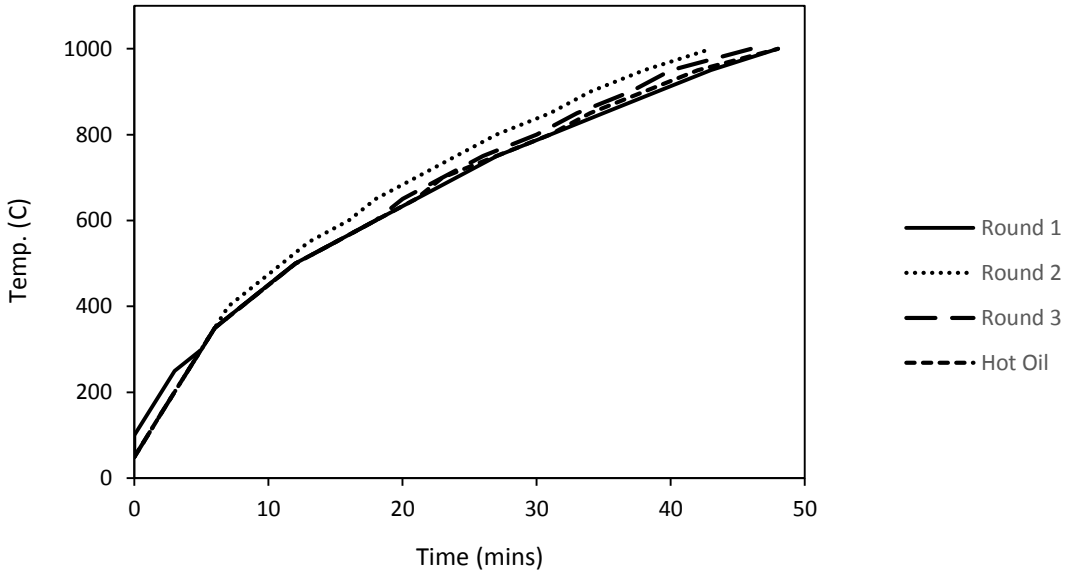

Figure 3.20: L80 Long Bar Heating Rates

After heat treatment was complete, the samples were surface ground to a thickness of 3 mm. Approximately 20 mm was removed from either end of each sample with a water cooled diamond saw and then the samples were cold mounted in epoxy. All mounted samples were then ground and polished as a group to a final polish of 1 micron diamond using an autopolisher.

3.5.2 Ultrasonic Tests

The small samples were ultrasonically tested as described in Section 3.2 to determine ultrasonic velocity and attenuation. The ultrasonic properties, velocity and attenuation, are shown in Table 3.14.

Table 3.14: L80 Small Bar Heat Treated Ultrasonic Properties

Sample	Long		Shear (T)	
	Velocity (m/s)	Attenuation (dB/mm)	Velocity (m/s)	Attenuation (dB/mm)
Coated - Air Cooled	5893	0.258	3258	0.356
Air Cooled	5905	0.250	3249	0.316
Coated - 200 C Oil Quench	5893	0.263	3245	0.199
200 C Oil Quench	5913	0.268	3232	0.317
Coated - Oil Quench	5895	0.252	3215	0.243
Coated - Water Quenched	5900	0.230	3199	0.293
Oil Quench	5895	0.258	3208	0.319
Water Quenched	5895	0.245	3194	0.261

The long bar samples were tested in the same manner as the small samples, but three readings were taken from each bar and the values for each heat treatment (three bars) were averaged to get the ultrasonic velocity. The standard deviation of the readings was taken as the error rather than the calculated instrument error used for single readings. The average ultrasonic properties are shown in Table 3.15 along with the standard deviations in Table 3.16.

Table 3.15: L80 Long Bar Heat Treated Ultrasonic Properties

Sample	Long		Shear (P)		Shear (T)	
	Velocity (m/s)	Attenuation (dB/mm)	Velocity (m/s)	Attenuation (dB/mm)	Velocity (m/s)	Attenuation (dB/mm)
Furnace Cooled (FC)	5896	0.25	3254	0.35	3266	0.34
Coated - Air Cooled	5900	0.24	3268	0.28	3285	0.29
Air Cooled	5897	0.20	3261	0.30	3275	0.28
Coated - 200 C Oil Quench	5908	0.18	3244	0.25	3253	0.25
200 C Oil Quench	5908	0.18	3236	0.23	3247	0.24
Coated - Oil Quench	5904	0.17	3220	0.23	3224	0.22
Coated - Water Quenched	5894	0.16	3207	0.23	3214	0.22
Oil Quench	5900	0.17	3207	0.23	3213	0.26
Water Quenched	5916	0.17	3215	0.25	3215	0.24

Table 3.16: L80 Long Bar Standard Deviation of Ultrasonic Properties

Long	Shear (P)	Shear (T)

Sample	Velocity (m/s)	Attenuation (dB/mm)	Velocity (m/s)	Attenuation (dB/mm)	Velocity (m/s)	Attenuation (dB/mm)
Furnace Cooled	2	0.01	6	0.03	3	0.04
Coated - Air Cooled	9	0.00	7	0.00	6	0.03
Air Cooled	6	0.02	5	0.03	5	0.04
Coated - 200 C Oil Quench	9	0.01	6	0.01	7	0.02
200 C Oil Quench	5	0.01	7	0.03	7	0.02
Coated - Oil Quench	12	0.02	11	0.03	14	0.02
Coated - Water Quenched	6	0.01	10	0.05	4	0.03
Oil Quench	8	0.01	5	0.01	6	0.05
Water Quenched	29	0.01	17	0.06	19	0.06

3.5.3 Vickers Hardness

Microhardness tests were obtained using a manual Vickers hardness indenter with a 500 g load. Three to five indents were done on each sample, depending on measurement variation. The values were averaged to determine the hardness of the sample. Both the hardness and heat treatment were then compared with the ultrasonic properties measured. The microhardness values for each sample are shown in Table 3.17.

Table 3.17: L80 Small Bar Microhardness

Sample	Average Hardness ($HV_{0.5}$)	Standard Deviation ($HV_{0.5}$)
Coated - Air Cooled	177	2
Air Cooled	200	21
Coated - 200 C Oil Quench	230	20
200 C Oil Quench	349	8
Coated - Oil Quench	455	24
Coated - Water Quenched	526	25
Oil Quench	490	39
Water Quenched	485	28

Microhardness was also done on the polished samples sectioned from the long bars. These samples were indented with a Wilson VH3100 automatic microhardness tester. A load of 1 kg and a dwell time of 14 seconds were used for each of the 15 Vickers hardness indents made on each sample. The automatic microhardness tester measured each indent and calculated the resultant Vickers hardness. The average of all the hardness tests done for each heat treatment was calculated and the standard deviation used as the error. These values are shown in Table 3.18.

Table 3.18: L80 Long Bar Microhardness

Sample	Average Hardness (HV_1)	Standard Deviation (HV_1)
Furnace Cooled	140	5
Coated - Air Cooled	166	4
Air Cooled	178	5
Coated - 200 C Oil Quench	281	24
200 C Oil Quench	306	8
Coated - Oil Quench	433	8
Coated - Water Quenched	433	7
Oil Quench	465	24
Water Quenched	513	13

3.5.4 Metallography

Once hardness tests were completed, the samples taken from the long bars were etched with 2% Nital and their microstructures viewed optically. One way of assessing the microstructures was by measuring grain size. This was done in accordance with ASTM E112 - Standard Test Methods for Determining Average Grain Size [91]. To measure grain size, a circle of known perimeter was overlaid on micrographs taken from each sample. The number of times the circle crossed a grain boundary was counted and the grain size calculated as the length of the circle divided by the number of intercepts. Figure 3.21 shows an example of such a circle and a micrograph; the grain size was measured as 88 µm.

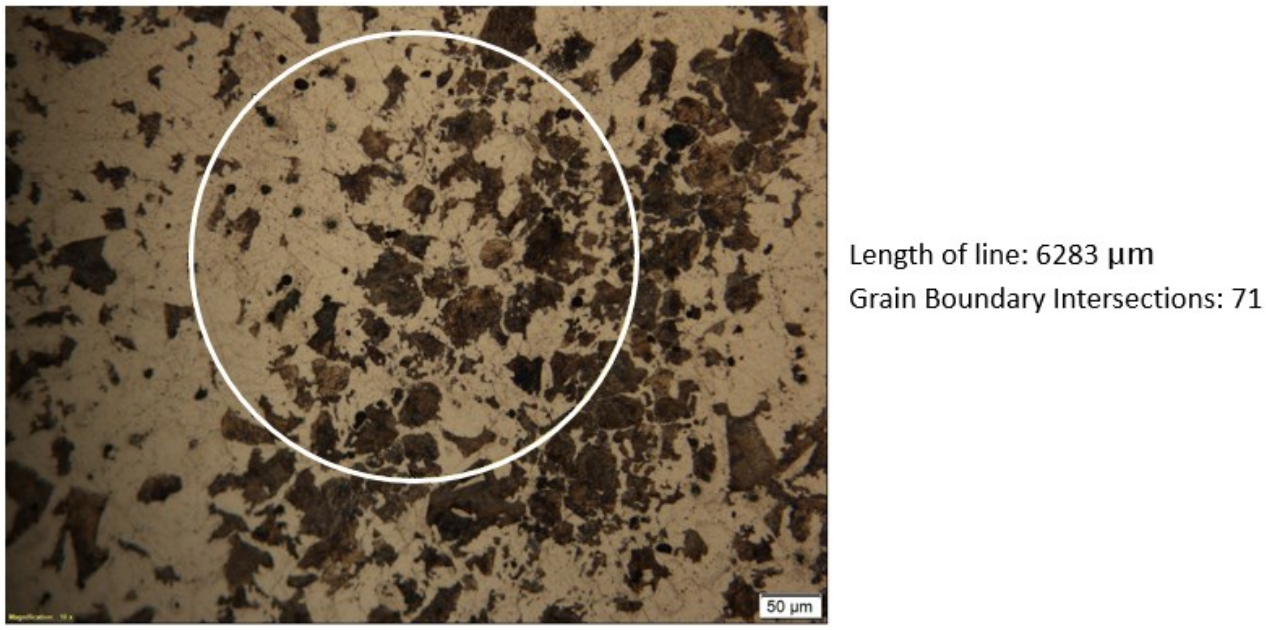

Figure 3.21: Circle Overlay for Grain Size Measurement of a Furnace Cooled (FC) Sample

This process was repeated for 9-30 fields of view on each heat treatment; the number depended on the ability to resolve individual grains at low magnification. For the FC, CAC, and AC samples grain size was measured, however in the remaining samples the colony size was measured as the grains could not be distinguished from one another (See Appendix A for further information). The values were averaged to get a grain size for each heat treatment. The grain sizes are shown in Table 3.19.

Table 3.19: L80 Long Bar Grain or Colony Sizes

Sample	Grain/ Colony Size (μm)	Standard Deviation (μm)
Furnace Cooled	72	55
Coated - Air Cooled	40	27
Air Cooled	81	44
Coated - 200 C Oil Quench	48	12
200 C Oil Quench	72	10
Coated - Oil Quench	66	19
Coated - Water Quenched	89	29
Oil Quench	81	21
Water Quenched	86	28

Quantitative phase analysis was also done on optical micrographs where possible. This was done by overlaying a grid of points on the micrograph in accordance with ASTM E562 – Standard Test Method for Determining Volume Fraction by Systematic Manual Point Count [92]. The fraction of points located in a phase is indicative of the area fraction of that phase in the micrograph. This analysis was only possible on samples which were cooled slowly. Those cooled quickly did not show enough of a second phase to allow for analysis. Figure 3.22 shows a sample grid overlay and phase fraction.

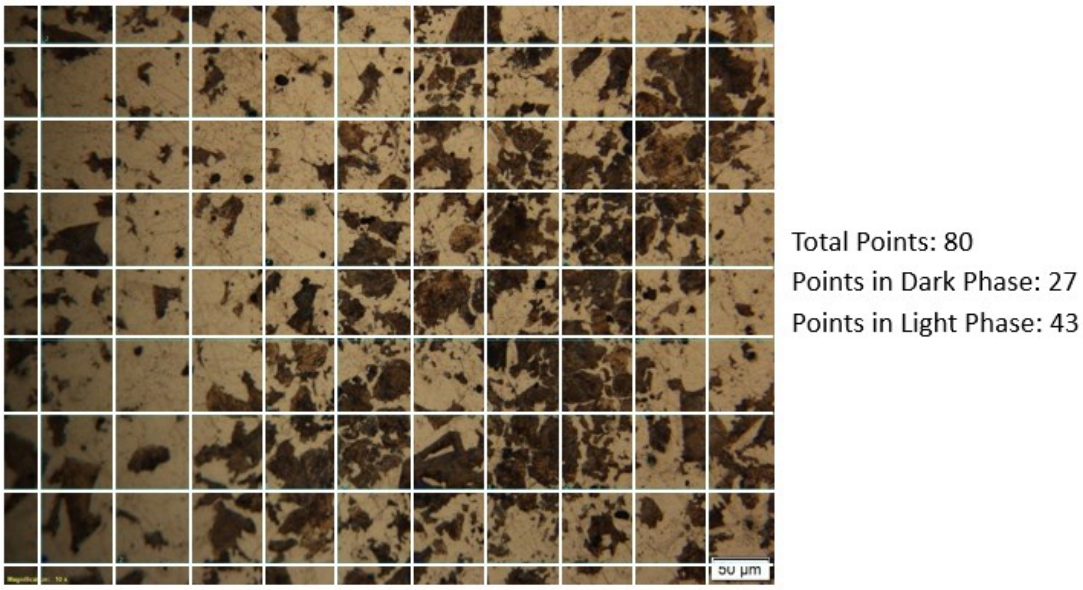

Figure 3.22: Grid Overlay for Phase Fraction Measurement of a FC Sample

In this case, the dark regions are pearlite and the light regions are ferrite. At higher magnification the dark regions showed a lamellar structure characteristic of pearlite, as well no martensite was seen in the samples with pearlite. The point count method of the image in Figure 3.22 yielded a microstructure fraction of 46% pearlite and 54% ferrite. This procedure was repeated for at least 14 micrographs of each of the furnace and air cooled sets. These heat treatments had clearly defined microstructures which could be differentiated, unlike the more rapidly cooled samples. In the martensitic samples it could not be determined optically if specific regions were martensite or not. The values from each field of view were averaged to get representative values, which are given in Table 3.20.

Table 3.20: L80 Long Bar Phase Fraction

Sample	Area % Pearlite	Area % Ferrite	Standard Deviation (%)
Furnace Cooled	48	52	18
Coated - Air Cooled	40	60	13
Air Cooled	41	59	13

3.5.5 Tensile Tests

After the ends of each sample were removed, the remainder of the sample was machined into a tensile dog bone sample in accordance with ASTM E 8M-04 – Standard Test Methods for Tension Testing of Metallic Materials [93]. The sample dimensions from the specification are shown in Figure 3.23.

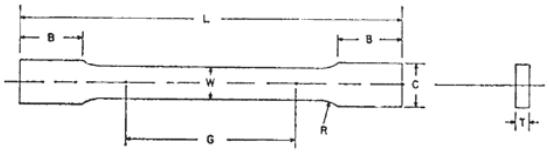

	G	W	T	R	L	B	C
Size (mm)	50	12.5	3	12.5	200	50	20

Figure 3.23: Tensile Test Sample Dimensions [93]

The tensile specimens were tested to failure with an Instron 8516 Loading Frame equipped with Instron 2743 100KN hydraulic wedge grips, an Instron 8800 controller and a 12.5 mm gauge length extensometer, which was attached to the specimens with elastic bands. The cross sectional area in the reduced section (W and T in Figure 3.23) of each specimen was measured prior to testing with a micrometer in the same manner as used prior to ultrasonic testing. The tensile test was conducted at a displacement rate of 3 mm/min. The extensometer generates a strain value in volts, which is converted to mm/mm using Equation 3.1 where $\varepsilon_{mm/mm}$ is the strain in mm/mm, ε is the extensometer output in volts and G is the gauge length of the extensometer (12.5 mm) [94].

$$\varepsilon_{mm/mm} = (\frac{\varepsilon_V}{2})/G \tag{3.1}$$

The stress was calculated using the output force measured by the instrument divided by the original cross sectional area. The resulting engineering stress was plotted as a function of engineering strain; an example of a stress-strain plot is shown in Figure 3.24 for the air cooled specimen that was heated in the first round (AC1).

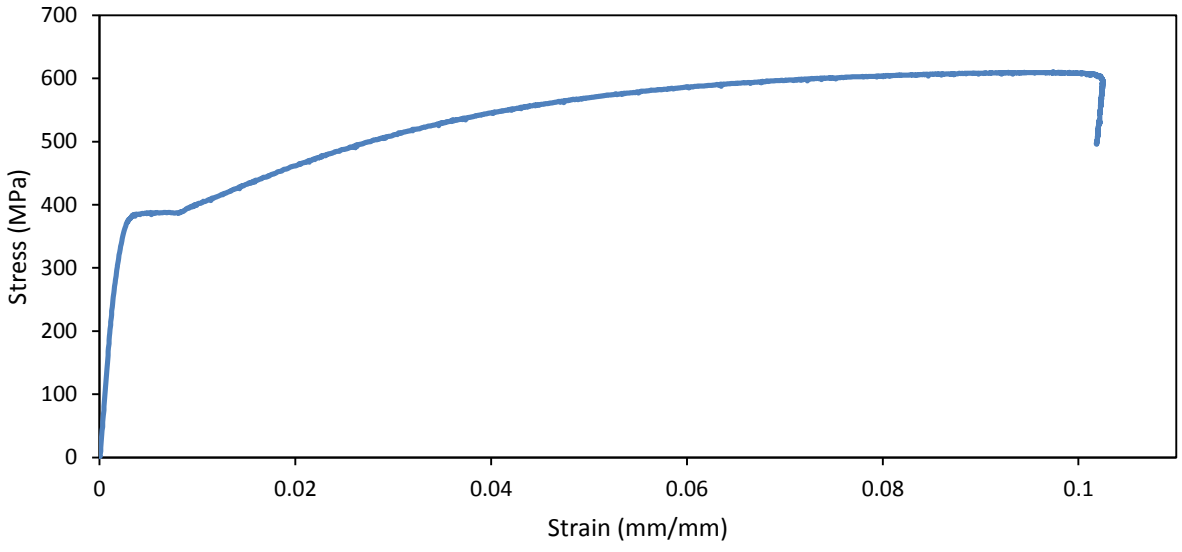

Figure 3.24: Stress-Strain Plot for AC1 L80 Specimen

The Young's modulus was measured by fitting a trend line to the linear portion of the stress-strain curve. Points were removed from the curve until a linear trend line fit well with a good R^2 value (above 0.9) and the initial and final points considered did not deviate from the trend by more than 10 MPa. This ensured that the same criteria were met for all tests and only the linear portion of the curve was considered to find the slope. The slope of the trend line corresponds to the Young's modulus for the sample. Figure 3.25 shows this trend line for the AC1 specimen.

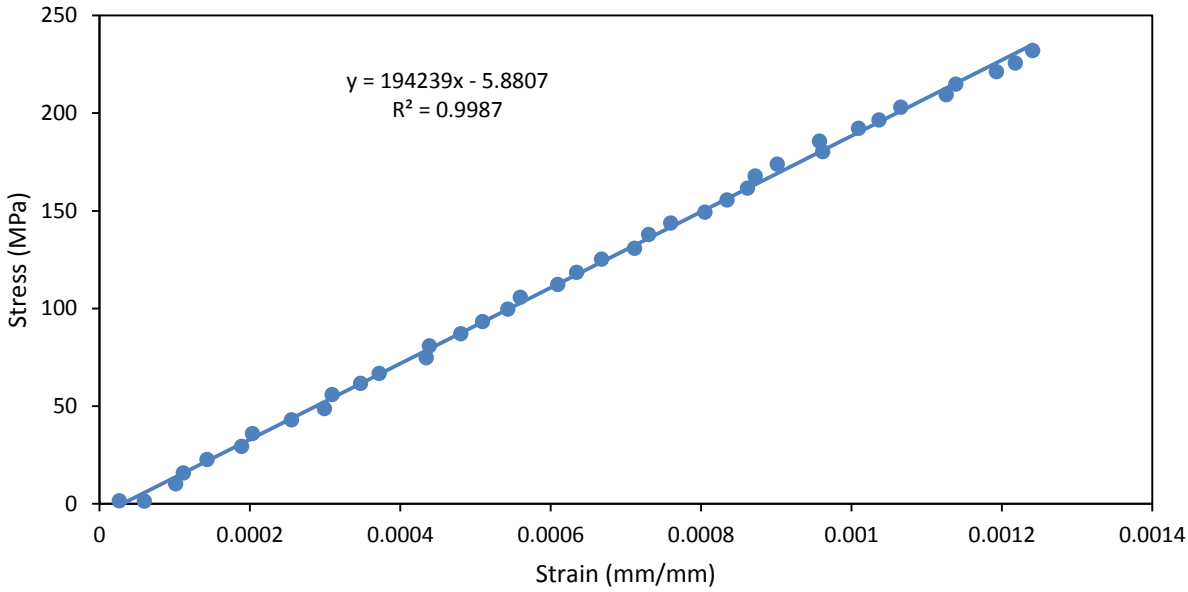

Figure 3.25: Trend Line for Determination of Young's Modulus of AC1 Specimen

The Young's modulus was calculated to be 194 GPa for the AC1 specimen. The Young's modulus for ferrite-pearlite has been reported as ~210 GPa and ~204 GPa for martensite in a 1050 steel [82]. The Young's modulus was then used to generate a 0.2% strain offset line to find the yield stress of the sample [93]. The stress at which the 0.2% offset line intersected the stress-strain curve was taken to be the yield strength (YS) of the sample. Figure 3.26 shows the two curves and their intersection.

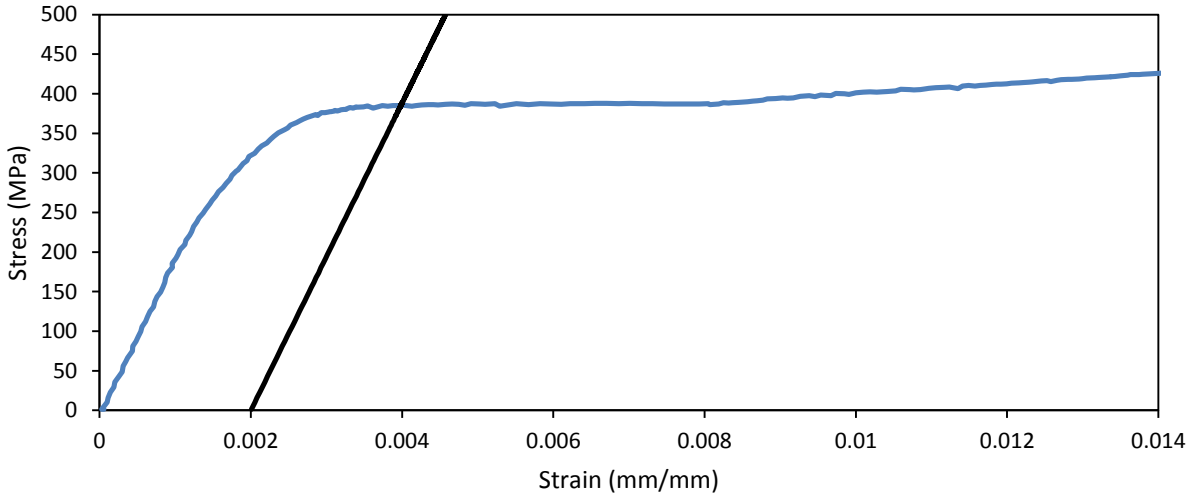

Figure 3.26: Stress-Strain Curve and 0.2% Offset Line for Yield Strength (YS) Determination AC1 Specimen

The 0.2% offset method for the AC1 sample generated a yield strength of 385.1 MPa. This value was compared with the average stress in the plateau region of the stress-strain curve (384.9 MPa), which is an alternative method for measuring yield strength in samples with a plateau in their stress-strain curve. The value using the 0.2% offset method was taken as the yield strength for the sample, since it agreed with the plateau method and could be used consistently on all samples, including those without plateaus. The Young's modulus was used to determine the elongation of the sample. The intercept of a line with slope equal to the Young's modulus with the strain axis was adjusted until it intersected the stress strain curve at the point of fracture. The strain intercept of this line was the elongation of the sample. A vertical line was also placed at this point to find the fracture strain. By using a line with slope equal to the Young's modulus the elastic portion of the fracture strain was removed to give the elongation for the sample. Both lines are shown in Figure 3.27.

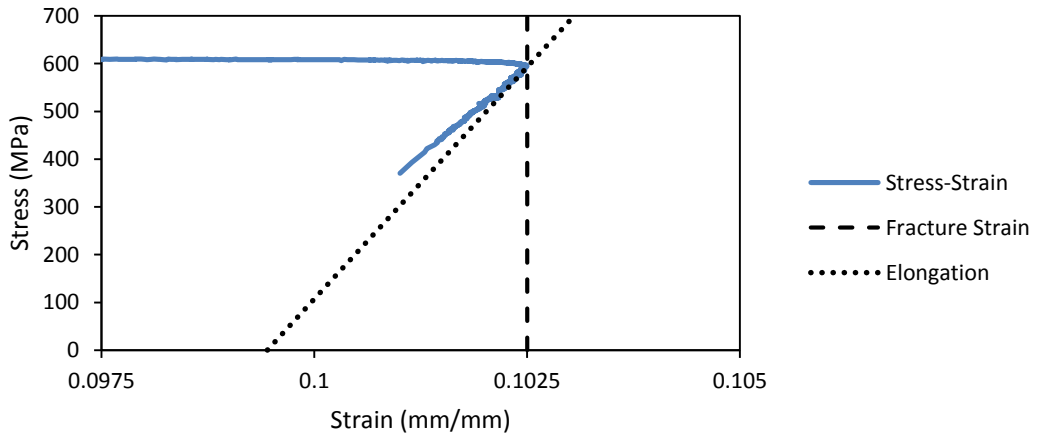

Figure 3.27: Fracture Strain and Elongation Determination

The fracture strain for this sample was 10.25% and the elongation was 9.95%. The fracture strain was used as a cut-off value when finding the area below the stress strain curve. To determine the area under the curve, the area of the trapezoid between each sequential pair of points and the x-axis was found by adding the area of the rectangle between the lower point, it's y-coordinate with the x-coordinate of the upper point and the x-axis to the triangle formed by the upper point and the top of the rectangle. The areas of all these trapezoids was summed up until the breaking strain was reached. These areas were then summed to get a value for the toughness of each sample. A simplified schematic of this method showing eight points rather than the full 2385 is shown in Figure 3.28 for the AC1 sample.

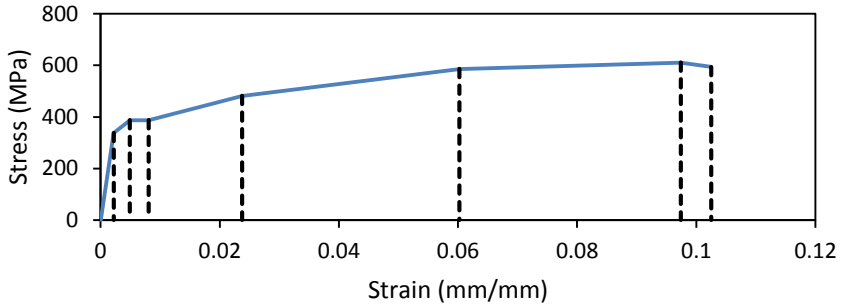

Figure 3.28: Trapezoid Method for Finding Area Under The Stress Strain Curve

For the AC1 sample (Figure 3.22) the toughness was 35 MJ/m^3. The ultimate tensile strength (UTS) was also calculated by finding the maximum value for stress among the data points for the sample. The AC1 sample had a UTS of 610 MPa. This process was repeated for all 27 heat treated tensile specimens and the values are shown in Table 3.21.

Table 3.21: L80 Tensile Test Results

Sample	Y (GPa)	YS (MPa)	UTS (MPa)	Fracture Strain (%)	Elongation (%)	Toughness (MJ/m^3)
Furnace Cooled	197	298	537	27	27	65
Coated - Air Cooled	200	365	583	23	23	62
Air Cooled	197	380	604	13	13	43
Coated - 200 C Oil Quench	203	655	830	4	3	18
200 C Oil Quench	202	725	910	3	3	18
Coated - Oil Quench	197	849	1145	8	7	30
Coated - Water Quenched	200	1059	1497	9	9	47
Oil Quench	206	1149	1588	7	6	50
Water Quenched	199	1158	1602	4	4	45

3.6 Industrial UT

Further tests were done with two commercially available steels with equipment and practices used in industry. 4130 was chosen as it can be treated into an L80 steel and should be comparable to the L80 tested previously while 5160 was procured as a production part which was not a rolled skelp like the other steels tested.

3.6.1 5160 and 4130 Experimental Design

Experimentation was conducted on 4130 and 5160 alloy steels similar to that done on the L80 small bars. The higher carbon contents of these steels facilitated the creation of differing microstructures. Eight samples, roughly 24 mm x 24 mm in size, were cut from a 5160 leaf spring using an abrasive cutting wheel. The samples were ground flat after sectioning, since the original leaf spring was curved. This resulted in a loss of thickness compared with the original spring; as such, each sample had a unique thickness. This is evident in Figure 3.29. The final thickness of the 5160 samples ranged from approximately 6.5-8 mm.

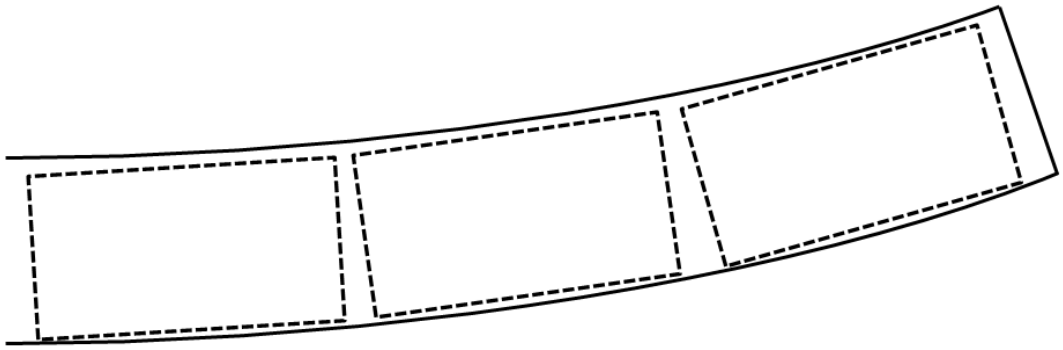

Figure 3.29: Schematic of Samples Taken from 5160 Leaf Spring

Nine 4130 samples, roughly 24 mm x 24 mm in size, were cut from commercially available 12 mm thick bar stock. Since the bar already had uncurved parallel faces, no thickness reduction was needed. Both sets of samples were subjected to a variety of heat treatments, beginning with a one hour austenization at 845ºC, to produce different microstructures including martensite, by quenching in water (Q), tempered martensite, by quenching and tempering at 650ºC (QT1) or 205ºC (QT2), fine pearlite, by air cooling (AC), and coarse pearlite by furnace cooling (FC). In addition, three methods to obtain spheroidized carbides were attempted by holding the samples at 770ºC for 6 hrs (H1) or 69 hrs (H2) after austenization or 16 hrs without austenization (H3). Figure 3.30 shows the heat treatments schematically with approximate cooling rates.

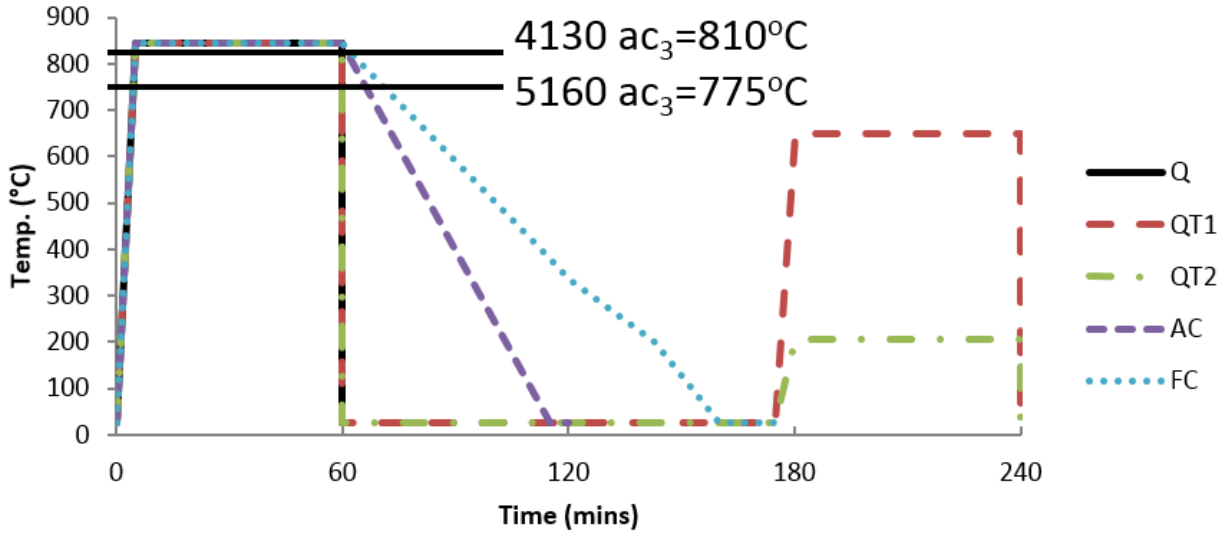

(A)

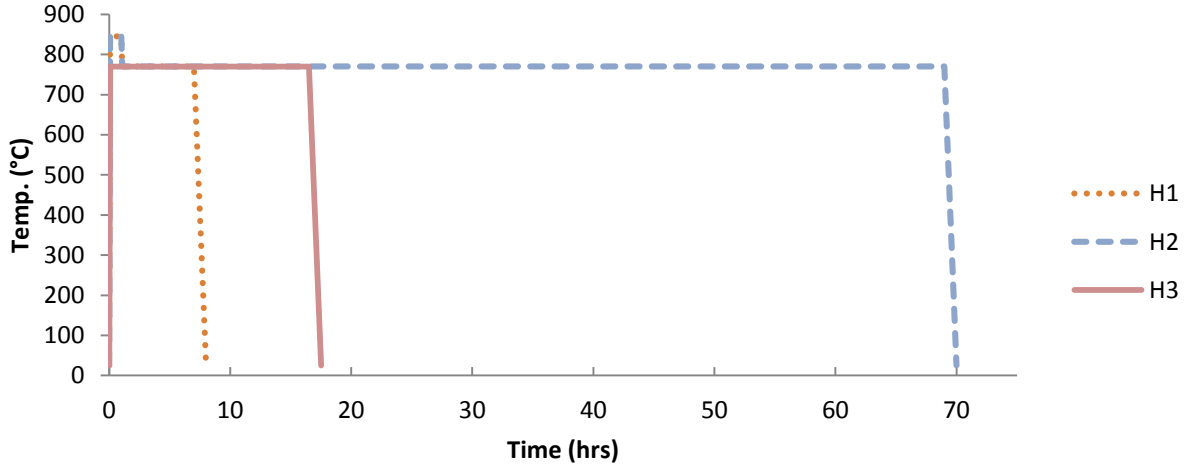

(B)

Figure 3.30: 5160 and 4130 Heat Treatments; (A) Short times and (B) High Temperature Holds

3.6.2 5160 and 4130 Ultrasonic Tests

Once the samples were heat treated, they were taken to UT Quality to have their ultrasonic shear wave velocities measured. Measurements were done with a Krautkramer USN58L pulser/receiver and a 15 MHz 0° shear wave piezoelectric transducer with stabilized molasses as a couplant. This equipment is standard in industry. The sample thickness was measured using a digital caliper. The couplant was put on the transducer and then spread using a small clamp to affix the transducer to the sample. The transducer and signal gain were simultaneously adjusted until the signal from the first backwall reflection was at 80% of the display screen height, which is the standard procedure for flaw detection [95]. The velocity of each sample was obtained by adjusting a pre-set velocity in the pulser/receiver software until the first two backwall reflection distances matched the

measured sample thickness. If a sample was measured to be 3 mm thick, the first backwall reflection would be displayed as 3 mm while the second reflection would be 6 mm away. The input velocity, which resulted in the reflections matching the measured thickness, was then the ultrasonic shear wave velocity in the sample. An example is shown in Figure 3.31.

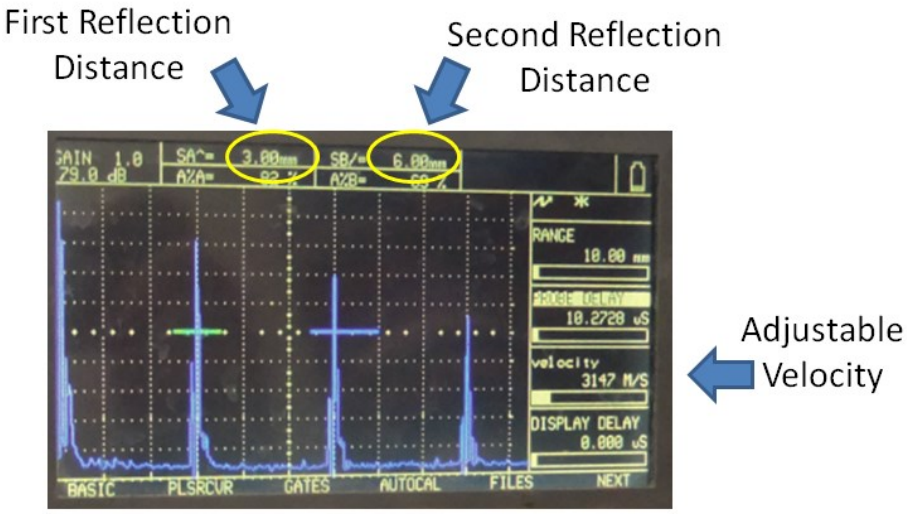

Figure 3.31: Krautkramer Ultrasonic Velocity Test

Since the resolution of the time measurement within the instrument was not known, only the error from the thickness measurement, ±0.01 mm, was considered. This procedure was followed to ultrasonically test all samples. The results of these tests are shown in Table 3.22.

Table 3.22: Industrial UT Results for 4130 and 5160

	Velocity (m/s)	
Sample	4130	5160
As Received	3219	3175
Quenched	3172	3157
Quench - Temper @ 650°C	3220	3148
Quench - Temper @ 205°C	3204	3129
Air Cool	3209	3288
Furnace Cool	3212	3200
High Temp. Hold 1 -770°C for 6hrs	3224	3205
High Temp. Hold 2 – 770°C 69hrs	3219	3183
High Temp. Hold 3 – 770°C 16.5hrs - no normalize	3105	-

Once ultrasonic testing was completed, the samples were prepared for optical microscopy to view the through thickness microstructure in each sample. Samples were cut using a water cooled

abrasive saw and then cold mounted in two part epoxy. Grinding and polishing was done by hand, down with one micron diamond slurry as the final step. The samples were microhardness tested in the same manner as the L80 long bar samples but with the five indents oriented through their thickness. The results of these hardness tests are shown in Table 3.23. The samples were then etched with 2% Nital and images were taken with an optical microscope at varying magnifications for qualitative analysis of the microstructure.

Table 3.23: 5160 and 4130 Microhardness

	5160		4130	
Heat Treatment	Hardness (HV1)	Standard Deviation	Hardness (HV1)	Standard Deviation
Q	702	28	567	10
AC	388	15	258	45
AR	540	15	233	8
FC	290	9	163	7
QT1	362	14	258	14
Qt2	659	34	526	10
H1	389	13	169	6
H2	252	7	158	3
H3	-	-	189	5

3.7 Summary of Experimental Methods and Results

Experimental work was conducted through the thickness of pipe skelps with UT and XRD, on IF steel cooled to room temperature after different annealing times with UT and microhardness, L80 steel after different heat treatments with UT, microhardness, tensile tests, and optical microscopy and 5160 and 4130 steel after heat treatment with UT and microhardness. The pipe skelps used for through thickness investigation were L80 and X70. UT and XRD were done on 1 mm thick samples obtained through the thickness of each skelp. The ultrasonic velocity and attenuation for shear and longitudinal waves was also obtained. Discussion of the ultrasonic properties and location through the skelps are presented in Section 4.1. The annealed IF steel shear and longitudinal wave velocity and attenuations as well as microhardness were obtained at room temperature after cooling from different times and annealing temperatures. Discussion regarding the IF steel and its ultrasonic properties after different amounts of annealing is given in Section 4.2. The L80 steel samples which were austenitized then cooled at different rates to obtain different microstructures are discussed in Section 4.3. Ultrasonic velocity and attenuation for shear and longitudinal waves as well as microhardness, Y, YS, UTS, fracture strain, elongation, and toughness were found for the different L80 heat treatments used. Heat treatments were also done to 5160 and 4130 samples to obtain different microstructures. The ultrasonic shear and longitudinal wave velocity and attenuation were obtained for these heat treatments as well as the microhardness, the discussion of which can be found in Section 4.4.

Chapter 4 Discussion

The tabulated ultrasonic results found in the previous chapter are compared with materials properties, processing and microstructure. The ultrasonic properties of two pipe skelps, L80 and X70, are compared with the domain size, microstrain, dislocation density and texture index found using quantitative XRD as well as their location through the thickness of the skelp. This was done to see if the ultrasonic properties changed through the thickness of the skelp and if the correlated to the information obtained from quantitative XRD. The ultrasonic properties of the annealed IF steels are compared with the hold times at high temperature and the resultant hardness values to see how ultrasonic properties varied as annealing progressed. The ultrasonic properties of the heat treated L80 samples are compared with the heat treatment procedure, hardness values and material properties from tensile tests to see if changes in morphology and structure affect the ultrasonic properties. The ultrasonic properties of the 4130 and 5160 heat treated samples were also compared with the heat treatment and hardness values to see if changes in structure could be detected with industrial equipment and procedures.

4.1 Pipe Skelp Through Thickness Investigation

Pipe skelps for two different grades of pipe, L80 and X70, were ultrasonically tested and the results compared with materials properties gathered through XRD. The ultrasonic properties through the skelp thickness were also compared with one another to see if any significant variation occurred through the skelp. They were also compared with the calculated velocities found in Section 2.2. Rietveld refinement of XRD patterns was used to find the texture index (J) of each sample as well as the dislocation density, microstrain and domain size. These were then compared with the ultrasonic properties.

4.1.1 Ultrasonic Velocity Through Skelp Thickness

The ultrasonic velocity through the thickness of each skelp was analyzed. The velocities were also compared with those calculated using the anisotropic method in Section 2.2.

4.1.1.1 X70 Through Thickness Velocity

The ultrasonic velocities through the thickness of the X70 skelp did not show significant variation (Figure 4.1). While there was some scatter in the velocities, including a significant spike upwards in both the longitudinal (VL) and shear waves parallel to the rolling direction (VsP) for the sample at a depth of 9 mm, the velocities largely remained constant throughout the thickness of the X70 skelp.

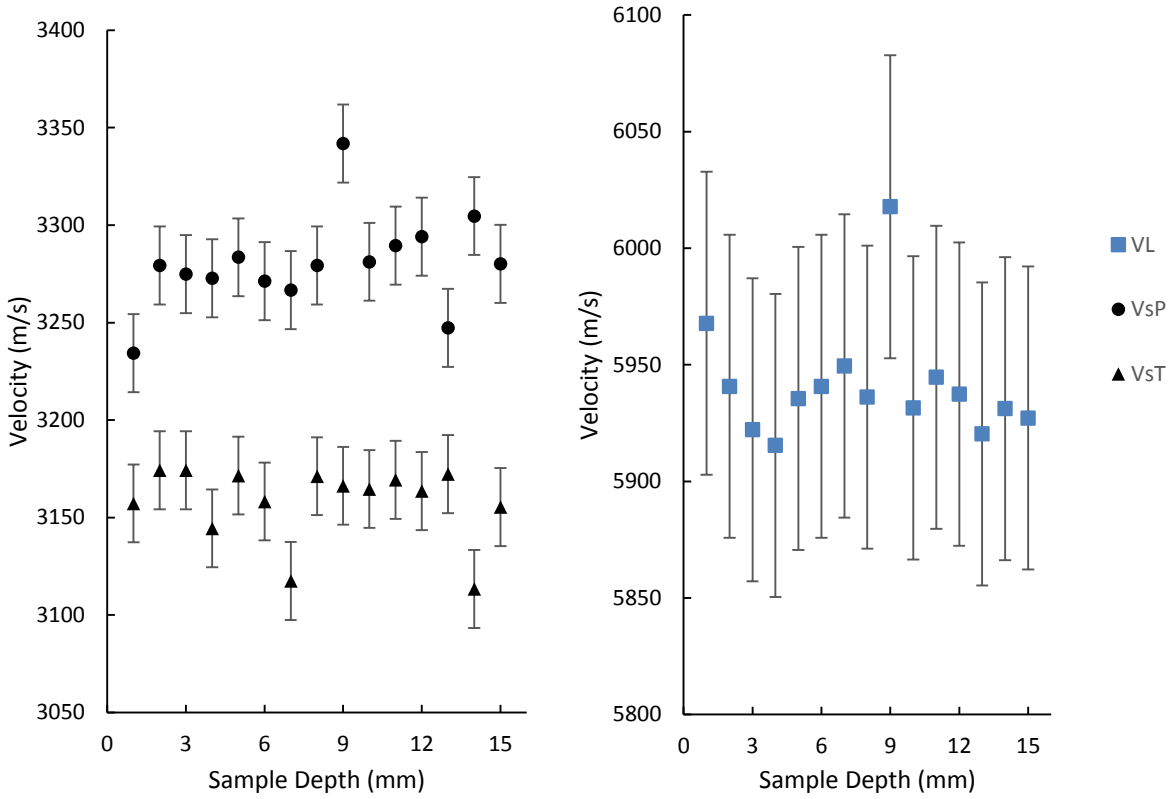

(A) (B)

Figure 4.1: Shear (A) and Longitudinal (B) Velocities Through X70 Skelp

The consistency in velocity is desirable for flaw detection applications. If there was significant variation in velocity through the skelp, accurate location and sizing of flaws would be greatly complicated. In addition, consistency in velocity points towards consistency in microstructure and mechanical properties through the skelp. Qualitatively the microstructure appeared consistent through the skelp with optical microscopy (Figure 4.2). The micrographs taken from the center of the skelp appear very similar to those at the top or bottom surfaces in both the rolling direction and transverse direction. This agrees with the velocity results and suggests that there is little centerline segregation if any.

There is no overlap in velocity between the three wave modes. The shear waves have much lower velocities than the longitudinal waves. The longitudinal wave velocities (VL) average 5941 m/s, while the transverse oriented shear waves (VsT) average 3158 m/s and the shear waves oriented along the rolling direction (VsP) average 3280 m/s.

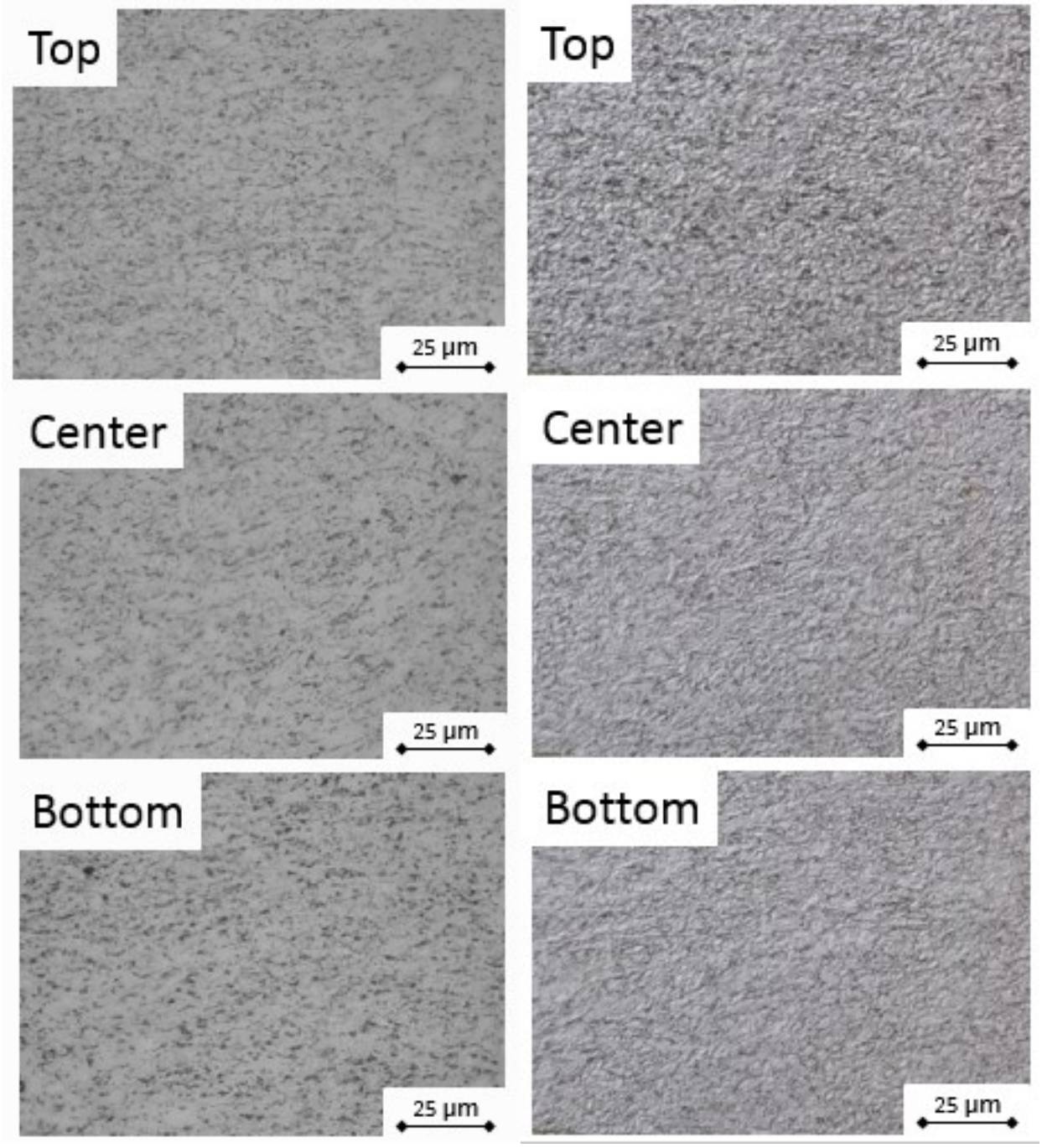

(A) (B)

Figure 4.2: X70 Skelp Through Thickness Optical Images Showing Consistency In Microstructure with: (A) Brightfield, Rolling Direction and (B) Direct Interference Contrast, Transverse Direction. Etched with 3% Nital

Only the transverse oriented shear waves match the isotropic velocity calculations done in Section 2.2. The longitudinal velocity is much higher than the calculated value, i.e., 5941 m/s vs roughly 4600 m/s, which further confirms that the isotropic assumption is not sufficient to accurately

represent ultrasonic behavior. All the velocities fall within the range of velocities for each wave type calculated in Section 2.2 for anisotropic ferrite in 1050 steel. The longitudinal waves agree with velocities calculated for the longitudinal velocity (V_1), as shown in Figure 4.3. The longitudinal velocities fall very close to the average calculated longitudinal velocities (V_{1avg}), which indicates that there is very little preferential orientation in the sample. If significant preferential orientation was present, favouring directions with velocities far from the average, the velocities would be closer to the maximum or minimum calculated values (V_{1max}) and (V_{1min}). The shear wave comparisons with calculated values are shown in Figure 4.4.

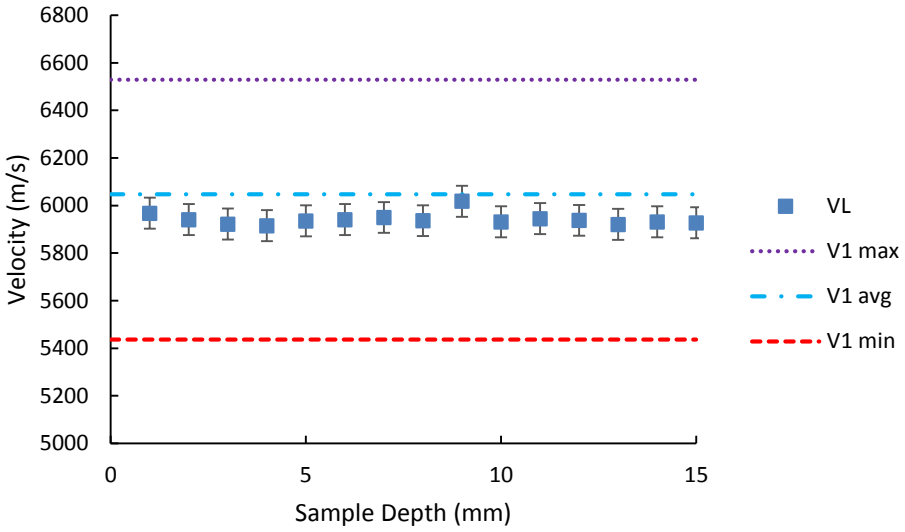

Figure 4.3: X70 Longitudinal Velocities and Calculated V_1

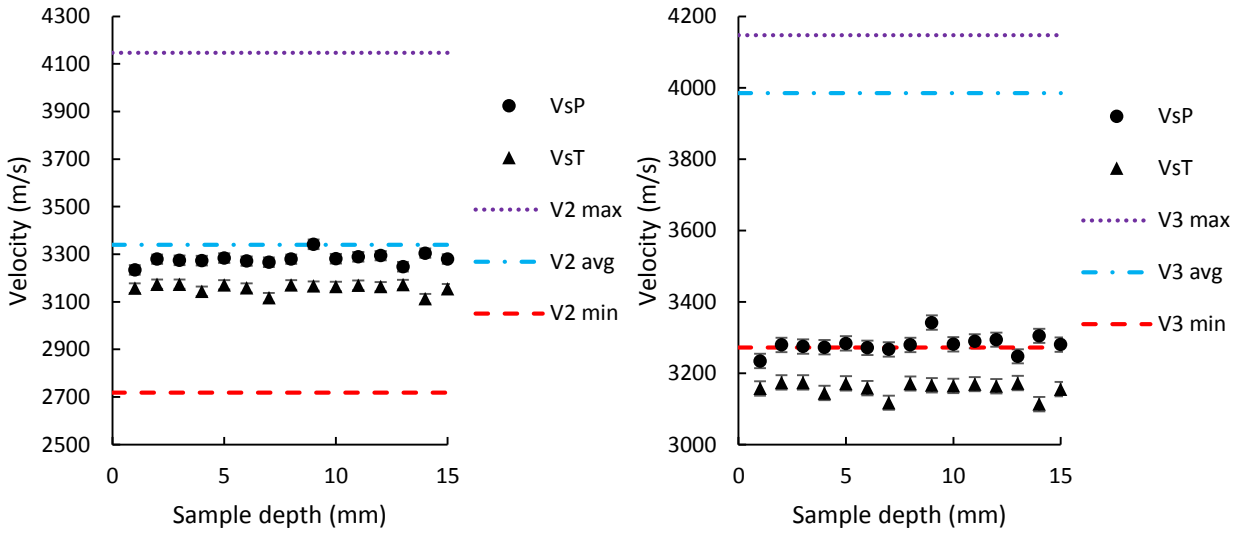

(A) (B)

Figure 4.4: X70 Shear Velocities and Calculated (A) V_2 and (B) V_3

VsP falls within the range for both V_2 and V_3, the calculated shear velocities, while VsT falls within the range of only V_2. Since VsT is not within the range for V_3, it can be assumed that VsP is analogous with V_3 and not V_2. VsT velocities are near the average for V_2, but not as close as the longitudinal wave velocities are to V_1, similarly indicating that there should not be much preferential orientation in the skelp. The VsP velocities averaged only slightly above the minimum values for V_3. In order for the velocity to be that low, the grains would almost all have to be oriented along the <111> direction. If the other velocities also deviated greatly from the average, this hypothesis could be possible; however, the other velocities were much closer to the average values than the minimum values. It is possible that the difference in behaviour is, instead, due to differences in the X70 steel composition and morphology, which is a low carbon rolled product, and the 1050 steel used in calculations, which is a medium carbon, normalized steel [82]. Each velocity may not be equally sensitive to these changes. While V_1 and V_2 appear to agree very well with the X70 velocities, V_3 may be more sensitive and show different velocities from the calculated ones.

4.1.1.2 L80 Through Thickness Velocity

As with the X70 skelp, the L80 steel also did not show significant variation in ultrasonic velocity through the thickness of the skelp. The variation present in the L80 skelp was less than that for X70, with no significant outliers outside the margins of error. In addition, the velocities all agreed within error with the corresponding velocity through the entire skelp thickness taken at one time. This can be seen in Figure 4.5, where the lines across each graph are the full thickness velocities and the points represent the individual samples at 1 mm depth intervals.

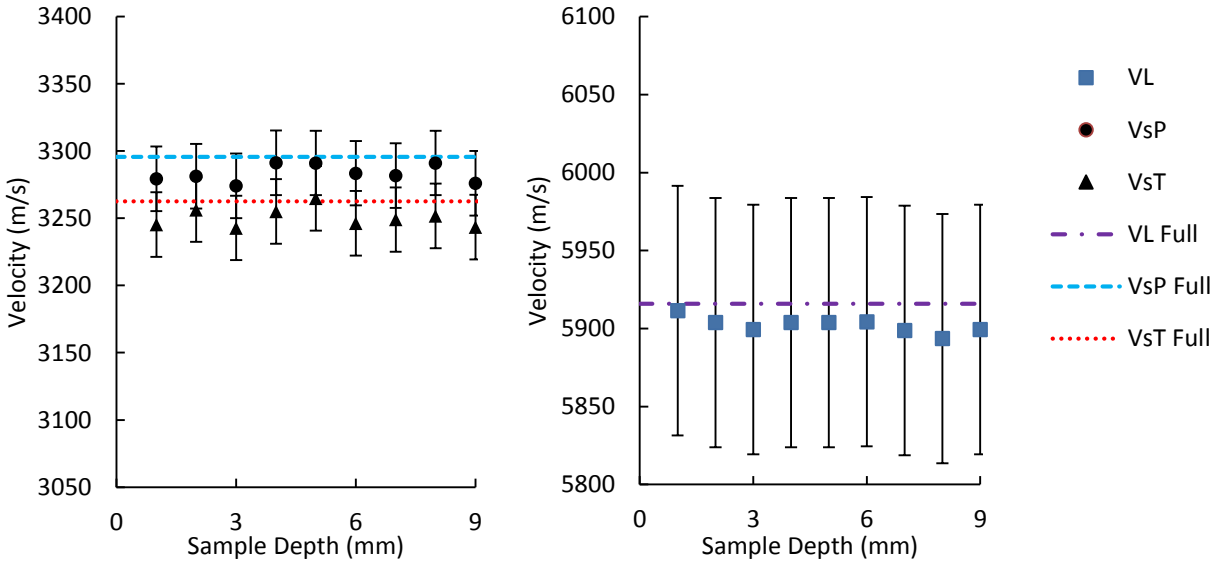

(A) (B)

Figure 4.5: Shear (A) and Longitudinal (B) Velocities Through L80 Skelp

This is again desirable for flaw detection applications, as well as indicating good consistency in properties through the skelp. Unlike the X70 skelp, the L80 shear velocities, VsP and VsT, are within the error range for one another. The L80 skelp also showed good consistency of microstructure through the skelp with optical microscopy (Figure 4.6)

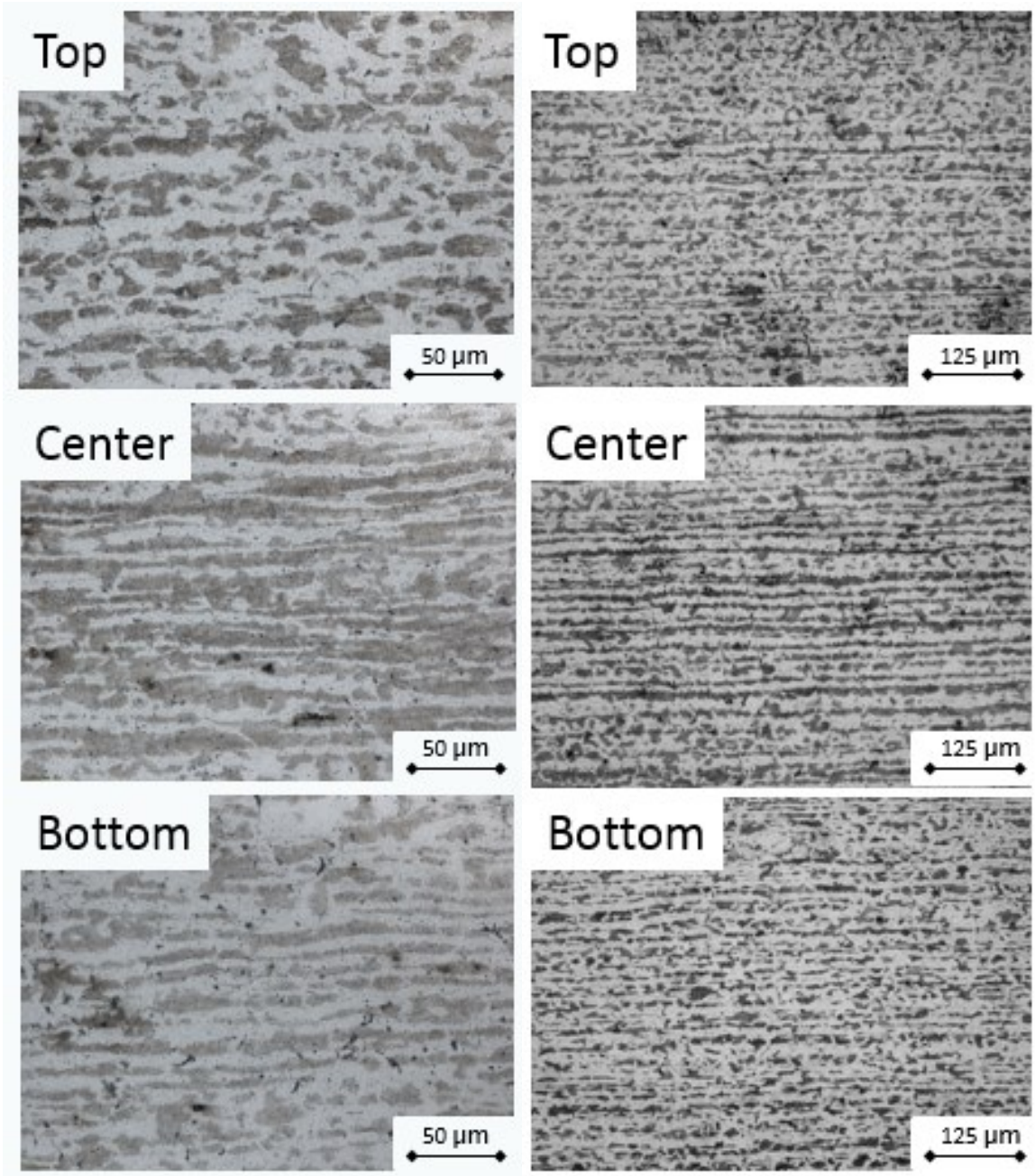

(A) (B)

Figure 4.6: L80 Skelp Through Thickness Optical Images Showing Consistency In Microstructure along: (A) Rolling Direction (B) Transverse Direction. Etched with 3% Nital

The longitudinal waves were slower in L80 than in X70 with an average of 5902 m/s, but both shear wave velocities were faster with average velocities of VsP 3283 m/s and VsT 3251 m/s. All three wave types correspond to the calculated velocities in the same manner as they did for the X70 skelp, where VL is V_1, VsT is V_2 and VsP is V_3. The comparison of VL and V_1 is shown in Figure 4.7.

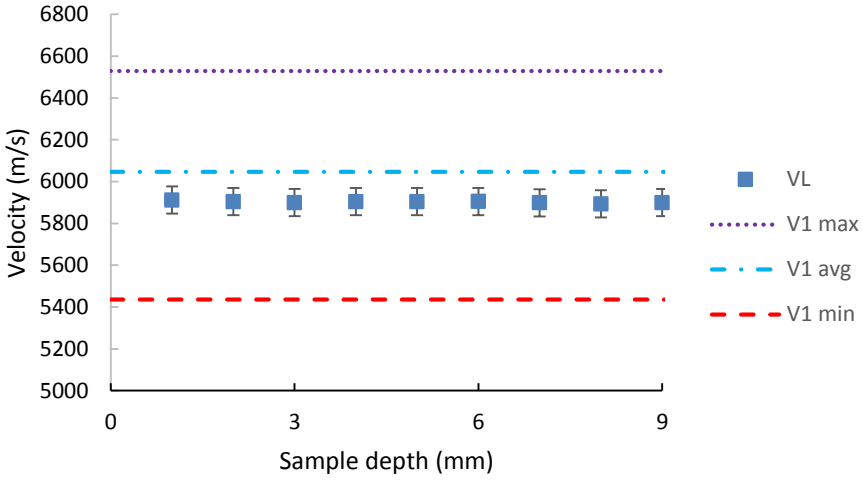

Figure 4.7: L80 Longitudinal Velocities and Calculated V_1

The longitudinal velocities are lower than those found in X70 and are slightly further from the average calculated value. They are still, however, relatively close to the average value which suggests minimal texture effect. The shear velocities also agree with calculated values, as shown in Figure 4.8.

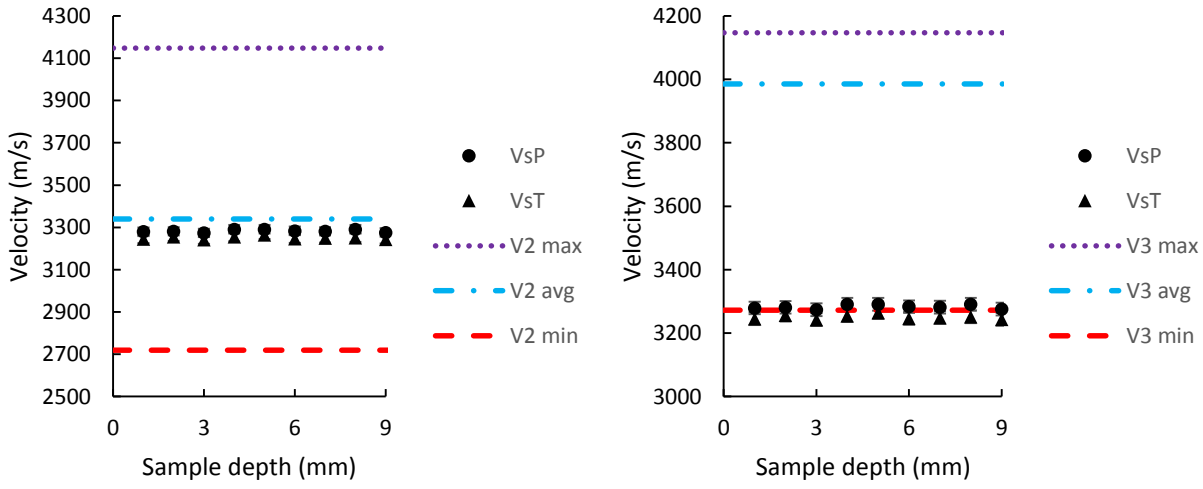

(A) (B)

Figure 4.8: L80 Shear Velocities and Calculated (A) V_2 and (B) V_3

In the L80 skelp, the shear values are all closer to the average calculated ones than in the X70 steel. As with X70, VsT agrees well with V_2, while VsP is only just inside the range of V_3. The shear values are so far from the average V_3 values, which again suggests that there is some orientation effect, but this is not borne out in the V_1 and V_2 results. Since both L80 and X70 are rolled products and the calculations were done with values obtained from a normalized sample [82], it is possible that the rolling process affected the structure in such a way that V_3 is more sensitive than the other velocities.

4.1.2 Through Thickness Attenuation

The attenuation was also found through the thickness of each skelp sample to see if there was any variation. In the X70 skelp there was little variation through the skelp thickness or among wave types. Figure 4.9 shows the attenuations through the X70 skelp, where AL is the longitudinal attenuation, AsP is the shear attenuation parallel to the rolling direction and AsT is the transverse attenuation.

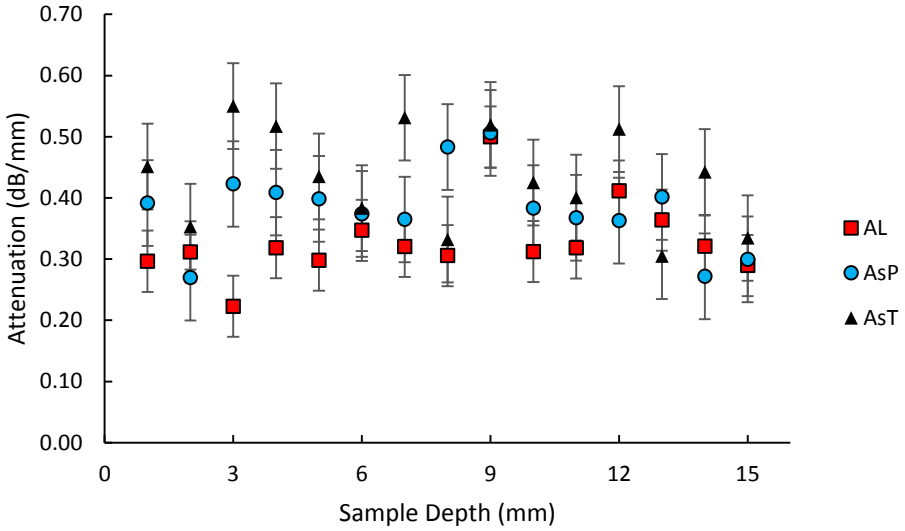

Figure 4.9: Attenuation Through X70 Skelp

The attenuation of the three wave types are not distinct from one another through the X70 skelp. For a given sample any of the three types could have the minimum attenuation at a given depth. The shear attenuations are normally higher, which could be due to the thick couplant that does not disperse as evenly or easily as the longitudinal couplant; however, this does not explain why the longitudinal attenuation is not consistently the minimum value. It is also noteworthy that both the AsP and AL have a distinct increase in attenuation for the sample at a depth of 9 mm. This same sample also had increases in VsP and VL at the same depth. None of the three wave types show any trend in their attenuation through the skelp. All show scatter around the average attenuation, i.e., 0.33 dB/mm for AL, 0.38 dB/mm for AsP and 0.43 dB/mm for AsT. This scatter is significant

enough to make it unlikely that the detected wave type could be determined the attenuation value. This is unlike the L80 skelp, where the longitudinal attenuation, AL, is lower than the shear attenuations in all cases (Figure 4.10).

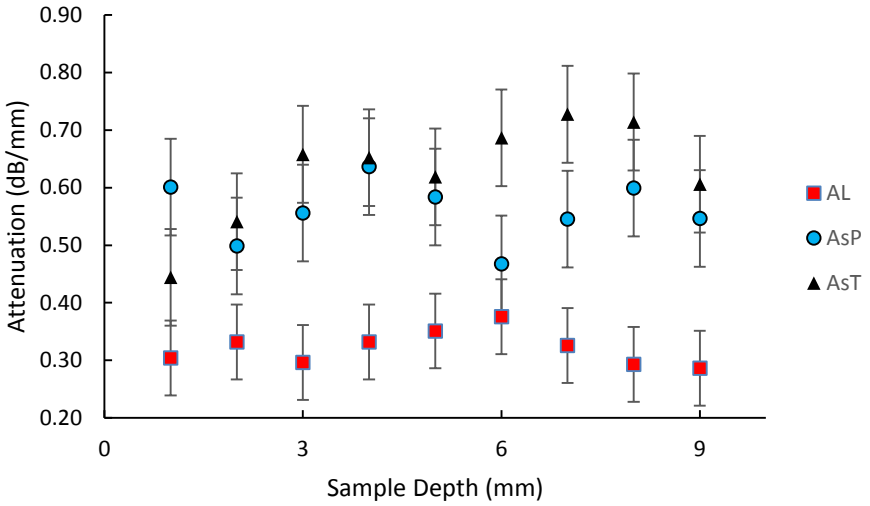

Figure 4.10: Attenuation through L80 Skelp

The shear attenuations, AsP and AsT, overlap with the longitudinal attenuation, AL, for one case each. For the rest of the samples, the longitudinal and shear attenuations are distinct. The lower longitudinal attenuation could again be attributed to couplant effects. This is more likely in L80 compared with X70, since the longitudinal attenuation is consistently lower than the shear attenuations in L80. There are no significant spikes in any of the L80 attenuations and the values are consistent through the skelp, especially the AL attenuations since all the values are within the error of one another. The attenuation was also determined through the whole skelp at one time, rather than through each sample individually. The attenuations were significantly lower than those in the individual samples; 0.19 dB/mm for AL, 0.2 dB/mm for AsP and 0.26 dB/mm for AsT. Again this is attributed to couplant effects, since on a per mm basis the couplant will have a greater effect for a 1 mm sample than a 9 mm sample. The difference between individual sample attenuations and full thickness values was less for the longitudinal case than for the shear case, again likely because of the high viscosity of the shear couplant.

Both velocity and attenuation in L80 and X70 skelps indicate little variation in the properties of either skelp. The velocities agree with those calculated and suggest little preferential orientation is present. The VsP was far from the average calculated V_3, but remained within the range of possible values. The difference between V_3 and VsP is attributed to the difference in composition and morphology of ferrite in the skelp samples and the normalized sample used to calculate V_3. The attenuations did not show significant variation through the skelp. For X70, attenuation was scattered amongst the three wave types, whereas for L80 the longitudinal attenuation was lower than the shear attenuations.

4.1.3 Pipe Skelp Through Thickness Summary

The ultrasonic velocity and attenuation through the skelp thickness of the L80 and X70 steels did not show significant variation. Velocities agreed with those calculated in Section 2.2 for samples with no texture. The agreement was worse for V_3 (2^{nd} shear mode) than for V_2 shear or V_1 longitudinal waves. In order to better understand how the ultrasonic properties are affected by microstructure further investigation was needed. This was done by annealing IF steel, chosen since only ferrite forms on air cooling, to see the effect of recrystallization and grain growth on ultrasonic properties and L80 steel after heat treatment to see the effect of forming different microstructures such as ferrite-pearlite or martensite.

4.2 Annealing Interstitial Free Steel

Interstitial free steel was annealed at 700°C and 775°C to see the effect on ultrasonic properties. Samples were held at 700°C for up to an hour or 775°C for up to two hours. The resultant ultrasonic properties were compared with the holding time at each temperature, as well as the hardness of each sample.

4.2.1 Effect of Holding Time on Microstructure

The effect of hold time on microstructure was investigated for both 700°C and 775°C holding temperatures. Samples were polished and etched for optical microscopy. Difficulties in etching did not allow for quantitative metallography of grain size. Hardness tests were then done to obtain quantitative differences between samples.

4.2.1.1 700°C Holding Temperature

The interstitial free (IF) steel was held at 700°C for up to an hour to increase the grain size. Etching proved to be extremely difficult for these samples. Nital did not etch the samples well; long etching times were needed and Nital selectively etched some grain boundaries, but not others, making analysis of the micrographs difficult. A sample micrograph only etched with Nital is shown in Figure 4.11.

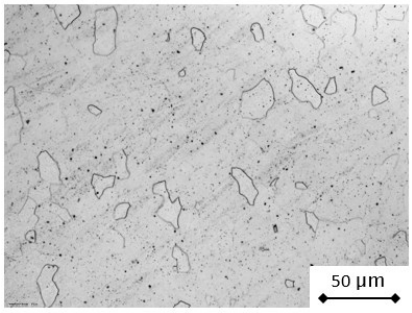

Figure 4.11: IF Sample Heated at 700°C for 0 Min, Etched in Nital for 5 Min

Some grain boundaries are quite distinct, others are faint and some do not show up at all. Marshall's reagent was chosen as a second etch, since it is often used for low carbon steels to etch ferrite boundaries when Nital does an incomplete job [96]. Marshall's reagent consists of two parts; part A is 5 mL of concentrated sulfuric acid added to 100 mL of water followed by 8 g of oxalic acid. Part B is 30% hydrogen peroxide which is combined in equal volume with part A. Marshall's reagent was found to be ineffective when used alone, but performed much better after a Nital etch was used to remove any passive layer present on the sample. Figure 4.12 shows the as received (AR) IF sample, along with samples heated to 700ºC for 0-60 minutes.

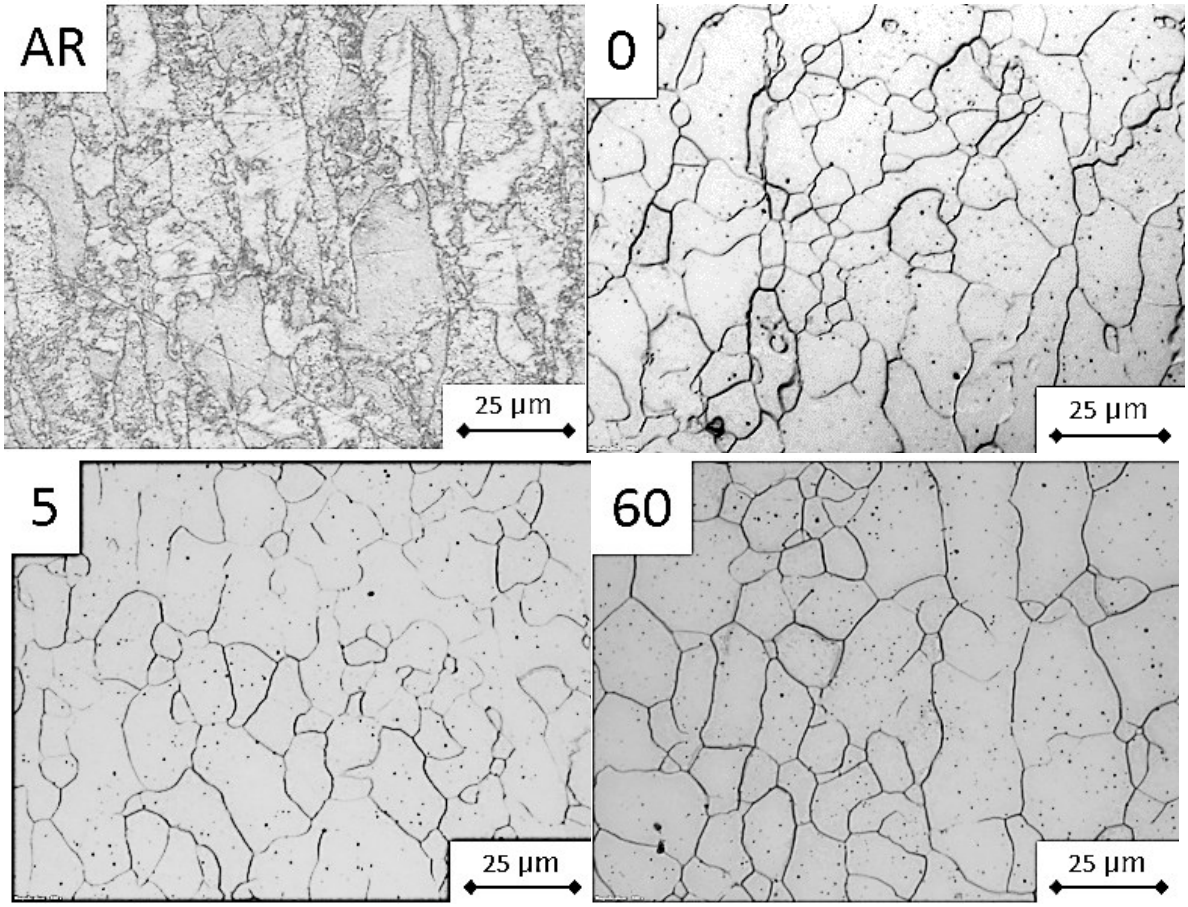

Figure 4.12: IF Steel, Heated to 700ºC for 0-60 Min, Etched in Nital and Marshall's Reagent

It should be noted that Marshall's reagent was more effective etching the IF steel when a mixture using only 80% of the recommended volume of hydrogen peroxide. Both 40% sulfuric acid and 95% sulfuric acid were tested; the 40% solution produced better results. The addition of oxalic acid prior to the sulfuric acid also improved etching response. The micrographs taken after Marshall's reagent etching show much better grain boundary etching, but there are still many boundaries which are not completely etched. The micrographs are then only useful for qualitative examination, since quantitative metallography for grain size is only accurate if all the grain boundaries are clearly visible. The 0 and 5 minute holds should have smaller grain size, while the

60 minute hold should have a larger grain size. Qualitative analysis of the micrographs in Figure 4.12 do not show a significant change in grain size. The 5 and 60 minute holds appear to be quite similar, with possibly a higher area fraction of large grains in the sample with longer hold time. Approximate grain sizes were measured using the procedure described in Section 3.5.4 from the best fields of view of the polished and etched samples. The results are given in Table 4.1 and show that the grain size did not change significantly from 0 to 60 minutes of holding.

Table 4.1: Grain Size For IF Samples Held at 700ºC

Sample Hold Time (mins)	Grain Size (μm)
AR	7
0	12
5	11
60	12

Microhardness was then done to see if a quantitative difference could be determined between the samples. The hardness change as a function of holding time is shown in Figure 4.13.

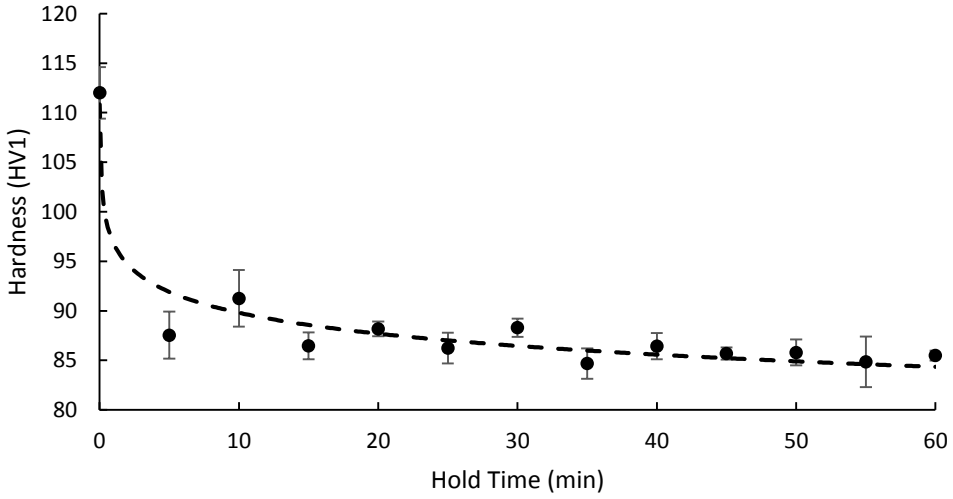

Figure 4.13: Hardness vs. 700ºC Hold Time

The 0 min hold has the highest hardness by a large margin, while the remaining samples show similar hardness which slightly decreases from approximately 90 HV to 85 HV. The hardness readings are helpful when looking at the microstructures, since there is a relationship between grain size and yield strength, i.e., the Hall-Petch relationship [97] [98].

$$YS = \sigma_0 + \frac{k_y}{\sqrt{D}} \tag{4.1}$$

where σ_0 and k_y are material constants, YS is the yield stress and D is the average grain size. This relationship has been shown to be true in IF steels [99] [100]. The YS is proportional to the hardness in steel [101], so as the average grain size decreases the hardness and yield strength increase. The process of recrystallization is also known to decrease the hardness of metals [102]. The sharp decrease in hardness after the 0 minute hold could be the result of recovery and recrystallization, eliminating work hardening in the as-received sample. The small change in hardness for the remaining samples also confirms the observation that their microstructures are similar.

4.2.1.2 775°C Holding Temperature

Since little change was found in the microstructure of the samples held at 700°C for up to one hour, 5 samples were held at 775°C for up to two hours in an attempt to change the microstructure more drastically. The increased temperature should speed grain growth, since grain growth is exponentially dependent on temperature; longer times should enhance grain growth as well. The same issues with sample etching were encountered with the 775°C holds as discussed previously with the 700°C holds. The difference in grain size is much more obvious in Figure 4.24. The 0 min hold has a smaller grain size than the 120 min hold sample.

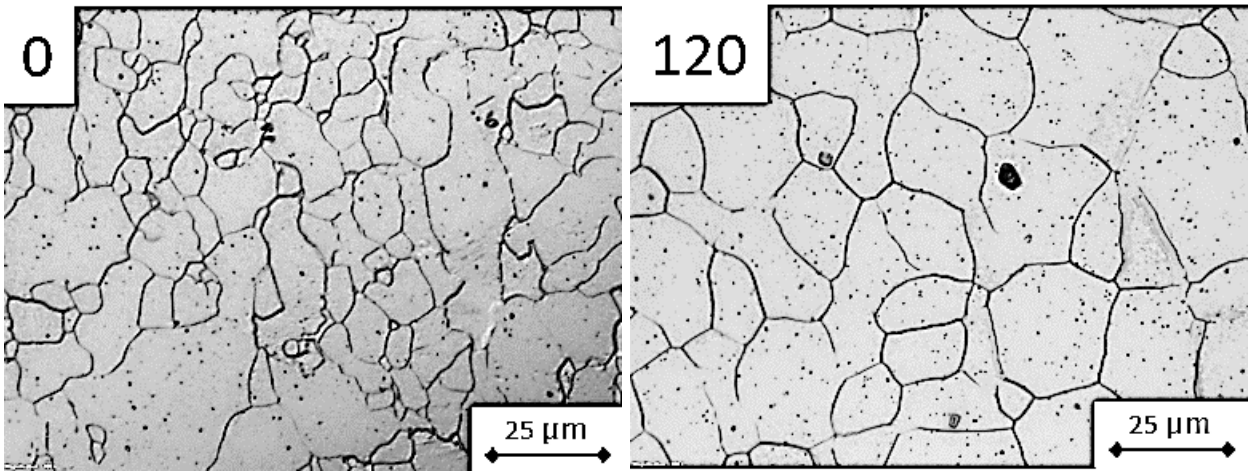

Figure 4.14: IF Sample Held at 775°C for 0 and 120 Min, Etched in Nital and Marshall's Reagent

Grain sizes were measured, using the method described in Section 3.5.4, for the samples held at 775°C. The results are shown in Table 4.2; there is an increase in grain size as hold time is increased from 0 mins to 120 mins.

Table 4.2: Grain Size For IF Samples Held at 775°C

Sample Hold Time (mins)	Grain Size (µm)
0	10
120	18

The hardness values for the 775ºC holds are shown in Figure 4.25. The hardness shows a similar trend to the 700ºC holds, where the 0 min sample has higher hardness than the remaining samples which show a slow decrease in hardness after the initial drop. There is, however, only a difference of 11 HV between the two samples compared with the 27 HV difference between the 0 and 60 min holds for the 700ºC case. The 0 min, 775ºC hold has a hardness in the range of the samples held at 700ºC. This makes sense since it spent 6 minutes heating from 700ºC to 775ºC in the furnace before being removed. The 120 min hold also shows fewer small grains than the 60 min, 700ºC sample.

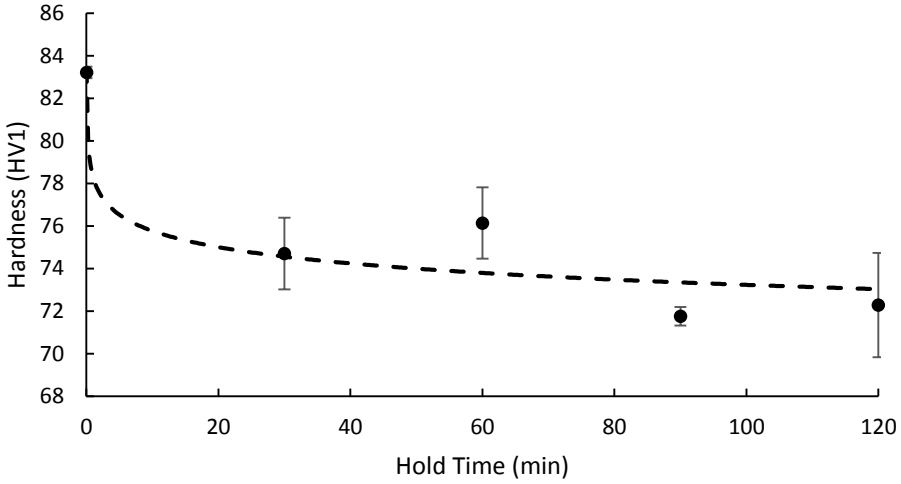

Figure 4.15: Hardness vs 775ºC Hold Time

It is hard to say if the maximum grain size is increased, since what appears to be large grains could be made up of smaller grains whose boundaries did not etch. Qualitatively the large grains in the 60 min, 700ºC sample tend to have more etched lines protruding into them than those in the 120 min, 775ºC sample. This may indicate that the grain size is in fact larger in the 120 min, 775ºC sample. When the hardness is compared between the two hold times, the samples held at 700ºC are harder than those held at 775ºC, as shown in Figure 4.16. This is again the likely result of the relationship between strength (hardness) and grain size [97]. The 0 min 700ºC sample is the hardest by far and likely has not recrystallized while the others are similar and likely all were recrystallizing before being removed from the furnace. The lower hardness of the 775ºC samples indicate that more recrystallization has occurred than in the 700ºC samples due to their higher temperature and longer hold times. The increased softening in the 775ºC samples also agrees with the qualitative analysis of the micrographs that the grain size is increased compared with the 700ºC samples, which makes sense due to the higher annealing temperature.

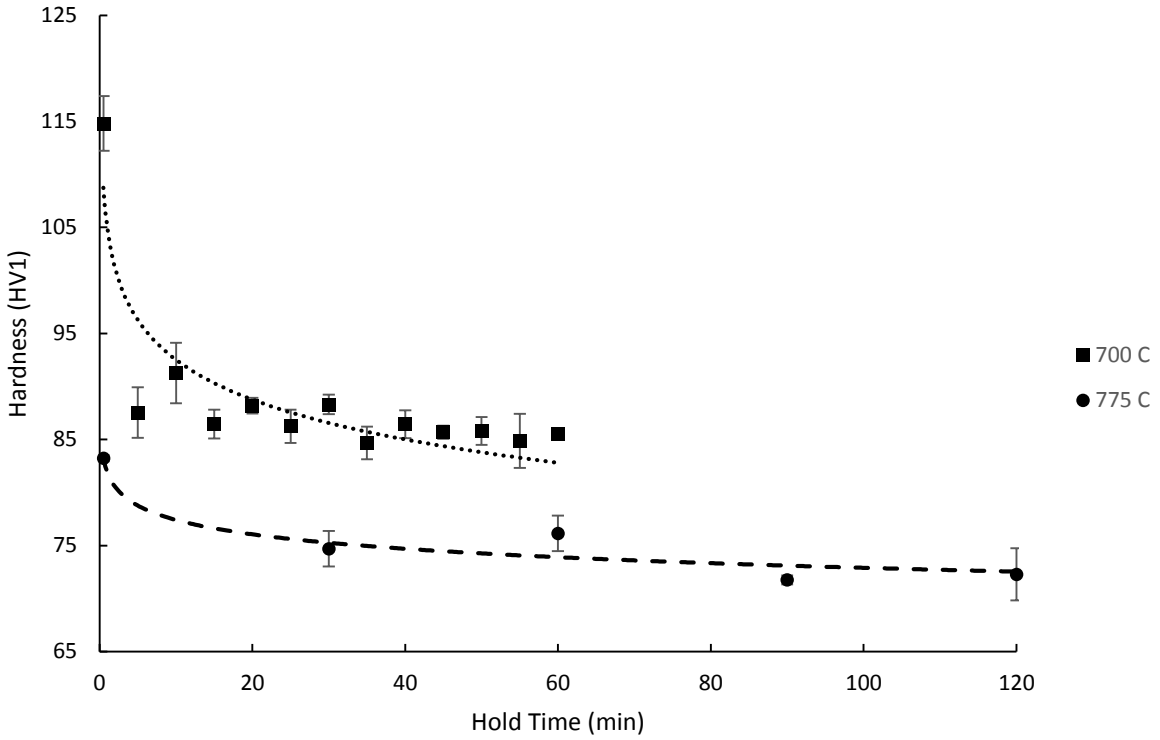

Figure 4.16: Hardness vs Hold Time For IF Steel

4.2.2 Effect on Ultrasonic Velocity

The ultrasonic velocities were compared with both the hardness of each sample and the time held at either 700ºC or 775ºC. The behaviour was also compared with annealing behaviours found in literature.

4.2.2.1 700ºC Holding Temperature

The ultrasonic velocities were compared with hold time and hardness, both of which are used to indirectly represent the grain size in the samples. The shear velocities tend to increase as holding time progresses, while the birefringence remains near constant. The longitudinal velocities also increase with holding time. Both trends are shown in Figure 4.17.

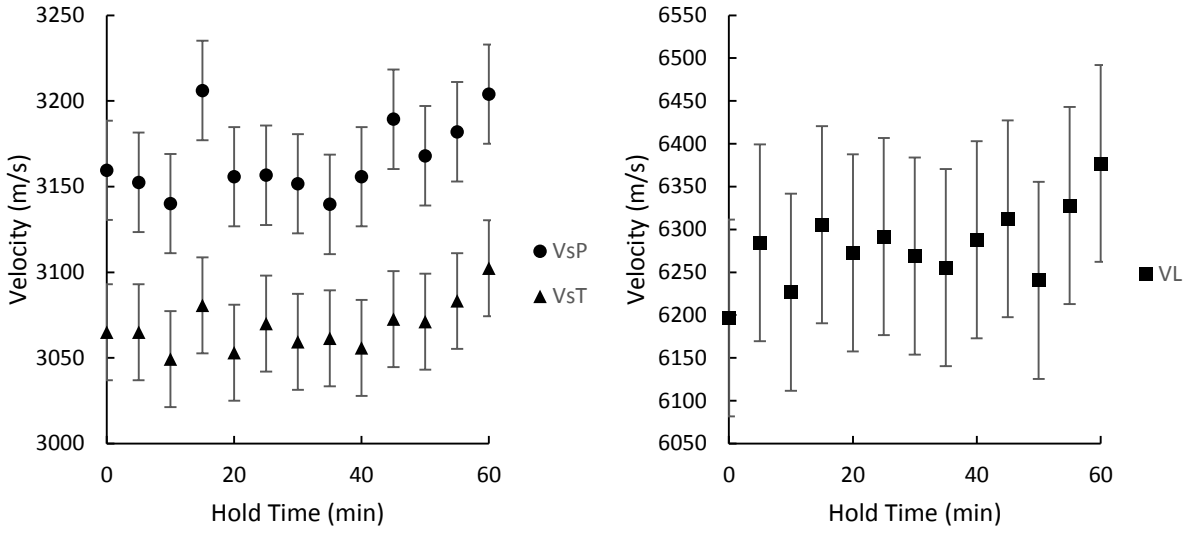

(A) (B)

Figure 4.17: Ultrasonic Velocity vs. 700ºC Hold Time

The velocity increases slowly as holding time increases after 30 minutes for both shear and longitudinal waves. Assuming the grain size increases with hold time this is the opposite effect to that found in other work on steel where the velocity decreased with increasing grain size [44] [48]. However, it does not appear from the micrographs (Figure 4.12) that the grain size has increased significantly as hold time increased. An increase in ultrasonic velocity occurred with fraction recrystallized for IF steels studied in-situ with laser ultrasonics at high temperature during continuous cooling (Figure 4.18) [48]. There was a difference in the velocity behaviour in their work between IF steels and austenitic stainless steels. The IF steel had an inhomogeneous texture change as recrystallization progressed. The texture remained constant through the first half of recrystallization until the "<111>//ND (normal direction) recrystallization texture replaces the elastically softer <100>//ND deformed structure" [48]. This is the same behaviour shown in Figure 4.17, where the velocities remain relatively constant until 30 minutes have passed and then the velocities increase. The literature IF steel longitudinal velocity increased by 150 m/s from ~25% recrystallized to 100% recrystallized. The increase seen in Figure 4.17 is only ~100 m/s from the average of the initial velocities to the final velocity. The smaller velocity change in the samples tested in this work relative to those in the literature indicates that recrystallization may be incomplete in the samples tested. It is likely then that the reduction in hardness is the result of recrystallization, not pure grain growth as suspected.

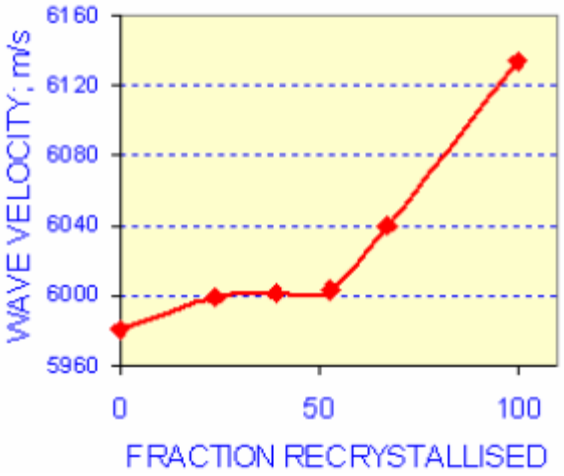

Figure 4.18: Longitudinal Velocity vs. Fraction Recrystallized in Ti-Stabalized IF Steel [48]

Both shear velocities and longitudinal velocity are scattered with respect to hardness (Fig. 4.28). There is scatter in the velocities at low hardness; however, a similar trend is seen for the hardness as the hold time increases. As hardness decreases the velocity remains relatively constant until approximately 86 HV when it begins to increase. This roughly corresponds to the 35 minute hold, which is close to the onset of increasing velocity shown in Figure 4.17. The hardness readings had a standard deviation of 1-3 HV depending on the sample and the maximum range of hardness values considered was less than 10 HV. This makes any trends with the hardness difficult to confirm with certainty. The scatter along with the small difference in hardness values points towards the hold time being a better indicator of the progress of recrystallization and more representative of real trends with velocity.

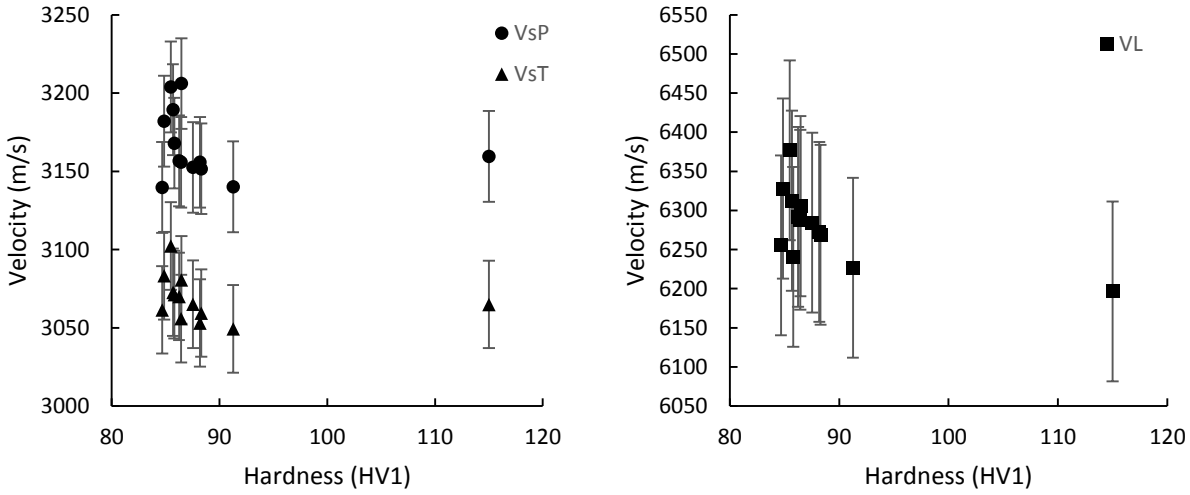

(A) (B)

Figure 4.19: Ultrasonic Velocity vs. 700°C Hardness

4.2.2.2 775ºC Holding Temperature

The velocities were also compared for the 775ºC samples with their hold times and hardness values. The velocities and hold time relations are shown in Figure 4.20.

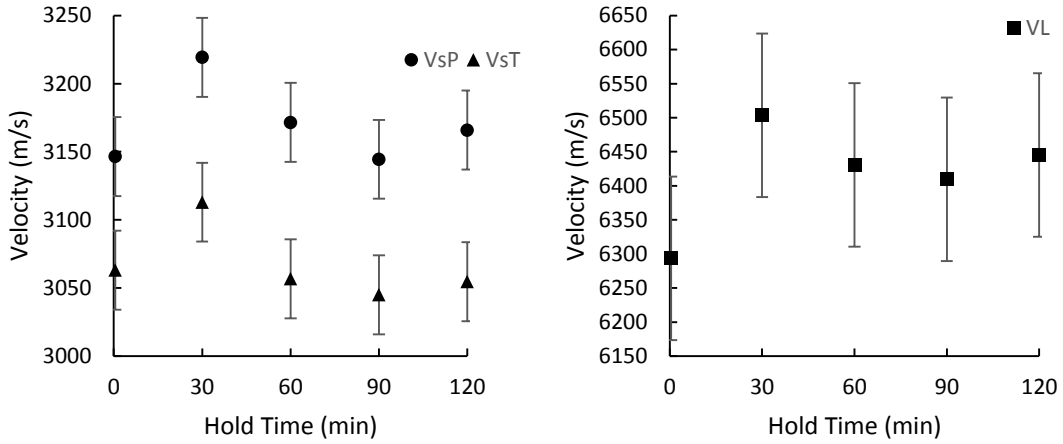

Figure 4.20: 775ºC Hold Time and Ultrasonic Velocity

Both the longitudinal and shear velocities increased from 0-30 minutes, then decreased and leveled off. This is similar to the behaviour reported for annealing of stainless steel in the work done by Palanichamy [47], where the velocity peaked then decreased as recrystallization progressed. This behavior in stainless steel is shown in Figure 4.21, where the different shear and longitudinal waves relate to their propagation direction through the sample. VS1 and VS2 correspond to VsT and VsP in this work, respectively.

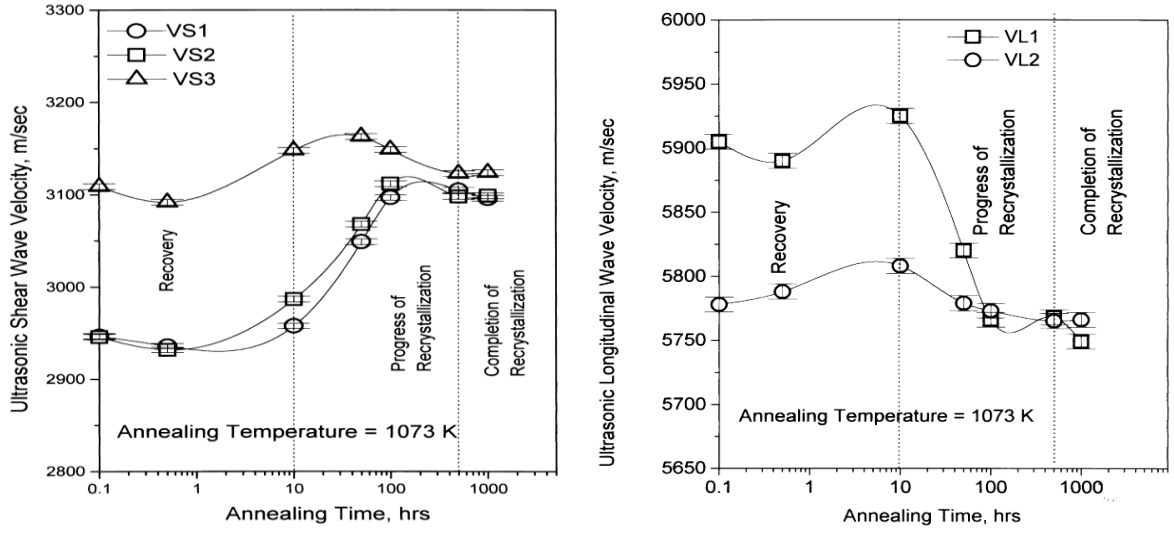

Figure 4.21: Shear (A) and Longitudinal (B) Velocity vs Annealing Time at 1073 K in D9 Stainless Steel [47]

The initial and final velocities between the stainless steel and experimental IF steel are reversed for one another. The initial shear velocities are lower in the stainless steel, while the experimental shear velocities appear similar or higher than the final. The specific behaviour for the ultrasonic velocity has been shown to depend on what texture forms during annealing. Work done by Lamouche showed the velocity change could be directly related to the texture change in cold rolled, low carbon steel [103]. As the probability of the <111> direction being oriented along the wave propagation direction decreased, so did the longitudinal velocity. This agrees with the calculations done in Section 2.4 that showed the <111> direction to be the fastest for longitudinal waves. The relationship between the W_{400} texture index, longitudinal velocity and annealing time from the literature is shown in Figure 4.22.

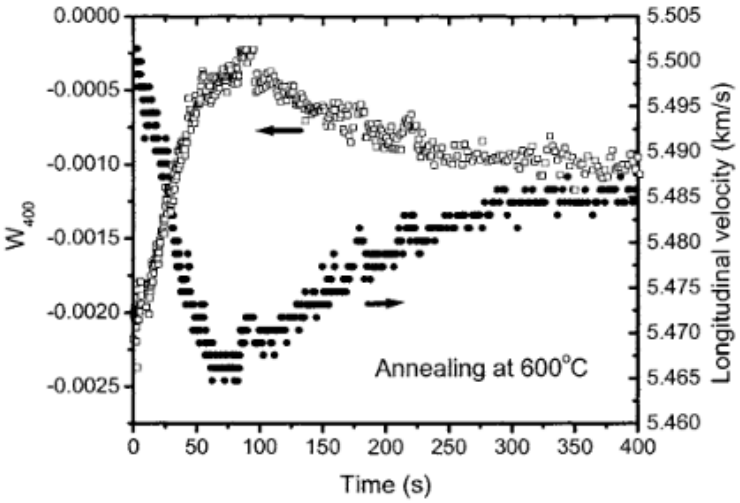

Figure 4.22: W_{400} Texture Index and Longitudinal Velocity vs Annealing Time [103]

It is then possible that the differences between the literature results (Figure 4.21) and the experimental work presented here (Figure 4.20) could be the result of different textures present in the as received material producing different texture changes on annealing. Both cases had initial structures which were cold rolled, although the as-received processing is not known for the experimental IF steel used in this work.

The same trends are also seen for velocity as the hardness changes. As with the 700°C holds, the trends are more clear for the hold times than for the hardness. Both longitudinal and shear velocity increases then decrease as hardness increases as shown in Figure 4.23Figure 4.23. The increases and decreases in velocity are in the same samples are they are seen in the hold time (Figure 4.20).

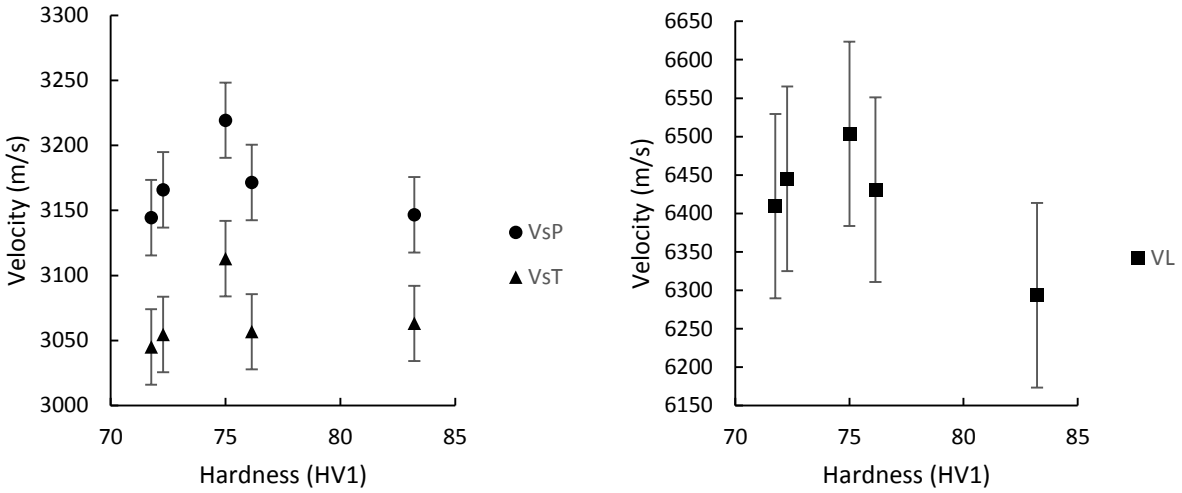

(A) (B)

Figure 4.23: 775°C Hardness and Ultrasonic Velocity

4.2.3 Effect on Ultrasonic Attenuation

The ultrasonic attenuation was also compared with the hold time and sample hardness for both holding temperatures.

4.2.3.1 700°C Holding Temperature

The ultrasonic attenuations were compared with the hold time and hardness for the 700°C samples (Figure 4.24).

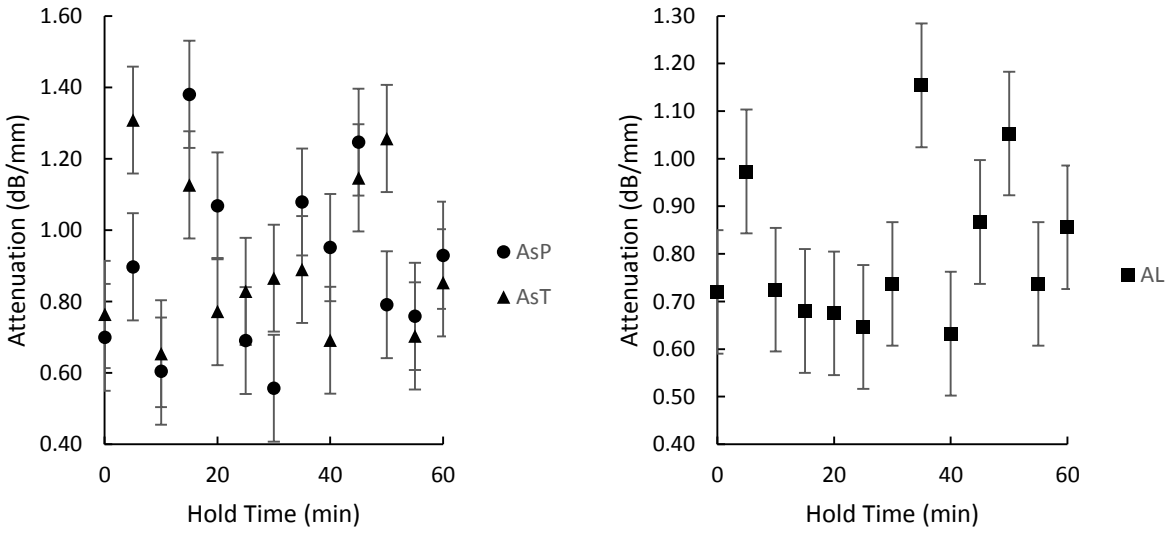

(A) (B)

Figure 4.24: Ultrasonic Attenuation vs. 700°C Hold Time

The scatter in the shear values makes it difficult to determine any trends. The attenuation appears to not change significantly with hold time. The longitudinal attenuation seems to increase with the hold time; however, the data is too scattered to confidently associate this with recrystallization as done with the velocity. Similar scatter is seen for the longitudinal and shear attenuations with hardness (Figure 4.25).

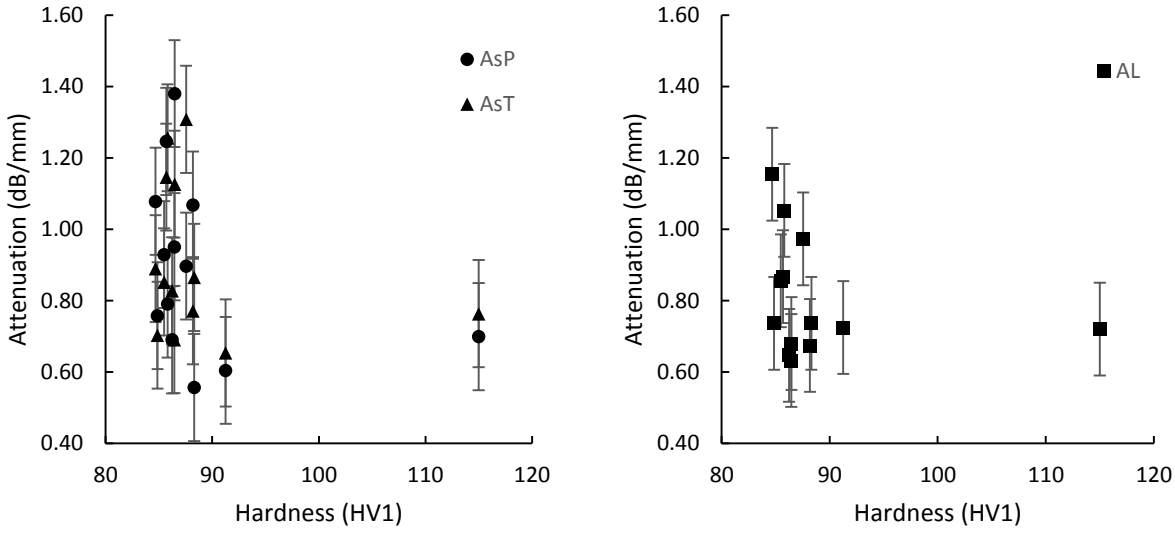

(A) (B)

Figure 4.25: Ultrasonic Attenuation and Hardness, IF Samples Held At 700ºC

There is still scatter in the longitudinal attenuation in the samples which have lower hardness, but again they seem scattered about a decreasing trend. The increased scatter in the shear attenuations compared with the longitudinal attenuation is likely the result of differences in the coupling medium used for each transducer as discussed earlier. This could potentially be mitigated by taking a significant number of readings until the effects of particularly good or bad coupling are negated. Neither shear nor longitudinal attenuation show significant trends with hold time or hardness. There may be an increase in attenuation as recrystallization progresses, but the scatter in the data makes verification difficult.

4.2.3.2 775ºC Holding Temperature

A similar comparison was done for attenuation with the 775ºC samples. The comparison of hold time and attenuation is shown in Figure 4.26.

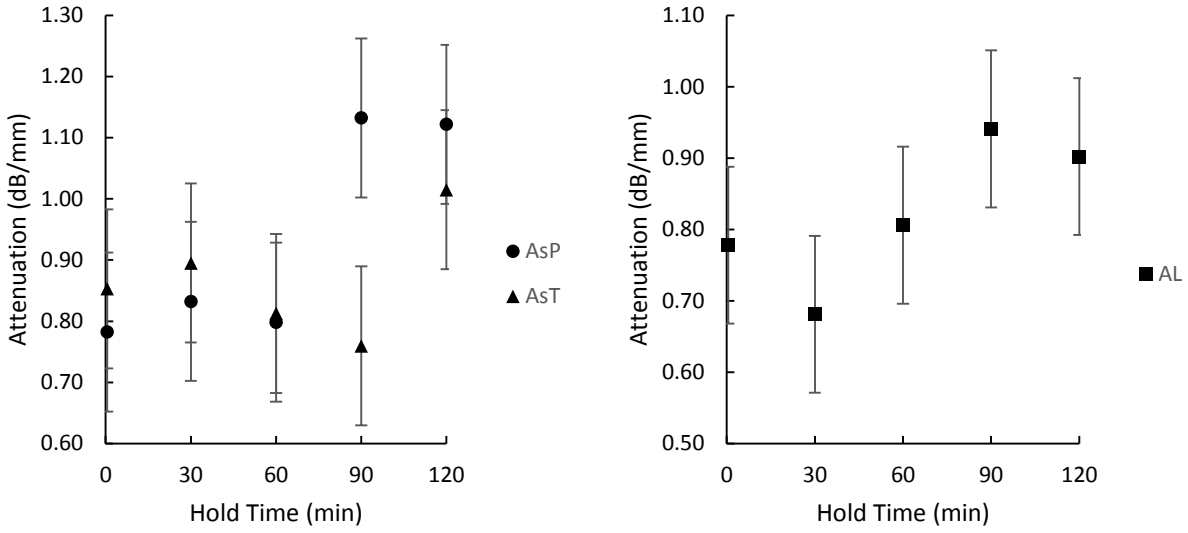

(A) (B)

Figure 4.26: Ultrasonic Attenuation and 775ºC Hold Time

The attenuation shows the reverse behaviour compared with the velocities. There was not much change in the attenuation for lower hold times (<90 minutes); significant changes occurred for samples held for 90 and 120 minutes. The velocity showed a more marked change at lower hold times. The velocity is then more sensitive to the texture change during recrystallization, while the attenuation appears more sensitive to the phenomenon after recrystallization, grain growth. The attenuations were also compared with the hardness as shown in Figure 4.27.

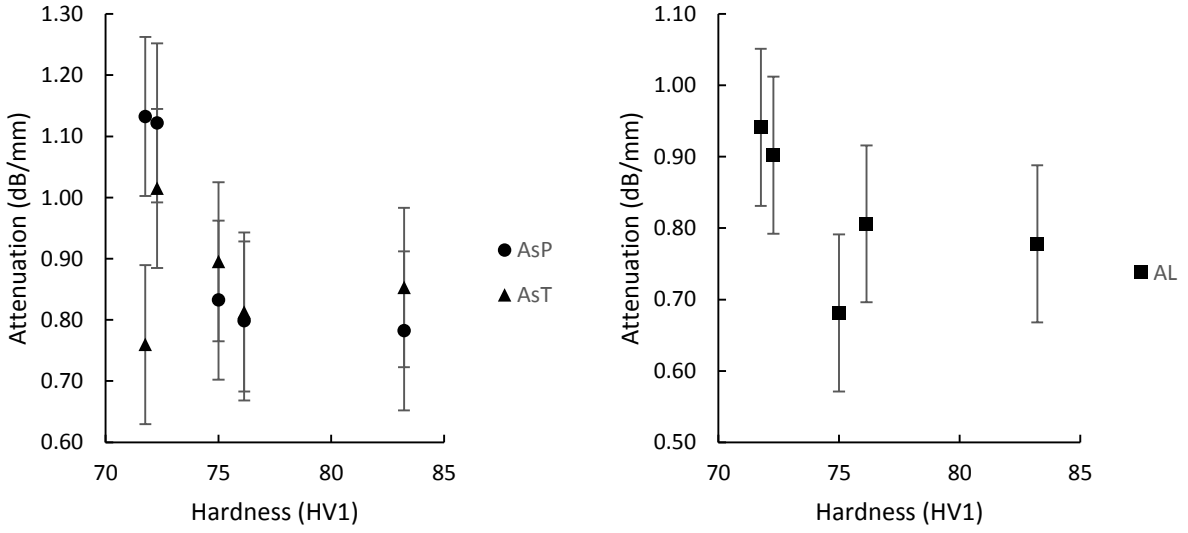

(A) (B)

Figure 4.27: Ultrasonic Attenuation and Hardness with 775ºC Hold Time

Both the shear and longitudinal attenuations increase with decreasing hardness. The 90 minute sample, 72 HV1 (Vickers hardness with 1 kg test weight), has a lower AsT than suggested by the trend; the 30 minute sample, 75 HV1, also has a lower AL than suggested by the trend.

The initial softening, after short hold times, shows little change in attenuation, while the small change in hardness in the samples held for longer times shows a sharp increase in attenuation. The 120 min sample did appear to have larger grains than the 0 min sample in Figure 4.14, indicating that there is grain growth between the samples. Since attenuation has been shown in previous works to be particularly sensitive to grain size [67] [48], it is likely that the initial changes in velocity after short hold times are the result of recrystallization where the attenuation shows little change. The changes in the attenuation in the samples after longer hold times, where the velocity shows little change, are then likely the result of grain growth. The velocity is more sensitive to the recrystallization process while the attenuation is more sensitive to grain growth. The micrographs for the 700ºC samples, Figure 4.12, do not show significant grain size variation between the short and long hold times. Their velocities changed during the latter holding times, while their attenuations did not show significant variation, only scatter. It follows that recrystallization was not complete and pure grain growth did not occur. Since there was no significant grain growth, the attenuations did not change. The velocity and attenuation together then show both the phenomena of recrystallization (velocity) and grain growth (attenuation) when annealing steel.

4.2.4 Annealing IF Steel Summary

The difference between microstructures on annealing was difficult to quantify in the IF steel due to problems with etching. For 700ºC holds there did not appear to be a significant change in grain size between samples regardless of hold time; however, the hardness dropped significantly once the samples were held for five minutes and then remained relatively constant. Ultrasonic velocity did not change significantly until 30 minutes of annealing had passed, which correlates with the point where significant texture change began occurring in work done by other researchers on IF steels. The samples held at 700ºC were likely then in the process of recrystallizing after one hour and had not yet begun grain growth, which is why the micrographs appeared similar to one another and was confirmed by the similar grain sizes found quantitatively (~10 μm in all samples). The scatter in the attenuations for the 700ºC samples made analysis difficult and no strong conclusions could be drawn.

The samples held at 775ºC qualitatively showed grain growth in the final sample compared with the others. The drop in hardness was less significant between the first and second sample than in the 700ºC holds. The peak and valley behavior of the velocity from 0-90 minutes agreed with the behavior seen in stainless steels and is likely due to texture changes as the samples recrystallized. The attenuation in these samples showed greater change after the recrystallization period than the

velocity, indicating that the attenuation is more sensitive to grain growth which occurred in these samples as the grain size was measured to increase from 10 μm to 18 μm after annealing.

4.3 L80 Steel Microstructure Variation

L80 pipe skelp was heat treated to generate a variety of microstructures to see the variation in ultrasonic properties. Small samples were tested initially with only transverse shear waves and longitudinal waves to see if differences existed between samples. Long bars were then ultrasonically tested and then broken with tensile tests to obtain more material properties as well as using an optical microscope for quantitative metallography. The relationships between these material properties and ultrasonic properties were compared.

4.3.1 Heat Treated L80 Small Bars

Small samples for one ultrasonic test were austenitized and cooled at varying rates to generate martensite and other structures. They were then analyzed with optical microscopy to see the resultant structures, hardness tested and ultrasonically tested. Their hardness and structure were compared with the ultrasonic velocity and attenuation in each sample.

4.3.1.1 L80 Small Bar Microstructures

The heat treated small L80 bars showed a variety of microstructures. The samples which were quenched formed martensite (M), while those that were cooled slowly formed a ferrite-pearlite mix (F-P) and the sample which was cooled in hot oil, without a clay coating, formed bainite (B). Table 4.3 shows the sample designations and their cooling process as well as the resultant microstructure in each sample. Figure 4.28 shows optical micrographs taken from each sample.

Table 4.3: L80 Small Bar Heat Treatments and Resultant Microstructures

	CAC	AC	C200	200	COC	OC	CWC	WC
Quenching media	Air	Air	200°C Oil	200°C Oil	Oil	Oil	Water	Water
Coating	yes	-	yes	-	yes	-	yes	-
Microstructure	F-P	F-P	F-P	B	M	M	M	M

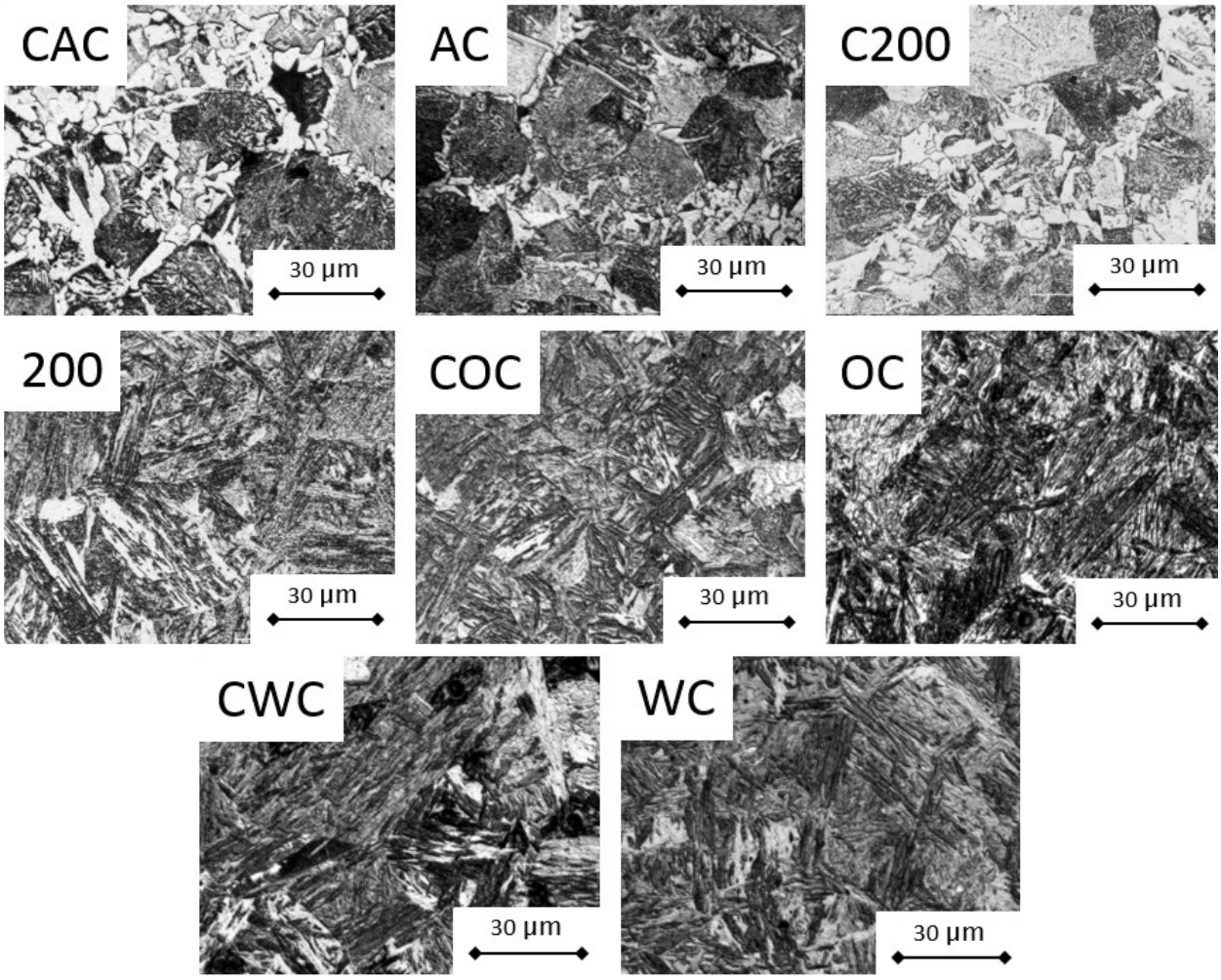

Figure 4.28: L80 Small Bar Microstructures

The predominant microstructures can be seen quite clearly in each micrograph. The air cooled sample (AC) qualitatively appeared to have more pearlite colonies (dark contrast regions) than the coated air cooled sample (CAC). The coated hot oil quenched sample (C200) appeared similar to the CAC sample. The uncoated hot oil quenched sample (200) showed regions which appeared to be bainite. It is possible that some regions were also martensite and that a mixed microstructure was present. The four martensitic samples, COC, OC, CWC and WC, all appear very similar with microstructures consisting of largely lath martensite.

4.3.1.2 L80 Small Bar Shear Velocity

The microstructures were compared with the transverse shear velocity in each sample, as shown in Figure 4.29.

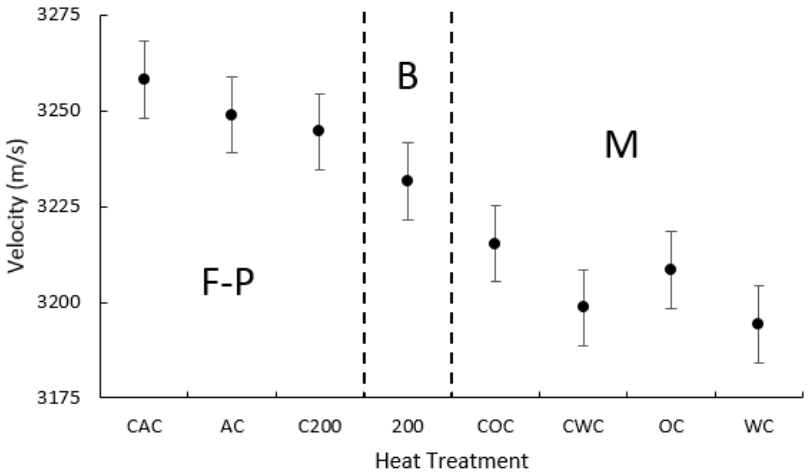

Figure 4.29: Transverse Shear Velocity vs. L80 Heat Treatment

The ferrite-pearlite samples have the highest shear velocity, followed by the bainite and then martensitic. The decrease in velocity from F-P to B to M was also reported in work done on other steels [30] [31] [32]. Additionally, the hardness of each sample was compared with the ultrasonic shear velocity, as shown in Figure 4.30.

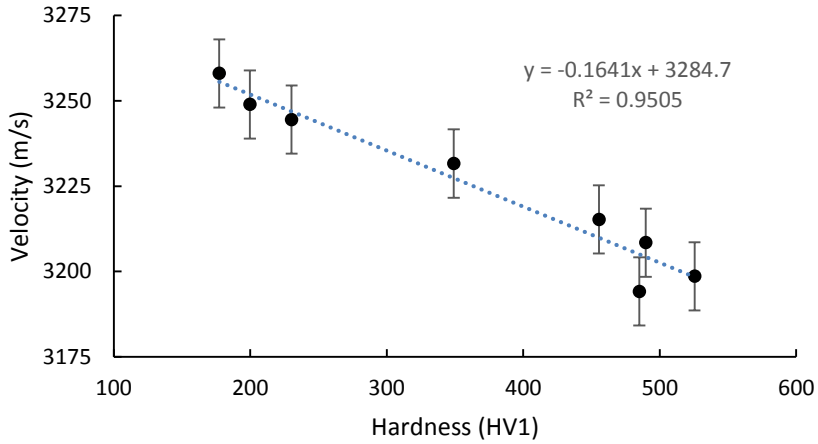

Figure 4.30: Microhardness and Transverse Ultrasonic Shear Velocity

The uncoated hot oil sample (349 HV1) is shown, in this case, to be distinct from the other morphologies, as both the martensite and ferrite-pearlite samples have hardness values grouped apart from it. This indicates its morphology is different from F-P or M and is likely either bainite or a mixed B-M structure. There is a linear trend between hardness and shear velocity. This relationship can be quantified as:

$$VsT = -0.1641(HV) + 3284.7 \quad (4.1)$$

where HV is the Vickers hardness of the sample and VsT is the shear velocity transverse to the rolling direction. The experimental velocities found all agree with the trend, which has an R^2 value of 0.95. The ferrite-pearlite samples, which have low hardness, have higher velocities than the martensite samples, which have higher hardness. This agrees with the anisotropic velocity calculations done in Section 2.2, where ferrite had the highest ultrasonic velocity followed by ferrite-pearlite and then martensite. Comparison between the shear velocities found in the L80 samples and those calculated in Section 2.2 are shown in Figure 4.31. The points in the figure are the experimental L80 velocities, while the horizontal lines are the calculated shear velocities with J=1 from Section 2.2 for ferrite-pearlite (F-P) and martensite (M).

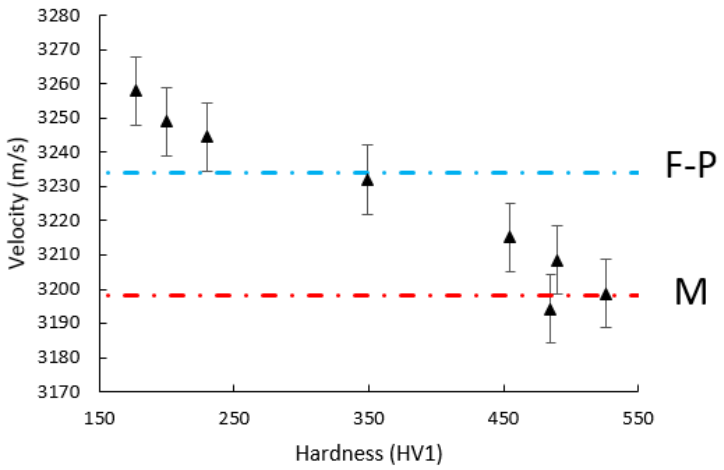

Figure 4.31: L80 Shear Velocities and Calculated V_2

The martensitic samples have velocities close to those calculated. The calculated values do not take into account how changes in morphology such as lath or colony size affect the ultrasonic velocity. The calculations are for a specific martensitic structure obtained by water quenching a 1050 bar, the agreement between the 1050 calculated velocities and experimentally obtained L80 velocities suggests that structure is of greater importance to ultrasonic velocity than composition. The water quenched L80 (485 HV1) agrees within error with the complete range of calculated velocities. Both the martensite and ferrite-pearlite calculated V_2 values have very small ranges, 8 and 6 m/s respectively, making it difficult to determine if velocity differences between the calculations and experiments are due to orientation or other factors such as composition differences between the L80 and 1050. Calculations were not done for bainitic velocities since the work done to get the elastic properties of 1050 structures did not include a bainitic sample [82]. The properties of the ferrite-pearlite sample used to calculate the velocity are not entirely known. The average grain size is 10 μm [82] and the micrograph shown in Figure 4.32 is the only information known.

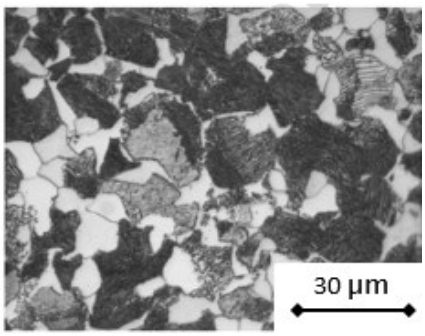

Figure 4.32: Ferrite Pearlite Sample Used for Determination of Elastic Constants [82]

There could be more or less ferrite in the tested samples than those used to determine elastic constants. The ferrite morphology also appears to be different in the L80 samples. The 1050 bar used has a much more polygonal morphology than the Widmanstätten, angular and sharp, structure seen in the L80. The calculated velocity could be lower due to an increased fraction of pearlite compared with the experimental samples or another morphological difference such as the presence of precipitates or difference in ferrites. Precipitates were seen in all structures found in the L80 samples. These precipitates, which are characterized by their cuboidal shape, are most likely titanium nitrides.

4.3.1.3 L80 Small Bar Longitudinal Velocity

The longitudinal velocities of the samples was also compared with their microstructures. Unlike the shear velocities, the ferrite-pearlite and martensite samples both showed velocities within the same range, as shown in Figure 4.33.

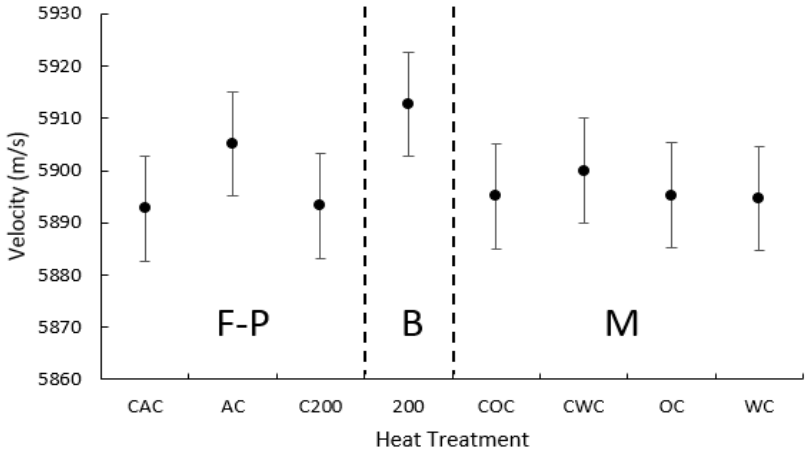

Figure 4.33: Longitudinal Velocity vs. L80 Heat Treatment

The consistency seen in longitudinal velocity across microstructures initially appears inconsistent with the trend found in shear velocities. When the experimental velocities are compared with the calculated values from Section 2.2 this velocity behaviour can be explained. Figure 4.34 shows

the experimental longitudinal velocities as points while the calculated longitudinal velocities (V_1) for ferrite-pearlite (F-P) and martensite (M) are shown as horizontal lines.

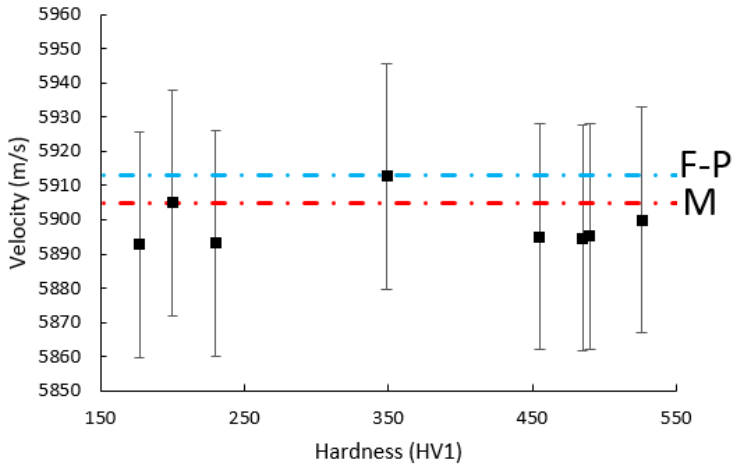

Figure 4.34: L80 Longitudinal Velocity vs Hardness and Calculated V_1 (F-P and M)

The calculated range of longitudinal velocities for ferrite-pearlite and martensite lie within the error bars of the experimental values. The longitudinal velocity is a poor indicator of change between these structures, due to their small difference in velocities. The bainitic sample does not show significant deviation in longitudinal velocity from the other samples.

4.3.1.4 L80 Small Bar Ultrasonic Attenuation

The attenuation of both the shear waves and longitudinal waves were compared with the microstructures and hardness of each sample. Both attenuations are shown in Figure 4.35.

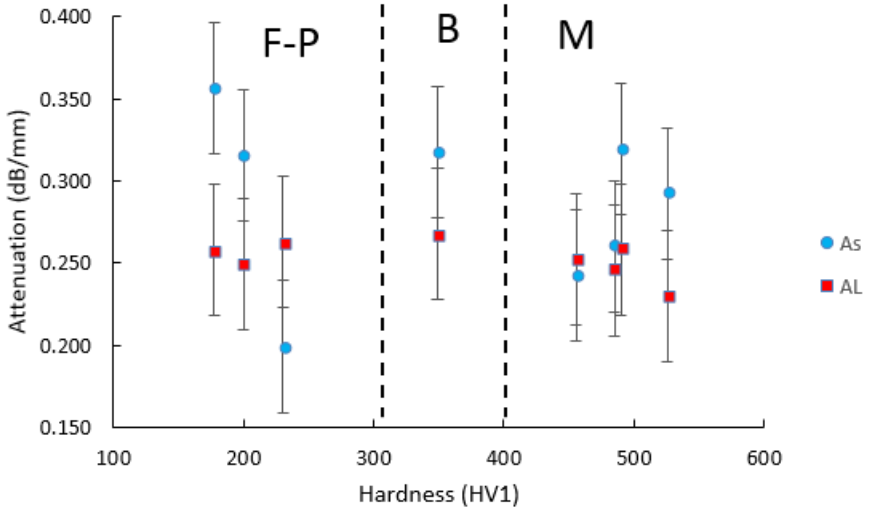

Figure 4.35: L80 Attenuation vs. Hardness

There is no significant trend in the attenuations with hardness or microstructure. This could be similar to the longitudinal velocities where there is not actually a significant difference between the samples or it could be the result of scatter in the experimental data. The structure of each sample does not appear to affect the ultrasonic attenuation for the L80 samples.

4.3.2 Heat Treated L80 Long Bars

To further the investigation into microstructure changes in L80 and their effect on ultrasonic properties, larger samples were produced of each heat treatment used for the small bars as well as a furnace cooled (FC) treatment. These larger samples were in the form of long bars, 240 mm x 20 mm x 4 mm, so that multiple ultrasonic tests and metallographic specimens could be done from each sample. The length of the sample was chosen so tensile tests could be performed on each sample after metallographic specimens were sectioned. Three samples were produced using each heat treatment. Each sample was ultrasonically tested on either end of the sample, as well as the center of its length. The nine values obtained for each ultrasonic wave type (longitudinal, shear parallel to the rolling direction and shear transverse to the rolling direction) were used to obtain average values for each heat treatment and the standard deviations in their readings were used as the error. The same process was used to obtain values from the three tensile tests performed for each heat treatment.

4.3.2.1 Long Bar Microstructures

The heat treated L80 long bars showed a variety of microstructures similar to those found in the small bars. The quenched samples showed martensitic structures, while the slow cooled samples were a ferrite-pearlite mix. In the long bar samples the 200ºC, both hot oil quenched samples showed bainitic structures unlike the small bars where only the uncoated hot oil quenched sample appeared bainitic. The heat treat designations for the L80 long bars and the resultant microstructures are shown in Table 4.4, while example micrographs for each heat treatment are shown in Figure 4.36.

Table 4.4: L80 Long Bar Heat Treatments and Resultant Microstructures

	FC	CAC	AC	C200	200	COC	OC	CWC	WC
Quenching media	Furnace	Air	Air	200ºC Oil	200ºC Oil	Oil	Oil	Water	Water
Coating	-	yes	-	yes	-	yes	-	yes	-
Microstructure	F-P	F-P	F-P	B	B	M	M	M	M

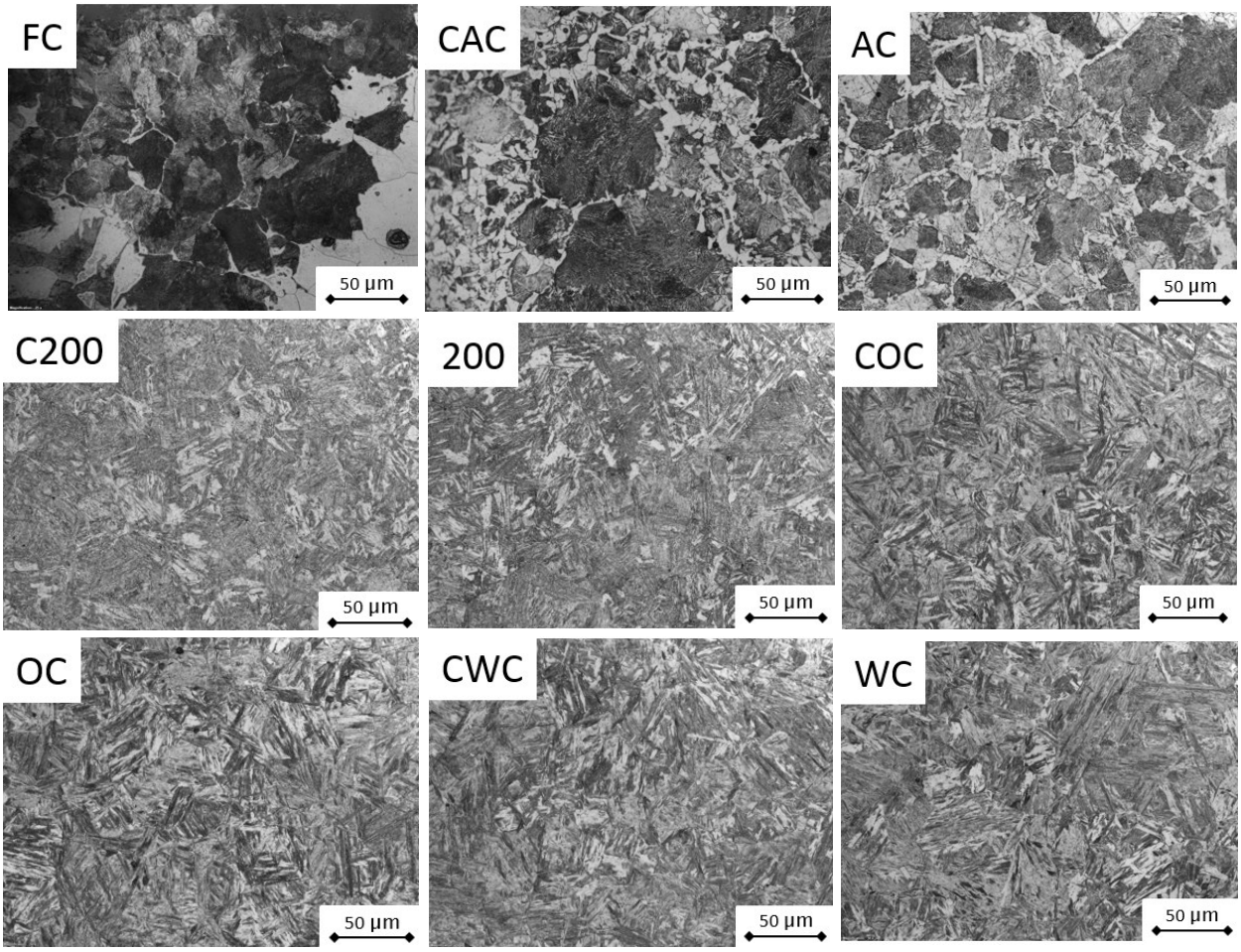

Figure 4.36: L80 Long Bar Microstructures

The quenched samples all showed a consistent structure of lath martensite. The samples that were cooled in 200ºC oil show similar primarily bainitic structures, but may also contain some martensite. The more slowly cooled samples contain predominantly ferrite and pearlite. The furnace cooled sample had a banded structure (Figure 4.37), with regions oriented along the rolling direction being sparse in pearlite or ferrite. This was not seen in either of the air cooled treatments. Quantitative phase fraction over multiple micrographs showed approximately 10% more pearlite present in the furnace cooled sample, 50% area fraction pearlite, than the air cooled samples, 40% area fraction pearlite. This is contrary to the expectation that samples which are slowly cooled contain more ferrite than those cooled more rapidly which should contain more pearlite. All samples showed distinct precipitates with a cuboidal morphology that was likely titanium nitride.

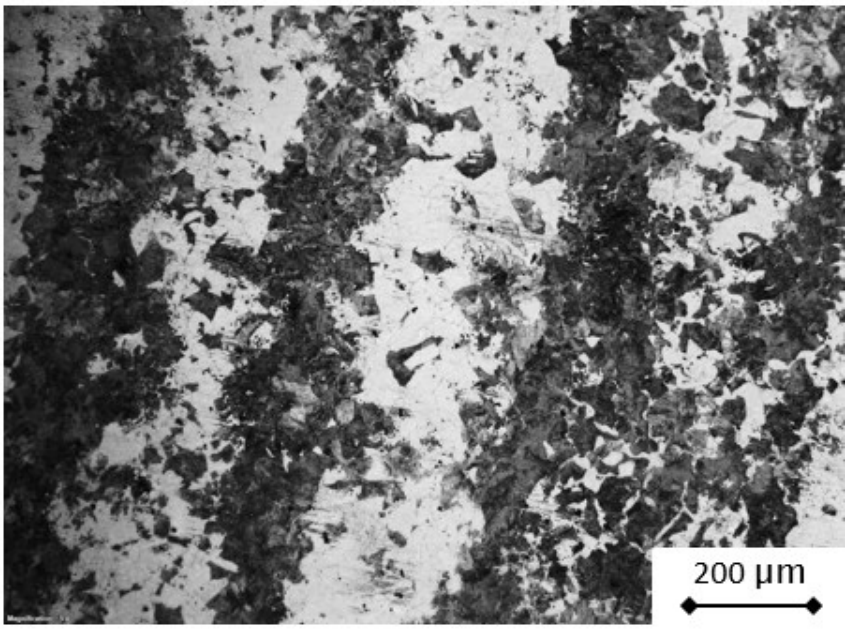

Figure 4.37: Furnace Cooled L80 Long Bar Sample with Banded F-P Structure

4.3.2.2 Long Bar Shear Velocity and Microstructure/Hardness

In order to better demonstrate the relationship between microstructure and shear velocity the slowly cooled samples can be ordered based on increasing pearlite content rather than increasing cooling rate, since the FC samples had the greatest pearlite content. It is difficult to determine the phase fraction of martensite or bainite in the more rapidly cooled samples so they remain ordered by increasing expected cooling rate in Figure 4.38. The error bars now represent standard deviation in the samples tested rather than instrument error, as shown previously.

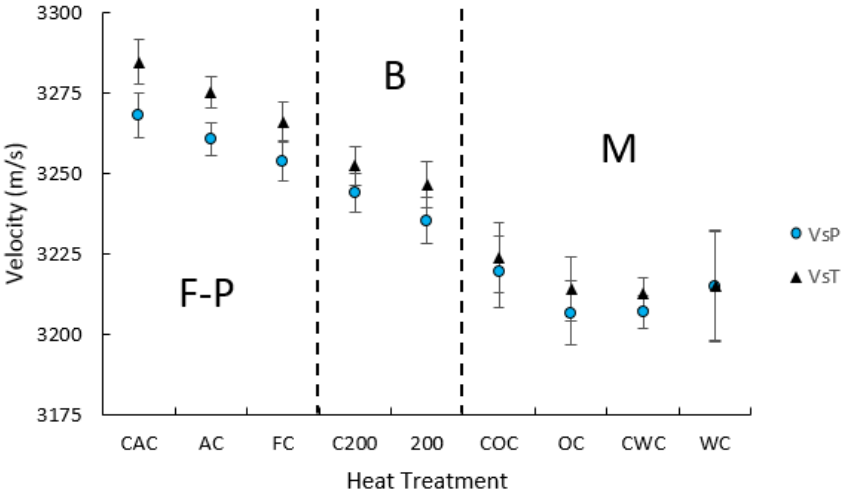

Figure 4.38: L80 Long Bar Shear Velocities vs. Heat Treatment

Both shear velocities show a decrease from ferrite-pearlite through bainite and into the martensitic structures. It is hard to differentiate between the martensitic structures in a quantitative manner from the optical micrographs. Hardness was then used as a manner to quantify the difference in between the samples. The variation in ultrasonic velocity with hardness in the long bar samples is shown in Figure 4.39.

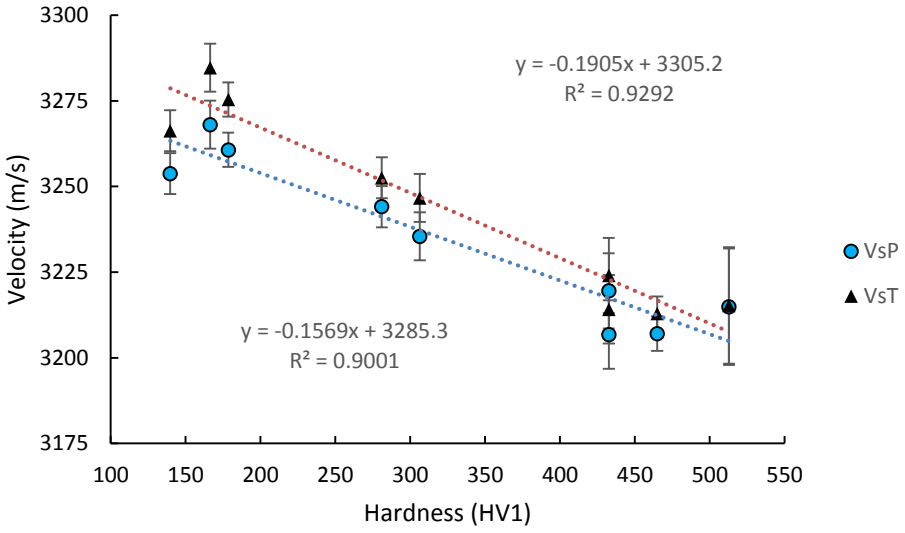

Figure 4.39: Ultrasonic Shear Wave Velocities vs. Hardness for L80 Long Bars

As with the small bars, the hardness values for each structure are grouped together, with the hardest samples being martensite followed by bainite and finally ferrite-pearlite. The martensitic samples are also all above 400 HV, which is the manufacturer provided hardness for a 90% martensite structure [104]. The quenched samples then all contain between 90 and 100% martensite. Linear trends were found between the hardness and both shear velocities in the long bars.

$$VsT = -0.1905(HV) + 3305.2 \quad (4.2)$$

$$VsP = -0.1569(HV) + 3285.3 \quad (4.3)$$

Both trends fit well with the experimental data, R^2>0.9, as the samples change from ferrite-pearlite to bainite to martensite. Neither trend accurately shows the change between martensitic structures at high hardness (>400 HV). Since both parallel and transverse readings were taken on the long bar samples, the birefringence can also be compared with the hardness and heat treatment as seen in Figure 4.40.

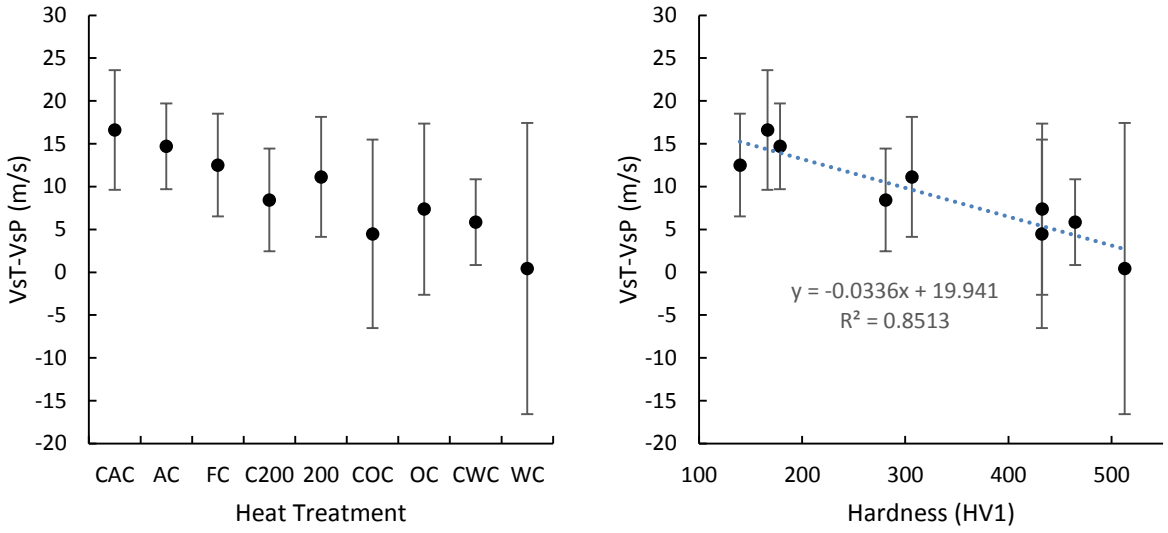

(A) (B)

Figure 4.40: L80 Long Bar Shear Wave Birefringence vs. (A) Heat Treatment and (B) Hardness

The birefringence relates to the microstructures and hardness in a similar manner to the shear velocities. Both decrease as hardness increases; the birefringence also shows an approximately linear trend with hardness. Note, however, the large scatter for the highest hardness value. The linear trend is given in the following, where V_B is the shear wave velocity birefringence.

$$V_B = -0.0336(HV) + 19.941 \tag{4.4}$$

The trend found in the birefringence has a lower R^2 value (0.85) than those found from both shear velocities. The birefringence is then, along with the shear velocities, a useful tool in differentiating between microstructures. The birefringence in the calculated velocities found in Section 2.2 are almost identical in ferrite-pearlite and martensite; however, as discussed above the F-P in the tested samples varies from that used to calculate the velocities. The shear wave velocities in the heat treated samples, shown as points, are shown in Figure 4.41 with the calculated J=1 velocities, shown as lines.

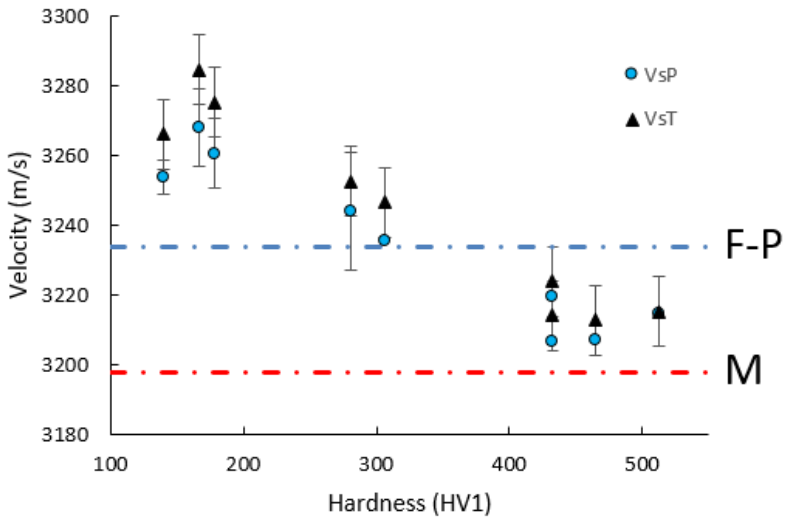

Figure 4.41: Ultrasonic Shear Wave Long Bar Velocities vs Hardness and Calculated Shear Velocities (F-P and M) Ferrite Calculated Velocity = 3340 m/s

The ferrite-pearlite velocities were further from the calculated values than those for the small bars. The velocity of the ferrite-pearlite samples was shown to decrease as pearlite content increased in Figure 4.38. It is possible that the ferrite-pearlite mix used in the calculated velocities had more pearlite than in the tested samples since the velocity is lower. This would also be the case when considering the birefringence. The calculated birefringence in ferrite could be as high as 550 m/s. If the experimental samples had a higher ferrite content than those used in the calculations, the birefringence could move away from the F-P value and closer to the ferrite values, which they did, increasing to 17 m/s which is almost three times the maximum calculated birefringence of ferrite-pearlite.

4.3.2.3 Long Bar Longitudinal Velocity

As with the short bars, the longitudinal velocities did not show a significant trend with microstructure. With the exception of the water cooled sample, which had significant variation in longitudinal velocity within its samples, the samples show consistent velocities across the heat treatments. This is shown in Figure 4.42.

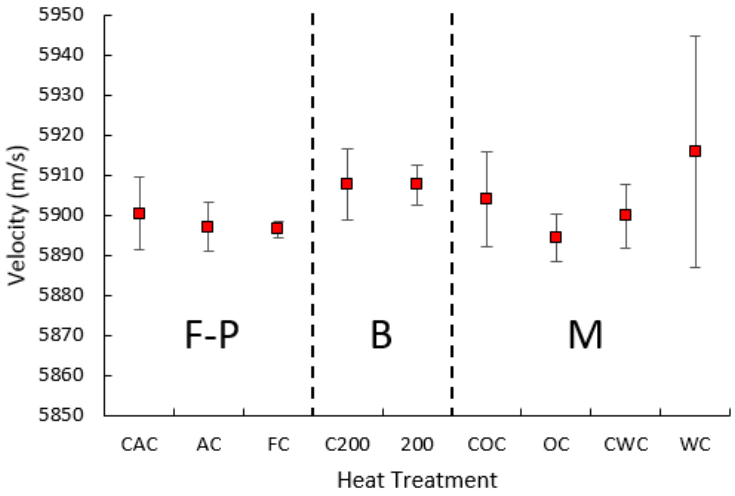

Figure 4.42: Longitudinal Velocity in Long Bars vs. Heat Treatment

These velocities agree with the calculated values from Section 2.2 for longitudinal velocities (V_1). The martensite samples are within the error for the entire range of martensite velocities, with the exception of the oil quenched sample which falls less than 2 m/s short of the calculated minimum. The bainitic samples are almost exactly between the calculated ferrite-pearlite and martensite samples, as shown in Figure 4.43, where the lines are again the calculated J=1 (randomly oriented) values and the points are the experimental values.

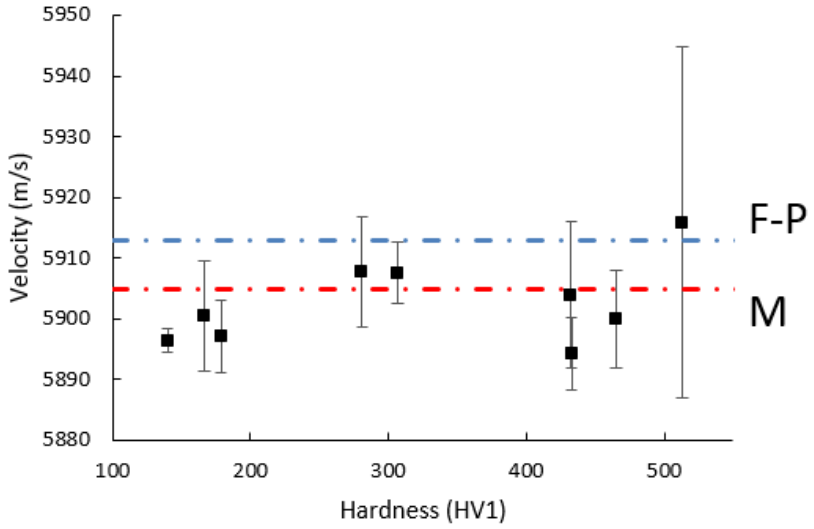

Figure 4.43: L80 Long Bar Longitudinal Velocity vs. Hardness and Calculated V_1 (F-P and M) Ferrite V_1=6047

The ferrite-pearlite samples had velocities all below the calculated V_1 range. It is possible that the differences between the ferrite-pearlite in the experimental samples and the ferrite-pearlite used to

obtain elastic constants for calculations discussed previously could account for this difference. Longitudinal velocity remains a poor indicator of microstructure in the long bars, due to the small difference between longitudinal velocities for the various structures present.

4.3.2.4 Long Bar Ultrasonic Attenuation

Unlike the small bars (Figure 4.35), the ultrasonic attenuation in the long bars does show a relationship with the hardness, as shown in Figure 4.44. This is likely the result of multiple tests being performed which averaged the effects of good and bad coupling. This reduced the effect of the couplant on the attenuation readings enough that the effect of structure changes could be seen, which could not be in the small bar tests.

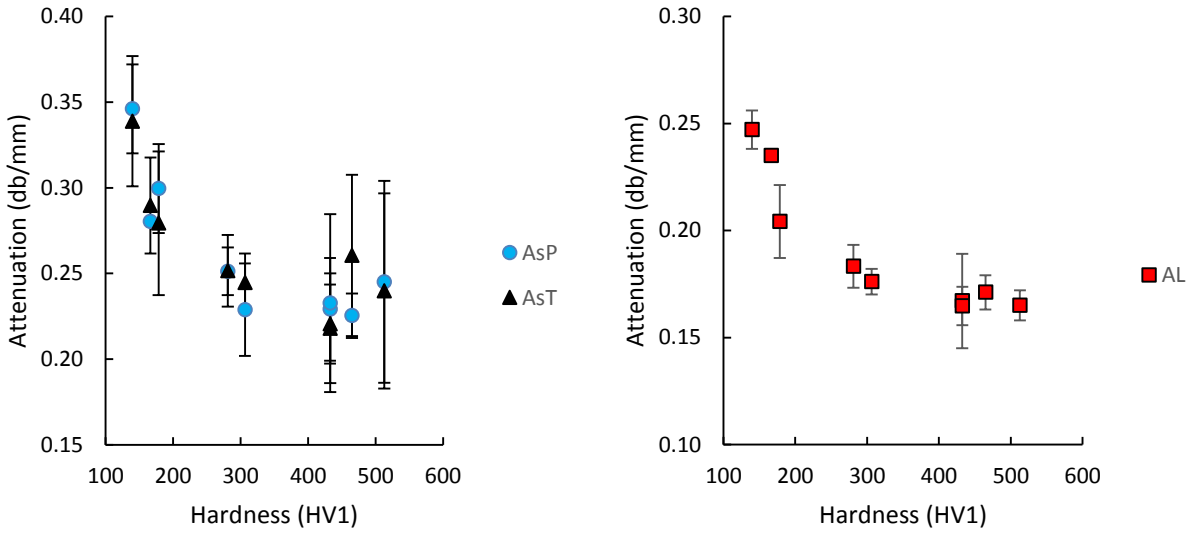

(A) (B)

Figure 4.44: L80 Long Bar (A) Shear and (B) Longitudinal Attenuation vs. Hardness

The trend is not linear for the attenuations, but appears to decrease as the hardness increases in the F-P and B samples then level off in the martensite samples. The ferrite-pearlite samples have much higher attenuations than the bainite or martensite. The bainite samples have higher attenuations than the martensitic, but the difference is much less and the attenuations are within error of the martensitic shear attenuations. There is not a significant change in the martensitic longitudinal attenuations; however, the large deviation in martensite shear attenuations makes correlation with the shear values.

In the L80 skelp through thickness trials, Section 4.1.4.4, the shear wave attenuation was shown to be more sensitive to domain size than the longitudinal attenuation. A similar phenomena is not seen in Figure 4.45 when comparing the martensite colony size to the ultrasonic attenuation.

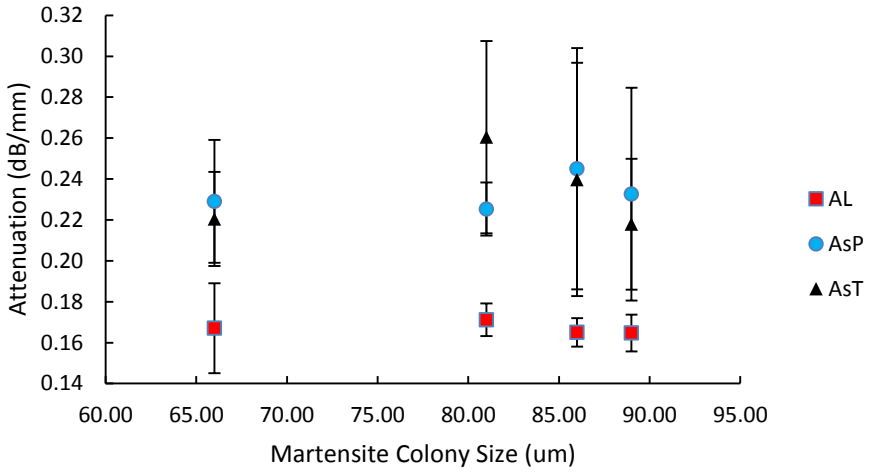

Figure 4.45: L80 Ultrasonic Attenuation vs. Martensite Colony Size

Neither the longitudinal nor the shear attenuations appear to change significantly with colony size (see Section 3.5.4 for metallography procedure). While previous work shows a relation between grain size and attenuation [64] [65] [67], the literature did not consider colony size. It is likely that the size of the martensite laths is relatively constant within the samples, since the attenuation does not change significantly for different martensitic samples. The difference in martensite colony size indicates that something is changing between the martensite samples that is not reflected in their hardness. Further information is required about these samples to explain these differences.

These trends show longitudinal attenuation to be a good indicator of microstructure when a significant number of readings is taken. There is less variation between longitudinal readings due to more consistent couplant effects than possible in the shear case, allowing phases to be more easily distinguished. The shear attenuations are an indicator of phase difference between F-P and the other samples, but variations in the martensitic samples cause differentiation between bainite and martensite to be impossible. The shear attenuations also show much more scatter than the longitudinal attenuations, probably due to couplant effects.

4.3.3 L80 Tensile Tests and Ultrasonic Properties

Since the microstructures were difficult to quantify, tensile tests were used to gain more information about each sample. The yield stress (YS), ultimate tensile stress (UTS), Young's modulus (Y), elongation, breaking strain and toughness of each sample were compared with the ultrasonic properties of each sample.

4.3.3.1 YS and UTS

The yield strength and ultimate tensile strength both correlated well with the hardness values obtained from the polished metallographic samples. These correlations are shown in Figure 4.46.

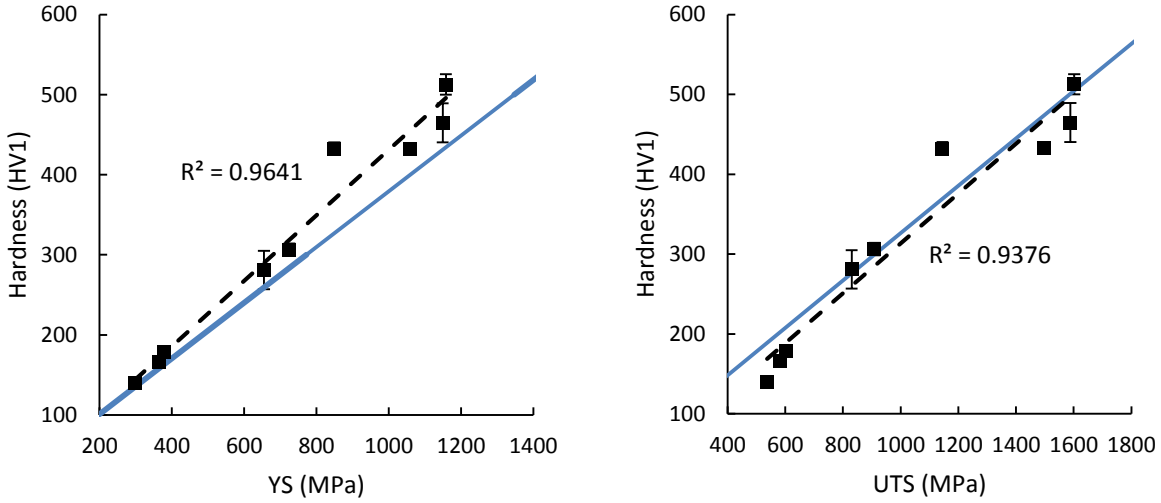

(A) (B)

Figure 4.46: L80 Long Bar Hardness vs (A) YS and (B) UTS (Points are Experimental Data, Dashed Line Is The Experimental Trend and Solid Line The Trend From Literature)

The increase in hardness with yield strength is well documented [105] [106] [101] and confirms that hardness, YS and UTS measurements relate in a reasonable manner. Both UTS and YS show linear trends with hardness which have R^2 values above 0.9.

$$YS = 2.446(HV) - 54.6 \quad (4.5)$$

$$UTS = 3.201(HV) - 3.707 \quad (4.6)$$

These relations resemble those taken from an aggregate of different steels found in the literature [101].

$$YS = 2.876(HV) - 90.7 \quad (4.7)$$

$$UTS = 3.737(HV) - 99.8 \quad (4.8)$$

Neither the literature equations nor those from the experimental data predict the COC (~450 HV1) YS or UTS accurately. Equations 4.7 and 4.8 consistently predicted higher YS than that obtained experimentally, while predicting lower UTS for the F-P samples and higher UTS for the B and M samples. Both the COC and WC samples had YS and UTS outside the 102 MPa and 112 MPa error of equations 4.7 and 4.8. Both were significantly weaker (lower YS and UTS) than predicted. The YS and UTS also correlate well with the microstructures. The ferrite-pearlite samples have low hardness, YS and UTS, while the bainitic samples have higher values and the martensitic even higher values. The COC sample, which is the slowest cooled of the martensitic samples, shows a reduced YS and UTS compared with the other martensitic samples, but a similar hardness. The

COC sample also has a different lath colony size, 66 µm, compared with the other martensitic samples, 81-89 µm. The difference in colony size shows a microstructural difference between the COC sample and the other quenched samples. If the individual lath size could be measured reliably, it is possible that the lath size would also be different from the other samples.

Similar trends were present in the velocity relations with the YS and the UTS as were seen with the velocity and hardness. The shear velocities both drop significantly as the YS increases, while the longitudinal velocity remains roughly constant. This makes sense since the hardness and YS correlate so well together. The relationship between UTS and velocity and YS and velocity are almost identical. The YS velocity relations are shown in Figure 4.47.

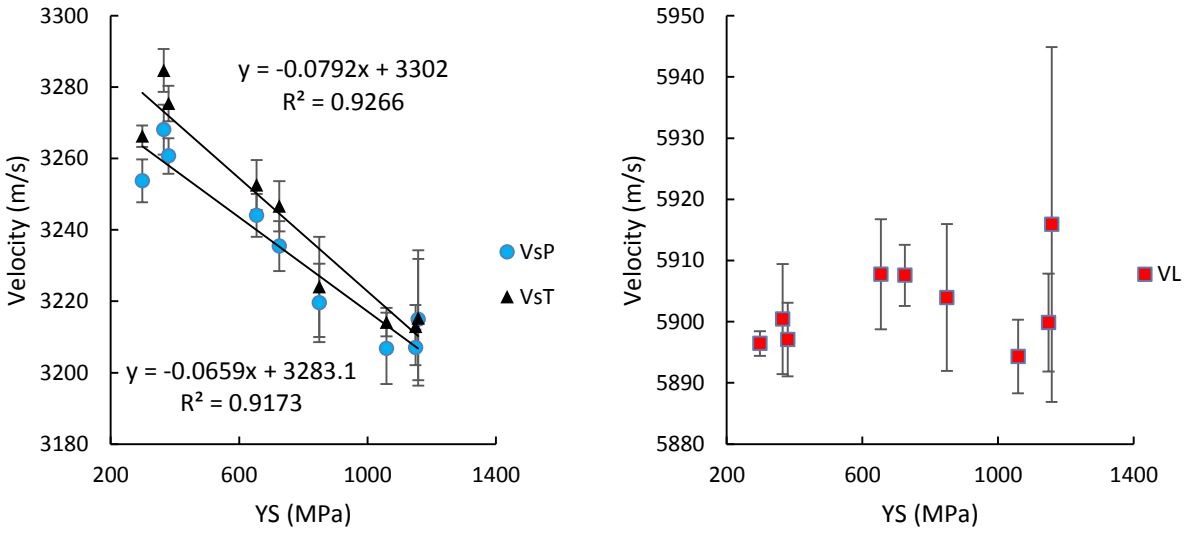

(A) (B)

Figure 4.47: Ultrasonic (A) Shear and (B) Longitudinal Velocity and YS

Linear trends were fit between the shear velocities and the YS.

$$VsT = -0.0792(YS) + 3302.0 \quad (4.9)$$

$$VsP = -0.0659(YS) + 3283.1 \quad (4.10)$$

The linear trends fit the data well with R^2 values greater than 0.9; however, the COC and FC samples are not predicted well. The COC sample, with a YS of 750 MPa, again appears different from the other martensitic samples in a manner not seen when comparing velocity and hardness. The shear velocities are higher in the COC sample than the other martensitic which, with the reduced YS, further supports the trend of reducing velocity with increasing strength. The increased velocity and decreased strength place the COC sample between the bainitic and other martensitic samples. The trends predict a higher YS for the COC sample than the value measured, as do the trends for hardness. The COC longitudinal velocity also places it near the bainitic samples but, as

is the case with longitudinal velocity, the samples are almost all within the error range of one another making differentiation difficult. The FC samples have lower hardness and YS than predicted from their velocity and phase fraction. It is possible that the banding in its microstructure resulted in more hardness tests being performed in the ferrite regions than pearlite, reducing the average. It is also possible that the banding decreased the YS and UTS relative to the more homogeneously mixed CAC and AC samples. A similar trend can be seen in the shear velocity birefringence (FC=298 MPa) shown in Figure 4.48.

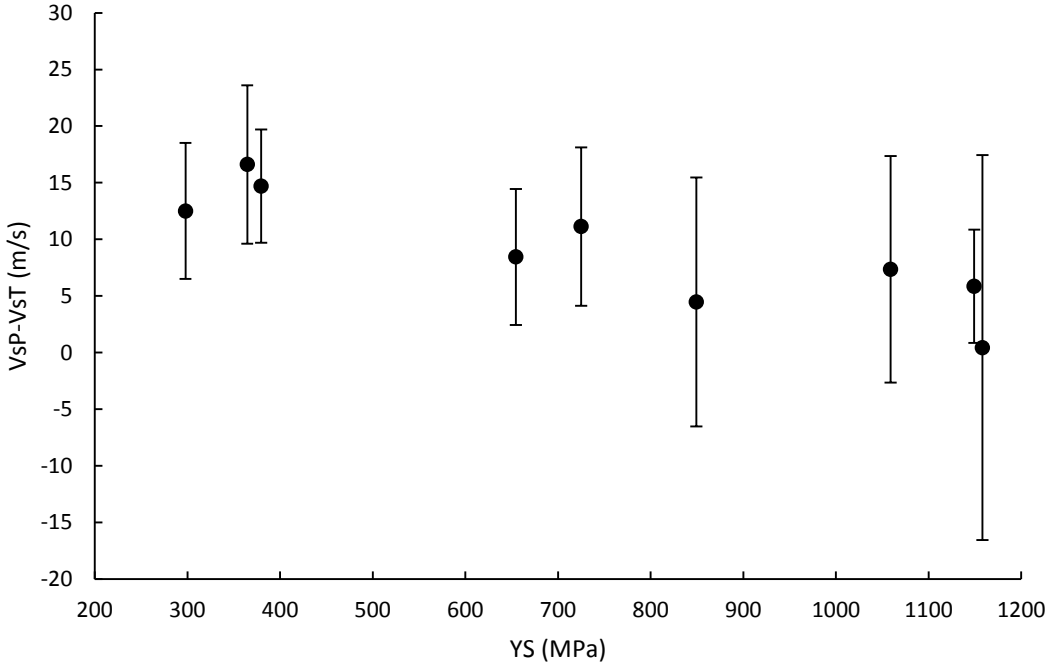

Figure 4.48: Shear Velocity Birefringence vs. YS

Since the birefringence was shown both in the literature and Section 4.1.4.3 to correlate to residual stress and microstrain in the sample, it is likely that the strain in the COC sample is not different from that found in the other martensitic samples and that some other microstructural effect accounts for the strength and velocity differences.

The ultrasonic attenuation correlates with the strength of each sample. As the strength increases the attenuation appears to decrease until the martensitic samples (800 MPa). This is particularly apparent in the longitudinal attenuation (Figure 4.49).

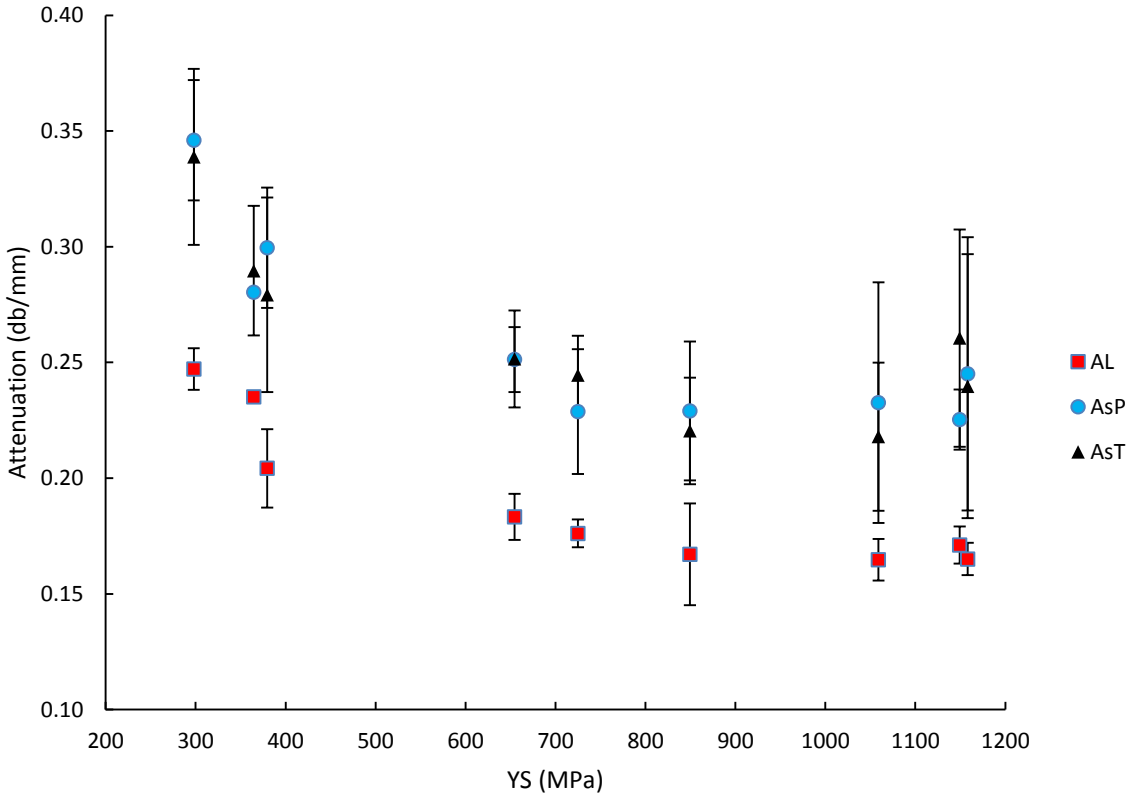

Figure 4.49: YS and Ultrasonic Attenuation

The shear attenuations in the martensitic samples show significant scatter in their attenuations and do not appear to vary significantly. The longitudinal attenuation shows a similar trend as found when compared with hardness, with the largest attenuations found in the F-P samples and the lowest in the martensite. The bainite and martensite samples have similar attenuations, while the F-P samples attenuate the beam more. The attenuation then appears to be a good indicator of strength, and thus structure, at low strengths but much less so at high strengths since the attenuation change is much lower.

4.3.3.2 Young's Modulus

The Young's Modulus did not correlate well with the ultrasonic velocities or attenuations. The shear velocities were scattered with no discernable trend, as shown in Figure 4.50, where the blue points are the ferrite-pearlite samples, the orange points are the bainite samples and the black points are martensite samples.

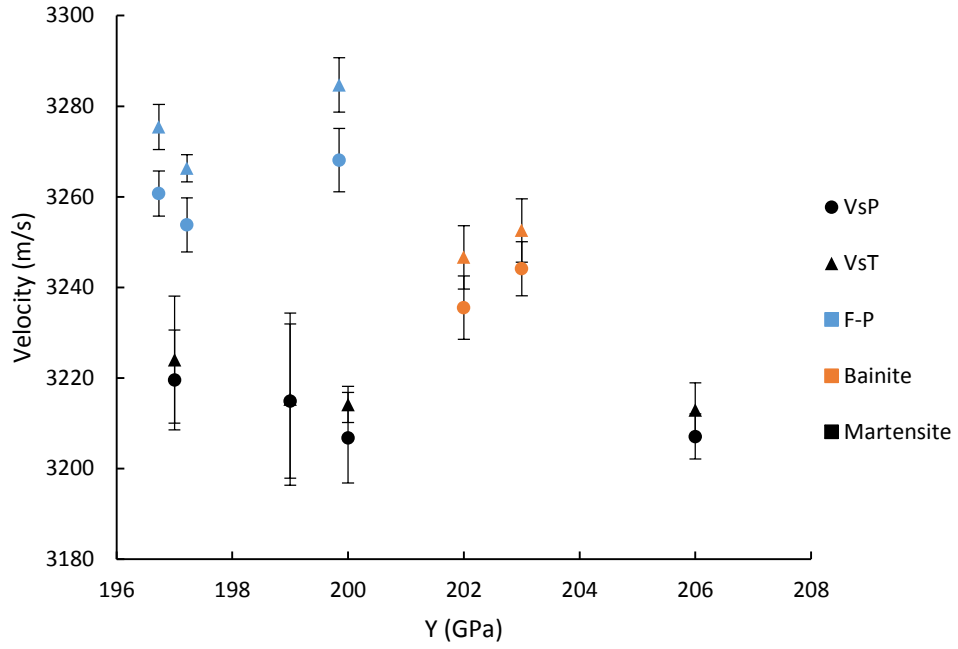

Figure 4.50: Shear Velocity vs. Young's Modulus (Y)

Even if the shear velocities are separated based on structure, no trends are apparent. There does not appear to be a relation between measured Y and measured shear velocity. Similarly, no trends are seen with the longitudinal velocities (Figure 4.51).

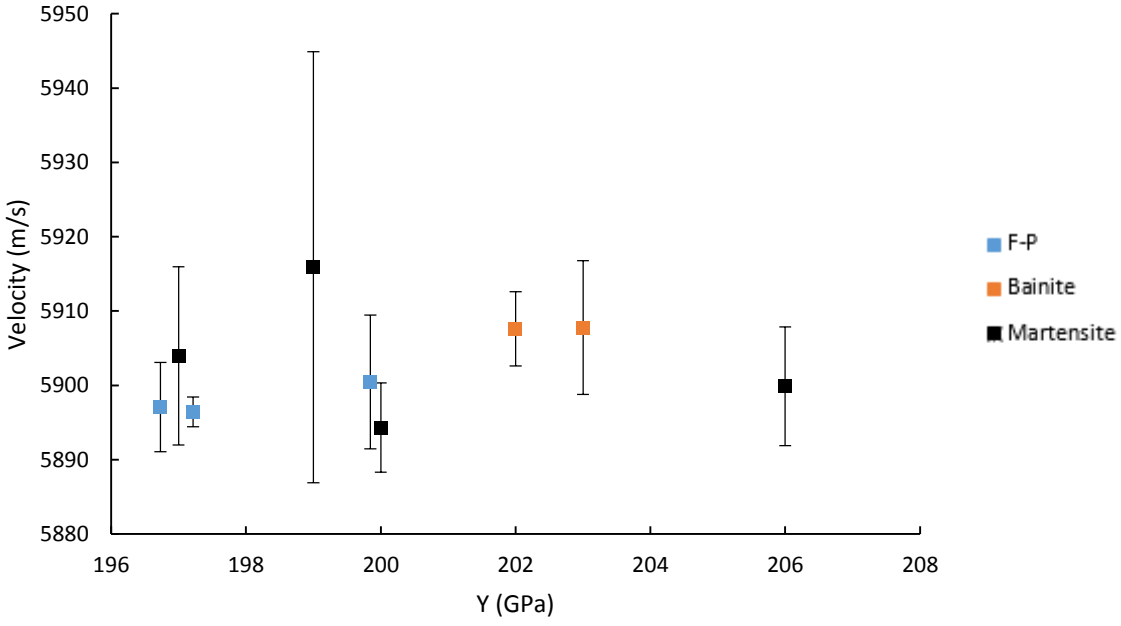

Figure 4.51: Longitudinal Velocity and Young's Modulus (Y)

According to Equation 2.6, the velocity is proportional to the square root of the Young's modulus.

$$V_o = \sqrt{\frac{Y}{\rho}} \tag{2.6}$$

This relation is not seen experimentally; however, Equation 2.1 is the generalized velocity of sound and the behaviour of the longitudinal and shear waves may be affected by the density and Poisson's ratio, as described in Section 2.3 and quantified in Equation 2.7 and 2.8.

$$V_s = \sqrt{\frac{Y}{2\rho(1-\sigma^2)}} \tag{2.7}$$

$$V_L = \sqrt{\frac{Y(1-\sigma)}{\rho(1+\sigma)(1-2\sigma)}} \tag{2.8}$$

The Poisson's ratios and densities from the literature [82], shown in Table 2.1, along with the experimental Young's moduli, were used to compare calculated values for each sample with those obtained experimentally (Figure 4.52).

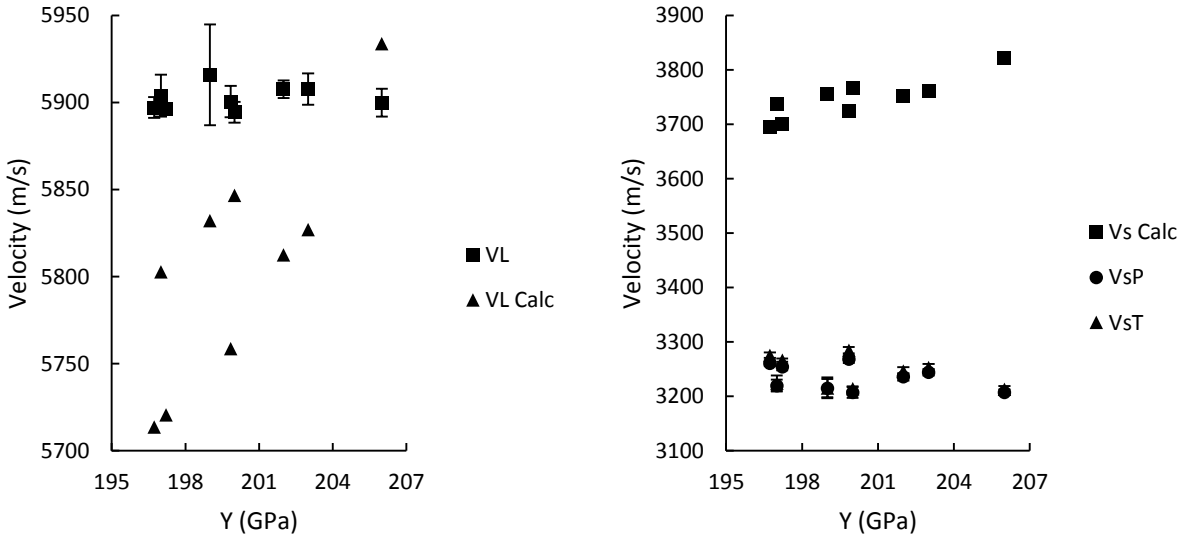

(A) (B)

Figure 4.52: Experimental and Calculated Velocities Using Young's Moduli

The difference between the maximum and minimum Young's modulus is less than 10 GPa; however, when Equations 2.7 and 2.8 are used for longitudinal and shear waves, differences of 220 m/s and 126 m/s respectively are found across this range. This does not represent the velocities found experimentally which vary by less than 100 m/s for both longitudinal and shear waves. The velocity calculations done in Section 2.1 using the Christoffel equation and the stiffness tensor were shown in Figure 4.41 and Figure 4.43 to agree well with the experimental velocities. It is

then likely that Equations 2.7 and 2.8 are insufficient to describe ultrasonic behaviour in steel because it is anisotropic, and the full stiffness tensor is required for accurate velocity calculations.

The attenuation is quite scattered with respect to Young's modulus. There does not appear to be a relation between Y and attenuation, as shown in Figure 4.53.

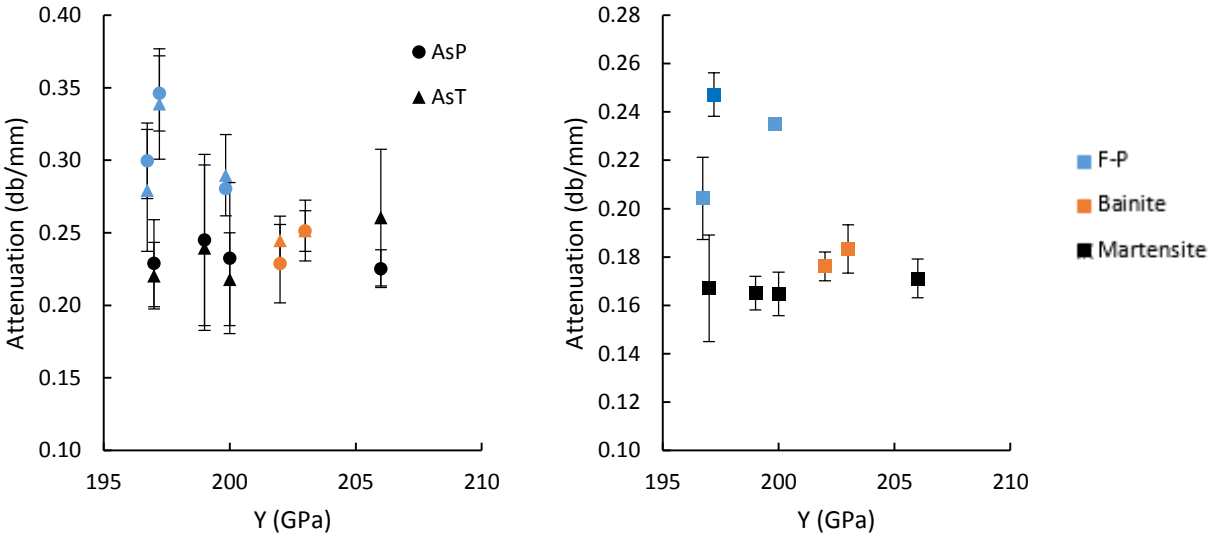

(A) (B)

Figure 4.53: L80 (A) Shear and (B) Longitudinal Attenuation vs. Young's Modulus

There may be a decrease in attenuation as Y increases but the trends are not conclusive. There are high and low attenuations at near identical Y values from 195-200 GPa for both the shear and longitudinal attenuations. The increased attenuations at low Y occur for samples which have F-P structures. As the attenuation was shown to relate to structure previously, Y then has no apparent effect on attenuation.

4.3.3.3 Strain

The elongation and the breaking strains were compared for each heat treatment. Both values were extremely similar in each case, with the ferrite-pearlite samples having the closest correlation with the values only 0.26% apart, followed by bainite with 0.42% separation and martensite with 0.69% separation on average. The breaking strain and elongation for each heat treatment is shown in Figure 4.54.

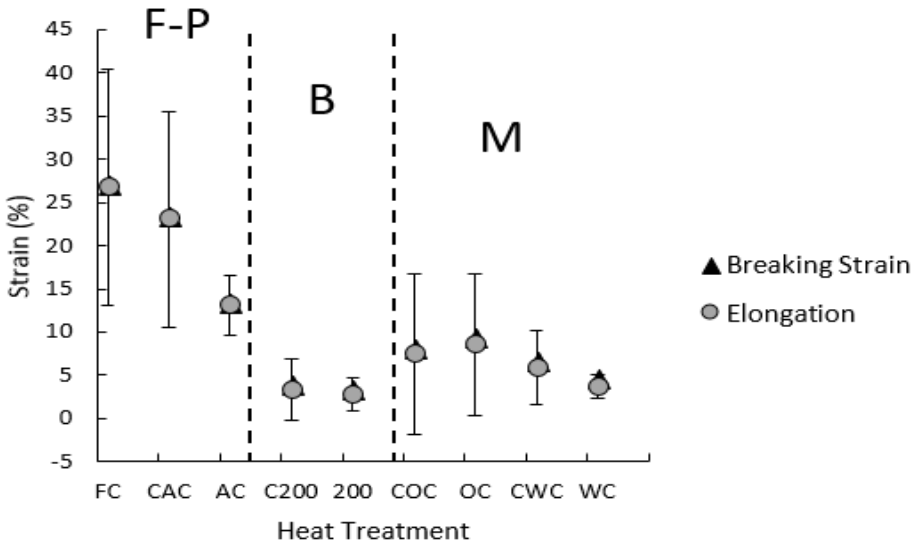

Figure 4.54: Breaking Strain and Elongation for L80 Long Bars

The F-P samples have the highest elongation, ~13-27%, followed by the martensitic samples, ~4-9% and then the bainitic samples, ~3%. For the other properties, i.e., Y, YS and UTS, the bainite tended to have values between those of martensite and F-P. The trend in the elongations with heat treatment would predict the bainite to have an elongation in the 10-15% range. This is further reinforced by comparing the elongation with the ultrasonic shear velocities as shown in Figure 4.55A.

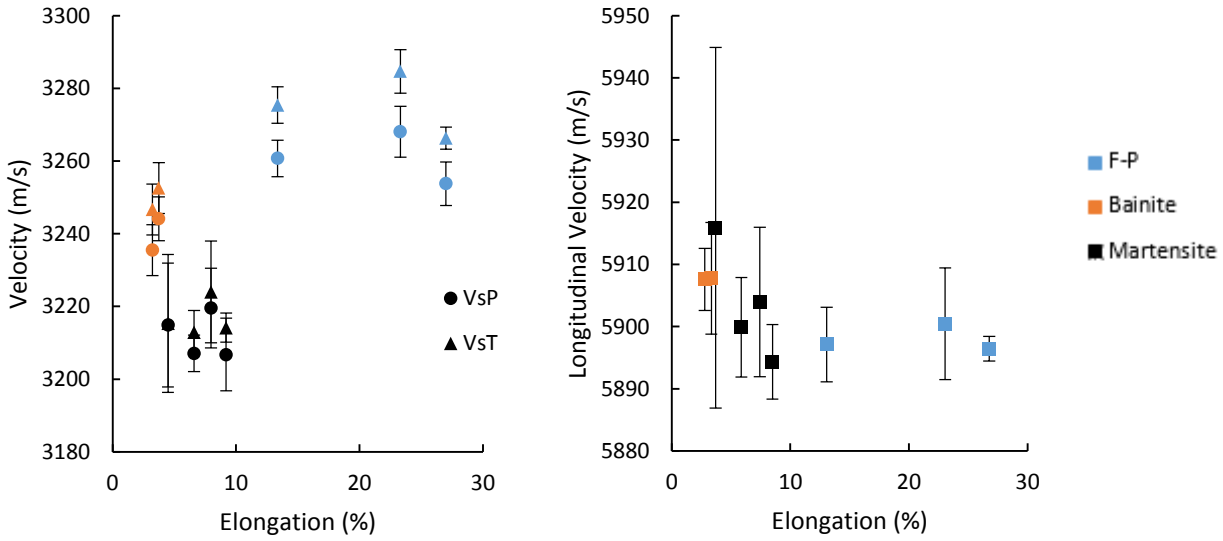

(A) (B)

Figure 4.55: Ultrasonic Velocity vs. Elongation

The bainitic values do, however, fit well with the longitudinal velocities shown in Figure 4.55B, where there appears to be a relationship between the velocity and elongation. This is the strongest relationship the longitudinal velocity shows to a material property gathered in this investigation. The error in longitudinal velocity, however, still makes it difficult to confidently predict elongation.

While the velocities do not show strong relations with the elongation, both the shear and longitudinal attenuation show an increase as the elongation increases, as shown in Figure 4.56.

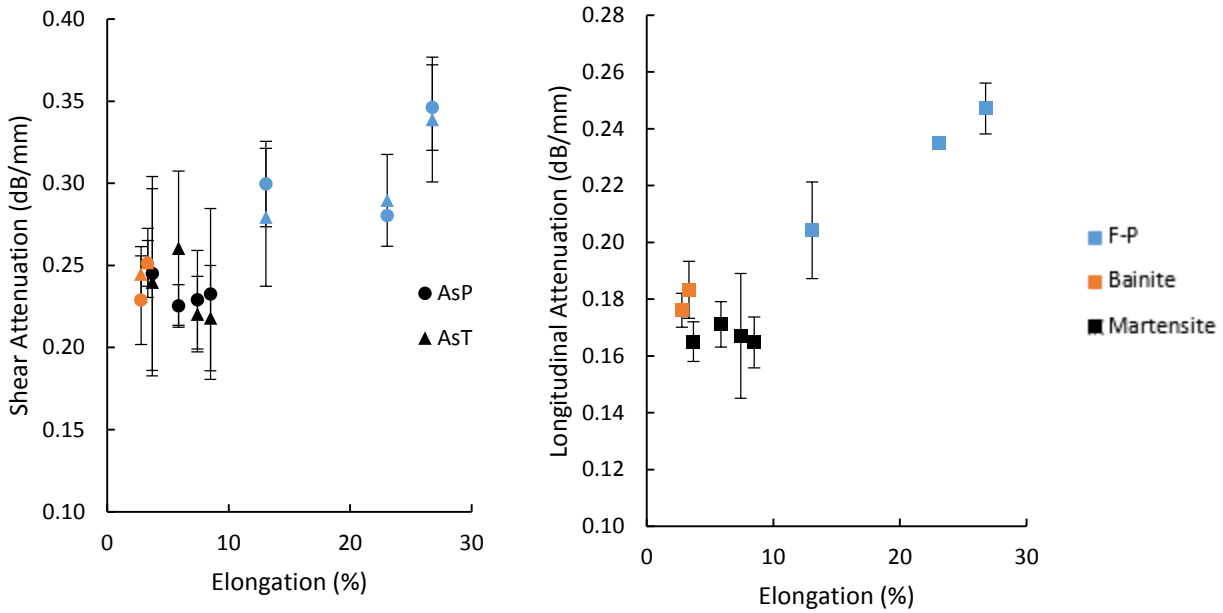

(A) (B)

Figure 4.56: Ultrasonic Attenuation and Elongation

It is possible that the bainitic samples have some embrittlement, possibly related to the processing being performed in two steps, a 200ºC hot oil quench for three minutes followed by a water quenched, rather than a single step like the other samples. Bohlooli found bainite to have higher elongations than ferrite in a 4340 steel [107]. His dual phase microstructure varied from 37-51% ferrite and had elongations from 25-22%. The birefringence was compared to the elongation in Figure 4.57 to see if there was greater residual stress in the bainitic samples compared to the ferrite-pearlite and martensite samples [52].

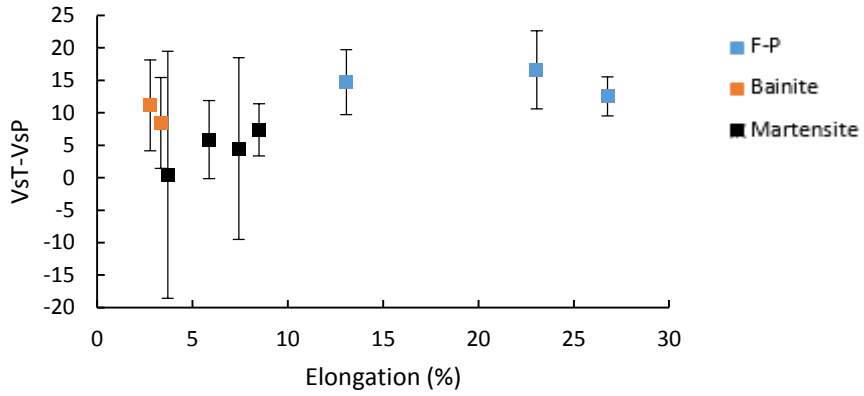

Figure 4.57: Shear Velocity Birefringence vs. Elongation

The bainite samples have birefringence between that of the martensite and ferrite-pearlite samples. There is then not an increase in residual stress in the bainite samples relative to the martensite. It is possible that the bainitic structure in the samples may contain some martensite which is embrittling them. If the transformation from austenite to bainite was not completed in the 200ºC oil quench, the remaining austenite would have transformed to martensite on water quenching. This could explain why the COC sample had similar YS to the bainite samples, as well as the uncharacteristically low elongation of the bainite samples. The presence of phosphorus has been shown to embrittle lower bainite [108]; however, phosphorous content in the experimental bainitic samples was lower than those which showed embrittlement in literature.

4.3.3.4 Toughness

The toughness obtained from the tensile stress-strain curve is closely related to the elongation, as shown in Figure 4.58.

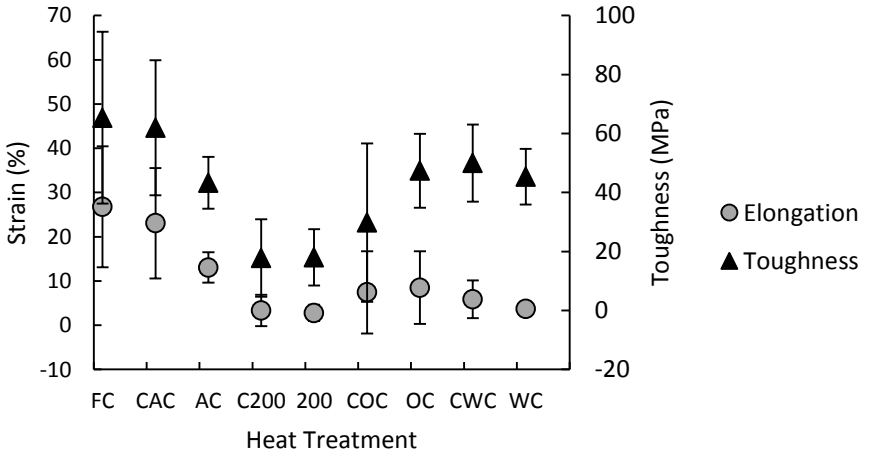

Figure 4.58: L80 Heat Treatment Toughness and Elongation vs. Heat Treatment

The toughness values show more overlap between martensite and F-P than the elongations but the bainite retains uncharacteristically low values, likely due to some form of embrittlement as discussed earlier. The velocities are also compared with the toughness in Figure 4.59.

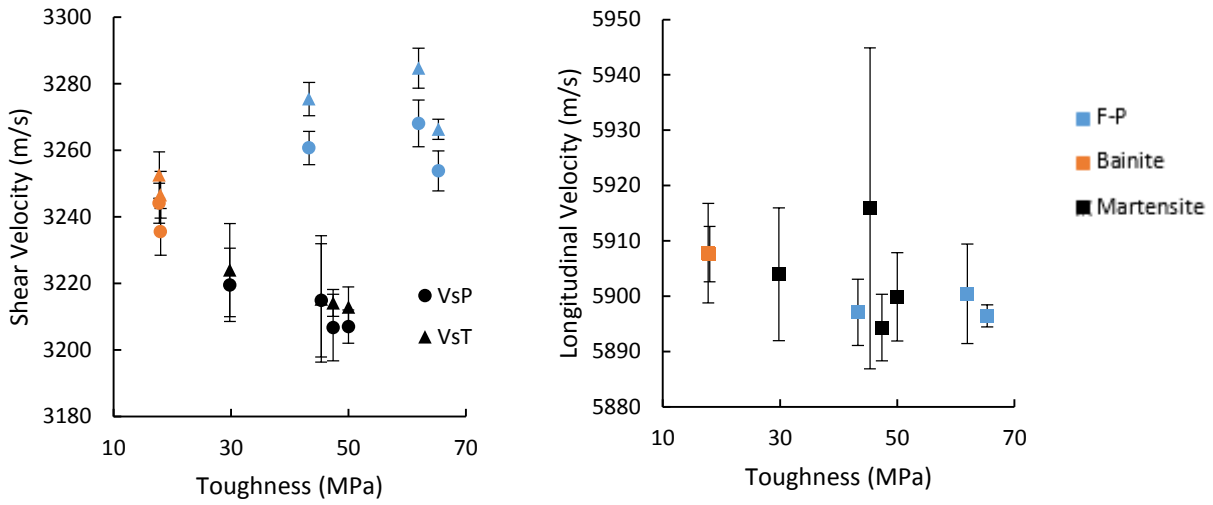

(A) (B)

Figure 4.59: Ultrasonic Velocity vs. Toughness

The longitudinal velocities show a trend with the toughness, as did the elongation. The shear values appear quite scattered unless the individual structures are considered, in which case the shear velocity may drop as the toughness increases in martensite. The amount of scatter makes this difficult to conclude confidently and the shear velocity does not show a similar pattern in the other microstructures.

The relationship between shear velocity birefringence and toughness was analyzed to see if the bainitic samples agreed with the trend in the other samples (Figure 4.60).

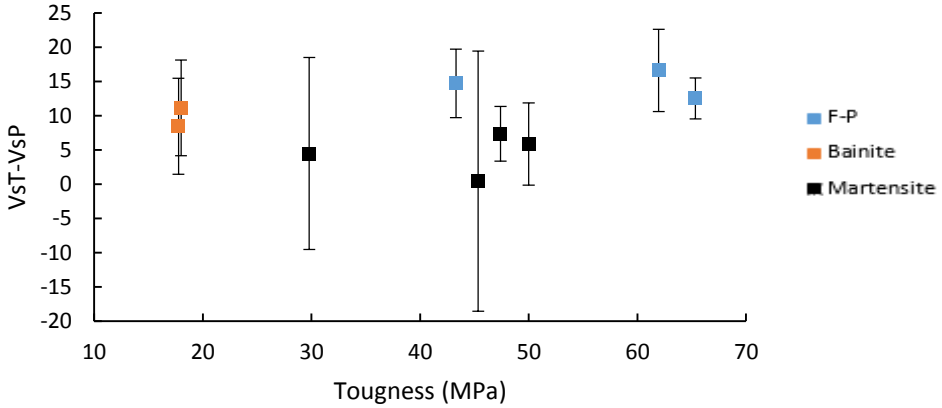

Figure 4.60: Shear Birefringence vs. Toughness

The bainite samples are the weakest of those tested and do not fit the trend as well. The birefringence trend suggests that the bainitic samples should have higher toughness than measured.

The attenuation showed an increase as the toughness increased. The bainitic values again appear to be lower than the trend in Figure 4.61 suggests.

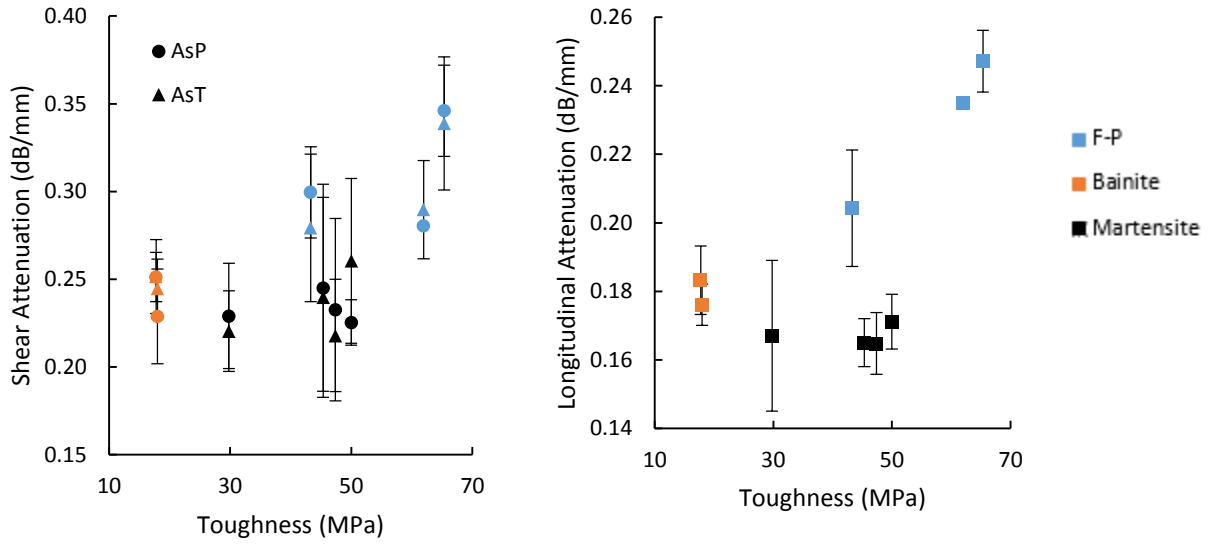

(A) (B)

Figure 4.61: Ultrasonic Attenuation and Toughness

The shear and longitudinal attenuation both increase with toughness in the martensite and F-P samples. The strong relationship between ultrasonic velocity and strength/hardness suggests that the measured velocity of the bainite samples was accurate. The bainite samples do not fit the trends seen in ferrite-pearlite or martensite samples for ultrasonic velocity or attenuation with toughness or elongation. Literature values for bainite elongation are much higher than those found in this work [107]. It is then likely that the bainite samples are embrittled, but not by a characteristic to which the ultrasonic properties are sensitive.

4.3.4 L80 Microstructure Variation Summary

The ultrasonic shear velocity decreased as sample structure changed from ferrite-pearlite (F-P) to bainite (B) and then to martensite (M). This corresponded to an increase in sample hardness, which increased linearly with decreasing velocity. The longitudinal velocity did not appear to change significantly with structure. This result agreed with the small difference between F-P and M longitudinal velocities calculated in Section 2.2. The longitudinal and shear attenuation also decreased as the structure changed and hardness increased. The attenuation reached a minimum with the martensite samples and did not continue decreasing as their hardness increased.

The yield stress (YS) and ultimate tensile stress (UTS) both increased with increasing hardness. Ultrasonic shear velocities also varied linearly with the YS and UTS. Attenuation showed similar behavior when compared with YS, UTS and hardness. The velocities did not change with Young's modulus (Y), as might be expected from equations in the literature. This is likely due to the anisotropic nature of steel, which requires the full stiffness tensor to calculate velocities which agreed with experimental work. Elongation and fracture strain increased as ultrasonic velocity and attenuation increased; however, the bainitic samples appeared embrittled as they had lower values than the martensite samples. The attenuation increased with increasing toughness, but not velocity, although again the values for bainite were lower than expected.

4.4 Industrial UT

Two steels, 4130 and 5160, were chosen to heat treat and ultrasonically test with industrial equipment other than that used in the laboratory. Testing was done to see if similar trends to those found in this work existed for other steels and if the same trends could be detected with equipment and procedures already in use in industry. The 4130 was chosen as it is an alternate steel which can be processed into an L80 grade, while the 5160 is a higher carbon steel that was available as a processed part which was not rolled skelp like the other steels tested.

4.4.1 4130 Heat Treated Samples

4130 steel was chosen to heat treat into a variety of microstructures. It has a different composition than the L80 skelp studied previously, but can also be treated and used as an L80 steel [109]. Eight heat treatments were performed, furnace cooled (FC), air cooled (AC), three high temperature holds (H1, H2, H3), water quenched (Q) and two quench and tempers (QT1, QT2). A sample of the as received material (AR) was also analyzed. The heat treatments produced ferrite-pearlite (F-P), martensite (M), tempered martensite (TM) and a bainitic structure (B). The heat treatments performed are detailed in Table 4.5 along with the resultant microstructures obtained.

Table 4.5: 4130 Heat Treatments

	FC	AC	H1	H2	H3	AR	QT1	QT2	Q
Step 1	870°C 1 hr	870°C 1 hr	870°C 1 hr	870°C 1 hr	-	-	870°C 1 hr	870°C 1 hr	870°C 1 hr
Step 2	Furnace Cooled	Air Cooled	770°C 6 hrs	770°C 69 hrs	770°C 16.5 hrs	-	Quench	Quench	Quench
Step 3	-	-	Air Cooled	Air Cooled	Air Cooled	-	650°C 1 hr	205°C 1 hr	-
Microstructure	F-P	F-P	F-P	F-P	F-P	B	TM	TM	M

The normalizing time and temperature were taken from the ASM Handbooks [110]. The high temperature holds were variants of the spheroidizing treatment from the ASM Handbooks, although all treatments produced ferrite-pearlite mixtures and not spheroidized carbides. Representative micrographs from the heat treatments are shown in Figure 4.62.

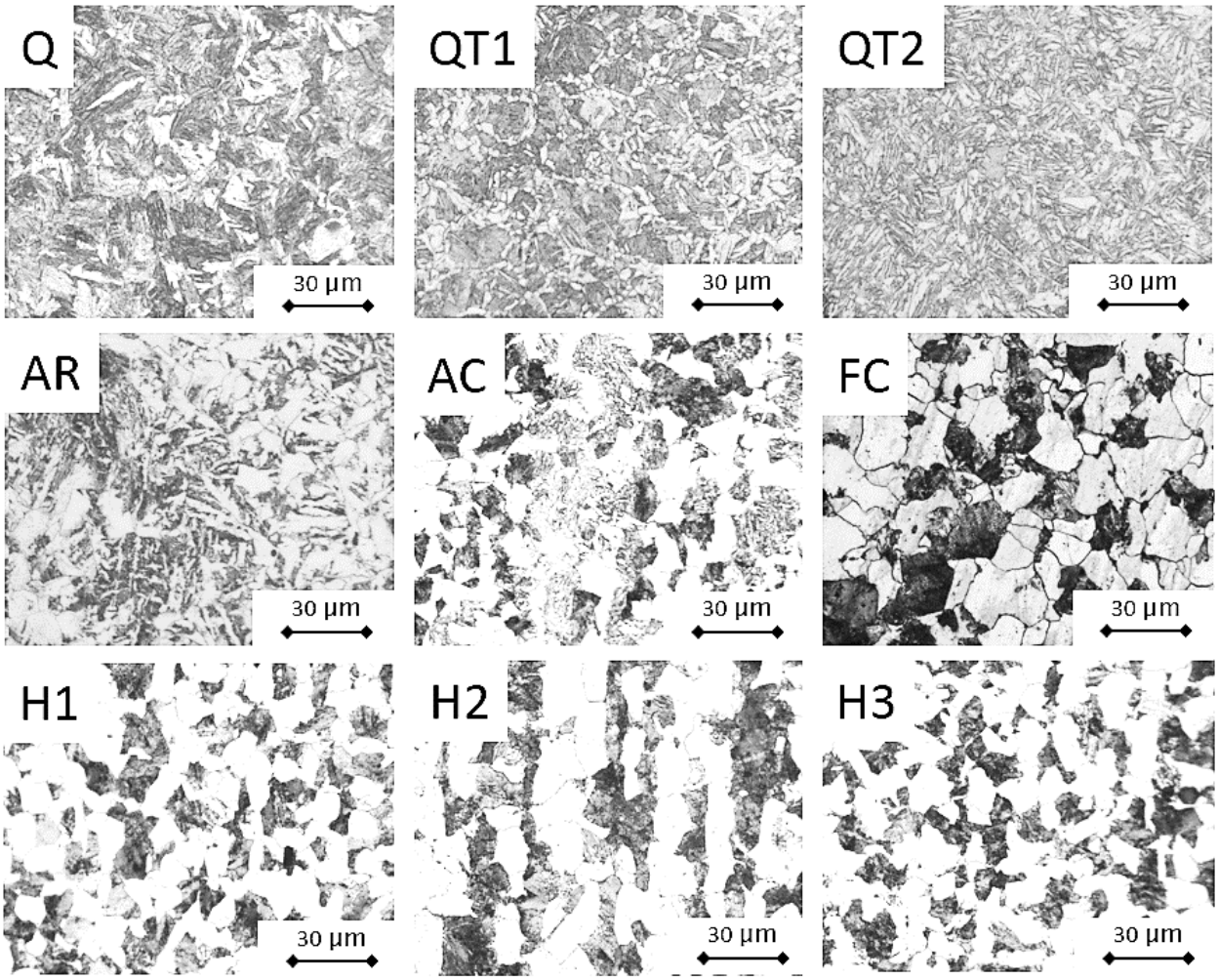

Figure 4.62: 4130 Heat Treated Microstructures

Higher magnification images of the dark areas in the furnace cooled and H1-3 micrographs in Figure 4.62 showed them to contain lamellae characteristic of pearlite. The dark areas in the air cooled sample were then also assumed to be pearlite. The as received structure appears to be either an acicular ferrite structure or possibly a bainitic structure. Since the processing is not known it is difficult to determine the microstructure exactly with optical microscopy. The three high temperature hold (H1-3) samples all qualitatively show similar F-P structures. Micrographs from the surface of these samples show that significant decarburization occurred. This can be seen in Figure 4.63, where the structures no longer show dark pearlite colonies but rather only ferrite grains. The H3 sample shows a significantly smaller ferrite grain size in the decarburized region than the H1 and H2 samples, which do not qualitatively have a significant difference in grain size.

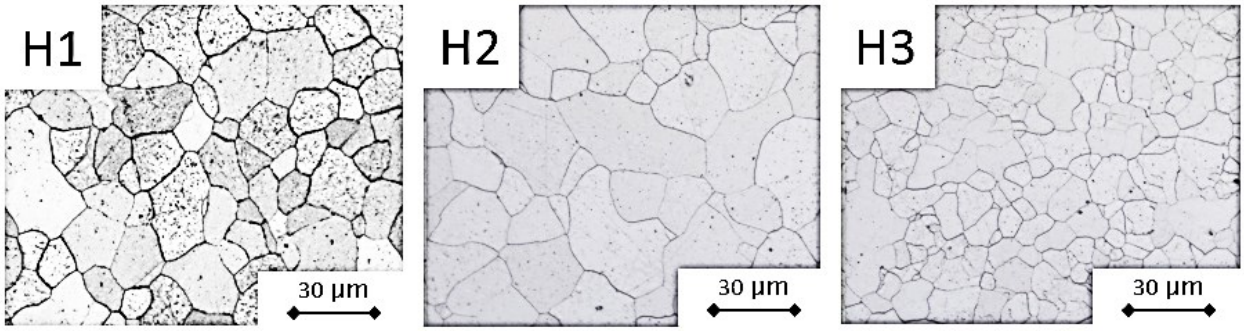

Figure 4.63: 4130 Decarburized Surface Images

Hardness tests were performed across the thickness of each sample to get an average hardness. Through thickness hardness was chosen so the effect of the decarburized regions as well as the F-P regions in the H samples would be represented in the same amount the wave travelled through them. The average hardness for each sample is shown in Figure 4.64.

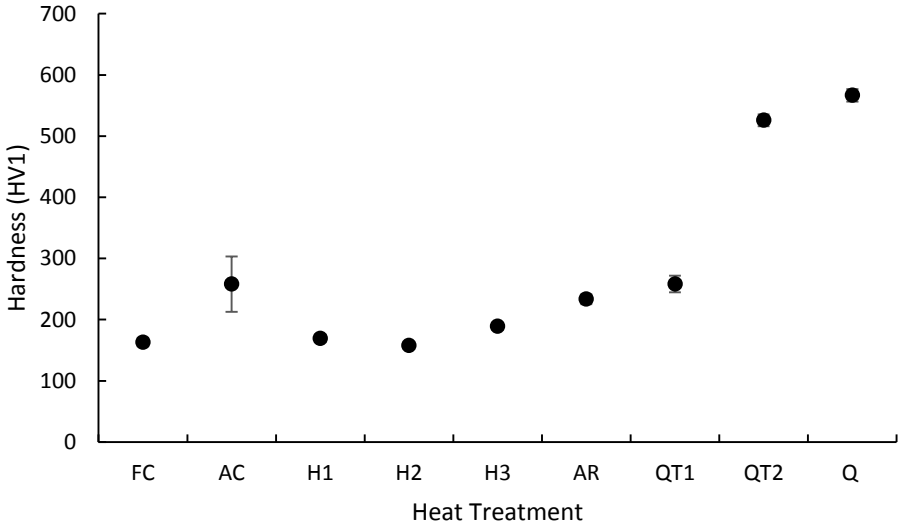

Figure 4.64: 4130 Heat Treated Sample Hardness

The quenched and QT2, low temperature (205°C) tempered, samples show significantly higher hardness than the remaining samples. The air cooled, as received and QT1, high temperature tempered (650°C), samples have higher hardness than the furnace cooled and H1-H3 samples. The H samples have lower average hardness values than the air cooled sample due to their decarburized surfaces. The hardness in the center regions of the AC and H samples were similar as they had similar F-P structures, whereas the FC sample had more ferrite in its F-P structure.

The ultrasonic shear velocities of each sample were taken using industrial equipment at UT Quality in Edmonton, Alberta, to see if differences in microstructure could be detected using the same

procedures as performed with the laboratory equipment. Shear velocities were chosen since they showed a good correlation with microstructure in Section 4.3. The shear velocity for each heat treatment is shown in Figure 4.65.

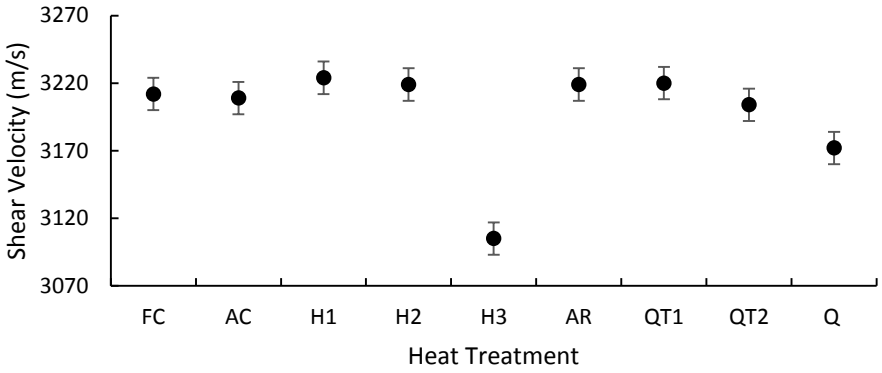

Figure 4.65: 4130 Heat Treated Shear Velocity

The velocities seem to agree with trends in heat treatments seen in the L80 samples (Section 4.3) with the exception of the H3 sample, which has a significantly lower velocity than any of the others. The H3 sample was not austenitized, unlike the other samples. The remaining heat treated samples were all austenitized for the same amount of time, so their structures all formed from the same high temperature austenite structure. The H3 structure did not form from this structure, but from annealing of the as received structure and as such could have very different texture than the other samples. If the H3 sample is removed from the comparison because of this difference, the remaining samples show a relationship between hardness and shear velocity, as shown in Figure 4.66.

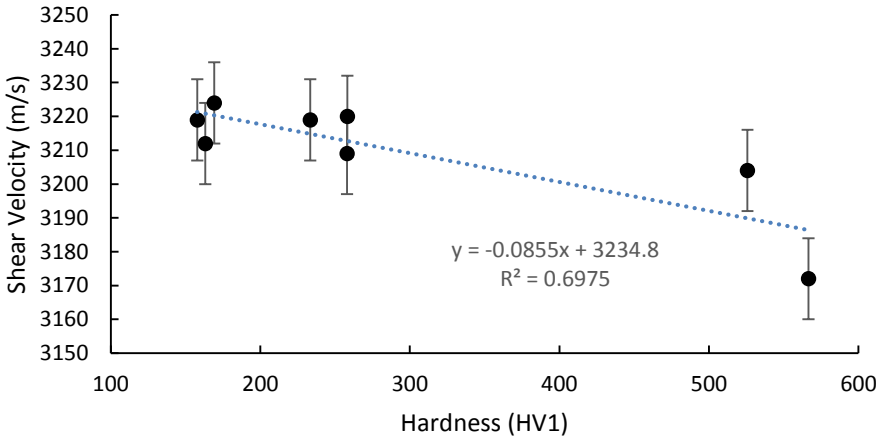

Figure 4.66: 4130 Hardness vs. Shear Velocity

The shear velocity in the 4130 samples shows a linear trend with hardness, going from a F-P microstructure to martensite. The linear equation between the hardness and shear velocity did not fit as well as for the laboratory tested samples in Section 4.3.1.2 or 4.3.2.2 and had an R^2 value of only 0.7.

$$Vs = -0.0855(HV) + 3234.8 \quad (4.11)$$

The poorer fit is likely the result of having different structures such as decarburized layers and tempered martensite as well as the F-P, B and M found in the L80. Tempering of martensite can have a drastic effect on both hardness and ultrasonic velocity. Depending on tempering temperature the TM samples show hardness and velocity similar to F-P at high tempering temperature or martensite at lower tempering temperature. The shear velocity could then be useful in an industrial application to determine the difference in structure between similar materials. However, as shown with the H3 sample, initial conditions, e.g. austenitized vs annealed, must be similar or velocities can change drastically. The velocity difference between martensite and ferrite-pearlite could be useful as a method of confirming that samples are quenched properly, while the difference between martensite and tempered martensite could confirm proper tempering. These measurements could be done with existing ultrasonic equipment and methods without the need to look at more than two backwall reflections or calculating attenuations.

4.4.2 5160 Heat Treated Samples

In order to see if the trends between hardness and velocity were present in a steels besides the L80 and 4130 a 5160 spring steel was analyzed in a similar manner to see if a steel used for very different applications will show a similar trend. The 5160 samples came from an automotive leaf spring, a complete processed part, as opposed to bar stock for the 4130 and pipe skelp for the L80. The heat treatments and resultant microstructures for the 5160 samples are shown in Table 4.6.

Table 4.6: 5160 Heat Treatments and Microstructures

	FC	AC	H1	H2	AR	QT1	QT2	Q
Step 1	870°C 1 hr	870°C 1 hr	870°C 1 hr	870°C 1 hr	-	870°C 1 hr	870°C 1 hr	870°C 1 hr
Step 2	Furnace Cooled	Air Cooled	770°C 6 hrs	770°C 69 hrs	-	Quench	Quench	Quench
Step 3	-	-	Air Cooled	Air Cooled	-	650°C 1 hr	205°C 1 hr	-
Microstructure	F-P	F-P	F-P	F-P	TM	TM	TM	M

The 5160 samples were heat treated in the same manner as the 4130 samples, but the spheroidization heat treatment without austenization was not performed since the velocities were

quite different relative to the other 4130 samples. The as received sample was tempered martensite as opposed to the rolled ferrite for the as received L80 skelp or ferrite-pearlite for the 4130 bar. Representative micrographs for each heat treatment are shown in Figure 4.67.

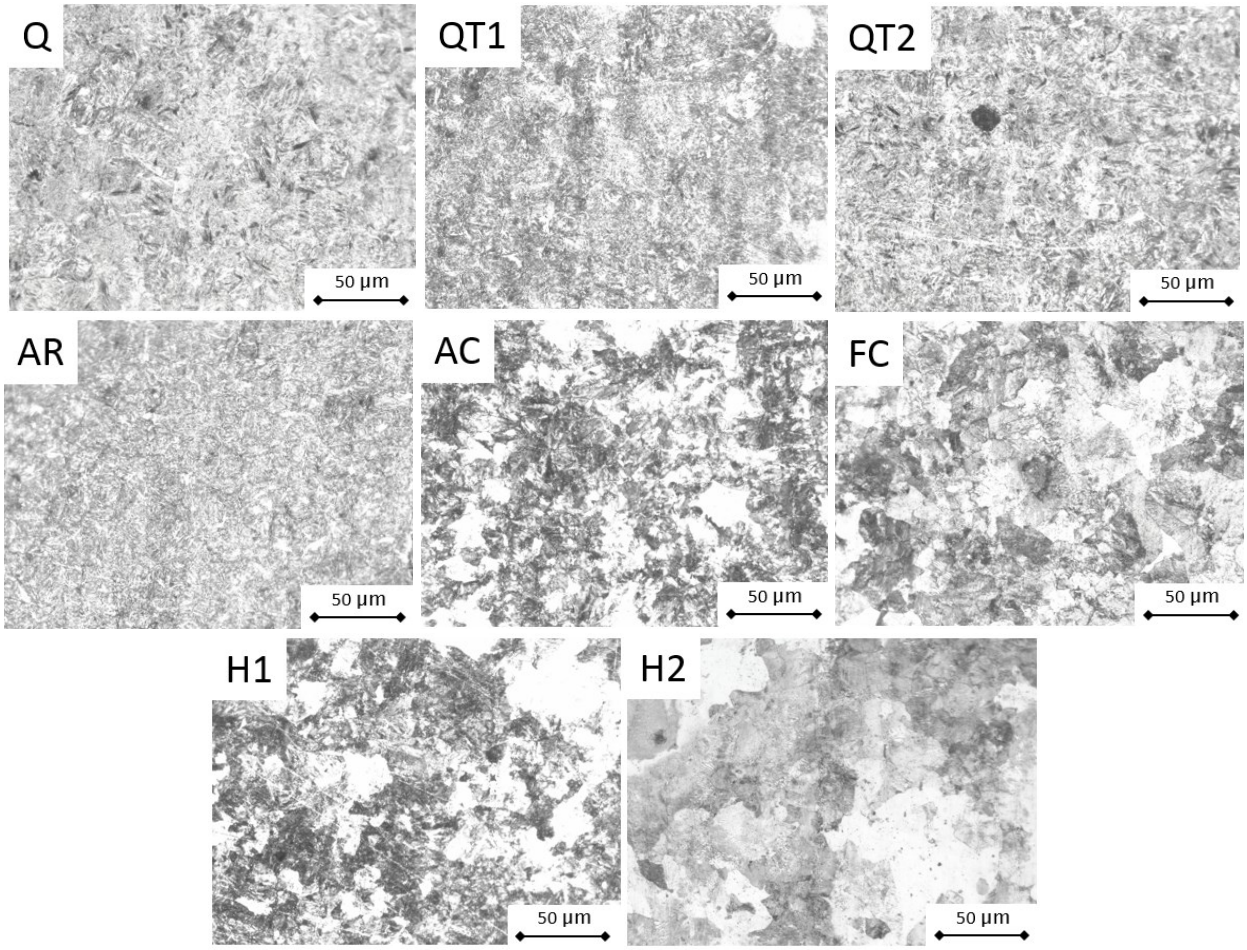

Figure 4.67: 5160 Heat Treated Microstructures

The 5160 samples held at high temperature show more variation than the 4130 samples held at high temperature. The longer hold time (H2) appears to have a much larger grain size and the pearlite lamellae are visible at lower magnification, but not in the H1 sample. These samples also had similar structures at their surfaces and center. It is possible that there was a smaller area fraction of pearlite at the surface due to decarburization, but pearlite was still present as shown in Figure 4.69.

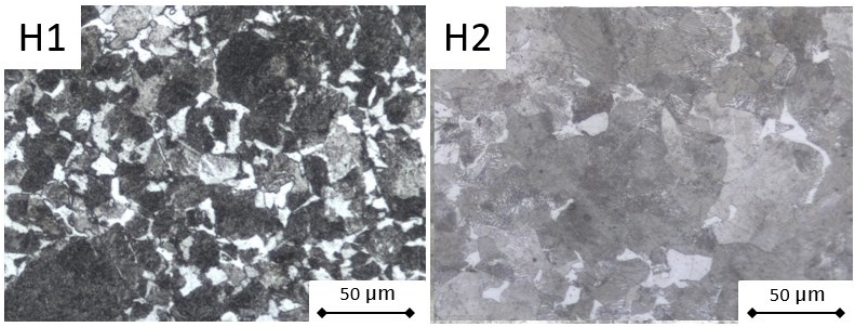

Figure 4.68: 5160 Surface Images of Samples Held at High Temperature

The H2 surface and center look very similar to one another, while the H1 surface and center appear to have different morphologies; however, both morphologies contain ferrite and pearlite. The center of the H1 sample bears more resemblance to the FC sample than the H2 sample. The FC sample is more similar to the H1 than the AC sample. This is also reflected in the ultrasonic shear velocities measured, as shown in Figure 4.69.

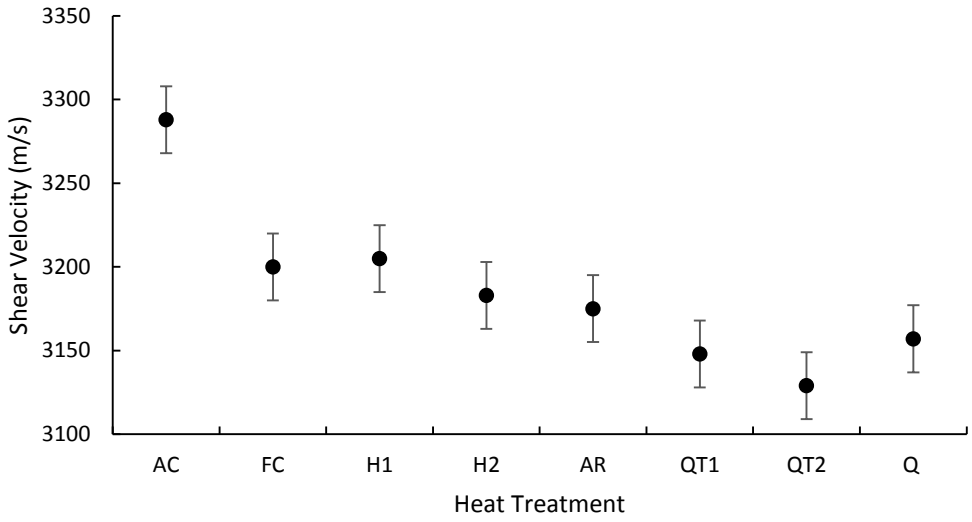

Figure 4.69: 5160 Heat Treated Shear Velocity

There appears to be a good relation between structure and ultrasonic shear velocity in the 5160 samples. The FC and H1 samples, which showed similar structures also have similar velocities. The air cooled sample may contain more ferrite than the FC, as seen in the L80 samples, resulting in its increased velocity. The martensite and tempered martensite show similar velocities relative to one another unlike the 4130 steel. The as received sample has a velocity between those of the martensitic and H2 samples. The processing done to the leaf spring is not known. It is possible that the tempering performed to the part is greater, higher temperature or longer time, than that done to the heat treated samples in this work, which could cause its velocity to be increased relative to the TM samples. The velocity was also compared to the hardness of the samples, shown in Figure 4.70.

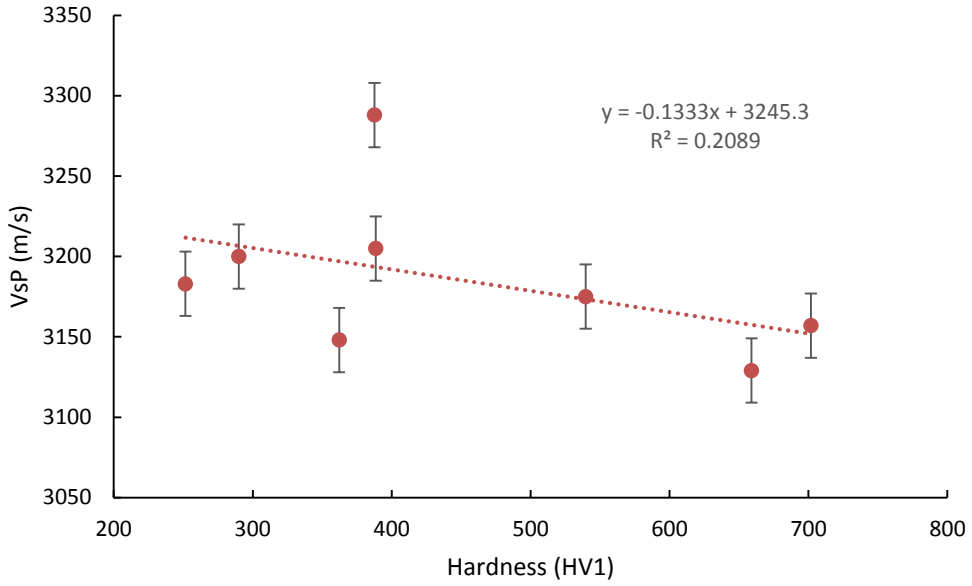

Figure 4.70: 5160 Shear Velocity vs. Hardness

The linear equation between the hardness and shear velocity did not fit as well as for the laboratory tested samples in Section 4.3.1.2 or 4.3.2.2 and had an R^2 value of only 0.2.

$$Vs = -0.1333(HV) + 3245.3 \quad (4.12)$$

The poorer fit is likely the result of having different structures such as tempered martensite as well as the F-P, B and M found in the L80. There may also be precipitates or other microstructural differences between the samples which were not analyzed that could affect the ultrasonic velocity. The difference between maximum and minimum velocities in the L80 (61 m/s), 4130 (119 m/s) and 5160 (159 m/s) increases with increasing carbon content. The shear velocity is then more effective at differentiating between high carbon microstructures than low carbon microstructures; however, a difference was still apparent in the L80 steel which had the lowest carbon content (0.244 wt%).

4.4.3 Industrial UT Summary

Velocities for both 4130 and 5160 decreased as the structure changed from ferrite-pearlite (F-P) to martensite (M). Both sets of samples showed a linear relationship with hardness; however, the fit was not as good as that found with the L80 samples. The 4130 sample which was not austenitized showed a significantly different velocity than those samples which were. The ultrasonic velocity was able to differentiate between martensite and other structures using industrial equipment and practices.

4.5 Velocity Comparison Across All Samples

All the ultrasonic shear tests done for all the samples were compared with the structures found in each sample. This is shown in Figure 4.71 where each number corresponds to a microstructure: 1 is ferrite (F), 2 is rolled ferrite (RF), 3 is ferrite-pearlite (F-P), 4 is bainite (B), 5 is martensite (M) and 6 is tempered martensite (TM). The velocities agree with those calculated in Section 2.4, where ferrite has a large range of velocities which encompass the other structures but has a higher maximum velocity. The F-P samples have the next highest maximum followed by the B and finally the M and TM have similar ranges.

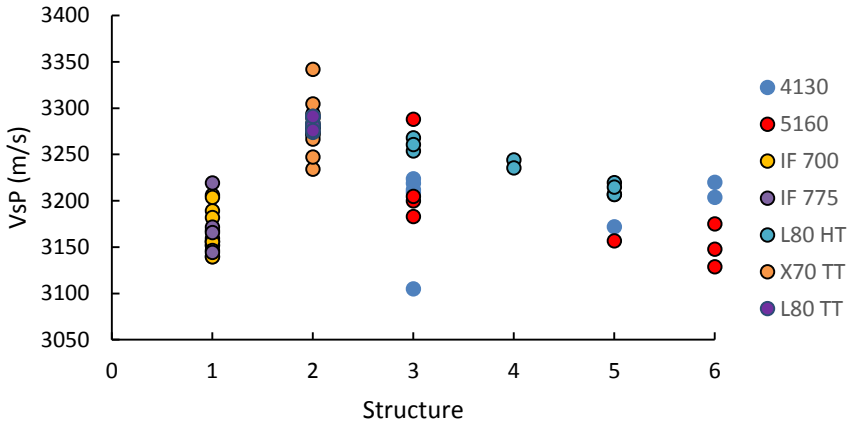

Structure	
F	1
RF	2
F-P	3
B	4
M	5
TM	6

Figure 4.71: Cumulative Ultrasonic Shear Velocity and Microstructure

The ferrite samples (structure 1) may have lower ultrasonic velocities than the rolled ferrite samples (structure 2) since they are the annealed IF samples. The IF samples have little precipitation or strain compared to the L80 or X70 as received skelps. Work done by other researchers showed that precipitation [37] and stress [50] increased the ultrasonic velocity. The range in velocities found in each structure could be the results of many factors including composition differences between the steel types and differences in processing. Not all the samples which were martensite would have the same precipitates, microstrain, colony size or lath size any of which could be affecting the velocities.

The ultrasonic shear velocities were also compared to sample hardness across all the samples which were hardness tested and ultrasonically tested (Figure 4.72). It is likely that changes in composition and structure effect the ultrasonic velocity in manners not detectable by hardness.

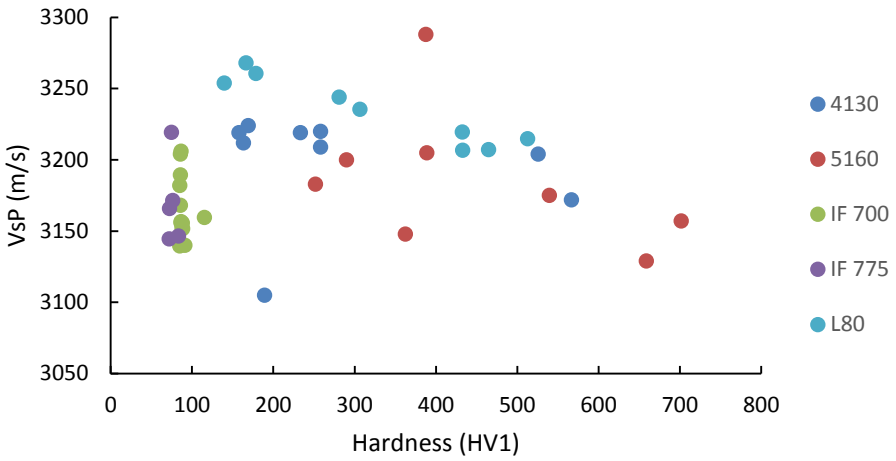

Figure 4.72: Cumulative Ultrasonic Shear Velocity vs. Hardness

As with the velocity structure plot (Figure 4.71) the IF steel appears to have lower velocity than suggested by the general trend. The 4130 outlier point at ~200 HV1 is the sample discussed in Section 4.4.1 which was not austenitized and showed significantly lower velocity than the other 4130 samples. If this point and the IF samples are not considered there appears to be a general trend of decreasing velocity with increasing hardness across the 5160, 4130 and L80 heat treated samples when considered together as well as independently. This may indicate that a correlation exists between hardness and ultrasonic velocity for samples with similar processing history.

Chapter 5 Conclusions, Recommendations and Future Work

This chapter reviews the significant findings from the velocity calculations and experiments. The industrial implications are also presented. Finally recommendations and future work are suggested.

5.1 Conclusions

The ultrasonic velocity calculations and experimental work have shown that both shear and longitudinal waves can be used to determine different important microstructural characteristics of steel such as the structures present or amount of microstrain.

The Christoffel equation using the full stiffness tensor as well as ultrasonic velocity equations using only the Young's modulus were used to calculate the ultrasonic shear and longitudinal velocities in a 1050 steel. Calculations with the stiffness tensor predicted two shear velocities and a longitudinal while the Young's modulus equations only predicted one shear and longitudinal velocity. Three structures of the 1050 steel were analyzed, ferrite (F), ferrite-pearlite (F-P) and martensite (M). Calculated velocities showed a greater difference between F and M velocities for shear waves than longitudinal waves. The shear waves were slower in each structure for 75% of directions vs. 66% of directions for longitudinal waves. There was also less difference between the calculated longitudinal velocities between structures than the shear wave velocities.

The experimentally obtained ferrite velocities from the X70 and L80 skelps (~5920 m/s for V_L and ~3240 m/s for Vs) were within the maximum and minimum velocities calculated using the Christoffel equation (5436-6529 m/s for V_L and 2995-4147 m/s for Vs). The L80 martensitic samples also had similar velocities (~5900 m/s for V_L and ~3210 m/s for Vs) to the calculated velocities (~5913 m/s for V_L and ~3200 m/s for Vs). The L80 F-P sample velocities (~5900 m/s for V_L and ~3255 m/s for Vs) were further from the calculated (~5910 m/s for V_L and ~3230 m/s for Vs) than the others but the exact fractions of ferrite and pearlite in the samples used for velocity calculations is not known and may be different from that seen experimentally which would account for the velocity difference. The velocity can then be calculated fairly accurately from the elastic constants of a material. The experimental work confirmed that the calculated velocities using the Christoffel equation were fairly accurate and that those calculated based on isotropic assumptions were inaccurate. The isotropic assumption as well as use of elastic constants as Young's moduli are then invalid since velocities calculated with these assumptions did not agree with the velocities obtained experimentally.

The work done on the X70 and L80 skelps showed little change in the ultrasonic properties through the thickness of either skelp. The velocities found through the whole L80 skelp (~3260 m/s for VsP) agreed with those found in the individual samples taken through the skelp thickness (~3250 m/s average for VsP). The IF steel which was cooled to room temperature after different annealing

times showed that ultrasonic velocity was sensitive to recrystallization while attenuation was more sensitive to grain grown after annealing. The ultrasonic shear velocity decreased as sample structure changed from ferrite-pearlite (F-P) to bainite (B) and then to martensite (M) in the heat treated L80 samples. This corresponded to an increase in sample hardness, which increased linearly with decreasing velocity. The longitudinal velocity did not appear to change significantly with structure. The longitudinal and shear attenuation also decreased as the structure changed and hardness increased. The attenuation reached a minimum with the martensite samples and did not continue decreasing as their hardness increased. Ultrasonic shear velocities also varied linearly with the YS and UTS. Attenuation showed similar behavior when compared with YS, UTS and hardness. Ultrasonic velocity and attenuation increased as elongation and fracture strain increased. The attenuation increased with toughness but not the velocity. The trends seen with hardness and velocity in L80 were also seen in the 4130 and 5160 samples tested with industrial equipment.

The ultrasonic shear velocity correlated well with changes in structure and hardness in the steels tested. The longitudinal velocity did not show significant change between structures or hardness. The attenuation of longitudinal and shear waves also correlated well with changes in structure and hardness as well as dislocation density, however longitudinal attenuation was easier to obtain repeatedly due to the difference in couplant between the shear and longitudinal transducers. The shear wave birefringence changed with microstrain as well as structure. Shear wave tests are then useful to obtain velocity and birefringence to see changes in steel structure while longitudinal wave tests can be used to obtain attenuation which also shows changes in steel structure.

5.2 Industrial Implications

The ability of shear wave velocity to differentiate between structures in steel could be used in industry for a variety of purposes. The velocity could be used to aid identification of pipe. A quench and temper pipe, e.g. L80, would have a different velocity than a microalloyed pipe, e.g. X70 (Section 4.1.1.2). Additionally the shear velocity could be used in quality control operations to ensure the structure produced is correct. As seen in the L80 heat treatment trials (Section 4.3.2.2), F-P, B and M all had unique shear velocities. If a steel was treated to form a bainitic microstructure but the ultrasonic velocities were lower for a pipe than normal it would be likely that some M had formed and the pipe would need to be re-heat treated.

The ability of longitudinal attenuation to differentiate between steel structures could be used in much the same manner as the shear velocities (Section 4.3.2.4) but could likely be implemented more easily since longitudinal waves are commonly used in flaw detection of pipes after production. The attenuation could likely then be measured with only a software addition rather than requiring new equipment.

The consistency of ultrasonic properties through the X70 and L80 skelps (Section 4.1.1) is also important for industry. Flaw detection on these types of pipes or skelp can be done knowing that the assumption of constant velocity is true and the location of flaws or defects using this assumption are accurate.

5.3 Recommendations and Future Work

This work could be used to progress into many different investigations. Of particular interest would be to perform through thickness investigations of higher grade, e.g. X80, X100, steels in a similar manner to that done in this work on L80 and X70. The higher texture index of X80 would be useful to look at how texture affects ultrasonic velocity and attenuation. A more complicated steel microstructure with differing surface and centerline properties would also be an interesting study. Direct measurement of the texture with EBSD or dislocation density with TEM or microbeam analysis rather than indirect measurements with XRD could also be beneficial in such a study. Work could also be done in an industrial setting to see how ultrasonic properties vary in steels which are produced in different heats but with similar structures and compositions to see if quality control by monitoring microstructure with ultrasonic properties is viable. Replication of the heat affected zones of welds would also be important for seeing how grain shape and dissolution of precipitates affects ultrasonic properties as well as how those changes could affect flaw detection. New equipment (or a new labview program for the current equipment if possible) could also be obtained for the laboratory which could output the entire ultrasonic waveform to see if more complicated analysis of the waveform such as Fourier transforms or combined velocity/attenuation factors may be useful.

In order to implement a quality control system for microstructure using ultrasonics, further developmental work is required. The results of the work done in this thesis show that there is a change in ultrasonic velocity for martensite and ferrite-pearlite; however, the sensitivity to the changes in microstructure encountered in an industrial process are not known. Before such a system is implemented on an industrial scale, work is required to assess how ultrasonic velocity varies for acceptable and unacceptable structures produced in an industrial setting. A first step is to ultrasonically test samples which are already sectioned from the pipe for quality control checks using hardness or metallography. Since these samples are already used to determine if a pipe meets specifications, a range of velocities could be found which correspond to pipes which meet specifications and those that do not. If the velocity ranges show minimal overlap they could be used as on-line indicators to verify specifications. These tests would have to be repeated for each grade of interest, since different steels have different shear velocity – hardness relationships, as shown in Figure 4.39, Figure 4.66 and Figure 4.70.

References

[1] X. Li, "Quantitative Characterization of Microstructure in High Strength," University of Alberta, Edmonton, MSc. Thesis 2009.

[2] V.B. Ginzburg, "Ch. 21 Microalloyed Steels," in *Metallurgical Design of Flat Rolled Steels*.: CRC Press, 2004, pp. 545-579.

[3] D.V. Edmonds, "Designing with microalloyed and interstitial free steels," in *handbook of mechanical alloy design*.: CRC Press, 2003, pp. 321-353.

[4] V.B. Ginzburg, "Structural changes in microalloyed steels during hot rolling," in *Metallurgical design of flat rolled steels*.: CRC press, 2004, pp. 367-397.

[5] T. Gladman, *The Physical Metallurgy of Microalloyed Steels*.: Maney, 2002.

[6] G.E. Linnert, *Welding Metallurgy, Vol. 1*. Miami: American Welding Society, 1994.

[7] A.O. Benscoter B.L. Bramfitt, "Ch. 2 Origin of Microstructure," in *Metallographers Guide: Practice and Procedures for Irons and Steels*.: ASM International, 2001, pp. 23-48.

[8] B.L. Bramfitt, "Effects of composition, procesing and structure on properties of iron and steels," in *ASM Handbook Vol. 20: Materials Selection and Design*.: ASM International, 1997, pp. 357-382.

[9] L.E. Samuels, *Light Microscopy of Carbon Steels*.: ASM International, 1999.

[10] A.R. Marder G. Krauss, "The Morphology of Martensite in Iron Alloys," *Metallurgical Transactions*, vol. 2, pp. 2343-2357, 1971.

[11] W.F. Hosford, "Ch. 11 Crystallographic Textures," in *Physical Metallurgy, 2nd Edition*.: CRC Press, 2010, pp. 161-180.

[12] C.E. Murray, C. Noyan H. Schaeben, "Ch. 11 Texture Measurement and Analysis," in *Analytical Characterization of Aluminum, Steel and Superalloys*.: CRC Press, 2005, pp. 575-606.

[13] M. F. McGuire, "Section 8.7: Texture and Anisotropy," in *Stainless Steels for Design Engineers*.: ASM International, 2008, pp. 120-121.

[14] J.J. Jonas L. Kestens, "Transformation Recrystallization Textures associated with Steel Processing," in *ASM Handbook Volume 14A: Metalworking: Bulk Forming*.: ASM International, 2009, pp. 685-700.

[15] W.F. Hosford, *The Mechanics of Crystals and Textured Polycrystals*.: Oxford University Press, 1993.

[16] JJ Wild, "The use of ultrasonic pulses for the measurement of biological tissues and the detection of tissue density changes," *Surgery*, vol. 27, no. 2, pp. 183-188, 1950.

[17] FW Stuthers GD Ludwig, "Detecting gallstones with ultrasonic echoes," *Electronics*, vol. 23, pp. 172-178, 1950.

[18] Y. Iizuka, "Ultrasonic flaw detection apparatus and ultrasonic flaw detection method for pipe," 8393217, march 12, 2013.

[19] F.A. Firestone, "Flaw detecting device and measuring instrument," 2280226 A, April 21, 1942.

[20] Canadian Welding Bureau, *Weld Inspection: Module 19*. Mississagua: CWB Learning Center, 2006.

[21] ASM Handbooks: Volume 17. [Online]. http://products.asminternational.org/hbk/index.jsp

[22] Stulen F Ensminger D, "Ch. 1: Oscillator Motion and Wave Equations," in *Ultrasonics Data Equations and Practical uses*. London New York: CRC Press, 2009, pp. 1-25.

[23] Marklein R, Mayer K Langenberg K.J., "Reflection, Transmission, and Mode Conversion of Elastic Plane Waves," in *Ultrasonic Nondestructive Testing of Materials: Theoretical Foundations*. Boca Rator FL: CRC Press, 2012, pp. 291-376.

[24] NDT Resource Center. NDT Course Material: Ultrasound, Physics of Ultrasound. [Online]. http://www.ndted.org/EducationResources/CommunityCollege/Ultrasonics/ccutindex.htm

[25] National Instruments. Tutorial: Fundamentals of Ultrasonic Imaging and Flaw detection. [Online]. http://zone.ni.com/devzone/cda/tut/p/id/3368

[26] Kundu T., "Mechanics of Elastic Waves and Ultrasonic NDE," in *Ultrasonic NDE: Engineering and Biological Materials Characterization*.: CRC Press, 2003, pp. 1-142.

[27] David J. Cheeke N., "Introduction to Vibrations and Waves," in *Fundamentals and Applications of Ultrasonic Waves*.: CRC Press, 2002, pp. 14-39.

[28] Lane C., "Wave Propagation in Anisotropic Media," in *The Development of a 2D ultrasonic Array Inspection for Single Crystal Turbine Blades*.: Springer, 2014, pp. 13-39.

[29] McMaster R.C., "Ultrasonic Test principles: Ultrasonic Wave propagation," in *Non-Destructive Testing Handbook: Volume II*. New York: The Ronald Press Company, 1959, pp. 43.22-43.23.

[30] Vera Lúcia de Araújo Freitas, "Nondestructive characterization of microstructures and determination of elastic properties in plain carbon steel using ultrasonic measurements," *Materials Science and Engineering A*, vol. 527, pp. 4431-4437, 2010.

[31] C. Hakan Gur, "Characterization of microstructural phases of steels," *Materials Characterization*, vol. 55, pp. 160-166, 2005.

[32] Silvio E. Kruger, "Monitoring austenite decomposition by ultrasonic velocity," *Materials Science and Engineering A*, vol. 425, pp. 238-243, 2006.

[33] Z. Opiekun W. Orlowicz, "Ultrasonic Detection of microstructure changes in cast iron," *Theoretical and applied fracture mechanics*, vol. 22, pp. 9-16, 1995.

[34] V.H. Albuquerque, J.P. Leite, A.C. varela, E.P. Moura, J.M. Tavares E.M. Silva, "Phase transformations evaluation on a UNS S31803 duplex stainles steel based on nondestructuve testing," *Materials Science and Engineering A*, vol. 516, pp. 126-130, 2009.

[35] V. Muthupandi, R. Jayachitra K. Vijayalakshmi, "Influence of heat treatment on the microstructure, ultrasonic attenuation and hardness of SAF 2205 duplex stainless steel," *Materials Science and Engineering A*, vol. 529, pp. 447-451, 2011.

[36] Belan J, "Identification of cast iron type with using of NDT metheds," *Archives of Foundy Engineering*, vol. 10, no. 1, pp. 103-106, 2010.

[37] Kumaran S. M., "Evaluation of Precipitation Reaction in 2024 Al-Cu alloy through ultrasonic parameters," *MSEA*, vol. 112, no. 01, 2011.

[38] Anish K, Srihar G, Jayakumar T, Ghosh R.N. Murthy G.V.S, "Charaterization of precipitation behavior in Nimonic 263 by ultrasonic velocity measurements," in *AIP Conference Proceedings: Review of progress in quantitative nondestructive evaluation*, vol. 1096, chicago IL, 2008, pp. 20-25.

[39] G. Sridhar, A. Kumar, T. Jayakumar G.V.S. Murthy, "Characterization of intermetallic precipitates in a Nimonic alloy by ultrasonic velocity measurements," *Materials Characterization*, vol. 60, no. 3, pp. 234-239, 2009.

[40] V. Rajendran, T. Jayakumar, P. Palanichamy, P S.M. Kumaran, "First Differential of temperature dependent ultrasonic parameters as an effecive tool for identifying precipitation reactions in a slow heat-treated 8090 Al-Li alloy," *Journal of Alloys and compounds*, vol. 464, pp. 150-156, 2008.

[41] C. Lane, "3D Ultrasonic inspection of anisotropic aerospace components ," *Insight: Non-Destructive Testing and Condition Monitoring*, vol. 52, no. 2, pp. 72-77, 2010.

[42] M.G. Silk, "Relationships Between Metallurgical Texture and Ultrasonic Propagation," *Metal Science*, vol. 15, pp. 559-565, 1981.

[43] Steve Dixon, "Characterisation of thickness and crystallographic texture of sheet using non-contact ultrasonic measurements," *Ironmaking and Steelmaking*, vol. 32, no. 5, pp. 385-390, 2005.

[44] A. Joseph, T. Jayakumar, B. Raj P. Palanichamy, "Ultrasonic Velocity Measurements for estimation of grain size in austenitic stainless steel," *NDT&E International*, vol. 28, no. 3, pp. 179-185, 1995.

[45] M.S. Kilickaya, S. Tuncel I.H. Sarpun, "Mean grain size determination in marbles by ultrasonic velocity techniques," *NDT&E international*, no. 38, pp. 21-25, 2005.

[46] I.H. Sarpun, A.Erol, A. Yonetken V. Ozkan, "Influence of mean grain size with ultrasonic velocity on microhardness of B4C-Fe-Ni composite," *Journal of Alloys and Compounds*, vol. 574, pp. 512-519, 2013.

[47] M.Vasudevan, T.Jayakumar, S.Venugopal, B. Raj P.Palanichamy, "Ultrasonic velocity measurements for characterizing the annealing behaviour of cold worked austenitic stainless steel," *NDT&E international*, vol. 33, pp. 253-259, 1999.

[48] E. Lindh-Ulmgren, L. Carlson B. Hutchinson, "Application of Laser Ultrasonics ot Studies of Recrystallisation and Grain Growth in Metals," in *1st International Symposium on Laser Ultrasonics: Science, Technology and Applications*, Montreal Canada, 2008.

[49] Crecraft DI, "The measurement of applied and residual stresses in metals using ultrasonic waves," *Journal of Sound Vibration*, vol. 5, no. 1, pp. 173-192, 1967.

[50] Ruud C, "Chapter 8. Residual Stress Measurment," in *Analytical Characterization of Aluminum, Steel and Superalloys*.: CRC Press, 2005, pp. 429-471.

[51] Buck O. James M.R., "Quantitative nondestructuve measurement of residual stresses," *CRC critical Review in Solid State Sciences*, pp. 61-105, August 1980.

[52] Creecraft D.I., "Ultrasonic Measurement of stresses," *ultrasonics*, vol. 6, no. 2, pp. 117-121, 1968.

[53] Szelaek J, Van Clark A. Schramm R.E., "Ultrasonic Measurement of residual stress in the rims of inductively heated railroad wheels," *Materials Evaluation*, vol. 54, no. 8, pp. 929-933, August 1996.

[54] Toda H, Hirakawa K, Sakamoto H, Toya Y Fukuoka H, "Acoustoelastic measurements of residual stresses in the rim of railroad wheels," *ASME Applied Mechanics Division, AMD*, vol. 62, pp. 185-193, 1984.

[55] Harzer R, Bruche D, Frotscher H, Schneider E.R., "Reliability assurance of railroad wheels by ultrasonic stress analysis ," in *Proc. of third european conference on residual stress analysis*, frankfurt, Germany, 1992.

[56] Bray D.E. Egle D.M, "Ultrasonic measurement of longitudinal rail stresses," *materials evaluation*, vol. 378, no. 4, pp. 41-46, 1979.

[57] Leon-Salamanca T, Bray D.E., "Zero-force travel time parameters of ultrasonic head waves in railroad rail," *materials evaluation*, vol. 43, no. 7, pp. 854-858, 1985.

[58] E.P. Papadakis, "Influence of Preferred Orientation on Ultrasonic Grain Scattering," *Journal of Applied Physics*, vol. 36, no. 5, pp. 1738-1710, 1965.

[59] Kailash, R. K. Srivastava K.M. Raju, "Orientation dependence of ultrasonic attenuation," *Physics Procedia*, vol. 3, pp. 927-933, 2010.

[60] R.J. Kolouch, K.A. McCarthey E.Y. Wang, "Orientation dependence of ultrasonic attenuation in copper," *physical review*, vol. 175, no. 3, pp. 723-728, 1968.

[61] P.C. Waterman, "Orientation Dependence of Ultrasonic Attenuation in Zn," *Journal of Applied Physics*, vol. 29, no. 8, pp. 1190-1195, 1958.

[62] J.A. Turner L. Yang, "Attenuation of ultrasonic waves in rolled metals," Lincoln, 2004.

[63] R.B. Thompson, P.D. Panetta S. Ahmed, "Ultrasonic attenuation as influenced by elongated grains," *Review of Quantitative non-destructive evaluation*, vol. 22, pp. 109-116, 2003.

[64] E.P. Papadakis, "Ultrasonic Attenuation and Velocity in SAE 52100 Steel Quenched From Various Temperatures," *Metallurgical Transactions*, vol. 1, pp. 1053-1057, 1970.

[65] Moreau A, Dawson A, Militzer M, Bussiere JF Dubois M, "Laser ultrasonic measurement of microstructure during metals processing," *Research Technology Organization*, vol. 9, pp. 11-1 - 11-9, May 1998.

[66] J.W.S. Rayleigh, "Chapter XV: Further Applications of the general equations," in *The Theory of Sound: Volume 2*. London: MacMillan and Co., 1896, pp. 149-154.

[67] B. Kopec, "Ultrasonic inspection of grain size in the materials for railway wheel sets," *Ultrasonics*, vol. 13, no. 6, pp. 267-274, 1975.

[68] M.S. Kilckaya I.H. Sarpun, "Mean grain size determination in marbles by ultrasonic first backwall echo height measurements," *NDT&E international*, vol. 39, pp. 82-86, 2006.

[69] L.J. Fradkin, B. Bridge L.R. Botvina, "A new method for assessing teh mean grain size of polycrystalline materials using ultrasonic NDE," *Journal of Materials Science*, vol. 35, pp. 4673-4683, 200.

[70] G.R. Jordan M.J. Crook, "Ultrasonic determination of grain size variations around weldments," *NDT International*, vol. 23, no. 4, pp. 221-227, 1990.

[71] K.J. Reimann D.S. Kupperman, "Effects of microstructure on ultrasonic examination of stainless steel," Risley England, 1976.

[72] B.K. Basu, K. Samudravijaya J. Philip, "Ultrasonic Attenuation of Longitudinal and Shear waves in superconducing lead," *journal of low temperature physics* , vol. 67, pp. 453-474, 1987.

[73] H. Ogi, M. Hirao N. Suzuki, "Noncontact Measurement of Ultrasonic Velocity and Attenuation in poycrystalline pure copper duiring initial stage of deformation," *Japan Institute of Metals*, vol. 62, no. 9, pp. 820-826, 1998.

[74] Z.G. Zhu G.K. Kuang, "A study of dislocation movement during push-pull fatigue by ultrasonic attenuation," *Physica status solidi (a)*, vol. 142, no. 2, pp. 357-363, 1994.

[75] W. Johnson, "Dislocation damping after plastic deformation in intersticial-free and carbon steels," *Journal of Alloys and Compounds*, vol. 310, pp. 423-426, 2000.

[76] B.M. Verma K.D. Chaudhuri, "Dislocation damping and the ultrasonic attenuation in tin," *Cryogenics*, vol. 19, no. 5, pp. 293-297, 1979.

[77] I. Delgadillo-Holtfort, T. Yohannes, J. Petzl M. Kaack, "Ultrasonic attenuation by dislocation formation in NiTi Shape memory alloys," *Materails Science and engineering A*, vol. 378, pp. 119-121, 2004.

[78] H, Ogi, N. Suzuki, T. Ohtani M. Hirao, "Ultrasonic attenuation peak during fatigue of polycrystalline copper," *acta materialia*, vol. 48, pp. 517-524, 2000.

[79] T. hamaguchi, M. Hirao H. Ogi, "In-Situ monitoring of ultrasonic attenuation during rotating bending fatigue of carbon steel with electromagnetic acoustic resonanc," *Journal of Alloys and Compounds*, vol. 310, pp. 436-439, 2000.

[80] K. nishiyama, S. Yoshikawa, H. Ogi, M. Hirao T. Ohtani, "Ultrasonic attenuation and microstructural evolution throughout tension-compression fatigue of a low-carbon steel," *Materials Science and Engineering A*, vol. 442, pp. 466-470, 2006.

[81] A. Kaselow,.: (Ph.D. thesis, Free University of Berlin), 2003, pp. 15-17.

[82] S.A. Kim W.L. Johnson, "Elastic Constants and internal friction of martensitic steel, ferritic-pearlitic steel and alpha iron," *Materials Science and Engineering A*, no. 452-453, pp. 633-639, 2006.

[83] M. Levy, "Introduction to fundamentals of elastic constants," in *Modern Acoustical Techniques for the measurement of mechanical properties*.: Academic Press, 2001, pp. 1-35.

[84] W. Soboyejo, "Ch. 4 Introduction to elastic behaviour," in *Mechanical Properties of Engineered Materials*.: CRC Press, 2002.

[85] R. W. Hertzberg, "Ch. 1 Tensile Response of Materials," in *Deformation and Fracture Mechanics of engineering Materials*.: John Wiley and Sons, 1996, pp. 12-15.

[86] Sonotech Inc., "Ultragel II ultrasonic Couplant Data Sheet," Bellingham Washington, 2012.

[87] Alloy Digest, AISI 5160 Datasheet, 1967.

[88] Alloy Digest, AISI 4130 Datasheet, 1988.

[89] J. Hollet, Technical Sales: Olympus NDT Canada Inc., august 7, 2013, private email.

[90] B.L. Bramfitt A.O. Benscoter, "Datasheet: Common etchants for irons and steels," 2002.

[91] ASTM, E112-13, Standard Test Methods for Determining Average Grain Size, 2013.

[92] ASTM, E562-11, Standard Test Method for Determining Volume Fraction by Systematic Manual Point Count, 2011.

[93] ASTM, E8m-04, Standard Test Method for Tensile Testing Metallic Materials, 2008.

[94] D. Engle, Tensile Testing Technician, 2014, Private Conversation.

[95] C. Met, Ultrasonic Testing Technician, Oct 10, 2012, Private Conversation.

[96] A.O Benscoter B.L. Bramfitt, "Ch. 8 The Art of Revealing Microstructure," in *Metallographer's Guide: Practice and Procedures for Iron and Steels*.: ASM International, 2001, pp. 224-227.

[97] E.O. Hall, "The deformation and ageing of miled steel III. discussion of results," *Proceedings of the Physical Society*, vol. 64, pp. 747-753, 1951.

[98] R. Honeycombe H. Bhadeshia, "Ch. 2: The strengthening of iron and it's alloys," in *Steels-Microstructures and Properties 3rd edition*.: Elsevier, 2006, pp. 17-38.

[99] W.Q. Cao, Q. Liu, W. Liu B.L. Li, "Flow stress and microstructure of the cold-rolled IF-Steel," *Materials Science and Engineering A*, vol. 356, pp. 37-42, 2003.

[100] S. Berbenni, F. Wagner, M. Berveiller, X. Lemoine N. Nicaise, "Coupled effects of grain size distributions and crystalographic textures on the plastic behaviour of IF steels," *International Journal of Plasticity*, vol. 27, pp. 232-249, 2011.

[101] Van Tyne C.J. Pavlina E.J., "Correlation of Yield Strength and Tensile Strength with hardness for steels," *Journal of materials engineering and performance*, vol. 17, no. 6, pp. 888-893, 2008.

[102] R.L. Plaut A.F. Pahilha, "Work Hardening, recovery, recrystallization and grain growth," in *Handbook of Aluminum Volume 2: Alloy production and Materials Manufacturing*.: CRC Press, 2003.

[103] S.E. Kruger, L. Gille, N. Giguere, S. Bolognini, A. Moreau G. Lamouche, "Laser-Ultrasonic Characterization of the Annealing Process of Low-Carbon Steel," in *AIP Conference Proceedings* , vol. 657, 2003, pp. 1681-1688.

[104] R. Stankievech, EVRAZ Research Engineer, 2013, Private email.

[105] Venkatesh T.A. Lan H, "On the relationships between hardness and the elastic and plastic properties of isotropic power-law hardening materials," *Philosophical Magazine*, vol. 94, no. 1, pp. 33-55, 2014.

[106] Berg M Radmard S, "New Method uses hardness to find yield strength," *oil & gas journal*, vol. 109, no. 12, pp. 122-127, 2011.

[107] M. Nakhaei H. Bohlooli, "Comparison of mechanical properties of bainite/ferrite dual phase 4340 steels with different percents of ferrite," *World of Science Journal*, vol. 3, no. 161-169, 2013.

[108] K.F. Lukens, J. Reinhold, W. Mahon J.V. Rinnovatore, "Ebrittlement of an AISI 8640 lower bainite steel," *Journal of Testing and Evaluation*, vol. 21, no. 5, pp. 329-338, 1993.

[109] American Piping Products. 4130 pipe. [Online]. http://www.amerpipe.com/products/alloy-pipe-and-products/4130-pipe

[110] T.J McCaffrey T.V. Philip, "Properties and Selection: Irons, Steels, and High-Performance Alloys," in *Vol. 1 ASM Handbook*.: ASM International, 1990, pp. 430-448.

[111] H.M. Rietveld, "A profile refinement method for nuclear and magnetic structures," *Journal of applied crystallography*, vol. 2, pp. 65-71, 1969.

[112] E. Dova, "Structure determination of Fe(II) spin-crossover complexes from powder diffraction data with direct space methods," Van't Hoff Institute for Molecular Sciences, Amsterdam, PhD thesis 2003.

[113] A. Paoletti, F.P. Ricci G. Caglioti, "Choice of collimators for a crystal spectrometer for neutron diffraction," *Nuclear Instruments*, vol. 3, pp. 223-228, 1958.

[114] A.A. Coelho R.W. Cheary, "Axial Divergence in a a conventional X-ray powder diffractometer I. Theoretical foundations," *Journal of applied Crystallography*, vol. 31, pp. 851-861, 1998.

[115] A.J. Vaars S.J. VanDer Gaast, "A method to eliminate the background in x-ray diffraction patterns of oriented clay mineral samples," *clay minerals*, vol. 16, pp. 383-393, 1981.

[116] B.K. Tanner D.K. Bowen, "Ch. 10Theory of XRD on Polycrystals," in *X-Ray Metrology in Semiconductor Manufacturing*.: CRC Press, 2006, pp. 151-171.

[117] A. Coelho, "Topas Academic Technical Reference," 2004.

[118] N Hansen D.A. Hughes, "Microstructure and strength of nickel at large strains," *Acta Materialia*, vol. 48, pp. 2985-3004, 2000.

[119] R.E. Smallman G.K. Williamson, "Dislocation densities in some annealed and cold-worked metals from measurements on the X-ray debye-scherrer spectrum," *Philosophical magazine*, vol. 1, pp. 34-46, 1956.

[120] P. Sahu, "Bainite and stress-induced martensite in an AISI type 300 steel: an X-ray diffraction study of the microstructure by the rietveld method," *Journal of applied crystallography*, vol. 38, pp. 112-120, 2004.

[121] C. Jiang, Z. Xu, V. Ji Q. Feng, "Effect of shot peening on the residual stress and microstructure of duplex stainless steel," *surface and coatings technology*, vol. 226, pp. 140-144, 2013.

[122] C.H. Jiang, Z. Xu, X.Y. Wu Q. Feng, "Microstructure thermostability of shot peened duplex stainless steel surface layer," *Surface Engineering*, vol. 29, no. 5, pp. 351-355, 2013.

[123] V.L. Kornilov, Yu.D. Morozov, S.V. Denisov, M.A. Molostov S.Yu. nastich, "New Steels for pipelines of strength classes K54-K60 (X70): Production Experiences at OAO MMK," *Steel in Translation*, vol. 39, no. 5, pp. 431-436, 2009.

[124] K. Gerald van den Boogart H. Schaeben, "Spherical harmonics in texture analysis," *Tectonophysics*, vol. 370, pp. 253-268, 2003.

[125] M. Jarvinen, "Texture effect in x-ray analysis of retained austenite in steel," *Textures and Microstructures*, vol. 26-27, pp. 93-101, 1996.

[126] M. Jarvinen, "Application of symmetrized harmonics expansion to correction of the preferred orientation effect," *Journal of Applied Crystallography*, vol. 26, pp. 525-531, 1993.

[127] B.H. O'Connor, D. Li H. Sitepu, "Comparatively evaluation of the March," *Journal of Applied Crystallography*, vol. 38, pp. 158-167, 2005.

Appendix A: L80 Metallography -- Grain or Colony Size Determination

The grain size presented in Section 3.5.4 is either the ferrite grain size and pearlite colony size for the FC, CAC and AC samples or the "colony" size for the C200, 200, COC, OC, CWC and WC samples. For the FC, CAC and AC samples the ferrite grains were easily distinguishable by their light appearance with dark grain boundaries (region F in Figure A.1). The pearlite regions were dark (region P in Figure A.1) and were differentiated from one another either by ferrite regions beside them, a colour or tint change from one dark region to the next or in higher magnification images by a change in the direction of the lamella within the regions. Figure A.2 shows a high magnification image of pearlite colonies distinguishable by the change in direction of their lamella indicated by the arrows in each colony.

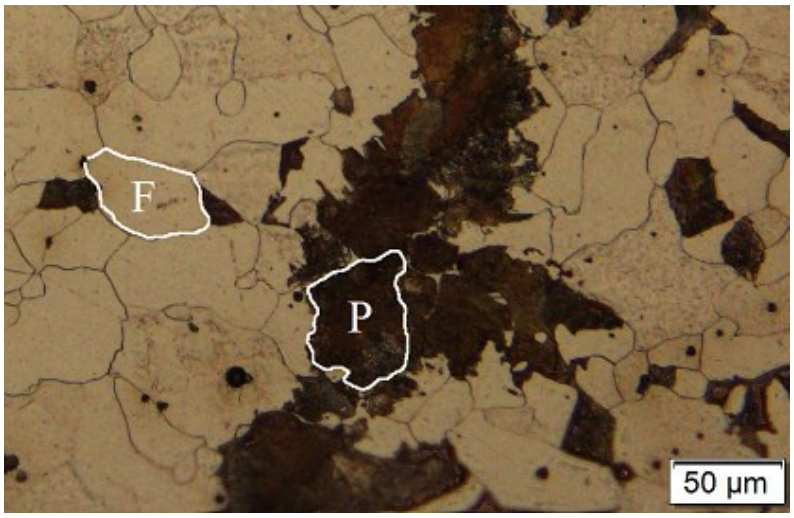

Figure A.0.1: L80 FC Sample Showing Ferrite Grain (F) and Pearlite Colony (P)

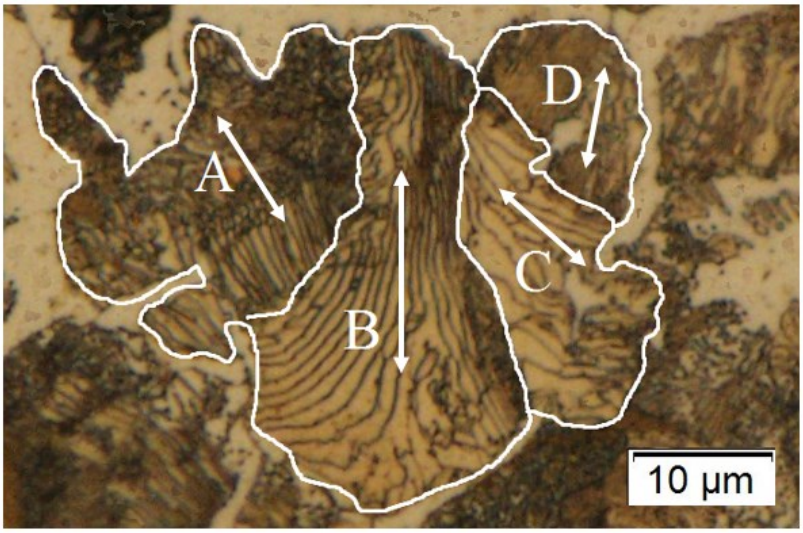

Figure A.0.2: L80 FC Pearlite Colonies (A, B, C, D) Distinguishable by Lamella Direction (Arrows)

In the samples which were not of a ferrite-pearlite mixed morphology, but rather bainite or martensite, distinguishing between individual grains was not possible optically. Instead the colonies of martensite or bainite were measured in the same manner as the pearlite colonies (Figure A.3). The edges were determined by a colour change between regions (e.g., regions A and C in Figure A.3) or a change in the direction of the sheaves (e.g., regions B and C in Figure A.3).

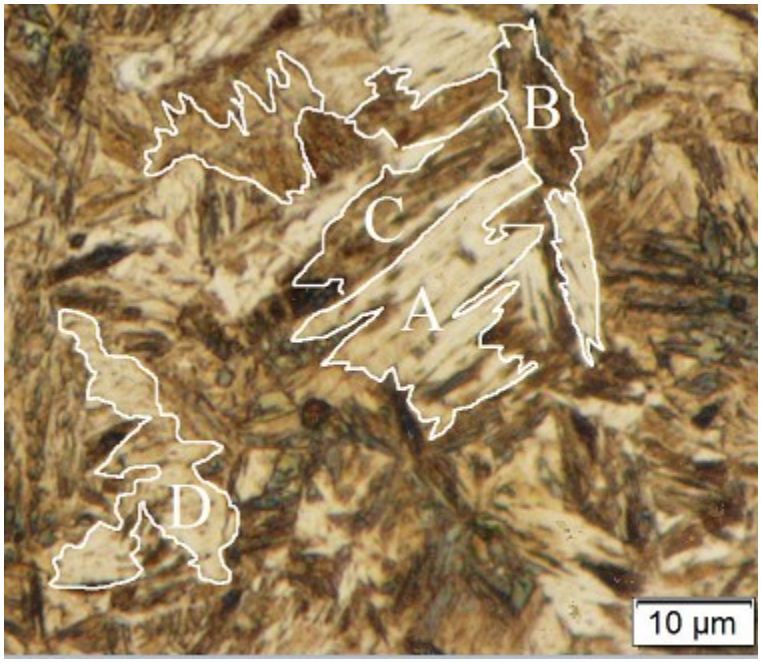

Figure A.0.3: L80 CWC Sample Showing Martensite Colonies (A, B, C, D)

These methods were used for all the L80 heat treated samples to obtain grain or colony sizes. If more accurate results are needed the micrographs can be taken with a scanning electron microscope for higher resolution or EBSD to ensure regions of specific orientation are grouped accurately.

Appendix B: XRD Analysis - Rietveld Refinement

For the reasons discussed in Section 3.3.2 the Rietveld refinement of XRD patterns is presented in this appendix rather than the thesis proper. Care should be taken when performing Rietveld refinement to ensure sample preparation does not adversely affect results and direct measurements should be taken to confirm that indirectly obtained parameters from Rietveld refinement are meaningful. The results presented here are not reliable due to the possible presence of work hardened layers from machining and a lack of independent confirmation of materials properties with other direct methods (e.g., electron microscopy).

B.1: Literature Review

Rietveld refinement is a quantitative method to analyze the pattern obtained from X-ray diffraction (XRD) of a polycrystal. Rietveld refinement reveals information from the XRD pattern beyond that of composition, including preferential orientation, microstrain and dislocation density [1]. The basis of Rietveld refinement is a least squares minimization according to the following equation [111]:

$$M = \sum_i W_i \left\{ y_i(obs) - \frac{1}{c} y_i(calc) \right\}^2 \quad \text{(B1)}$$

where y_i(obs) and y_i(calc) are the observed and calculated intensities of the XRD pattern at any given point, c is a scaling factor such that the total y_i(obs) is equal to the total y_i(calc) and W_i is a statistical accuracy term, set to $1/y_i$ in Topas [1]. The Topas software functions by calculating a curve, y_i(calc), repeatedly until M is minimized. y_i(calc) is found using the following equation [112]:

$$y_i(calc) = \sum_H L_H m_H |F_H|^2 \, \Phi(2\theta_i - 2\theta_H) P_H Y_H A_H + y_{bi} \quad \text{(B2)}$$

H denotes the Miller indices of a Bragg reflection (hkl), L_H is the Lorentz-Polarization factor, m_H is the multiplicity of the H^{th} reflection, F_H is the structure factor, Φ is the reflection profile function, θ_i is the angle at the i^{th} point in the XRD pattern, θ_H is the Bragg angle, P_H is the texture function, Y_H is the extinction correction factor, A_H is the absorption factor and y_{bi} is the background intensity. Many factors then affect the XRD pattern and, as such, there are many components to y_i(calc) which must be considered in order to generate a curve with a reasonably small M [1]. The parameters critical to the work done in this thesis are outlined below.

B.1.1 Instrument Parameters

Some of the factors critical to Rietveld refinement are not reliant on the sample but on the instrument being used. These include 2θ-zero error, axial divergence, background noise and

halfwidth parameters [1]. The halfwidth parameters are angle dependent [113] and can be simplified to three parameters (U,V,W) called the Cagliotti parameters [111]:

$$H_k^2 = U\tan^2(\theta_k) + V\tan(\theta_k) + W \tag{B3}$$

where H_k is the halfwidth, θ_k is the angle and U, V, and W are the refinable Cagliotti parameters. These parameters account for the variation of halfwidth with scattering angle [111]. The 2θ zero error is a general term that accounts for peak shifting due to the instrument reporting the 2θ values all a small amount plus or minus the expected caused by the measurement of the 2θ zero being offset from true [1]. Axial divergence is the spreading of the X-ray beam along the axis of rotation of the source, which results in peak asymmetry. This can be limited by the use of Soller slits which reduce both axial divergence and peak intensity [114]. The resultant peak asymmetry must be accounted for in order to obtain a good least squares minimization. The background is the intensity of X-rays detected that are not related to the sample tested. This background is shown in Figure B.0.1 as many effects (1-8) combine to form the total background (9). These effects include incoherent radiation, fluorescent radiation, air scatter, and more [115]. This is manifested as a sharply decreasing intensity from the 2θ-zero.

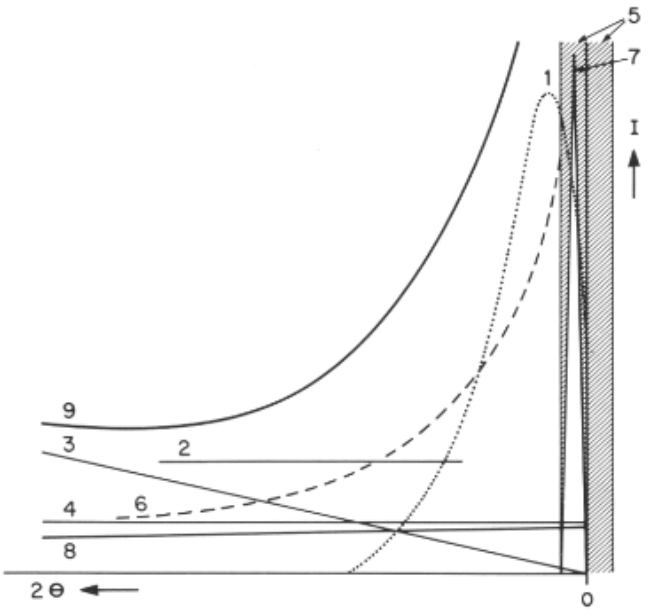

Figure B.0.1: Summation of Background Effects Into Overall Background Output in XRD Pattern (Line 9) [115]

The background radiation is most commonly accounted for using a 5th order polynomial to model its behaviour [1]. These instrument parameters are accounted for by running the Rietveld refinement on a sample of known material, normally LaB_6 powder. When the refinement has a good fit on the known sample, the instrument parameters obtained can then be used with an unknown sample in order to determine its properties.

B.1.2 Material Properties from Rietveld Refinement

Once the instrument parameters are known many useful materials properties can be obtained from Rietveld refinement. Of particular interest in this study are the texture index, dislocation density, domain size and microstrain. Each of these parameters are obtained by refinement done to match the peaks obtained by XRD. Microstrain can be determined from angular shifts in the peaks [116], domain size is obtained by refinement of the peak broadening function and texture, represented by spherical harmonics (the angular solutions to Laplace's equation), is obtained from the peak height ratios [117]. The domain size is related to grain size, subgrain size or cell size [1]. Grain size refers to regions separated from one another with high angle (>15^o) grain boundaries (HAGB), subgrain size is a region separated by low angle (<15^o) grain boundaries (LAGB) and cells refer to regions bounded by misorientations below the detection limits of EBSD or TEM (1-3^o) [1]. Cells are regions with very low dislocation density and very low angle grain boundaries [118]. When the domain size reported by XRD is lower than expected or found with EBSD or TEM, it can correspond to the cell size rather than subgrain or grain size. Specialized functions within the Topas software match these phenomena to their respective peak variations and output the values which result in the best fit.

B.1.2.1 Dislocation Density

The dislocation density for a sample can be obtained through XRD. In order to calculate the dislocation density both the microstrain and domain size values are used, as both contribute to the dislocation density. If the structure is assumed to be formed of blocks and the dislocations are present on the faces of the blocks the dislocation density due to domain size can be found using [119]:

$$\rho_D = \frac{3n}{D_s^2} \tag{B4}$$

D_s is the domain size found from Rietveld refinement, ρ_D is the dislocation density resulting from the domain size and n is the dislocations per block face. Since n is not known, a value of 1 can be assumed, yielding a minimum dislocation density [119]. Similarly the dislocation density due to microstrain can be calculated using [119]:

$$\rho_s = \frac{K\varepsilon^2}{F|b|^2} \tag{B5}$$

K is a material constant, ε is the strain, ρ_s is the dislocation density resulting from the strain, |b| is the magnitude of the Burgers vector and F is the interaction factor. Like in Equation 1.14, F is not a known value and can be assumed to be 1 in order to obtain a minimum dislocation density [119]. K is equal to 14.4 for a body centered cubic (BCC) structure with a Burgers vector along the [111]

direction. The two dislocation densities can then be combined to find the total dislocation density (ρ_{dis}) in the sample [119].

$$\rho_{dis} = (\rho_D \rho_s)^2 \quad \text{(B6)}$$

These equations were developed and used to find dislocation densities of annealed and cold worked Al and Fe. The values found ($2.7x10^7$-$3x10^8$ cm/cm^3 in annealed Al) corresponded well to those found with microbeam methods ($1.5x10^7$ cm/cm^3 in annealed Al) [119]. Bainite samples had dislocation densities on the order of 10^{13} cm/cm^3 upon plastic deformation [120]. Quenched duplex stainless steels tested showed dislocation densities on the order of 10^8 cm/cm^3, which increased up to 10^{12} cm/cm^3 upon shot peening of the surface [121]. The dislocation density was found to differ between ferrite and austenite, with ferrite having a lower dislocation density (10^{11} cm/cm^3) compared with austenite [122]. The expected range for X70 steels is 10^9-10^{10} cm/cm^3 [123].

B.1.2.2 Spherical Harmonics and Texture

XRD can be used to evaluate the preferential orientation or texture in a material. The two main methods of doing so are the March model and general spherical harmonics [117]. Both can be carried out in Topas; however, the spherical harmonics method was the one utilized in this work. Spherical harmonics give information on the orientation density function, i.e., which orientations are preferred. However, no information about grain size, shape or location is considered [124]. Polar axis densities can be obtained from the output spherical harmonics, which give information about specific crystallographic directions and the degree of their preference [112] [125] [126]. For the purposes of this work, an absolute magnitude of texture was sufficient to describe samples. This can be obtained with the texture index (J) [112]. The texture index (J) is obtained by using the spherical harmonics coefficients found using Rietveld refinement (C_l^{mn}) and Equation B7 [127].

$$J = 1 + \sum_{l=2}^{L} \frac{1}{2l+1} \sum_{m=-l}^{l} \sum_{n=-l}^{l} |C_l^{mn}|^2 \quad \text{(B7)}$$

A texture index (J) of 1 indicates no texture is present, while a single crystal would have an infinite texture index [112]. Practically, texture indices above three are normally the result of over fitting rather than an accurate representation of the magnitude of texture found in a material.

B.2: Experimental Results

Following the procedure detailed in Section 3.3.2 fitting was repeated for XRD patterns obtained from each of the L80 (Table B.0.1) and X70 samples (Table B.0.2), where each sample is numbered by its depth from the top surface of the skelp in mm.

Table B.0.1: L80 Parameters from XRD

Sample Depth (mm)	C_{41}	C_{61}	D_s (nm)	ε (unitless)	a (nm)
1	0.16	-0.06	143	1.11×10^{-3}	0.2869
2	0.26	-0.04	52	1.05×10^{-3}	0.2869
3	0.26	-0.05	115	1.16×10^{-3}	0.2869
4	0.13	0.03	29	5.70×10^{-4}	0.2869
5	0.20	-0.03	31	4.90×10^{-4}	0.2868
6	0.21	-0.05	31	4.30×10^{-4}	0.2869
7	0.24	-0.10	79	1.10×10^{-3}	0.2868
8	0.19	-0.12	114	1.19×10^{-3}	0.2869
9	0.13	-0.18	94	1.03×10^{-3}	0.2868

Table B.0.2: X70 Parameters from XRD

Sample Depth (mm)	C_{41}	C_{61}	D_s (nm)	ε (unitless)	a (nm)
1	0.03	0.07	32	1.11×10^{-3}	0.2872
2	0.04	-0.06	25	1.07×10^{-3}	0.2872
3	0.06	0.24	31	1.02×10^{-3}	0.2872
4	0.06	0.05	26	9.10×10^{-4}	0.2872
5	0.04	0.23	90	1.50×10^{-3}	0.2872
6	0.04	0.23	90	1.50×10^{-3}	0.2872
7	0.00	-0.06	72	1.82×10^{-3}	0.2872
8	0.13	-0.06	81	1.50×10^{-3}	0.2872
9	-0.04	-0.38	75	1.74×10^{-3}	0.2872
10	0.32	-0.29	94	1.50×10^{-3}	0.2872
11	0.17	-0.09	83	1.33×10^{-3}	0.2872
12	0.22	-0.30	45	1.37×10^{-3}	0.2872
13	0.15	-0.56	40	1.58×10^{-3}	0.2872
14	0.15	-0.34	47	1.79×10^{-3}	0.2872
15	0.32	-0.10	44	1.17×10^{-3}	0.2872

The parameters obtained from Rietveld refinement were then used to find the dislocation density (ρdis) and texture index J. The dislocation density was found using the domain size and microstrain values from XRD with Equations 1.14, 1.15 and 1.16. For the sample pattern shown in Figure 3.16, the dislocation density was found to be 2.88×10^{10} cm/cm^3. The values agree with the 10^9-10^{10} cm/cm^3 dislocation density measured in other X70 steels with TEM [123]. The spherical harmonics coefficients were used with Equation B.7 to find the texture index, which indicates the magnitude of preferred orientation present within a material. In this case, the texture index was

1.00 which indicates that this sample does not show any preferred orientation or texture. These calculations were then repeated for all L80 (Table B.0.3) and X70 (Table B.0.4) samples.

Table B.0.3: L80 Calculated Dislocation Density and Texture Index from XRD

Sample	ρ_{dis} (cm/cm^3)	J
1	2.06E+10	1.003
2	5.32E+10	1.007
3	2.66E+10	1.008
4	5.17E+10	1.002
5	4.19E+10	1.005
6	3.71E+10	1.005
7	3.70E+10	1.007
8	2.77E+10	1.005
9	2.89E+10	1.004

Table B.0.4: X70 Calculated Dislocation Density and Texture Index from XRD

Sample	ρ_{dis} (cm/cm^3)	J
1	9.07E+10	1.000
2	1.15E+11	1.000
3	8.84E+10	1.005
4	9.43E+10	1.001
5	4.40E+10	1.004
6	4.40E+10	1.004
7	6.69E+10	1.000
8	4.91E+10	1.002
9	6.13E+10	1.011
10	4.23E+10	1.017
11	4.23E+10	1.004
12	8.03E+10	1.012
13	1.05E+11	1.027
14	1.01E+11	1.011
15	7.09E+10	1.012

B.3 Through Thickness XRD Analysis

The material properties determined using Rietveld refinement of XRD patterns were compared through the thickness of each skelp. Those found directly from the Rietveld refinement, i.e., domain size and microstrain, are presented first followed by those calculated after Rietveld refinement, i.e., texture index (J) and dislocation density, for the X70 skelp and then the L80 steel.

B.3.1 X70 Through Thickness XRD

Rietveld refinement was done on each of the X70 through thickness samples to generate both domain size and microstrain values. In rolled product such as pipe skelp the domain size most likely corresponds to a subgrain or cell size and not the grain size [1]. Subgrains are regions bounded by misorientations less than 15°, while cells are regions of much less than average dislocation density bounded by very small misorientations [118]. Figure B.0.2 shows the variation in these parameters with skelp thickness.

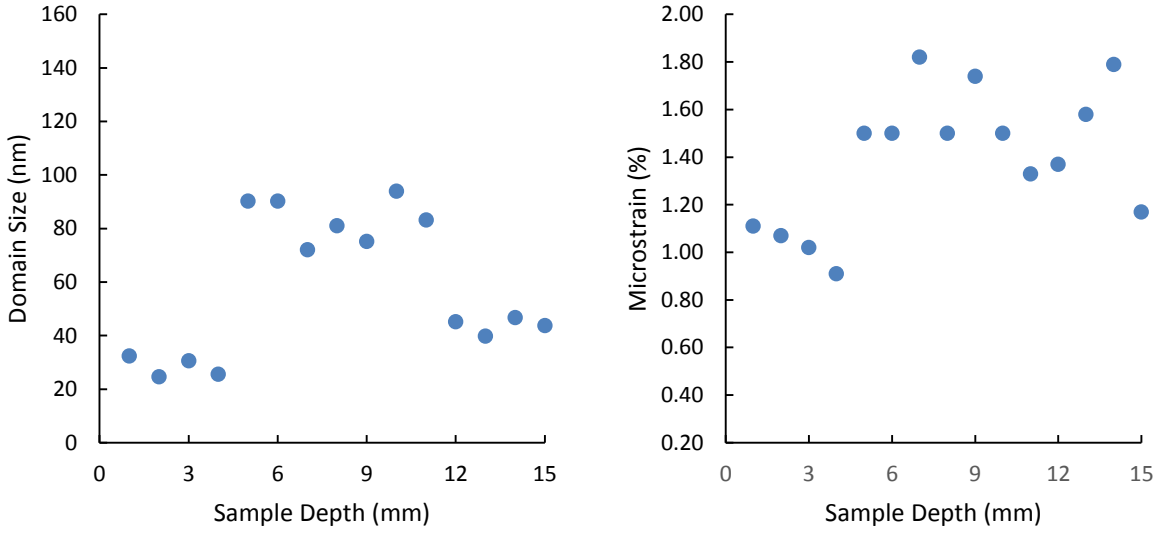

(A) (B)

Figure B.0.2: X70 Rietveld Refinement Output Parameters

It is interesting that the domain size is smaller closer to either face of the skelp and larger in the center. This is likely the result of the rolling process; however, since the exact processing of either skelp is not known it is difficult to accurately correlate this phenomena to rolling procedure. The domain size is also very small in the X70 skelp; none of the average subgrain sizes exceed 100 nm. The change between them is also not large, with a maximum difference of only about 70 nm. The small sizes observed suggest that it is the cell size not the subgrain size which is being detected [118]. The microstrain shows a band of low values at a depth of 1-4 mm, which corresponds with the smaller subgrain size found near the surface of the skelp. However, the microstrain near the

surface of the opposite face are scattered with values closer to those near the center of the skelp. This could be the result of different cooling rates for the two faces or some other difference in processing for the two faces of the skelp. The microstrain are all within 1% of one another so they are very similar. Since the error in measurement is not known, these trends could be the result of scatter and not processing differences as postulated.

Further information can be obtained by calculating the dislocation density and texture index from parameters output by the Rietveld refinement. The dislocation density (ρ_{dis}) can be calculated from the microstrain and subgrain size values. The spherical harmonics coefficients output by the Rietveld refinement are also used to determine the texture index (J) for each sample. A value of one signifies random orientation and values far from one indicate a preferred orientation. The calculated parameters from Rietveld analysis are shown in Figure B.0.3.

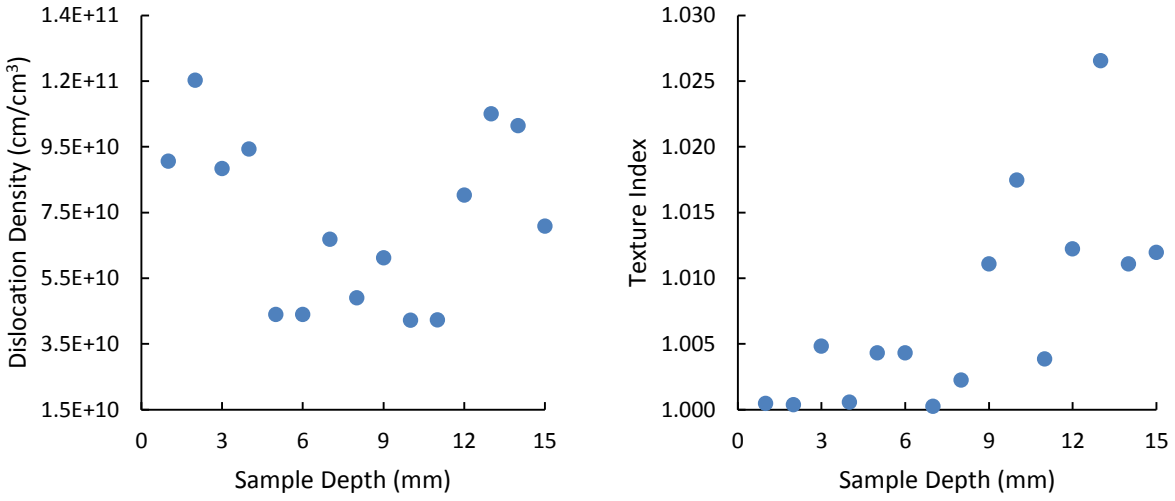

(A) (B)

Figure B.0.3: X70 Calculated Parameters from Rietveld Refinement

The dislocation density is higher in the samples close to either face of the skelp. The values are larger than expected (10^9-10^{10} cm/cm^3) [123], especially since the K and n values in Equations 1.14 and 1.15 were set to one which should give minimum dislocation densities. The dislocation densities near the surface are close to those found in shot peened stainless steel ferrite (10^{11} cm/cm^3) [122]. The dislocation densities found in the center of the skelp (3-7x10^{10} cm/cm^3) are not far from those found for a different X70 steel (10^9-10^{10} cm/cm^3) [123]. This, along with the smaller subgrain size near the faces, suggests that more cold work and plastic deformation could have been done during processing to the faces than the center of the skelp. This makes sense since the skelp is reduced in thickness by rolling which applies forces to both faces of the skelp, so more work is done near the surface than the center, which increases the dislocation density at the faces relative to the center.

The texture index appears to increase from the top face of the skelp to the bottom face. It is more likely; however, that this is random scatter and not a real trend. The largest texture index was 1.027, which is still quite close to 1. Work done by Li showed maximum texture indices in the center of X80 and X100 skelp, with values of 1.2 for X80 and 1.3 for X100 [1]. These values are much higher than the maximum found for the X70 skelp. It follows that there is little texture or preferred orientation within the X70 skelp. The Rietveld refinement then shows that there is some variation in parameters between the center and surfaces of the skelp, but generally there is good consistency of properties through the skelp thickness.

B.3.2 L80 Through Thickness XRD

The Rietveld refinement parameters obtained from the L80 skelp show similar patterns for both microstrain and domain size. Both parameters are shown in Figure B.0.4 as a function of L80 skelp thickness.

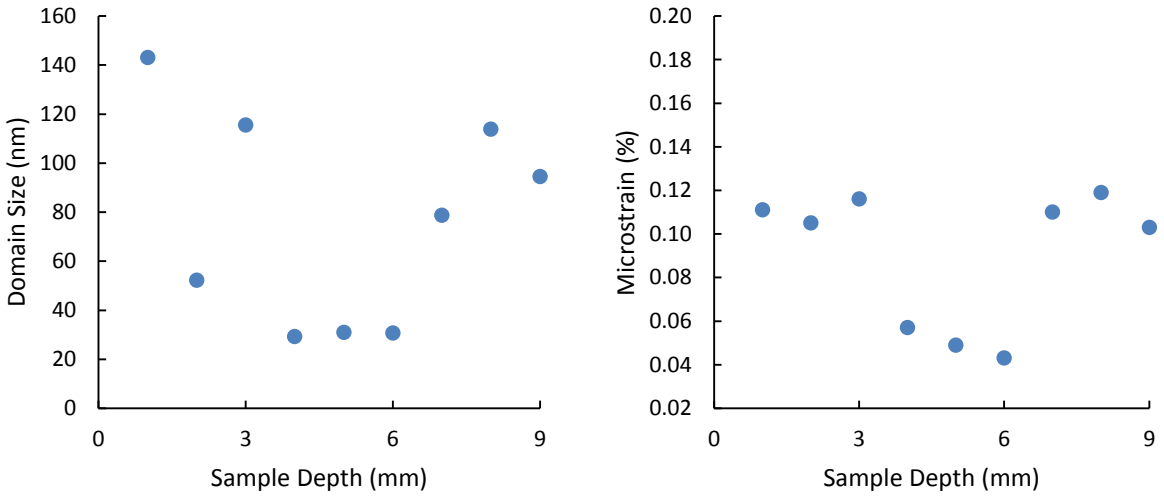

(A) (B)

Figure B.0.4: L80 Rietveld Refinement Output Parameters

Both the domain size and microstrain are higher close to the faces of the skelp relative to the center. The domain size distribution is larger in L80 than X70, with a maximum of 143 nm compared with 94 nm for X70. Additionally, the dependence with sample depth is opposite for L80 compared with the dependence for X70 with the maximum domain sizes for L80 near the faces of the skelp, whereas the minimum domain values were near the faces for X70. The microstrain is higher near the faces of the skelp than the center, which was not the case for X70. These differences are likely the result of differing rolling processes for the two steels. The X70 steel receives no further processing besides pipe forming after rolling; however, the L80 steel is quench and tempered after pipe forming. The L80 pipe is austenitized after pipe forming, so homogeneity of the through thickness properties of the skelp is less important and processing parameters like cooling rates do

not need as much control as in the X70 skelp. The microstrain, subgrain size and spherical harmonics coefficients can be used to calculate the texture index and dislocation density for the L80 steel (Figure B.0.5).

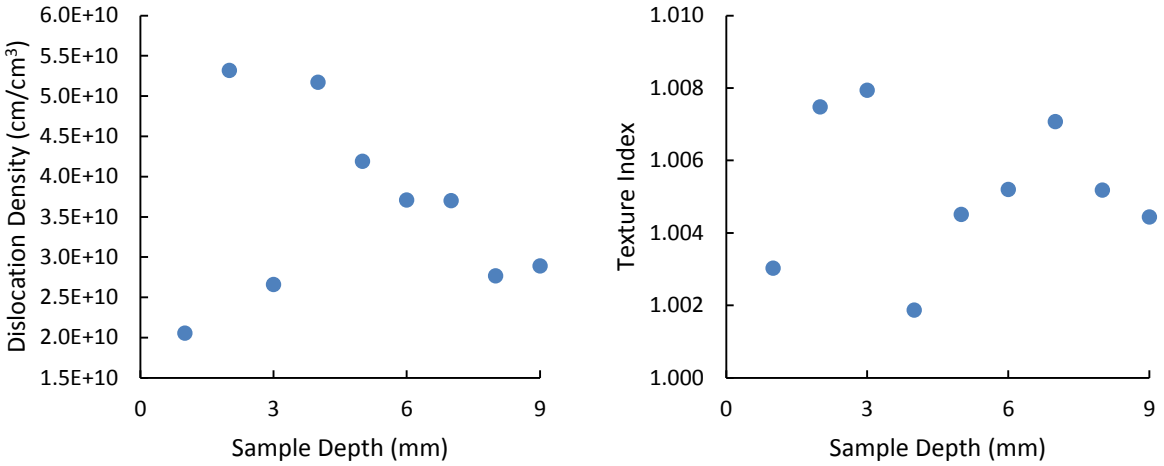

(A) (B)

Figure B.0.5: L80 Calculated Parameters from Rietveld Refinement

The increase in microstrain and domain size close to the faces of the skelp results in dislocation densities which are not significantly different from those found in the center. It can be seen in Equation 1.14 that an increase in domain size decreases the dislocation density while an increase in microstrain in Equation 1.15 increases the dislocation density. These two effects essentially cancel one another in the L80 skelp and the dislocation density shows little change through the thickness. The dislocation densities ($1.5\text{-}5.5\text{x}10^{10}$) agree with literature values for other rolled plates ($10^{9}\text{-}10^{10}$ cm/cm^3) [123]. This is different from the X70 skelp, which showed increased dislocation density near the faces. It is possible that the L80 has been exposed to less finish rolling and, thus, less cold work. This would result in lower dislocation densities near the faces of the skelp which are finish rolled less. This makes sense since any work done on the microstructure during finish rolling would be undone when the pipe is austenitized. Since working the skelp is easier when it is hot, it is likely that little of the final deformation of the skelp is done at cool finish rolling temperatures in favour of easier hot rolling; however, some finish rolling is likely done as the microstrain increases near the faces compared with the center.

The texture index does not differ significantly through the skelp thickness. The texture index stays below 1.01, indicating little if any preferred orientation. There is no increase through the thickness as seen in the X70 and the texture index values have less scatter. The skelp does appear banded in the micrographs in both the rolling direction and transverse direction (Figure 4.6). Rietveld refinement shows an increase in subgrain size and microstrain close to the faces of the skelp and consistent dislocation density and texture index through the entire skelp thickness.

B.4 Rietveld Refinement and Ultrasonic Properties

Comparisons were made between the ultrasonic properties in each sample and the corresponding parameters determined by Rietveld refinement. Each parameter is presented below with ultrasonic properties of interest for each.

B.4.1 Texture Index

The orientation of grains was shown to be an important factor in determining the ultrasonic velocity in Sections 2.2 and 2.5. The texture index is a measure of preferred orientation within a sample. Figure B.0.6 shows that all three ultrasonic velocities remain roughly constant as the texture index increased slightly in all the samples tested.

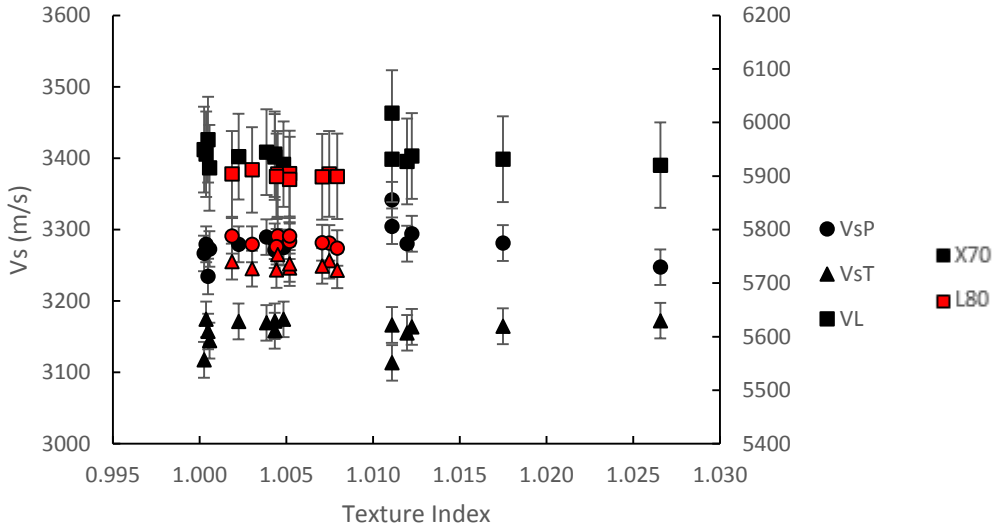

Figure B.0.6: Ultrasonic Velocity vs. Texture Index for Both L80 and X70 Samples

The only velocity which shows any significant variation with texture is the transverse shear velocity (VsT). This difference in VsT velocities from a texture index of approximately 1-1.01 is caused by the L80 skelp VsT being faster than that in the X70. The lack of any apparent trends is likely due to the change in texture index being very small, only 0.03; it is likely that the ultrasonic velocities are not sensitive to such small changes. This also agrees with the analysis from Section 4.1.1 where the experimental velocities were close to the average calculated velocities (based on a 1050 steel), indicating little preferred orientation. The velocities furthest from the averages were VsT, which also show variation with texture index. This again indicates that VsT is sensitive to some microstructural change between each experimental skelp, as well as some difference from the 1050 steel used as a basis for the calculated velocities.

The ultrasonic attenuation was also compared with the texture index to look for any correlation. The longitudinal attenuation (AL) vs. texture index is shown in Figure B.0.7.

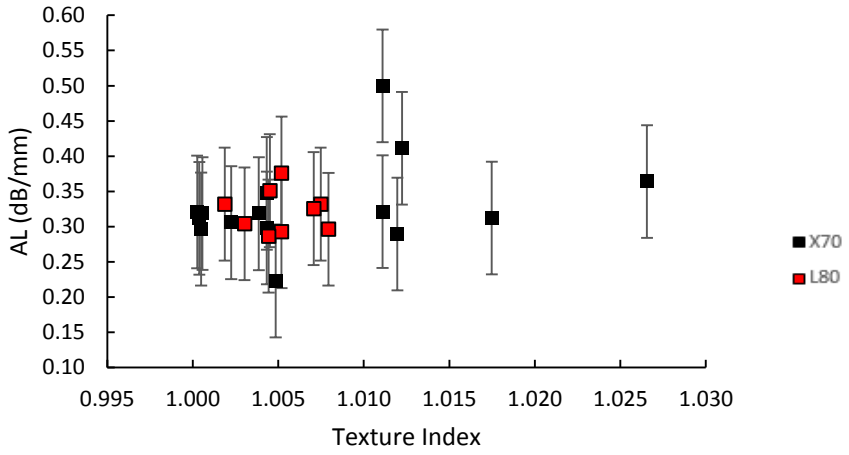

Figure B.0.7: Longitudinal Attenuation vs. Texture Index for X70 and L80 Steel

The longitudinal attenuation appears to increase slightly as the texture index increases, however, the values are within error of one another with the exception of two outliers which makes the validity of this trend suspect. Similarly a clear conclusion cannot be drawn from the shear attenuations due to the scatter in the data and error in the measurements (Figure B.0.8).

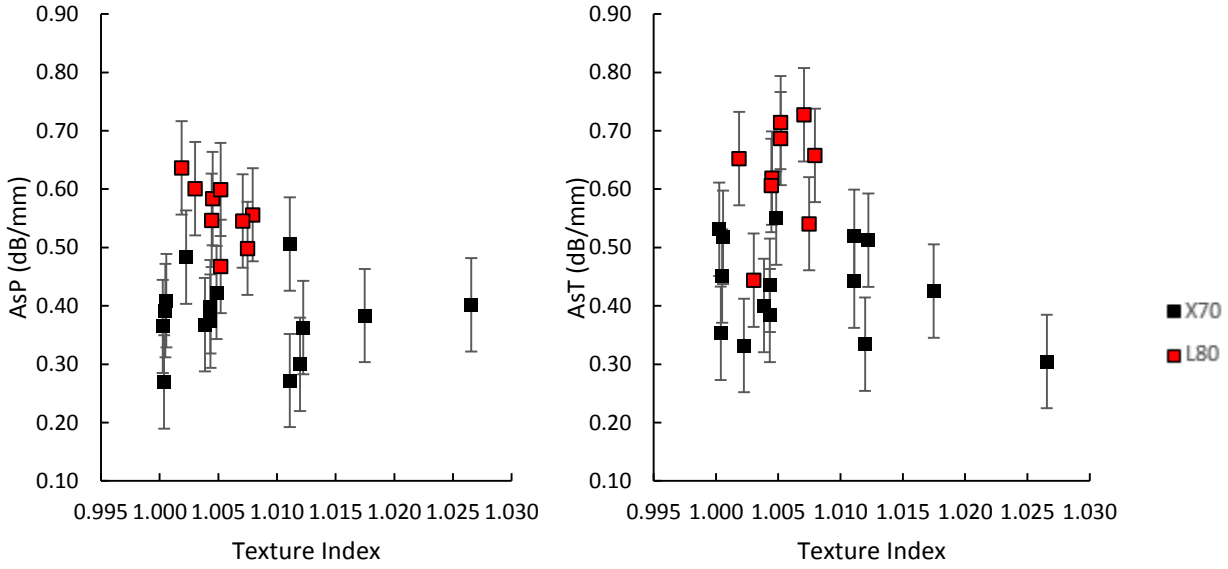

(A) (B)

Figure B.0.8: (A) Transverse and (B) Parallel Shear Attenuation vs. Texture Index for X70 and L80 Steel

The large scatter in shear attenuation values is likely due to couplant effects, since there is less scatter in the longitudinal values. The attenuation of a wave was shown to be affected by orientation in a zinc bar by Papadakis [58]. The limited range of texture indices made confirmation of these trends difficult. The slight dependence of attenuation on texture may disappear at higher texture values. Further samples with a greater amount of texture would have to be tested in order to validate the observed trends.

B.4.2 Dislocation Density

The ultrasonic shear wave attenuations decreased as the dislocation density increased for all samples tested. The trend was particularly apparent for parallel shear waves (AsP) compared with those transverse to the rolling direction (AsT), as shown in Figure B.0.9.

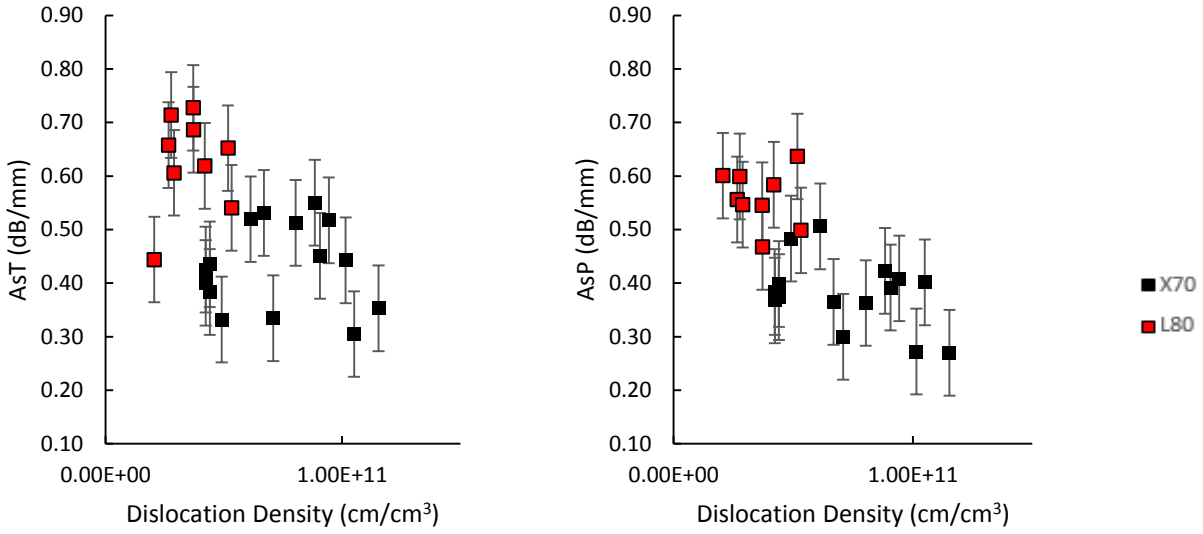

(A) (B)

Figure B.0.9: (A) Transverse and (B) Parallel Shear Attenuation vs. Dislocation Density For X70 and L80 Steel

This trend is in agreement with the literature presented in Section 1.5.5. The difference in the amount of scatter for the transverse and parallel shear waves could be the result of testing methodology. The transverse tests were done first, followed by the parallel tests without removing the transducer from the sample. The couplant could have significantly more time to spread and approach a sort of equilibrium, resulting in more consistent attenuation readings. The trend for shear wave attenuation as a function of dislocation density was not present for longitudinal values (Figure B.0.10). There is no variation, other than some scatter, for AL as a function of dislocation density. This is similar to the behaviour for texture index, shown in Figure B.0.7, where there is little real change in the values. This indicates that longitudinal waves are less sensitive to both dislocation density and texture index when compared to shear waves.

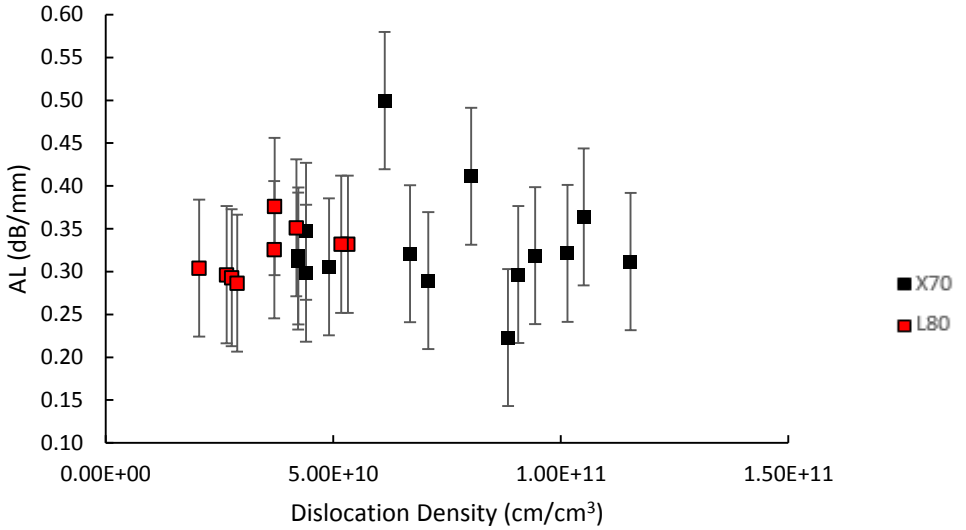

Figure B.0.10: Longitudinal Attenuation and Dislocation Density for X70 and L80 Steel

B.4.3 Microstrain

The microstrain values are compared to the shear wave birefringence, i.e., the difference between maximum (VsP) and minimum (VsT) shear wave velocities, in Figure B.0.11. There is a distinct increase in shear birefringence as the microstrain increases. Birefringence was shown by Creecraft to relate well to applied stress [52]. The relationship shown in Figure B.0.11 also shows a good relationship between birefringence and microstrain. The shear birefringence was also compared with other Rietveld parameters, but none showed significant trends. Shear birefringence is then a good indicator of microstrain within similar samples.

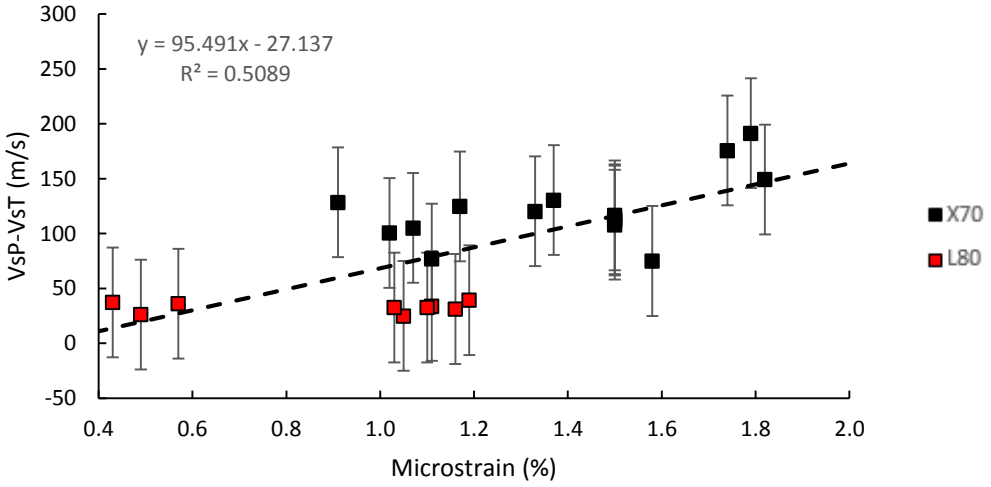

Figure B.0.11: Shear Wave Velocity Birefringence vs. Microstrain for X70 and L80

B.4.4 Domain Size

The attenuation of an ultrasonic wave is greatly affected by the grain size in the steel [64], [65]. Since this correlation was known, the ultrasonic attenuations were compared to the domain sizes determined by Rietveld refinement. The relationship between domain size and shear attenuation is shown in Figure B.0.12.

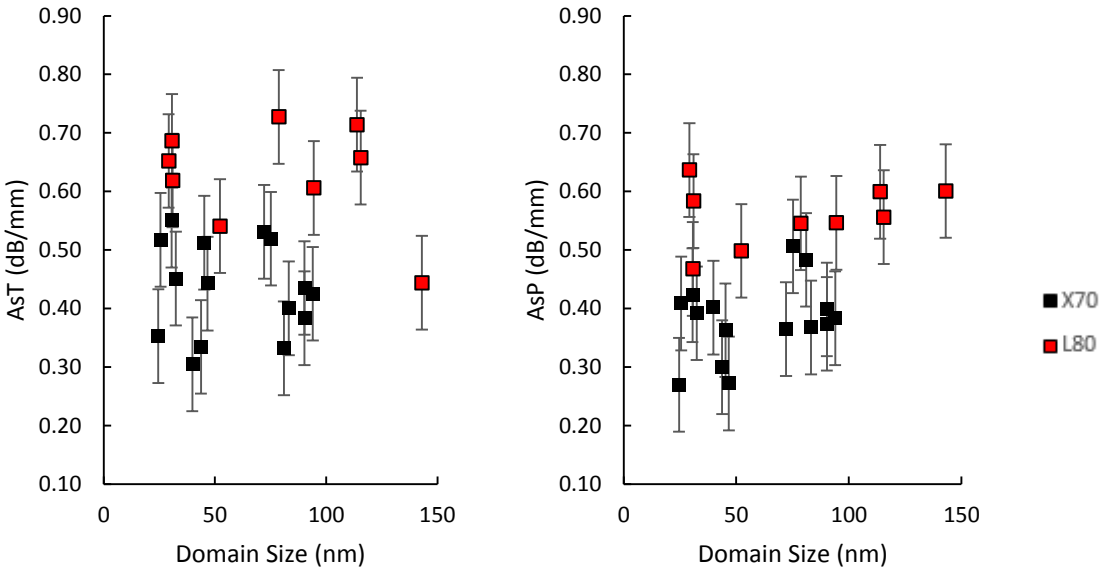

(A) (B)

Figure B.0.12: (A) Transverse and (B) Parallel Shear Wave Attenuation vs. Domain Size for X70 and L80 Steel

There is significant scatter in the shear attenuations. The wavelength of the shear waves is approximately 300 µm, which is much greater than the domain size. The domain sizes are in the Rayleigh regime for ultrasonic attenuation where the increase in size should result in an increase in attenuation [65]. However, in order for grains to have an effect on scattering they need to be at least 0.01x the wavelength [21] or in this case, 300 nm. The shear waves parallel to the rolling direction exhibit behavior to be expected in the Rayleigh regime, but not the transverse direction, as seen in Figure B.0.12. It is also not the case for the longitudinal waves shown in Figure B.0.13.

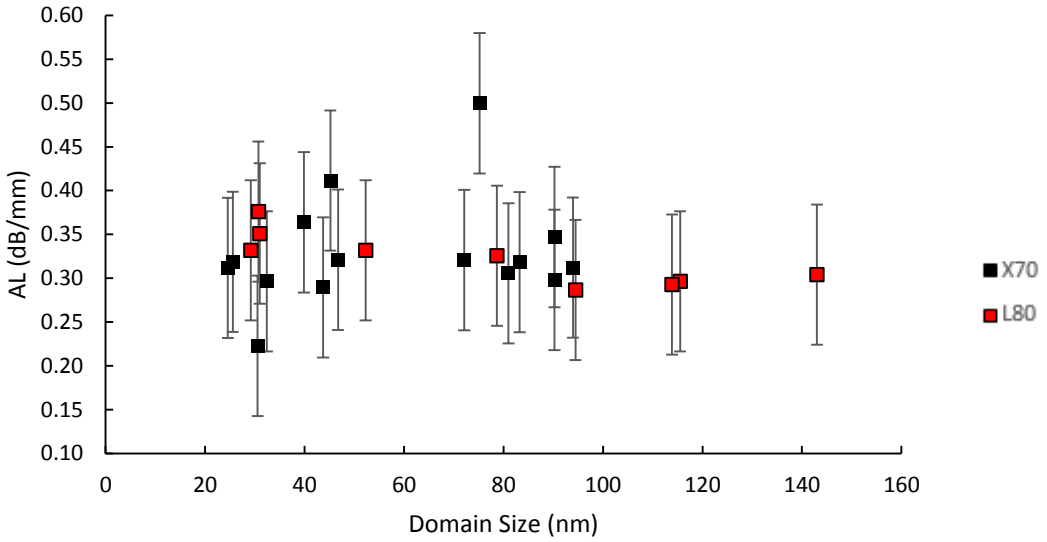

Figure B.0.13: Longitudinal Attenuation (AL) vs. Domain Size for X70 and L80 Steel

It is possible that the lack of correlation is because it is the domain size and not grain size being analyzed. If the domain sizes correspond to the subgrain or cell size [118] as discussed in Sections 4.1.3.1 and 1.6.2, they may have a different effect on attenuation than grain size. The waves which have particle motion through the skelp thickness (AL) or across the width of the skelp (AsT) show no relation between the reported domain size and attenuation. The shear waves which have particle motion along the rolling direction (AsP) seem to display Rayleigh scattering behavior, i.e., they attenuate more as the domain size increases. It is possible that the grains are elongated more along the rolling direction than the transverse direction or through thickness. The grain boundaries should have a greater effect on attenuation than the domain boundaries due to their higher misorientation angle. The shape of the subgrains or cells are not given by the Rietveld refinement. If the domains are equiaxed there would be more domain boundaries per grain along the rolling direction than the transverse or through thickness. If the through thickness and transverse oriented waves have a higher grain boundary to domain boundary ratio, the effect of the domain boundaries would be reduced compared with the rolling direction.

B.5 XRD Analysis Summary

Dislocation densities determined from XRD were on the order of 10^{10}-10^{11} cm/cm^3 with L80 on the lower end and X70 on the higher end. The domain sizes and microstrains were found to vary between the center and faces of each skelp, while neither had texture indices significantly greater than one. The variation in texture index was too small to draw any significant conclusions between texture and ultrasonic velocity. Ultrasonic attenuation decreased as dislocation density increased for shear waves but not for longitudinal waves. The microstrain related well to the shear wave birefringence; increased microstrain resulted in increased birefringence. Domain size

did not have a large effect on attenuation; there is some increase in the AsP with increasing domain size, but no effect on AsT or AL. The trends found between the ultrasonic properties and microstructural characteristics in the skelps are not particularly clear and have significant scatter. It is possible that some of this could be the result of work being done on the samples during machining affecting the results obtained with XRD (increased dislocation density and affecting domain size) [1].

Appendix C: Further Information for Future Work - Waveform Analysis

The current Socomate USPC7100LA used in the laboratory for ultrasonic testing does not output the entire waveform of the ultrasonic test but only the peak height and time within each gate. If more complex waveform analysis is required in the future then modification of the current equipment and Labview program should be investigated before new equipment is purchased. The Socomate USPC7100LA has its own proprietary software for controlling the card, the location of gates, frequency of pulses, gain added to pulses, etc. The card can also interface with Labview to output different information; the default Labview program included with the card can output B and C scans in addition to the A scans used in this work. This Labview program was modified in order to provide a 5 ns resolution (the resolution of the card itself) to the time of peaks found within gate 1. It is possible that there is a location in the Labview code which has the waveform as a possible output. If this is needed by someone not comfortable or experienced in writing Labview code the computer and card should be taken to an instrument technician to investigate this possibility and to modify the current Labview program to output the waveform if possible.